



UiT The Arctic University of Norway

Faculty of Science and Technology

Department of Physics and Technology

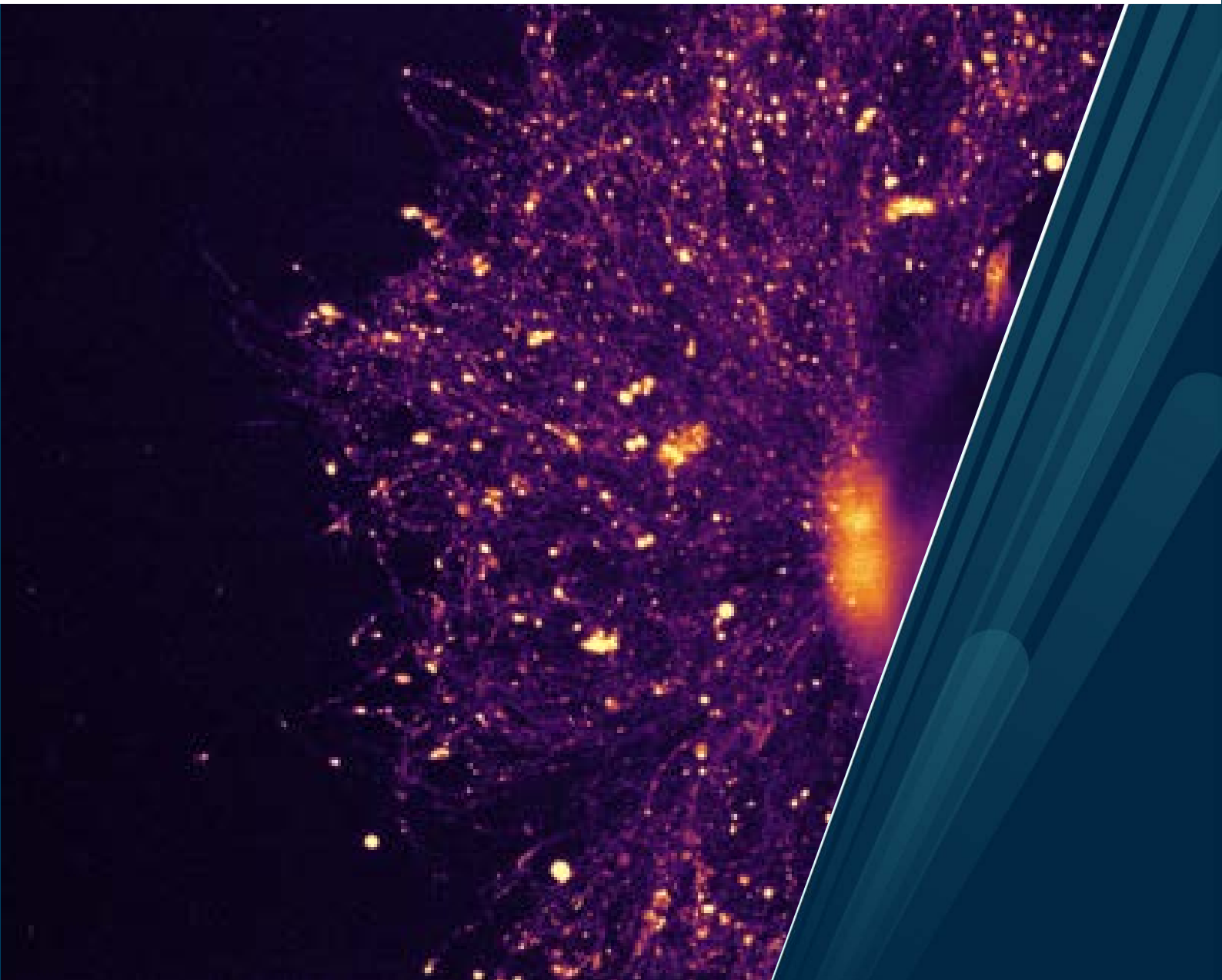
Bringing optical nanoscopy to life

Super-resolution microscopy of living cells

Ida S. Opstad

A dissertation for the degree of Philosophiae Doctor in Science

November 2020



*To the fantastic international community of Tromsø.
You make our town warm and thriving.*

*“Shall I refuse my dinner because I do not
fully understand the process of digestion?”*
–Oliver Heaviside

Abstract

Introduction: We want to see, learn and understand the fantastic machinery of *living* cells that every second performs tasks so perplexing that even after decades (or centuries) of scientific investigation, satisfying or definite answers might still be missing. In other words, detailed pictures of chemically-preserved specimens are insufficient and getting old.

The wonders are all around us: photosynthesis allows plants to grow and develop seemingly effortlessly; or ourselves, requiring coordinated tasks between billions of different cells to constitute a functioning body. Sometimes we become less well-functioning and might need the hospital. We might automatically heal ourselves, or our cells might eventually stop their coordinated efforts and disassemble to something different from living.

Biomedical research is about understanding us and the billions of living cells we are composed of, together with the stuff between cells and the stuff they interact with or seemingly ignore. Cellular morphology and functions under both healthy and diseased conditions are central topics in both pathology and biological research. Microscopy is possibly the best tool we have to peer into the microscopic world to enhance our understanding of the usually invisible, but highly complex and vital events taking place.

For example, just a century ago, how new humans were made was a big mystery. Today we know that they do not come as pre-made miniatures from the male, but are developed from the lucky encounter between two special cell types, one from the male and one from the female. We can even start human development in a dish, with both the parents obeying social distancing and even keeping their virginity for that matter. The technique is known as IVF, or *in vitro* fertilization, and would have been impossible without a microscope.

Microscopy is brilliant, but also has its physical constraints and technical limitations. Technical advances have in the last decade pushed optical microscopy past physical limits previously thought unbreakable by the introduction of super-resolution optical microscopy techniques, also referred to as optical nanoscopy.

This thesis is about bringing the recent advances in super-resolution optical microscopy to applications in living cells. It is a part of the *UiT Tematiske Satsinger* program, aiming to strengthen interdisciplinary research and collaboration between traditionally separate fields of science. It has allowed me many visits from the Physics department to, for example, the Medical and Pharmacy departments, and made exciting samples readily available for the quickly expanding line of new and high-end microscopes available at Physics.

Three imaging modalities with good prospects for the future of live-cell nanoscopy are covered: structured illumination microscopy (SIM), fluorescence fluctuation-based super-resolution microscopy (FF-SRM) and photonic chip-based total internal reflection fluorescence microscopy (C-TIRFM). In addition to their potential for gentle illumination and imaging under live-cell friendly conditions, these techniques were chosen over other imaging modalities (like STED or Airyscan) due to the system availability.

Results: SIM was found suitable for up to four-color volumetric and wide-field super-resolution imaging of living cells, but yet following fast, multicolor subcellular dynamics remains extremely challenging mainly due to technical constraints from the necessary light dose and acquisition time.

FF-SRM was found, for most current applications in bio-imaging, underdeveloped. While there seems to be a huge yet unharnessed potential for FF-SRM in future live-cell imaging applications, the tested techniques were found too simplistic and unrealistic in their basic sample assumptions. We developed an FF-SRM reconstruction software with improved computational speed and ease of use. Although large challenges were encountered, the FF-SRM method MUSICAL was employed with success in combination with machine learning for the analysis of nanoscale motion patterns of subcellular vesicles.

The reduction of background signal achieved by using TIRFM is widely exploited in super-resolution microscopy. The recently developed C-TIRFM, allowing for extreme FOVs compared to traditional implementations of TIRFM, was adapted for live-cell imaging applications. Multimodal imaging of living hippocampal neurons in a custom-made incubation chamber was shown on photonic waveguides. Furthermore, the exploitation of multimodal waveguide illumination patterns for super-resolution imaging via MUSICAL image reconstruction was demonstrated.

Overall, although many challenges have been encountered, and there are many factors that can still be improved, the fields of both conventional and super-resolution microscopy have already lots of opportunities to offer for researchers looking at small stuff, for both cases of static and dynamic samples.

Outline: The first chapter provides background knowledge to better appreciate the article summaries and results are presented in Chapter 2. In Chapter 3, the work is summed up, and in Chapter 4, future work and recent technical advances in the field of live-cell super-resolution microscopy are discussed. The complete published articles are contained in Appendices A-G.

Acknowledgements

As in most of modern science, the work and articles behind this thesis are a collaborative effort. It has been a great pleasure and honour to collaborate with so many fantastic human beings and scientists from, not all, but a significant portion of the world, in particular the ones from India, Germany, England, USA, Iceland, Bangladesh, Sweden, Romania, Chile, Nepal, Russia, Ethiopia, Brazil, Australia, China, the Netherlands, Austria, and (I should not forget) Norway.

First and foremost I would like to express my warmest gratitude to my main Ph.D. supervisor, Prof. Balpreet Singh Ahluwalia, who enabled my Ph.D. studies and research work. You have been a steady support under all weather conditions and encouraged me to follow my dreams and intuition.

Many thanks to my co-supervisor Assoc. Prof. Krishna Agarwal for persistent energy and drive in solving analytical challenges for live cell friendly nanoscopy. You have placed my foot inside the circle of artificial intelligence and its naturally intelligent developers. You have offered me a smooth transition to an intriguing Ph.D. afterlife and scooped your postdoc.

I am grateful to my co-supervisor Dr. Sören Abel for patiently introducing me to the basics of molecular and microbiology, and to the other lab members of the Infection Biology Research Group supporting me in the art of cloning and microbiology, especially Merete Storflor, Øyvind Myrvoll Lorentzen and Dr. Bhupender Singh.

Warm gratitude to Dr. Deanna Lynn Wolfson, Dr. Jean-Claude Tinguely and Dr. Habib Anowarul for excellent lab management and support. The work of our optics-related groups would be impossible without you.

The necessary expertise, experience and sample availability of human spermatozoa for the related microscopy work were brought by Daria Aleksandrovna Popova, Prof. Purusotam Basnet (both in the Women's Health and Perinatology Research Group) and the Tromsø IVF clinic. It was a great pleasure working with and being taught by you.

Cell cultures derived from heart tissue, their gene modifications and related expertise were faithfully provided by Assoc. Prof. Ása Birna Birgisdottir and Trine Kalstad in the Clinical Cardiovascular Research Group. Always a pleasure collaborating with you!

The implementation of MUSICAL for ImageJ and computational speed-up was achieved by Sebastian Andres Acuña Maldonado. Its excellent user interface was brought to life in collaboration with Dr. Florian Ströhl. In both of you, I greatly appreciate the responsiveness, bold optimism and solution-oriented mindset.

The fluorescence fluctuation-based super-resolution microscopy comparative study was done in collaboration with other Ph.D. students who individually brought their expertise on their samples: Luís Enrique Hernandez Villegas on tissue preparation, Jennifer Cauzzo on the preparation of liposomes, and Sebastian Andres Acuña Maldonado on generation of synthetic samples via the simulation of microscopy image data for a broad range of samples and imaging conditions.

Dr. Arif Ahmed Sekh and Prof. Dilip K. Prasad provided expertise on machine learning and conducted the related computational experiments and analysis. I appreciate that you let me be part of your team with ambitious goals, impossible deadlines and crazy working hours. I am looking forward to the continuation.

The ChipScope setup and related work on primary neurons at Cambridge University (UK) was generously supported by Prof. Clemens Kaminski, head of the Laser Analytics group. The contributions of many of his lab members were invaluable: Dr. Florian Ströhl designed and built the imaging system, Marcus Fantham programmed the microscope control software, Colin Hockings excised and cultivated primary rat hippocampal neurons, Francesca W. van Tartwijk excised *Xenopus* eye primordia and cultivated retinal ganglion cells, both cell types grown on photonic waveguides. Oliver Vanderpoorten made the heating and temperature control system for the ChipScope incubation system. Thank you all for making my research stay fruitful and unforgettable!

Waveguide design, production and expertise were contributed by Dr. Jean-Claude Tinguely, Dr. Firehun Tsige Dullo and Dr. Anish Priyadarshi. Thanks for your efforts and patience!

The FishScope, the newly installed chip imaging system at UiT with specialized features for high-resolution microscopy of fast-migrating arctic aquamarine species, was designed, built and synchronized by Daniel Henry Hansen. I am grateful that you could find the time and creativity amid your many

requests.

Samples from Atlantic salmon and related expertise on cell cultivation and fish biology were contributed by Assoc. Prof. Tore Seternes and Prof. Roy Ambli Dalmo at the Norwegian College of Fishery Science. I suspect we will have some future fishy business.

Warm gratitude to Dr. Deanna L. Wolfson, Assoc. Prof. Krishna Agarwal, Dr. Florian Ströhl, and Prof. Balpreet S. Ahluwalia for careful reading and providing useful feedback on my thesis.

My Ph.D. student position was funded by the *UiT Tematiske satsinger* program. Additional contributions are listed in the funding of the published articles.

Contents

Abstract	iii
Acknowledgements	vii
List of Figures	xiii
Glossary	xv
List of Abbreviations	xvii
1 Introduction	1
1.1 Optical microscopy in biology	1
1.1.1 Subcellular structures and fluorescent probes	4
1.1.2 Fluorescence microscopy	4
1.1.3 Imaging conditions and phototoxicity	6
1.1.4 The diffraction limit of optical resolution	9
1.1.5 Deconvolution microscopy	13
1.2 Optical nanoscopy	16
1.2.1 General approaches	16
1.2.2 Structured illumination microscopy	18
1.2.3 Fluorescence fluctuation-based techniques	21
1.2.4 Assessing image quality and resolution	23
1.3 Machine learning in microscopy	27
1.4 Total internal reflection fluorescence microscopy	29
1.4.1 Principle and applications	29
1.4.2 Optical waveguides	33
1.4.3 Implementations	35
2 Summary of articles	39
2.1 Structured illumination microscopy	39
2.1.1 Multi-color imaging of sub-mitochondrial structures in living cells using structured illumination microscopy	39
2.1.2 Live-cell imaging of human spermatozoa using SIM .	41

2.2	Fluorescence fluctuation-based super-resolution microscopy imaging	43
2.2.1	Adaptive fluctuation imaging captures rapid subcellular dynamics	43
2.2.2	MusiJ: an ImageJ plugin for video nanoscopy	44
2.2.3	Learning nanoscale motion patterns of vesicles in living cells	46
2.2.4	Fluorescence fluctuations-based super-resolution microscopy techniques: an experimental comparative study	49
2.3	Chip-TIRF	51
2.3.1	A waveguide imaging platform for live-cell TIRF imaging of neurons over large fields of view	51
2.3.2	FF-SRM using waveguided multimode illumination	54
3	Synthesis	57
4	Future work	61
	Appendices	63
A	Multi-color imaging of sub-mitochondrial structures in living cells using SIM	65
B	Live-cell imaging of human spermatozoa using SIM	79
C	Adaptive fluctuation imaging captures rapid subcellular dynamics	87
D	MusiJ: an ImageJ plugin for video nanoscopy	91
E	Learning nanoscale motion patterns of vesicles in living cells	105
F	Fluorescence fluctuations-based super-resolution microscopy techniques: an experimental comparative study	117
G	A waveguide imaging platform for live-cell TIRF imaging of neurons over large fields of view	135
H	Complete list of published articles	143
I	Scientific dissemination and exchange	145
	Bibliography	147

List of Figures

1.1	Subcellular components	2
1.2	Brightfield, fluorescence, and electron microscopy images . .	3
1.3	Fluorescence spectrum	5
1.4	Jablonski diagram	6
1.5	Apoptosis vs. necrosis	8
1.6	Alteration in mitochondrial morphology by phototoxicity . .	10
1.7	Airy function and the resolution limit	10
1.8	Refractive index and numerical aperture	12
1.9	Convolution	14
1.10	3D SIM images of mitochondria	17
1.11	Moiré patterns	18
1.12	Raw SIM data	19
1.13	Resolution measurements	24
1.14	Artificial intelligence	28
1.15	TIRF principle	30
1.16	Axial and lateral PSFs for 1.1 NA and 0.3 NA objectives . . .	31
1.17	Comparison of TIRF and EPI images	32
1.18	Schematic layout of an optical fiber	33
1.19	Waveguide geometries	34
1.20	TIRF options	37
2.1	Three-color 3D SIM image of mitochondria	40
2.2	Four-color 3D SIM of spermatozoa	42
2.3	Rapid, live-cell MUSICAL	43
2.4	MUSICAL algorithm	45
2.5	MusiJ GUI	46
2.6	Vesicular motion states	48
2.7	Summary of FF-SRM comparative study	50
2.8	ChipScope live-cell imaging setup	52
2.9	Multimodal TIRF imaging	53
2.10	Retinal growth cones	53
2.11	Fish-on-chip MUSICAL	55

Glossary

Diffraction is the bending of light waves as they interact with an object.

Diffraction limit is the theoretical best resolution offered by a conventional optical microscope.

Endocytosis is a cellular process in which substances are actively brought into the cell.

Fluorescence is the emission of light by a substance that has absorbed light or other electromagnetic radiation.

Fluorophore is a fluorescent chemical compound.

Optical nanoscopy is optical microscopy that achieves a resolution on the order of 100 nm or below.

Optical sectioning is slicing in the z-direction (along the optical axis) and exclusion of signal outside of that section, important for volumetric imaging/information.

Photobleaching is the photochemical alteration of a fluorophore such that it is permanently unable to fluoresce. This is caused by cleavage of covalent bonds or other reactions between the fluorophore and surrounding molecules.

Radical is an atom, molecule, or ion that has an unpaired valence electron that make them highly chemically reactive.

Reactive oxygen species are highly reactive oxygen-containing molecules such as superoxide (O_2^-), hydrogen peroxide (H_2O_2), and hydroxyl radical (OH^-), commonly associated with cell damage.

Resolution of a microscope the smallest distance between two objects that still allows them to be discriminated as separate objects.

Super-resolution is resolution beyond the diffraction limit of optical microscopy.

List of Abbreviations

2D two-dimensional

3B Bayesian analysis of blinking and bleaching

3D three-dimensional

ADM adrenomedullin

AI Artificial intelligence

c-TIRFM photonic chip-based total internal reflection fluorescence microscopy

DL Deep learning

dstORM direct stochastic optical reconstruction microscopy

EM Electron microscopy

ESI entropy-based super-resolution imaging

FF-SRM fluorescence fluctuation-based super-resolution microscopy

FOV field-of-view

FRC Fourier ring correlation

FWHM full width half maximum

GUI graphical user interface

HAWK Haar wavelet kernel

ML Machine learning

- MUSICAL** multiple signal classification algorithm
- MUSICAL-S** soft MUSICAL
- NA** numerical aperture
- NN** neural network
- PSF** point spread function
- RI** refractive index
- ROI** region of interest
- ROS** reactive oxygen species
- SACD** super-resolution imaging with autocorrelation two-step deconvolution
- SIM** structured illumination microscopy
- SMLM** single molecule localization microscopy
- SNR** signal-to-noise ratio
- SOFI** super-resolution optical fluorescence imaging
- SPARCOM** sparsity based super-resolution correlation microscopy
- SRM** super-resolution microscopy
- SRRF** super-resolution radial fluctuations
- STED** stimulated emission depletion microscopy
- TIRF** total internal reflection fluorescence
- TIRFM** total internal reflection fluorescence microscopy
- UNLOC** unsupervised particle localization



Introduction

1.1 Optical microscopy in biology

The optical microscope is a ubiquitous tool in many and vastly different fields like microelectronics, microbiology and histopathology [1]. Optical microscopy itself is also a large and quickly expanding field. This thesis is mainly concerned with *fluorescence* microscopy and its applications in *cell biology*, the study of the basic unit of living organisms. These basic units come in a great variety of shapes and functions; for example, cells of the green algae *Caulerpa taxifolia* can stretch over several meters in length [2], while some types of bacterial cells are only around $0.20\ \mu\text{m}$ in size: ten million times smaller [3].

The current work is mainly conducted on vertebrate cells in collaboration with biomedical researchers who share an interest in high-resolution microscopy and its development. When I started this doctoral work (and also the related work for my Master's thesis), super-resolution imaging techniques had been demonstrated for many applications on fixed samples, but had not yet been extensively tested nor adapted for applications in *living* cells (this new terminology will be explained shortly). My research contributes to making the tools developed within physics and related disciplines more available and applicable in the life sciences.

The studied cells can be divided into two classes: *primary cells* that are harvested directly from the organism under investigation (e.g. human spermatozoa, rat cardiomyocytes, rat hippocampal neurons, *Xenopus* retinal ganglion cells or

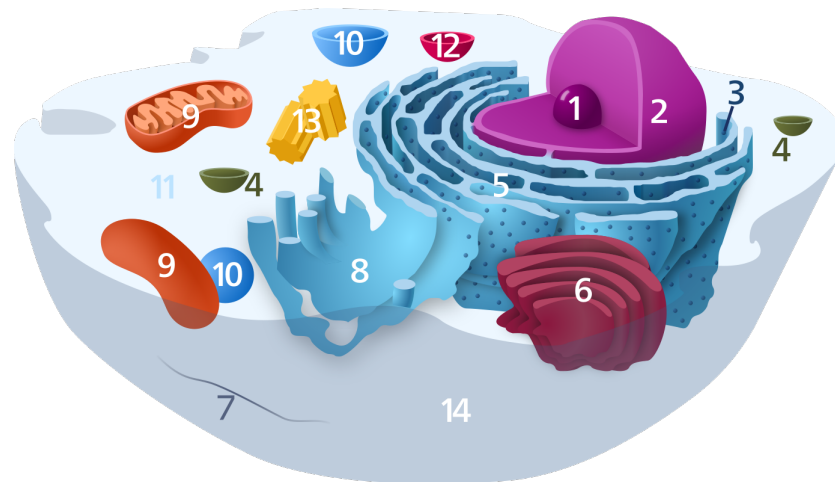


Figure 1.1: Sketch of an animal cell with its subcellular constituents: 1) Nucleolus, 2) Nucleus, 3) Ribosome (small dots), 4) Vesicle, 5) Rough endoplasmic reticulum, 6) Golgi apparatus, 7) Cytoskeleton, 8) Smooth endoplasmic reticulum, 9) Mitochondrion, 10) Vacuole, 11) Cytosol (cytoplasmic fluid), 12) Lysosome, 13) Centrosome, 14) Cell membrane. Figure from [5].

salmon keratocytes), and *cultured cells* that can be cultivated and replicated in the lab. Cultured cells have the advantages of (often) being easily accessible, as well as morphologically and functionally similar or even identical to each other in the case of a monoclonal cell population. Fluorescent tags can be genetically introduced and fused onto existing cellular proteins of interest, bringing valuable specificity to the imaging results. It is not impossible to genetically modify primary cells, but it is in general far more challenging [4].

Although convenient, and fewer animal sacrifices are made, the biological relevance must be critically assessed for each study, as the cells from a cell culture have usually never been inside an animal, but are replicated in the lab, derived from something that used to be part of an animal. These cells can appear very different to the primary cells taken directly from an animal, as these cells have experienced and responded to significant mechanical and chemical stimulus from the surrounding tissue. This surrounding tissue is again composed of a varied set of cell types, each individually responding to their microenvironment. Amazingly, the huge collection of heterogeneous bodily cells are often observed to respond to the outside environment as one whole. This condition is often referred to as *alive*.

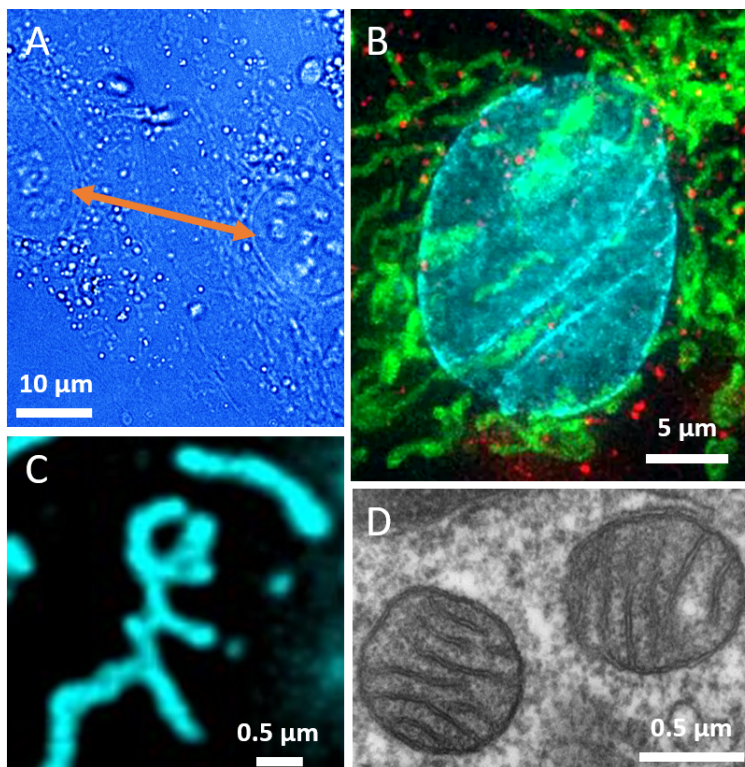


Figure 1.2: (A) Brightfield (transmission) microscopy with arrows indicating nuclei; (B) multi-color fluorescence (wide-field) microscopy, with the nucleus in cyan, mitochondria in green (some are even sprawling through a slit in the nucleus), and some tiny vesicles called endosomes in red; (C) deconvolution fluorescence microscopy of mitochondria; (D) transmission electron microscopy of mitochondria (TEM image by Louisa Howard [6]).

1.1.1 Subcellular structures and fluorescent probes

Although mammalian cells are already microscopically small (typically 10-100 μm [7]), they still possess a very complex inside, apparently jam-packed with different components that are tricky to get a complete picture of as they are small, dynamic, sensitive, and mostly transparent to light. Figure 1.1 shows a traditional cell sketch with various subcellular components like mitochondria and vesicles. Many of them can, under some conditions, be labeled for microscopy by using *fluorescent markers* (also referred to as probes, labels, or dyes).

Microscopy images of biological cells can appear very different for different imaging modalities or imaging conditions. For examples, Figure 1.2 A shows a brightfield (label-free, transmission) microscopy image, which provides decent contrast of the nucleus and several types of lipid vesicles, but most subcellular components are not recognizable. To bring contrast and specificity to cell images, one can introduce fluorescent markers and apply fluorescence microscopy. A multi-color wide-field fluorescence microscopy image with the nucleus in cyan, mitochondria in green (some are even sprawling through a slit in the nucleus), and some tiny vesicles called endosomes in red are displayed in Figure 1.2 B. Both mitochondria and endosomes are subjects of extensive research: mitochondria mainly because of their central importance in cell metabolism, and endosomes e.g. for their frequent interactions with mitochondria as an iron carrier [8]. Endosomes are formed from the outer cell membrane as part of *endocytosis* and have a heterogeneous size distribution, usually reported in the interval of 30 nm - 1000 nm [9].

Image C shows a deconvolution microscopy image of mitochondria (more about this in section 1.1.5) and D, an electron micrograph. Electron microscopy (EM) can achieve resolution far beyond what is possible with light microscopy (even internal mitochondrial structures are well resolved), but has its own limitations. EM is not a technique that should be applied to living samples and also suffers from expensive and time-consuming sample preparation that can alter the delicate cellular structures one wishes to study [10][11].

1.1.2 Fluorescence microscopy

For any details to be perceived, our eyes require contrast. One of the most popular ways of adding contrast is with targeted fluorescent labels. Fluorescence microscopy requires some particular pieces of instrumentation, most notably excitation light sources, and emission filter(s). These, together with one or several suitable fluorescent markers must be adequately chosen according to their spectral properties.

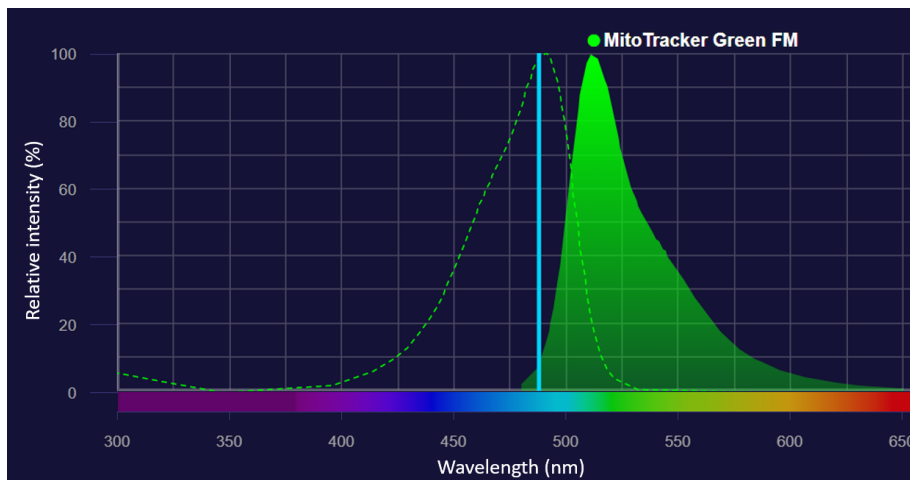


Figure 1.3: Fluorescence spectra. Normalized excitation (dotted line) and emission (full line) spectra for the common cellular probe MitoTracker Green FM using a 488 nm excitation wavelength (vertical blue line). The plots are made using Thermo Fisher Scientific's Fluorescence SpectraViewer [12].

The fluorescence excitation and emission spectra of a particular substance describe the likelihood of photon absorption for a range of excitation wavelengths, and the relative intensity and wavelength of the emitted photons. Figure 1.3 illustrates these for the particular cellular probe MitoTracker Green FM, together with a possible excitation light source (488 nm laser). As 488 nm is close to the excitation maximum of MitoTracker Green, the emission peak is shown almost at the level of the excitation maximum. The distance between the excitation and emission peaks is called the Stoke's shift (about 20 nm in this case). Although the amount of excitation and emission light appear similar in the plot, the amount of emitted light is nowhere near the amount of excitation light. The graphs are individually normalized to the excitation and emission maxima.

Other important parameters for the choice of fluorophore are the brightness (emitted light per amount of excitation light), the (photo)stability in the relevant physiochemical environment, and potential other special properties required for the particular imaging experiment (e.g. blinking, two-photon excitation, live-cell compatibility, etc.).

The Jablonski diagram

Fluorescence, the absorption and re-emission of light particles, is a complex quantum phenomenon. The photon is usually re-emitted by the excited molecule with slightly lower energy (i.e. with a longer wavelength) due to non-

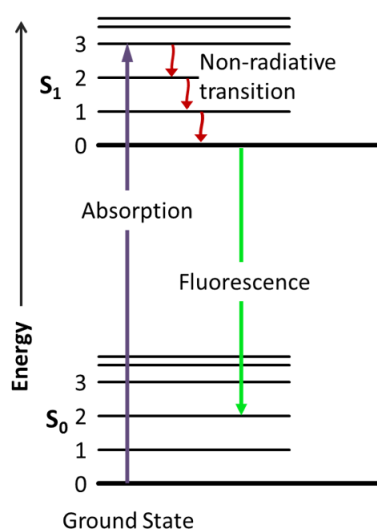


Figure 1.4: Jablonski diagram showing molecular energy levels relevant to the fluorescence phenomenon: photon absorption (purple arrow) causes the molecule (initially in the ground state S_0) to enter an excited state (S_1), followed by vibrational relaxation (short, red arrows) and photon re-emission (green arrow). Figure by Jacobkhed [13].

radiative energy transitions within the molecule. This is commonly described via a Jablonski diagram (Figure 1.4), where S_0 represents the *ground state* (lowest energy level of the molecule) and S_1 the first excited electron energy level resulting from photon absorption. The closely spaced horizontal lines within S_0 and S_1 represent non-radiative energy levels. Transitions between these can be caused by several mechanisms, e.g. internal changes in electron configuration or the dissipation of energy from the molecule to its surroundings (called vibrational relaxation) [14][15].

If more photons (or a higher energy one) hit the excited molecule, the electron(s) could reach an even higher energy level or cause the molecule to become ionized (completely lose the electron). Whatever new configuration was the fate of the molecule, the previously fluorescent molecule is now likely photobleached and not capable of producing fluorescence anymore. Both excited and ionized molecules are highly reactive and, when residing in living cells, likely to have unwanted damaging effects on the cellular microenvironment.

1.1.3 Imaging conditions and phototoxicity

Bioimaging experiments can be coarsely divided into *live-* and *fixed-cell imaging*. For live-cell imaging, we usually try to keep the cells under as similar conditions

as possible to their normal growth conditions, while for fixed-cell experiments we try to preserve the living cellular structures into their death, usually via toxic chemicals like paraformaldehyde, methanol, or glutaraldehyde. There are pros and cons with any imaging mode, and often both live- and fixed-cell imaging are conducted to reach any micrograph-based biological conclusions.

For instance, by imaging living cells, we can study dynamic processes without potential fixation artifacts. One can, however, usually not benefit from the convenience of immunolabeling approaches, which can provide specific information about protein localization via tagged antibodies, as is often performed on fixed cells. The reason immunolabeling is mainly a method performed on fixed cells, is that living cells would normally not let these large molecules through their membrane. It is sometimes possible to force molecules through the cell membrane by using e.g. an electric voltage to disrupt the normally impenetrable membrane in a process called *electroporation* [16].

Rather than applying foreign molecules to the cells as labels, one can achieve a similar (or better) label specificity by using genetically encoded fluorescent proteins. These can be imaged either live or fixed, but are especially a tool for visualizing cells alive and dynamics without possible fixation artifacts.

For fixed-cell imaging, time is on our side, and we usually do not have to worry too much about the cell sample conditions on the way to and on the microscope. When living cells are residing on the microscope, some additional considerations must be made, like the temperature and atmosphere surrounding the cells. For mammalian cells, normally 37°C together with (compared to the microscopy lab) elevated levels of CO_2 and humidity. Additionally, one must consider what effects the microscope illumination might have on the cells.

Light-induced cell damage is often referred to as phototoxicity. The radiation experienced under a microscope, especially a high-resolution one, is far from the cells' natural environment. Illumination can cause cell death directly or trigger more subtle cytotoxic effects that can influence the physiological relevance of an experiment or lead to false conclusions, especially if these experimental factors are ignored throughout the experiments and in the analysis.

Light-induced cell death rate depends on wavelength, illumination mode, fluorophore and, cell type. The cells can "freeze" dead (not changing morphology), or be induced to take a more gradual death path known as apoptosis or necrosis. The difference between these are portrayed in Figure 1.5. The toxicity can arise from e.g. localized heating, the direct destruction of biomolecules or via reactive species following the light excitation [18]. When e.g. a fluorophore is in an excited state it can react with oxygen to form reactive oxygen species

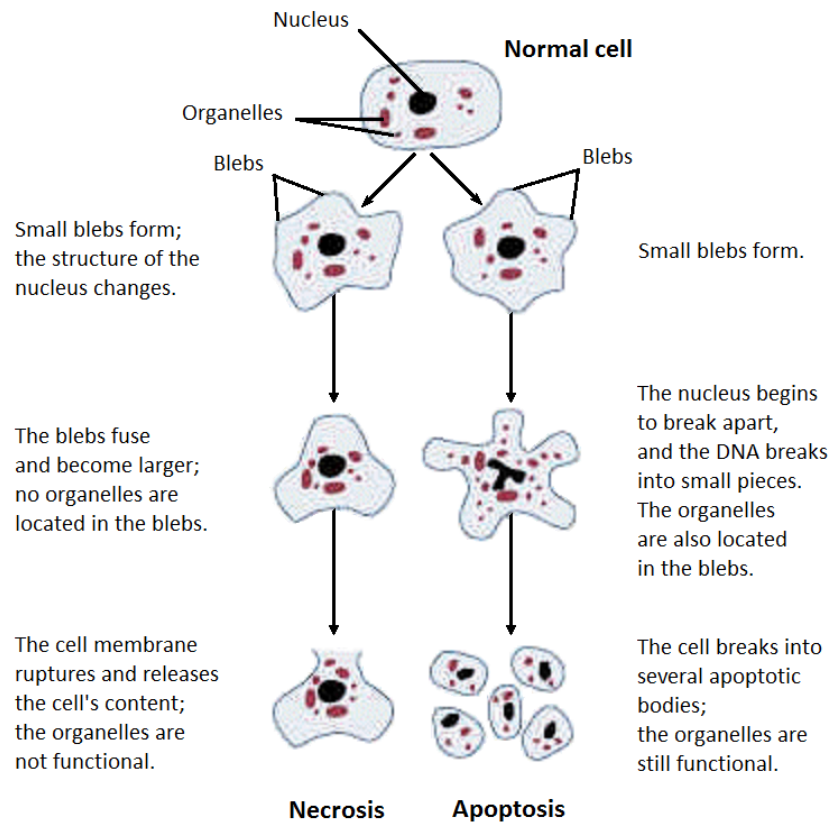


Figure 1.5: Outline of morphological changes undertaken by a dying cell. A cell undergoing *necrosis* (left path) is disassembling in an uncontrolled manner following some (to the cell) extreme trauma as intense light exposure or bacterial toxins. This is different from *apoptosis* (right path), which is a controlled disassembly of the cell, also occurring in healthy organisms. Apoptosis is also known as *programmed cell death*. Figure by the National institute on alcohol abuse and alcoholism (NIAAA) via Wikimedia Commons [17].

(ROS) that can destroy other cellular molecules and/or trigger a cascade of cellular events, as ROS also have a role to play in cell signaling [19][20].

When excited fluorophores have bonded with oxygen and formed ROS, they are not only likely to cause cell damage, but the fluorophores are likely also *bleached*, i.e. not longer fluorescing as desired. This makes phototoxicity closely connected to photobleaching, although they are distinct phenomena. Figure 1.6 displays two time-lapse sequences of mitochondria containing the fluorophore MitoTracker Green and imaged using repeated laser illumination. Because of extensive photobleaching, the sequence is bleach-corrected (i.e. brightness adjusted as a function of time-point) for visibility. For every time-point, the mitochondria become wider and shorter. This swelling of mitochondria is a hallmark of phototoxicity and rarely a good sign in fluorescence microscopy.

Light cannot only alter components within cells but also in the medium surrounding and nurturing the cells. Interestingly, in 2017 [21], Stockley et al. demonstrated the culture medium (containing riboflavin) to be the main source of photo-damage in oligodendrocytes by culturing the cells in media previously irradiated with blue light. Cells in previously irradiated medium showed the same degree of phototoxicity as was observed by irradiating the cells directly. They developed photo-inert media which, in combination with protective supplements of antioxidants and vitamins, "allowed cells to endure up to twenty times more light exposure without adverse effects". Thus, for many bio-applications involving light exposure, there could be much to gain from changing the medium composition before imaging [22][23][24].

1.1.4 The diffraction limit of optical resolution

The bending (or redistribution) of light waves as they interact with an object defines diffraction. It enables an image to be formed, but also imposes a limit to optical resolution. In the case of a microscope objective, we usually have a circular aperture through which the signal is collected. In the case of a point source object, the best result one can hope for is an intensity distribution resembling an Airy function, as displayed on the left of Figure 1.7. The signal on a two-dimensional (2D) camera chip would look more like one of the spots on the right panel.

In the case of an ideal, aberration-free imaging system, the central disk (called the Airy disk) contains 84% of the collected light signal and is surrounded by a series of bright concentric rings separated by dark intensity minima (at zero intensity) and with radially decreasing brightness.

The width of the Airy disk depends on the wavelength of light λ , the refractive

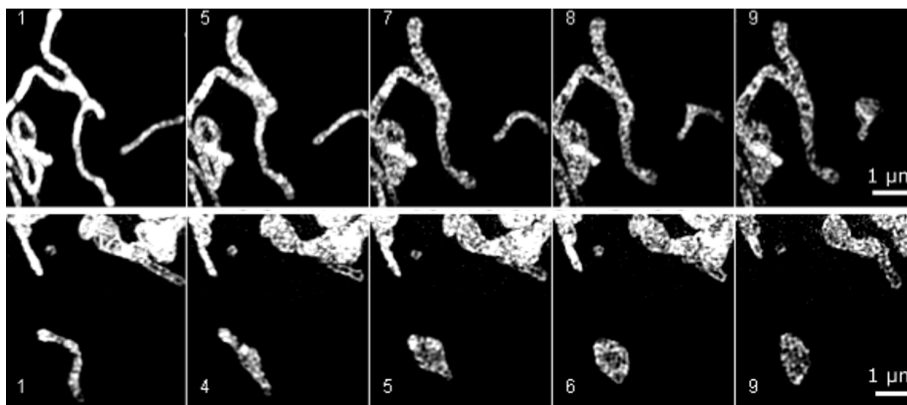


Figure 1.6: Alteration in mitochondrial morphology by phototoxicity. The upper and lower rows show excerpts from two different three-dimensional (3D) SIM time-lapse sequences of mitochondria. The numbers indicate the time-points of acquisition. The mitochondria appear visibly shorter and wider towards the end of both image sequences. This is a morphological artifact caused by phototoxicity. The images are of MCC13 cells labeled using MitoTracker Green, and were previously published in [25].

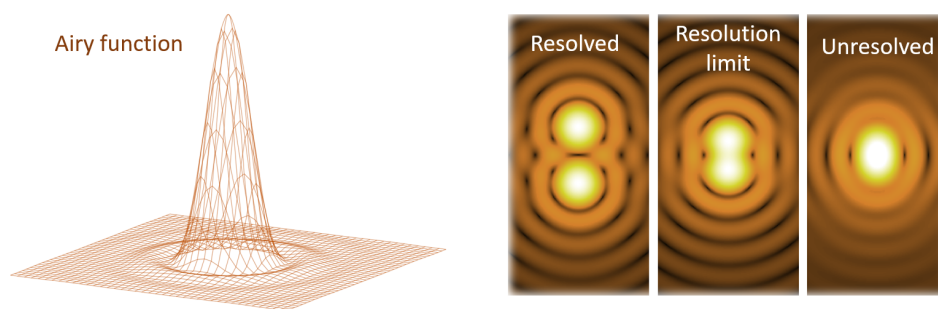


Figure 1.7: *Left panel:* Three-dimensional rendering of an Airy function. *Right panels:* Two-dimensional views of Airy functions resulting from two closely spaced point-like emitters at a separation *above*, *at*, and *below* the resolution limit (following the Rayleigh criterion). The figures are adapted from Sakurambo [26] and Spencer Bliven [27].

index (RI) of the imaging medium, n , and the aperture angle of the objective, θ (see Figure 1.8 B). In a focused and well-calibrated fluorescence microscopy system, the width of the central spot depends on only two parameters, λ and the numerical aperture, $NA = n \sin \theta$.

The RI of a medium is defined as the ratio of the vacuum speed of light ($c \approx 2.9979 \cdot 10^8$ m/s) to the light propagation speed in that medium, v . For example, the RI of ethanol is 1.36, meaning that light propagates 1.36 times slower in ethanol compared to in empty space. Air has a RI very close to that of vacuum, $n_{Air} \approx 1.00$. More physical properties of light together with an illustration of the aperture angle is provided in Figure 1.8.

In a particular microscope, the normalized intensity distribution of the diffraction pattern from a point source is called the point spread function (PSF). It turns out that the process of image formation introduces a systematic error that can be well characterized. Mathematically speaking, the captured image is described by a convolution between the microscope's PSF and the sample object (times the illumination pattern). Practically speaking, this causes image blurring and loss of resolution.

Defining resolution limits

As image formation is a linear process, non-point-like objects can be straightforwardly described as a distribution of points. Looking at the world (or tiny parts of it) as points, is therefore a popular simplification when considering the formation of images through an imaging system.

When two points are separated at a distance corresponding to the resolution limit, they can just barely be discriminated. Closer than this limit, one cannot differentiate the underlying distribution of points in the image (right side of Figure 1.7).

There are several definitions of the resolution limit in common use. The one illustrated in Figure 1.7 corresponds to the **Rayleigh criterion**,

$$R_{R,x} = 0.61\lambda/NA \quad (1.1)$$

It describes the separation such that the first intensity minimum of one emitter overlaps with the intensity maximum of the neighboring emitter, or equivalently, the radius of the Airy disk. The Rayleigh criterion is frequently applied in spectroscopy and astronomy.

In microscopy, the **Abbe limit** is more commonly applied and gives a slightly

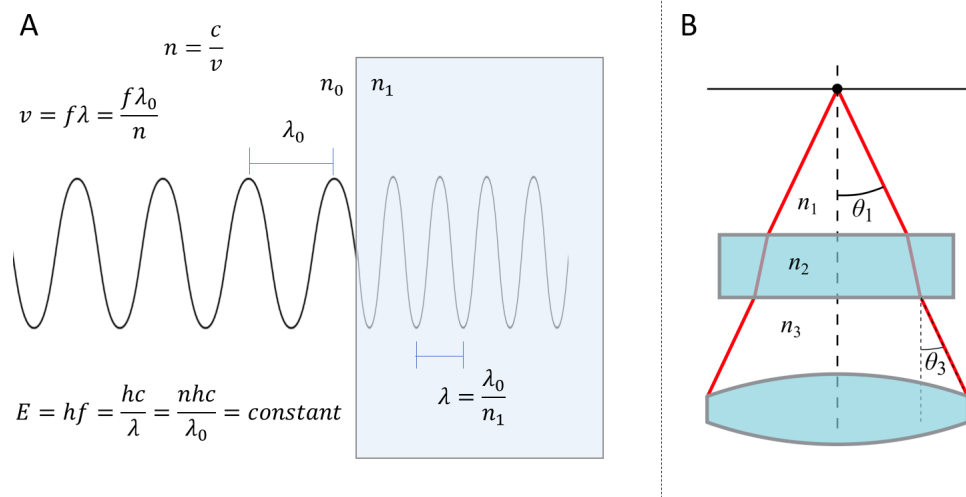


Figure 1.8: (A) A light wave travels through vacuum (shown in white) with RI $n_0 = 1$ at the speed of light $c = 3.0 \cdot 10^8$, and with a wavelength λ_0 and a frequency f . As the wave enters the new medium (in blue) with RI n_1 , both the speed and the wavelength of light (λ) changes. The refractive index, n , describes how a medium changes the speed of light compared to the vacuum speed c , following $v = c/n$. As the λ is proportional to the speed ($\lambda = v/f$), also the wavelength changes. The photon energy, $E = hf$, is proportional to the light wave frequency and remains unchanged while entering the new medium. h is Planck's constant ($h \approx 6.626 \cdot 10^{-34} \text{ m}^2\text{kg/s}$). (B) The cone of light that can be collected from an emitting point source in a medium with n_1 , which passes through a coverglass (blue rectangle) with RI of n_2 , before entering a third medium of n_3 , adjoined to a light gathering lens (blue curved component). Here n_3 (directly in contact with the lens) determines the NA, $n_3 \cdot \sin(\theta)$. This is why using oil immersion ($n_3 \approx 1.5$) gives a better light collection compared to e.g. air objectives ($n_3 \approx 1.0$). Additionally, increasing n_1 (by using a high-RI mounting solution) enhances light gathering, reduces aberrations, and enables crisp images to be acquired deeper into the sample. This is due to the refraction and reflection across surfaces of different NAs.

narrower estimate for the (maximal) lateral resolution,

$$R_{A,x} = \lambda / (2NA) \quad (1.2)$$

This equation is derived from Ernst Abbe's theory of diffraction and considers which diffraction orders are actually captured by the objective during image formation. Its inverse gives the microscope's cut-off frequency:

$$f_c = 2NA / \lambda \quad (1.3)$$

The fine details lost during image formation correspond, in the frequency domain, to low-pass filtering: in effect, image blurring.

The previous equations describe lateral resolution. The **axial resolution limit** is far worse,

$$R_{A,z} = 2n\lambda / (NA^2) \quad (1.4)$$

We will revisit axial PSFs and practical implications in section 1.4 in connection with TIRFM.

The equations for the diffraction limit describe the theoretically best achievable resolution by means of conventional optical microscopy. In practice, there will always be some level of aberrations from the sample, system imperfections, and noise that degrade the final image resolution and quality to below the theoretical maximum [28][14].

Optical microscopy techniques that achieve resolution beyond these conventional limits are commonly referred to as super-resolution microscopy (SRM) or optical nanoscopy.

1.1.5 Deconvolution microscopy

If the blurring and loss of resolution induced by the microscope is described by a simple mathematical operation, could the sample object be mathematically restored by simply conducting the inverse operation post-acquisition?

In an ideal fluorescence microscopy system (assuming linearity and shift invariance), the image, i , can be simply described by the operation convolution (symbol \otimes) of the object, o , with the system PSF, h ,

$$i(x, y, z) = \iiint o(x', y', z') h(x - x', y - y', z - z') dx' dy' dz' \quad (1.5a)$$

$$i(x, y, z) = h(x, y, z) \otimes o(x, y, z) \quad (1.5b)$$

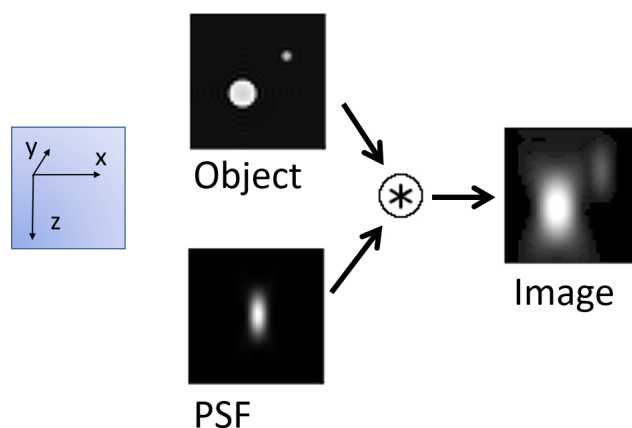


Figure 1.9: Image formation by a microscope is governed by the mathematical operation convolution between the sample object and the system PSF. One can imagine the PSF as a thick painting brush used to draw the object, resulting in a loss of fine image details. Figure modified from Default007, public domain [29].

equations 1.5 a and b being equivalent. In words, the convolution between two functions (like h and o) produces a third function that describes how the shape of one is modified by the other. It just states that the sample object o is modified by the imaging system to become the image i . This follows from the definition of the PSF and the linearity of incoherent imaging systems. One can imagine the PSF as a thick painting brush used to draw the object, giving a smeared-out, resolution-limited image as result.

This is valid for either a widefield imaging system (collecting an entire XY-plane in one go) or for a confocal scanning-type system, where excitation and collection are done in a point-wise manner, physically blocking out-of-focus light with a pinhole, one voxel at the time. The convolution image formation is illustrated in Figure 1.9. *Deconvolution* is, in principle, the same process just in reverse.

The PSF of an imaging system can be either estimated theoretically or measured experimentally. The theoretical estimate is often quicker but would lack information about the specific system's peculiarities, like field curvature, astigmatism, or coma. These are usually well-corrected for in high-quality optics.

An experimentally-obtained PSF has the disadvantage of noise and could suffer from experimental inaccuracies like variations within the sample. It is normally obtained by imaging fluorescent beads with a diameter smaller than the objective's PSF. Theoretically, the emitter should be a point source (as small

as possible), but practically the beads must be bright enough (often meaning big enough) to provide a decent signal for a good PSF measurement. Thus, beads not much smaller than half the Airy disk diameter (e.g. 100 nm) are often used experimentally. This will give a too large PSF estimate, but this can be corrected for by using the known bead size and "deconvolving" the PSF.

In either case, for the imaging experiment of the actual sample of interest, the PSF is likely at least slightly different and also varying within the sample, especially in the axial dimension [30] (thus breaking the condition of a shift-invariant imaging system presumed for eq. 1.5), but can still be usable for practical deconvolution purposes.

In the case we manage to obtain a good estimate of our system PSF, how can we now solve for the original object, o , knowing the PSF, h , and acquired image, i ?

The *convolution theorem* comes in handy here. It states that the Fourier transform¹ of the convolution of two functions is the product of the Fourier transforms of the individual functions, such that eq. 1.5 becomes $I = HO$, with the uppercase letters denoting the Fourier transform of the respective lowercase letters as previously defined.

So in the ideal case the solution to our problem is $O = I/H$, simple element-wise division of our (frequency) image with the (frequency) PSF (commonly referred to as the optical transfer function, OTF), before converting back to the spatial domain. Ideal problem solved²!

The real problem, of course, is that the real world is not the ideal case. Firstly, even if we got the PSF estimate right, the limited frequency support of H (the frequency space way of saying "resolution limited" or lack of fine details) implies division by zero (or zero matrix elements), making the operation impossible. Furthermore, the real measurements (our images) will have a significant presence of (random) noise being further amplified by the division by small numbers in H .

1. In case this is new to some readers, the Fourier transform is a neat way of decomposing a function (of e.g. space or time) into its frequency components. By swapping over to the frequency domain, many mathematical expressions and calculations can be simplified and sped up.
2. To get around any zero divisions, one can e.g. make the equation conditional such that (where O_{ij} , I_{ij} and H_{ij} represent the elements of the matrices O , I and H)

$$O_{ij} = \begin{cases} \frac{I_{ij}}{H_{ij}}, & \text{for } H_{ij} \neq 0 \\ 0, & \text{for } H_{ij} = 0 \end{cases}$$

Solving the equation analytically turns out to be a mathematical impossibility, but that is usually the case in physics, so no reason to be heavyhearted. Instead, the solution can be estimated. A simple and direct image restoration method, which is also often used in practice, is the (inverse) Wiener filter:

$$\hat{O} = \frac{H^*}{|H|^2 + K} \cdot I \quad (1.6)$$

The circumflex (or hat) is used to denote that it is an estimate of the object (O) and the asterisk the complex conjugate. K is a small constant (often empirically chosen in the range 0.001 to 0.1) used to avoid zero divisions and noise amplification.

Deconvolution is in practice an array of different techniques (like the Wiener filter) trying to estimate the object *o* in the real case of noise and non-ideal imaging systems. It is usually not referred to as a super-resolution technique, and the result is often contrast enhancement rather than resolution improvement. When the parameters are not right, or the images are too noisy (compared to the signal) or distorted in some other way, the result is image degradation and "restoration artifacts" [31].

1.2 Optical nanoscopy

We have seen in the previous sections that image formation comes with theoretical and practical limitations. During the last couple of decades, however, a new and expanding field has emerged, comprising an array of techniques that allow for resolution better than the diffraction limit, i.e. optical microscopy. Since the practical implications often correspond to a resolution on the order of 100 nm or less, the term *optical nanoscopy* is also applied almost synonymously. The most promising results so far in resolving nanoscopic details with optical microscopes are using fluorescence-based techniques.

1.2.1 General approaches

Although the list of creative names (and acronyms) for SRM methods is extensive, they can so far all be explained from a few basic concepts. To obtain resolution beyond the conventional limit, one can either modulate the illumination pattern (as in the SIM or stimulated emission depletion microscopy (STED) approach), or one can change the photon emission rate of the fluorophores like in single molecule localization microscopy (SMLM). One can also try to analyze the natural, *intrinsic* fluorescence intensity fluctuations as in FF-SRM. Or, very different from the previous approaches, one can expand the sample

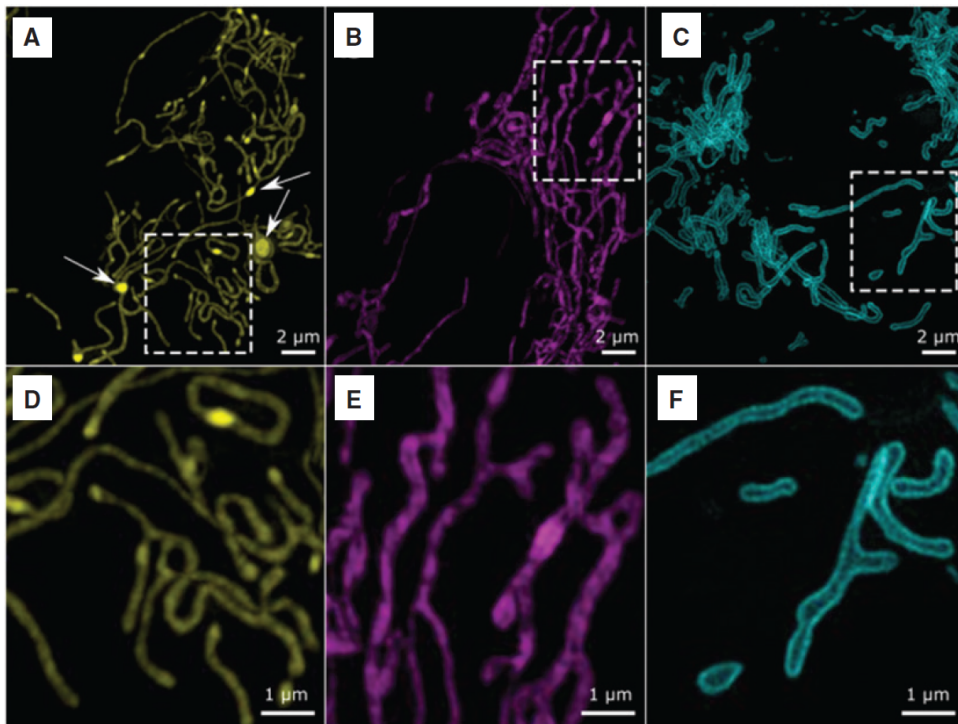


Figure 1.10: Maximum intensity projected 3D SIM images of mitochondria in living cancer skin cells (MCC13 cell line). The cells are labeled individually with three different mitochondrial probes. (A) CellLight Mitochondria-RFP BacMam 2.0, which targets the mitochondrial matrix. Larger aggregates (indicated by arrows) are thought to be labeling artifacts. (B) MitoTracker Deep Red accumulates in the intermembrane space, and gaps correspond to the presence of cristae. (C) mEmerald-TOMM20 targets the outer mitochondrial membrane. Panels (D–F) provide a closer look at the boxed regions in A–C. This figure was previously published in [25]

as in expansion microscopy [32][33][34].

In the following, only two of these SRM approaches will be described in more detail, namely SIM and fluorescence fluctuation-based super-resolution microscopy (FF-SRM). This is because of system availability and that SIM and FF-SRM are arguably the most promising among these techniques for live-cell imaging. Compared to its fixed-cell counterpart, live-cell imaging demands faster image acquisition, lower illumination light dose, and tight restrictions on what buffers and probes can be applied.

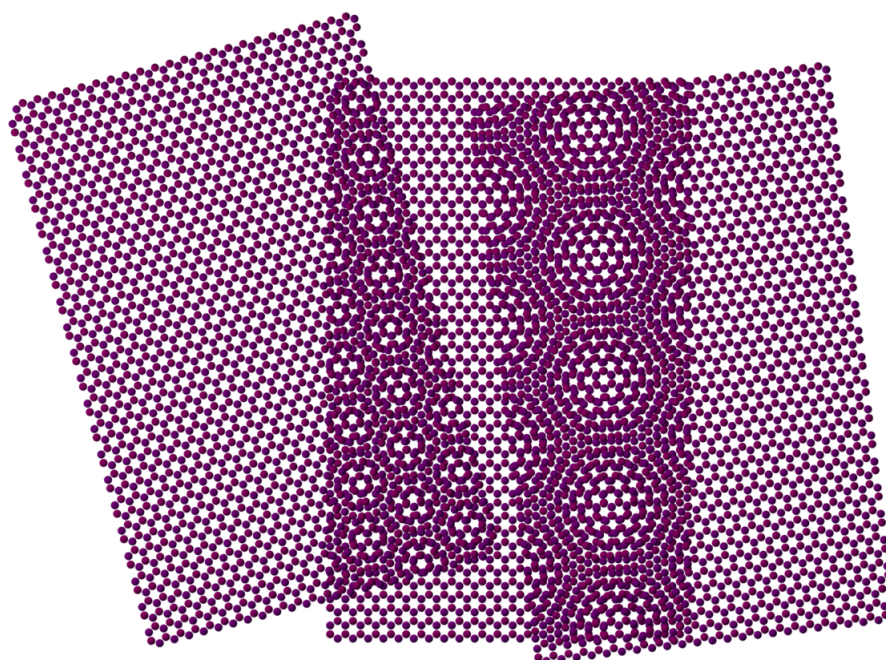


Figure 1.11: Moiré patterns arising from the superposition of two hexagonal lattices twisted by 15° and 7° compared to the middlemost lattice. The figure was inspired and modified from [35].

1.2.2 Structured illumination microscopy

Where SIM really shines compared to other SRM techniques, is the capability of fast volumetric imaging under conditions of live-cell imaging. Figure 1.10 shows an example of volumetric SIM imaging of different mitochondrial structures, targeted using different mitochondrial probes. Panel F shows the same mitochondria as in Figure 1.2 C, although the mitochondria changed shape during the seconds it took to switch excitation mode from structured laser illumination to incoherent wide-field illumination.

SIM principles

As seen in the previous sections, image formation in a microscope results in loss of resolution: in essence, a low-pass filter eliminating high-frequency content beyond the diffraction limit. We saw that deconvolution could partially reduce this blur, but that the Abbe diffraction limit largely remains.

Although deconvolution is an essential part of SIM reconstruction algorithms, SIM has an additional trick up the sleeve, so to speak. This trick is illustrated in

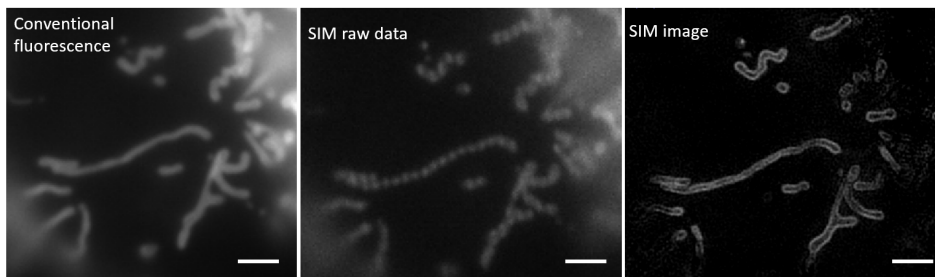


Figure 1.12: Comparison of raw data for conventional fluorescence microscopy and for SIM. The conventional fluorescence microscopy image was generated by summing up the 15 SIM raw images used to reconstruct one SIM image for the particular Z plane shown. The stripy raw data for SIM are interference fringes resulting from passing the excitation beam through a diffraction grating before being focused onto the sample. The SIM image was reconstructed using the commercial software accompanied with the GE Healthcare's OMX blaze v4 SIM system. The images are of the mitochondrial outer membrane, labeled using genetically encoded enhanced green fluorescent protein (EGFP). The scale bars are 2 μm .

Figure 1.11, where we can see larger (Moiré) patterns arising from the superposition of two (identical) hexagonal patterns overlaid at two different angles (and shifts). Even when the structures of our sample are below the observable limit of our microscope, Moiré patterns resulting from structured illumination exposed to the sample can still be observed through the objective aperture. The post-processing (or SIM reconstruction) then involves "frequency unmixing", trying to estimate what underlying patterns in the sample object caused the imaged Moiré fringes, knowing the illumination pattern and system PSF. An example of data for SIM as compared to data for conventional fluorescence microscopy, is shown in Figure 1.12.

How well SIM works in practice is highly sample dependent and fails in the case of small errors (or misassumptions) in the PSF or illumination pattern.

Practical considerations for SIM

In the particular implementation of SIM used for the current work (a high-end commercial OMX v4 Blaze 3D SIM system, EUR1 million), the excitation pattern is a series of sinusoidal stripes, consecutively illuminating each sample plane at three angles and five phase shifts. In the z-direction (orthogonal to the sample-holding coverglass), the sampling is every 125 nm. Per 1 μm thick sample volume, this corresponds to 120 raw images per color channel (imaged sequentially), each requiring exposure and read-out time of the camera.

Typically only 2-3 μm thick stacks are acquired for living samples, even though the imaged cells often are thicker than 10 μm . There are a few good reasons for choosing a modest volume size:

1. **Sample induced aberrations.** The deeper into the sample the imaging is, the poorer the quality of both the excitation interference fringes and the emission signal. This is a problem for the SIM reconstruction, which assumes and requires a certain excitation pattern and PSF of the collected signal from the sample. For fixed cells, this can be to some extent countered by using a high RI (e.g. ≈ 1.46) mounting solution, but for living cells, the only viable option is usually a water-based buffer (RI ≈ 1.33).
2. **Photobleaching.** Especially for live-cell compatible fluorescent labels, photobleaching becomes a killer. All these often hundreds of images must be of sharp modulation contrast (at least signal-to-noise ratio (SNR) 10/1.), and the light exposure necessary to fulfill this contrast requirement takes its toll on the fluorophores.
3. **Acquisition time.** Fluorophores typically bleach slower when using longer exposure times compared to higher illumination intensities for the same signal intensity, making longer acquisition times (e.g. 5-50 ms exposure + 8.40 ms camera read-out time) with lower illumination intensities (1-10% of the maximum of $\approx 0.1\text{W}$ laser) usually the best compromise of acquisition parameters.

To take a realistic example imaging three color channels, 3 μm sample thickness and with each frame having an exposure time of 30 ms + 8.40 ms readout time, the total acquisition time would be:

$$\frac{120 \text{ images}}{\mu\text{m} \cdot Z \cdot \text{channels}} \cdot 3\mu\text{m} \cdot Z \cdot 3 \text{ channels} \cdot \frac{38.40\text{ms}}{\text{image}} \approx 41.5\text{s}$$

To put this number in a biological context, in Giedt et al., mitochondria in vascular endothelial cells were measured to move on average $0.31\mu\text{m}/\text{s}$ (but also up to $2\mu\text{m}/\text{s}$) [36]. Multiplying this with 41.5 s, we get that mitochondria on average can move about 13 μm (likely back and forth) during a multicolor 3D SIM image acquisition. This is pretty horrifying considering the SIM resolution on the order of 0.1 μm , and the reconstruction artifacts this may cause. And this is with a system which is called Blaze for its speed.

4. **Phototoxicity.** In the 41.5 s it took to acquire this one 3D SIM image volume, the cells have been exposed 1080 times to a quite intense laser

illumination (about 0.1 – 1 W/mm using 10%T, enough to destroy cells in the human retina). Most live-cell compatible fluorescent probes would, after this first volumetric SIM image, be largely photobleached, and a second super-resolved time-point would be effectively out of reach. As outlined in section 1.1.3, the cell damage caused by the light exposure and excited fluorophores is likely considerable, although dependent on the particular experimental conditions like cell type, imaging medium, illumination wavelength, and fluorescent markers.

The OMX is a nice imaging system for live-cell 3D SIM applications, but it is also clear that many compromises must be made to have any chance of following subcellular processes.

This (a few years ago state-of-the-art 1 million Euro) 3D SIM system enabled and inspired my first two articles which were on the application of 3D SIM in living cells. These are further described in the first section of Chapter 2.

Although capable of relatively fast imaging and suitable for many volumetric and multi-color SRM applications in living cells, this implementation of 3D SIM is still not fast and gentle enough to follow fast (sub 1-2 s) subcellular dynamics in a light-sensitive environment.

Fast-moving structures are a big challenge in SIM reconstruction. When structures move a distance of only the resolution of SIM ($\approx 100nm$) before all the images needed for the 3D SIM reconstruction are acquired, sample frequency calculations become erroneous and cause reconstruction artifacts and effectively failed imaging experiments [37].

Improvements to the SIM technique or the reconstruction algorithms have not been covered in the current work but have been briefly reviewed and discussed in Chapter 4. Instead, the slightly newer field of FF-SRM has been explored as an alternative for fast, live-cell super-resolution imaging.

1.2.3 Fluorescence fluctuation-based techniques

We have seen in the previous section that 3D SIM requires an expensive system exposing the sample repeatedly to damaging structured laser illumination (typically hundreds of times for a single 3D SIM volume). Still, even under optimized conditions and using bright, photostable fluorophores, 3D SIM is largely unable to follow fast, subcellular dynamics.

A different approach to SRM, advertising live-cell compatibility, and even friendliness, is fluorescence fluctuation-based super-resolution microscopy (FF-SRM).

This encompasses different techniques, most notably super-resolution optical fluorescence imaging (SOFI) [38], entropy-based super-resolution imaging (ESI) [39], super-resolution radial fluctuations (SRRF) [40], multiple signal classification algorithm (MUSICAL) [41], and super-resolution imaging with autocorrelation two-step deconvolution (SACD) [42]. We will revisit these in more detail in Chapter 2.

Although different algorithms, they can be applied to similar sets of image data and have a shared three-fold motivation emerging from challenges in the applicability of the earliest SRM techniques:

- **Gentle:** Low-intensity widefield illumination in live-cell friendly buffers.
- **Fast:** Not limited by point scanning (STED) or the acquisition of thousands of "single emitter blinking" events (SMLM).
- **Low-cost:** Obtain SRM images using a conventional (possibly already installed) microscope and open access software.

The practical imaging experiment is then to acquire a fast time-lapse (series of images) on a conventional microscope and feed it to a program that should (hopefully) return a super-resolved image from the time-sequence.

The motivation is good. There are, however, practical problems or limitations applying to all of these methods.

Challenges:

1. **Acquisition speed:** The sample moves or morphs before the images needed for one time-point are acquired. This is especially the case for 3D image stacks.
2. **Number of frames:** The number of frames necessary for an accurate reconstruction is often too high compared to the cellular dynamics and/or photon budget.
3. **Photo- and label-induced toxicity:** The techniques require fluorescently labeled structures and often a considerable light dose.
4. **Computational speed:** When many time-points, large FOVs, and/or many parameters should be tested, the required reconstruction time can become a big hurdle.
5. **Reconstruction artifacts:** The reconstructed "super-resolved" images

can show structural features other than what are actually present in the imaged sample.

6. **Choice of reconstruction parameters:** Often FF-SRM algorithms come with many parameters that can drastically alter the results, but without clear guidelines for how these parameters should be chosen. When the user can change the experimental outcome and biological conclusions by a subjective choice of parameters, it renders the scientific validity highly questionable.
7. **Validation of results:** Usually, and especially for live-cell image data, the ground truth is not available. Validation of results on fixed-cell data does not hold, because the fluctuation character is completely different in living samples due to the different chemical environment of the fluorophores and the mobility of the excited molecules and imaged objects.
8. **Scarcity of fluorescence intensity fluctuations:** Relying only on the natural variations in fluorescence emission of fluorescence molecules can be problematic due to the scarce presence of fluctuations from many common fluorescent labels. This is in sharp contrast to the SIM and SMLM techniques, where a suitably-engineered illumination pattern or chemical environment can be optimized separately from the reconstruction algorithms, ensuring sufficient and appropriate intensity fluctuations and data information content. If there are no signal fluctuations across an image stack, the information content is the same as in a single image, and a super-resolution image cannot be further extracted from this.
9. **Additional sources of signal fluctuations:** The three-dimensional dynamics of living samples — together with out-of-focus signal, photobleaching and camera noise — render intensity fluctuation classification and analysis an extremely challenging problem in optical nanoscopy.

All of these challenges are considerable, sometimes all in the same experiment. These challenges, and possible solutions, together with some considerable differences between the various techniques, are further considered in Chapter 2.2, where the associated published articles are summarized.

1.2.4 Assessing image quality and resolution

Assessing basic parameters such as image quality and resolution can be surprisingly challenging even for conventional images not subjected to any reconstruction procedure. As a starting point, some common characteristics of *good fluorescence microscopy data* are:

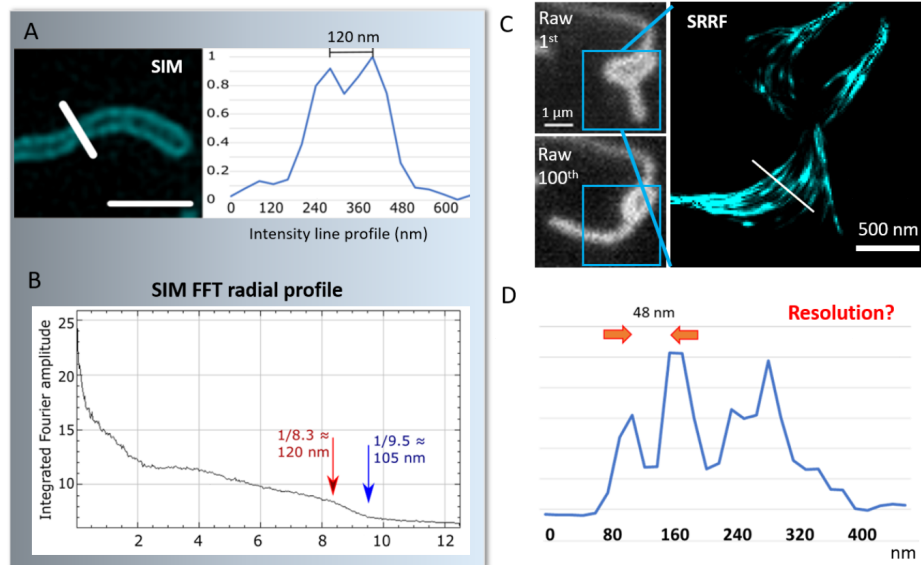


Figure 1.13: (A) Line profile of a mitochondrion (outer membrane) drawn across a SIM image. (B) Fast Fourier Transform (FFT) radial profile plots ($amplitude^2$) of the same 3D SIM stack as in A. The blue arrow indicates an estimated resolution and frequency support from the inflection point of the curve (giving 105 nm) following the methodology used in the SIMcheck publication, while the red arrow indicate resolution based on the microscope system specifications. (C) *Left panels:* Excerpts from the raw data stack of fast-moving mitochondria (first and last frame of a 100 time-point stack). The imaging speed was as fast as possible, limited only by exposure time and camera readout. *Right panel:* SRRF reconstruction of the same image stack using a radius of 0.5 and other default parameters. (D) Line profile of the line indicated in the above SRRF image. Here, the distance between intensity peaks cannot be counted as resolution as they are reconstruction artifacts and not real structures present in the sample. The artifacts result from the SRRF algorithm drawing a thin line for each frame as the mitochondrion moves during the acquisition of the 1st to the 100th frames, as observed in the left panels. Panels A and B are adapted from work previously published [25].

- i) Aberration-free: the data is acquired using a well-focused and otherwise aligned microscope
- ii) Good contrast: bright structures and dark/low background
- iii) Good use of camera dynamic range

As various SRM acquisition and reconstruction routines, together with a diverse set of other image processing possibilities, enter the scene, the tasks of image quality and resolution assessment become more involved. Mere images can no longer be assessed, but also the chain of events that led to the final image must be considered. For the more mature SRM techniques like SMLM, STED and SIM, quality assessment methods have had time to develop and many of their artifacts are now fairly well known and characterized [43][44][45][46].

To assess the *image resolution*, a few common approaches are applied in microscopy:

1. **Measure a line's profile full width half maximum (FWHM)** to estimate the PSF from the widening of a (hopefully) point-line object. The FWHM is measured as the width across a (preferably) bell-shaped curve at half the height compared to the highest intensity value of the curve (i.e. intensity line profile). This approach might be valid for unprocessed widefield images in specialized samples like nano-beads. *Problems:* •For images of samples not specifically designed for PSF measurements (like nano-sized beads), the unknown width of the measured structure will add to the "PSF estimate". •Subjectivity: the choice of where to draw a line profile is chosen by the user based on where they think might show good resolution results. •Image processing like intensity scaling or deconvolution can change the measurement. For example, deconvolved images can make structures appear much slimmer than the actual resolution.
2. **Measure distance between two nearby resolved structures.** This approach indicates actual resolution much better than a line profile of a single structure as in the previous point. A SIM image example is provided in Figure 1.13. Special samples (nanorulers) for system characterization are available [47]. *Problems:* •Subjective choice of where to measure (in a non-uniform image). •Small distances can be measured between noise signals or reconstruction artifacts that do not accurately represent the actual sample. An example of this type of error from FF-SRM is provided in Figure 1.13 panel C.
3. **Fourier (power) spectrum analysis.** In contrast to the two previous approaches, this measurement does not rely on a subjective choice of structures for the resolution estimate but takes the entire image into

equal consideration. *Problems:* • Subjective or non-standardised choice of frequency cut-off parameter. • Noise and image artifacts also appear as high-frequency image content, thus may give a misleadingly high resolution result. This is illustrated in Figure 1.13 panel B on 3D SIM data. Due to noise and reconstruction artifacts the measured resolution (in blue) is better than the theoretical best possible from that microscope (in red). The plot and measurement were generated following the SIMcheck plugin [46].

4. **Fourier ring correlation (FRC).** This approach considers the entire image stack and eliminates noise and many image artifacts from the frequency-based resolution analysis. The correlation is done between two independent images of the same structure, which makes it well-suited for EM (which it was originally developed for) and for SMLM data, as their image stacks can be readily divided into two independent datasets of the same image object. *Problems:* • For many microscopy experiments, and especially so in live-cell imaging, two independent image datasets of the same sample structure are simply not available nor obtainable. • The frequency cut-off parameter is subjectively chosen by the user [48].
5. **Fourier (phase) decorrelation analysis** This approach is different from the two other Fourier-based methods by emphasizing the frequency phase component, instead of only considering the frequency amplitude components (as in the power spectral or FRC approaches). This is possible since most of the image structural information is contained in the phase component. This method does not estimate the theoretical resolution, but the highest frequency with enough signal in comparison to noise. It hence overcomes the problem of Fourier power analysis's inability to discriminate noise from structural details, the problem of a reference image in FRC, and the problem of both of these in choosing a suitable and objective frequency cut-off for the resolution [49]. *Problem:* Image artifacts (in e.g. SIM and FF-SRM) can still be confused for real, high-frequency data.

The ImageJ plugin NanoJ-SQUIRREL [50], part of the *NanoJ super-resolution microscopy toolbox*, with an emphasis on "demands for live-cell super-resolution microscopy" [51], is developed to assess SRM image quality and reconstruction artifacts. However, and quite paradoxically, the generation of error maps relies on having an *a priori* ground truth image, making it in effect useless for assessing live-cell (and most other) microscopy image data.

We are actually left with no standardized method of assessing our live-cell SRM images. For SIM, artifacts are well characterized and can usually be easily

recognized by the experienced SIM operator. Based on extensive testing under conditions of both live- and fixed-cell imaging, together with knowledge of normal biological structures, I have developed some additional criteria for the evaluation of FF-SRM image reconstructions.

Criteria for the evaluation of FF-SRM image reconstructions

(-) BAD, (+) GOOD

(-) Definite structures appear in reconstructed images where there is clearly only noise or background signal in the raw images.

(-) Structural patterns appear in reconstructed images which are inconsistent with known biological patterns, especially if these shapes change for different reconstruction parameters.

(+) Reconstructed images reveal very little or no signal in 'no object areas', but significant signal where real structures are expected to be.

(+) Image structures are consistent across different parameter values (if available).

(+) Images reveal sub-resolution sized structures in the object-of-interest areas and nowhere else. It is great if these structures are in accordance with what is already known about these structures/organelles, although this cannot be strictly required as most nanoscale cellular structures in living cells cannot be strictly assumed to have the same nano-structure as seen by EM of fixed, starkly treated cells.

(+) Excludes out-of-focus structures, rather than producing image artifacts and nonsense sample details.

In summary, the evaluation of SRM images is a challenging and often subjective task. The quickly expanding field of Machine learning (ML), continuously conquering new grounds in diverse areas of science and society, might eventually also hold the key to faster, better, and objective image analysis in the complex field of SRM.

1.3 Machine learning in microscopy

Artificial intelligence (AI) is a broad concept where machines can be put together to exhibit behaviors or perform tasks requiring some sort of intelligence, traditionally the sort of tasks only performed by living beings.

ML is a sub-field of AI where computer programs are made to learn their own

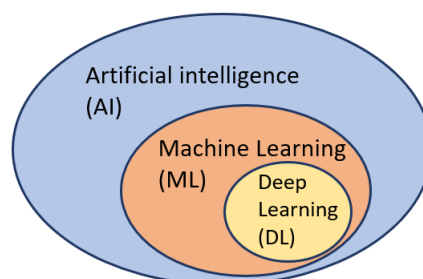


Figure 1.14: Overview of the connection between the fields of AI, ML and DL.

classification rules based on a set of *training data*, often including some sort of *ground truth* reference. The rules found from the training data can then be used to classify data where the ground truth is desirable but lacking.

Deep learning (DL) is a sub-field of ML involving more complex algorithms with a more flexible learning process possessing many layers. These algorithms are often able to recognize data features otherwise overlooked by humans and to train themselves to a very efficient classification protocol that does not (after training) require much computational resources or time. The main issue here is that there are many "hidden layers" and it is usually not clear to the humans applying the programs what is going on inside these layers, called the program's neural network (NN). Recently, many DL algorithms have become available for free online (including processing power) for anyone to test out on their biological images and get started with applying DL to their particular data [52].

ML has, for example, been applied to learn "high-signal" images from low signal ones. This is used to reduce acquisition time and thus protect the cells from phototoxicity by minimizing the SNR in images needed to reach certain biological insights [53]. ML has also been developed to achieve a similar level of specificity as with fluorescent labels but only requiring the imaging of unlabeled samples; this enables long-term time-lapse imaging without being limited by photobleaching and the possible toxicity of fluorescent labels [54].

Work in ML is also done to recover high-resolution images from low resolution images, in a sense similar to a SRM algorithm (but not limited to only microscopy data) [55][56]. Although ML in combination with SRM algorithms can be a powerful tool to enhance and speed-up SRM reconstruction procedures [57][58][59], one should also exert extreme caution against learning and superposing information in images that is simply not there [60].

In Article E we employed ML in combination with the FF-SRM technique MUSICAL for automated detection and analysis of nanoscale motion patterns of vesi-

cles in cardiomyoblasts. This work is described further in section 2.2.3.

1.4 Total internal reflection fluorescence microscopy

1.4.1 Principle and applications

In this last introductory section, microscopy with a completely different mode of illumination is introduced: evanescent fields. They are present on an interface between two media of different refractive indices (RI), when light is shone on the surface (from the medium with higher RI) at an angle greater than the *critical angle*, θ_c (see upper panel Figure 1.15). Beyond this angle of incidence, the electromagnetic wave cannot propagate through the surface but is completely internally reflected. However, across the surface in medium n_2 , a high-density *evanescent field* can be present, but with exponentially decaying intensity away from the surface. In a typical lens-based total internal reflection fluorescence (TIRF) microscope, the intensity can be five times higher across the surface than of the incident beam [61]. Denoting the intensity at the substrate ($z = 0$) I_0 , and δ the decay length, the intensity at a distance z away from the substrate is given by

$$I = I_0 e^{-z/\delta} \quad (1.7)$$

$$\delta = \frac{\lambda}{4\pi(n_1^2 \sin^2(\theta_{in}) - n_2^2)^{1/2}} \quad (1.8)$$

where λ is the excitation wavelength, θ_{in} the angle of incidence, n_1 and n_2 are the refractive indices of the substrate and the sample, respectively. The decay length (or penetration depth) is defined as the distance, z , into the sample where the intensity has fallen to I_0/e (i.e. about 37% of I_0). From equation 1.8, we see that the penetration depth scales linearly with the wavelength: the longer the wavelength, the deeper the penetration depth. Other determinants for δ are the angle of incidence and the RI difference between the two adjoined media [14].

The lower panel of Figure 1.15 shows the dependence of the evanescent field penetration depth (per wavelength) on the ratio n_1/n_2 and on the angle of incidence. From the graph we can see that:

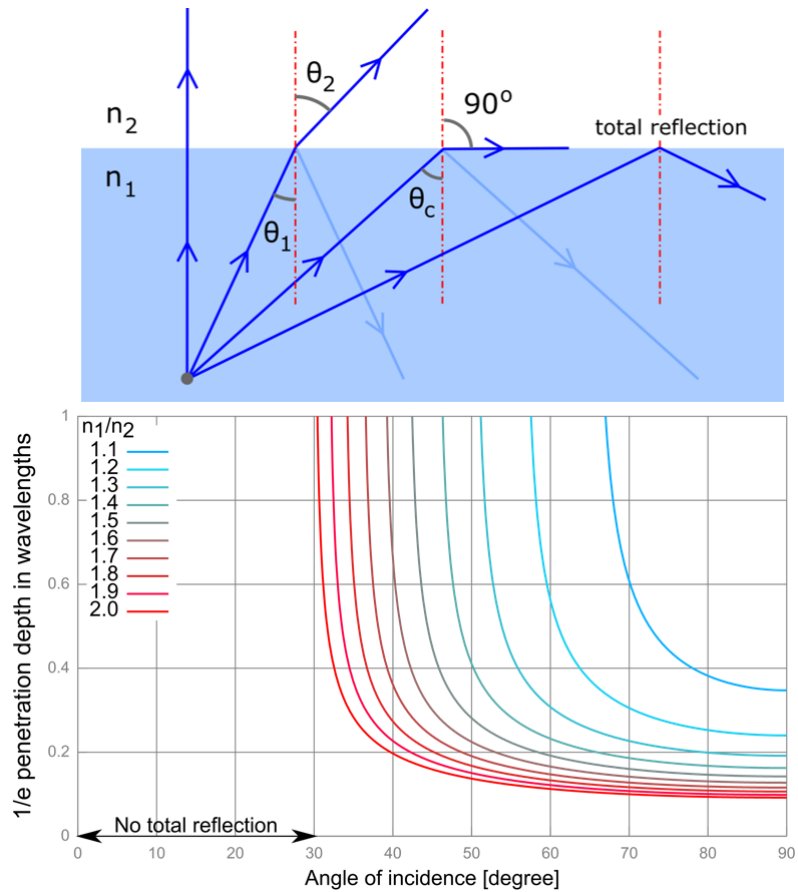


Figure 1.15: *Upper panel:* Behaviour of rays hitting a surface towards a medium of lower refractive index. θ_1 is the angle of incidence and θ_c the critical angle. When $\theta_1 > \theta_c$, electromagnetic waves (or rays) are completely reflected back into the substrate. The figure was retrieved from [62]. *Lower panel:* The different colored graphs show penetration depth for different ratios of n_1/n_2 as a function of angle of incidence, θ_1 . The graph was adapted from [63].

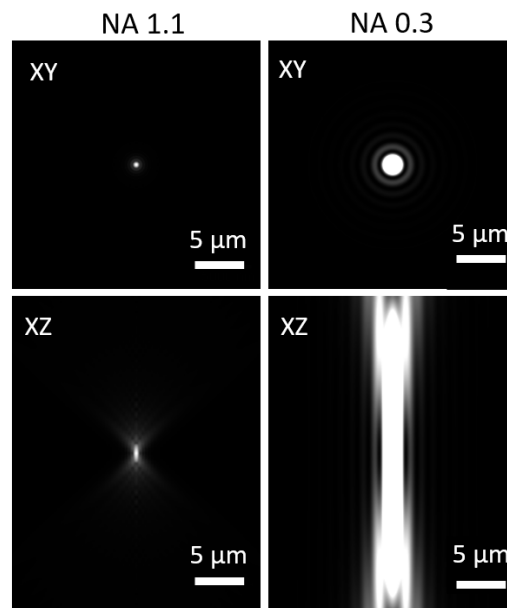


Figure 1.16: Lateral (top) and axial (bottom row) PSFs for 0.3 NA and 1.1 NA objectives. Generated using Richards & Wolf 3D optical model via the ImageJ plugin *PSF Generator* by Hagai Kirshner and Daniel Sage.

1. Higher ratio n_1/n_2 gives total internal reflection at drastically smaller angles of incidence, e.g. from 30° for $n_1/n_2 = 2.0$, while from about 67° for $n_1/n_2 = 1.1$.
2. For angles close to the critical angle, the penetration depth is close to 1 unit of wavelength for all RI ratios, while for larger angles, e.g. 10° above θ_c , the different ratios of RIs give very different penetration depths: more than double in the case of $n_1/n_2 = 1.1$ compared to $n_1/n_2 = 2.0$.

Hence, within the range of 0.1λ to 1λ , the penetration depth can be tailored according to particular applications by adjusting n_1/n_2 and the angle of incidence.

For substrate-near applications, there are two main **advantages** of using evanescent field illumination:

1. Elimination of background signal. This is of special importance in applications of SMLM and in substrate-specific studies (e.g. cell membrane domains) that might lack the necessary contrast when illuminating thicker sample sections.
2. Reduced sample light dose/phototoxicity.

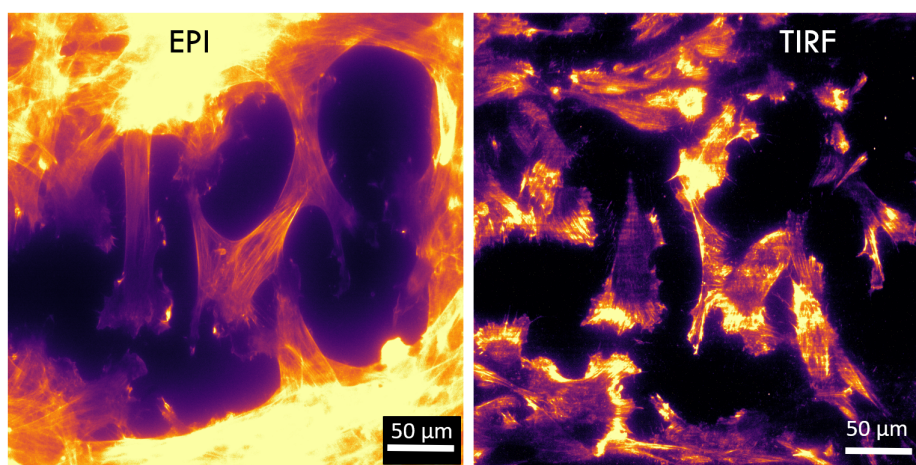


Figure 1.17: Images of the same cells (fixed fibroblasts labeled using SiR-Actin) using episcopic (left panel) and waveguide TIRF illumination (right panel), both acquired using a 1.1 NA water dipping objective. Episcopic illumination excites fluorophores through the entire sample volume, while TIRF selectively excites only the bottom ≈ 100 nm.

The importance of having this narrow illumination field in high-precision techniques like SMLM can be intuitively understood from the axial PSFs of objective lenses, as displayed in the bottom row of Figure 1.16. The upper row displays the corresponding lateral PSFs as discussed in section 1.1.4. The axial precision is far worse than the lateral one, and the effect becomes stronger for lower NA objectives (the axial resolution scales with $1/\text{NA}^2$). One can imagine that having molecular precision laterally (as could be obtained with SMLM) would be of little value if one cannot tell if two laterally co-localized molecules were close or distant to one another also axially.

When the illumination field is narrow and at a well-defined location at the substrate, much more accurate localisations (and co-localisations) can be made. How much more depends primarily on the collection objective NA. Figure 1.17 shows a comparison of pictures acquired using episcopic (left) and evanescent field illumination (right) from photonic waveguides (topic of next section), using a 1.1 NA water dipping objective. In the TIRFM image, the cellular details at the surface are clearly visible, while using episcopic illumination, the above-substrate layer cellular structures outshine the substrate layer structures.

It can be tempting to call this *axial nanoscopy*, and arguably so according to the first resolution measurement strategy of section 1.2.4, i.e., measuring a line profile FWHM. However, consulting the very definition of resolution, namely as the smallest distance between two distinct points or features that can be discriminated, this does clearly not hold for the axial dimension employing

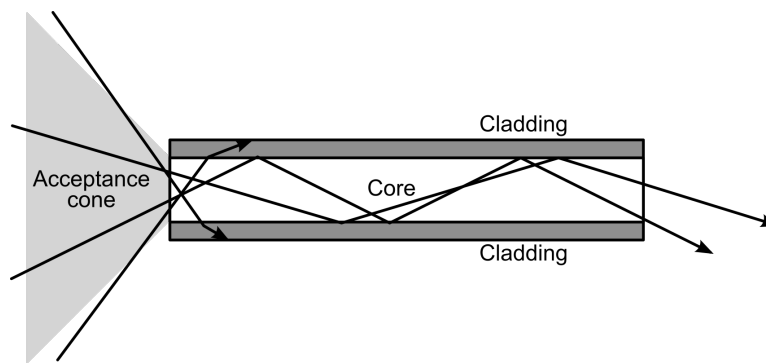


Figure 1.18: Optical fiber/photonic waveguide. The light is guided through and along the core of the waveguide, confined by total internal reflection. The acceptance cone describes the light ray directions which can propagate through the waveguide. Figure by Gringer talk [67].

pure TIRFM, as the result is a single sampling point in the axial dimension. That is, unless TIRFM is combined with additional experimental and analytical sophistication. Axial nanoscopy via TIRFM can be achieved when executed under a range of illumination conditions which alters the TIRF penetration depth, as in e.g. multi-angle TIRF [64][65] or single molecule intensity analysis [66].

1.4.2 Optical waveguides

In optics, a waveguide is a structure used to guide and confine the flow of light. An example in wide everyday use is the optical fiber, outlined in figure 1.18.

Not any light can enter and propagate through the waveguide. Usually, the smaller the waveguide geometry, the fewer modes can propagate. By a mode, we mean a certain intensity pattern that stays constant during the wave propagation. In addition to being within the "acceptance cone" for propagation (illustrated in Figure 1.18), also the wavelength and polarization of light influence the propagation, intensity pattern, and evanescent field penetration depth.

Waveguides are characterized as either single or multimode. The single-mode waveguides are typically of small dimensions (width $< 1 \mu\text{m}$) and have a smooth Gaussian intensity profile. They can be slowly broadened (called tapering) to excite a wider area but still (possibly) retain the single-mode characteristics. Multimode waveguides can be arbitrarily large from the start of the coupling facet and have a speckled intensity distribution from the interference of the

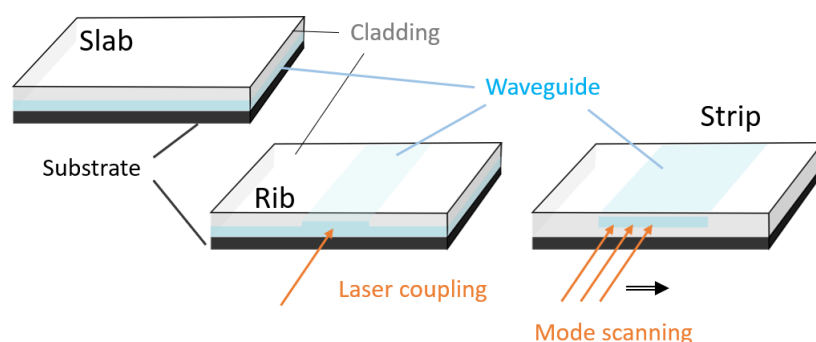


Figure 1.19: Waveguide geometries and mode scanning. 3D views of the slab, strip, and rib waveguide geometries. For single-mode conditions, the strip or rib designs can be used with small dimensions (widths of strip $< 1 \mu\text{m}$, and rib 1 to $1.5 \mu\text{m}$). The heights of the guiding layers used for the work presented in Ch. 2, are on the order of 150-250 nm. The small height pushes more of the propagating electromagnetic field into the evanescent field used to excite fluorophores. Mode-scanning is conducted to achieve a, in sum, more homogeneous illumination field on multimode waveguides (referred to as mode-averaging).

different propagation modes, which can be thousands [68].

Here, we consider dielectric waveguides, with some typical geometries and dimensions outlined in Figure 1.19. The substrate is for mechanical support and is usually made of silicon. The waveguide material guides the light and has a higher refractive index than the adjacent materials. The cladding functions as a protective layer and is typically made of silicon oxide. For the work presented in this thesis, only the multimode strip geometry was used with silicon nitride or tantalum pentoxide as guiding materials.

To get light into the waveguides (i.e. laser coupling), the most efficient for the particular experiments presented in Ch. 2, is by focusing the laser beam (using an objective lens) onto the input facet. For some applications, the use of a fiber connector or grating coupler can facilitate the process, as manually focusing light into an about $0.2 \mu\text{m}$ thick waveguide can be quite fiddly and time-consuming.

To obtain a fairly uniform illumination field from multimode waveguides, the coupling point is scanned along the waveguide edge (see Figure 1.19) (e.g. using a nanopositioning piezo stage), sequentially exciting different sets of modes, whose speckled interference patterns on average should (hopefully) yield an illumination field uniform enough for one's application.

Which modes can propagate in a certain waveguide geometry and material composition can in theory be determined by solving the Maxwell wave equations with boundary conditions, although this can be a tough task. In practice, commercial softwares are used to simulate their propagating modes for different materials and geometries. These numerical approximations are not necessarily perfectly accurate, and the same holds for the fabrication process. An important step in the fabrication process is hence characterization (or testing) of the waveguides [69].

Noteworthy considerations and challenges concerning waveguide work include:

- **Design and fabrication:** time, reproducibility, cost and equipment availability.
- **Coupling:** getting the light from an optical fiber (from a laser source) into the waveguide at the (tiny) input facet.
- **Propagation loss:** drop in signal intensity per distance from coupling facet.
- **Autofluorescence of the waveguide material:** can interfere with fluorescence imaging experiments (and is positively correlated with propagation loss).

I have not worked to solve any of these challenges. They are taken by other team members (thank you JC, Firehun, and Anish!). My contributions in this field have been on the design and implementation of the surrounding technicalities to make the waveguide chips usable for applications in live-cell bioimaging.

1.4.3 Implementations

Some possible options for TIRFM setups are shown in Figure 1.20. The by far most common implementation is displayed in panel A, where a high NA oil immersion objective is employed both for excitation and signal collection. The advantage of such a setup is an easy fit with standard glass-bottom dishes for cell microscopy, together with commercial availability and support. Downsides are a fairly small illumination area (rarely above 40 by 40 μm), non-uniformity of illumination intensity (usually a Gaussian profile), a mandatory and expensive high-NA TIRFM lens that does not invite for experimental flexibility.

Another option that has been around for some decades is TIRFM using a quartz

prism, displayed in panel B. This might be a good option if TIRFM images of the top of the specimen are desirable. This TIRFM implementation also gives some flexibility concerning the illumination area and choice of collection objective. Downsides compared to the objective-based TIRFM implementation, are that the signal must travel through the specimen before being collected by the objective, together with non-standard microscopy setup and sample preparation that might be found cumbersome in the bio lab workflow.

Another non-standard TIRFM implementation, is via photonic waveguide chips, like the one displayed in panel C. From now on, only chip-based TIRFM will be discussed.

The waveguide imaging options in panels D and E are not fundamentally different but modified for different applications. Option D, with a coverglass on-top of the sample, can e.g. be employed for high-resolution SMLM applications with a high-NA oil immersion objective (e.g. like presented by Diekmann and Helle et al. in [70]).

For live-cell imaging, rather than squeezing the cells with a very small amount of liquid between the chip and the coverglass, option E, using a water dipping objective is a much more practical solution. This option was employed for the images in Figure 1.17 and for on-chip TIRFM of living neurons, described in more detail in Section 2.3.1 and Appendix G.

Panel F illustrates the option of *transparent* waveguide chips (a topic of current development), which will allow for photonic chips to be employed more like an ordinary coverslip for microscopy with signal collection through the chip instead of through the specimen. This reduces potential specimen-induced aberrations and allows for use with inverted microscopes, an important aspect for a smooth transition of chip-based microscopy into the workflow of cell culture laboratories.

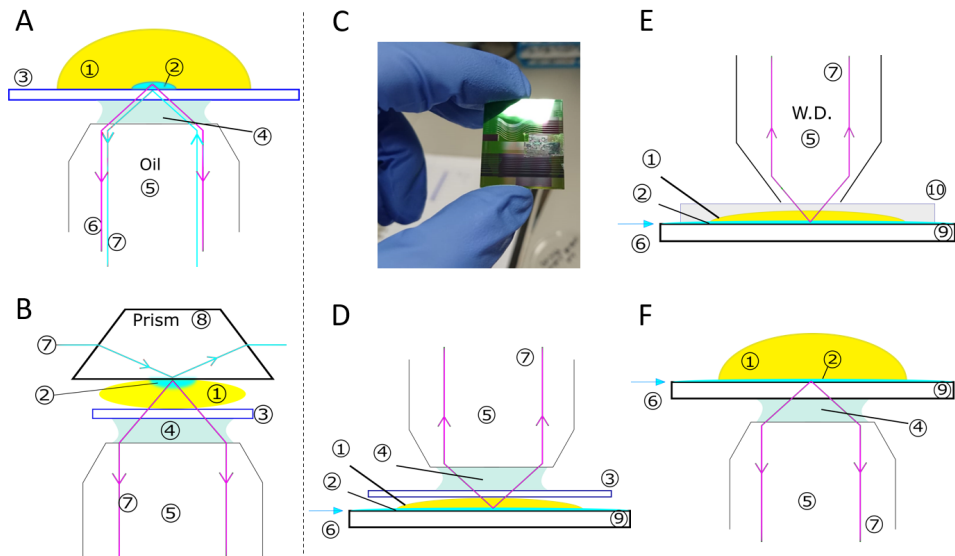


Figure 1.20: Options available for TIRFM. A and B show traditional implementations using either a high-NA objective or a prism for TIRFM excitation. C-F show C-TIRFM options: C, a (optically opaque) photonic chip with both single- and multimode waveguide options; D, upright microscopy configuration with coverglass and immersion objective (also air objective is possible). E, upright configuration with water dipping objective. This is the preferred option for live-cell imaging. Instead of confining the sample between the chip and coverglass, the sample with a cell culture medium is confined with an open PDMS fence. F, transparent chip (under development). A transparent chip allows for use with inverted microscope setups and evades image aberration caused by imaging through a thick specimen. 1. Sample, 2. evanescent wave, 3. coverslip, 4. immersion oil, 5. objective, 6. emission signal 7. excitation beam 8. quartz prism, 10. PDMS cell medium container/fence. A and B adapted from work by Dawid Kulik [71].

/2

Summary of articles

This chapter summarises the main findings of the articles forming the basis for this doctoral thesis. The articles are included in their complete form in Appendices A-G.

2.1 Structured illumination microscopy

2.1.1 Multi-color imaging of sub-mitochondrial structures in living cells using structured illumination microscopy

SIM imaging requires an expensive and well-aligned system together with sample-specific optimization of imaging parameters like the immersion oil RI, laser intensities, and exposure times to obtain an acceptable trade-off between signal, photobleaching, and imaging time. For such an acceptable trade-off to be at all possible, good groundwork must be laid during sample preparation, as any non-specific labels or misplaced samples (e.g. too far from the coverslip) can distort the SIM modulation pattern so critically needed for reliable image reconstruction.

The importance of "good stripes" in the SIM raw data for successful SIM reconstruction was well known to the SIM community before I started this doctoral work. However, how this translates to conditions for live-cell imaging

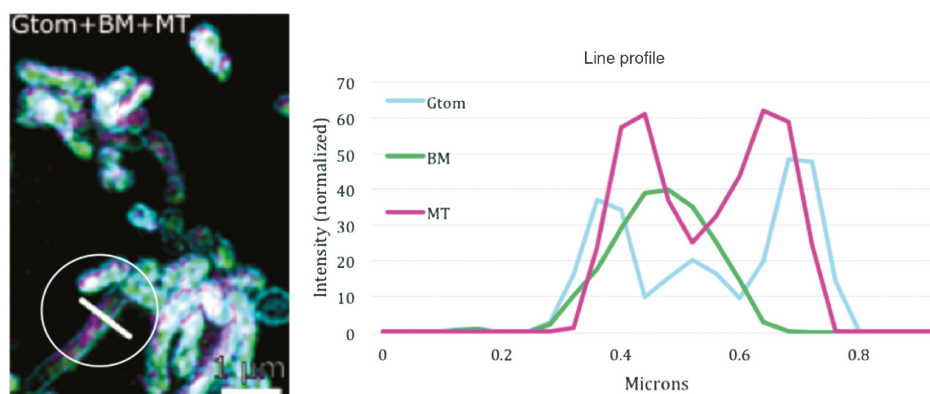


Figure 2.1: Three-color 3D SIM image of mitochondria in living cells with multi-channel intensity line profiles of the indicated line. The three different colors represent the outer mitochondrial membrane (cyan, Gtom), the mitochondrial matrix (green, BM), and the mitochondrial inter-membrane space (magenta, MT). This figure was published previously in [25].

and creates boundaries for what applications the current SIM technology is useful for were largely unknown and unexplored. These questions have been central topics in my doctoral research, naturally arising from the desire to understand the intricate and fascinating cellular machinery.

Fluorescent labeling for conventional imaging experiments rarely considers which part of a cellular organelle is labeled, as these do not achieve a resolution high enough to distinguish between different parts of the subcellular organelles. In this work, we optimized labeling protocols for multi-color 3D SIM imaging of mitochondria by targeting different sub-mitochondrial regions with spectrally separated fluorophores in living cells. This 3D SIM system achieves just sufficient resolution to distinguish the different regions of mitochondria, as illustrated in Figure 2.1.

The relatively long image acquisition time, together with intense light exposure (both compared to conventional microscopy) required for an image stack of decent 3D SIM raw data, were recognized as significant hurdles strongly limiting the applicability of 3D SIM in following nanoscale dynamics and interactions in living cells.

Additional results, complete sample preparation protocols together with further discussion of challenges and opportunities with multi-color live-cell SIM imaging are contained in the complete manuscript (Appendix A).

2.1.2 Live-cell imaging of human spermatozoa using SIM

The spermatozoon, or sperm cell, is the male reproductive cell. In animals, the spermatozoa are extremely motile, with a compact head containing the genetic material (about 3-5 μm diameter), and a comparatively long tail (about 50 μm) propelling the head.

Spermatozoon is a more specific term than sperm cell, as sperm can contain other cell types as well, usually referred to as *round* cells. High-quality sperm is characterized by a high spermatozoon count and a low round cell count. The health of the male subject is strongly influencing these numbers. During e.g. a cold, the sperm can for a period be of lesser quality. These quantities can and are usually measured (i.e. counted) by eye using normal light microscopy. There can, however, be other factors of infertility that are both permanent and non-detectable using light microscopy.

In addition to the many interesting questions concerning the fundamental biology of reproduction that can be elucidated with help from high-resolution microscopy studies, the structure of sperm cells is of particular interest in the context of infertility diagnostics and sperm selection for in vitro fertilization (IVF). Human egg harvesting and embryo implantation are both costly and stressful (to especially the woman), so there is a strong preference for the pregnancy being successful the first time, without the need for repeat experiments.

To fertilize an egg in a dish, one can choose one spermatozoon (using a micropipette) and add it to the egg. One wish to choose a good cell that accomplishes to fertilize the egg and leads to embryo development and brings about a successful pregnancy. Which cell to choose? Usually, one follows the example of nature and takes a fast swimmer. For IVF, there might be better sperm cell selection criteria for embryo development of which we are still unaware of.

Despite considerable interest in their ultrastructure, SIM imaging of *living* spermatozoa had not been done (or published) before we recently did it. The reason why live-cell SIM imaging of sperm cells had not been done previously, might be that they are really fast swimmers, $\approx 66\mu\text{m}/\text{s}$ [72]! Considering the normal SIM imaging FOV of about $40\mu\text{m} \times 40\mu\text{m}$, one would be lucky just to notice the cells' presence before they are out of sight.

There was a trick, of course, that enabled beautiful pictures like the one in Figure 2.2 to be acquired. To make the cells sit still and well-behaved at the coverslip for the entire duration of four-color 3D SIM imaging, I came up with a solution inspired by a procedure commonly applied in microbiology

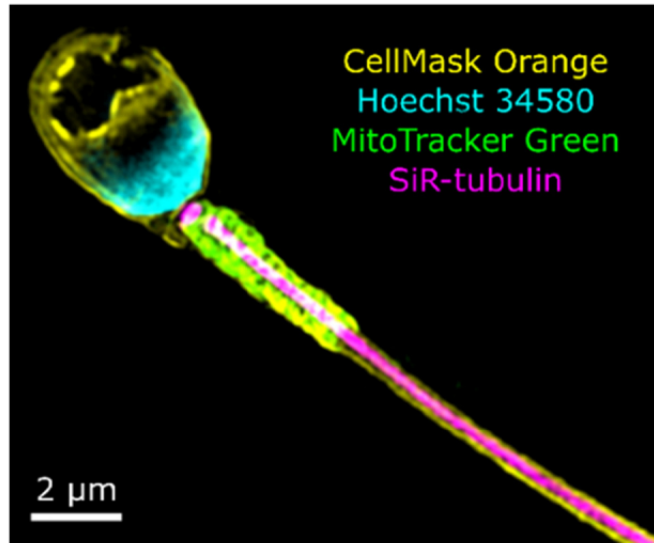


Figure 2.2: Four-color 3D SIM of living spermatozoa. The different colors represent spectrally separated fluorescent probes targeting different cellular structures: Plasma membrane (orange), nuclear DNA (cyan), mitochondria (green), and microtubulin (magenta). This figure was published previously in [73].

for immobilizing suspension bacteria: covering the cells with a thin patch of agarose gel. Short protocol: 1) Label and wash cells, 2) add cells + agarose to coverglass, 3) image.

Labeling and general sample preparation of these primary suspension cells required very different procedures from those applied to the adherent cell cultures presented in the previous work. The cells being alive and primary excludes both genetically encoded tags or antibody labeling. The cells being in suspension (free-floating) makes it more challenging and time-consuming to wash away the unbounded fluorophores, which require a centrifugation step in enough buffer to remove unspecific dye molecules, but without losing the precious cells in too much solution. Too hard centrifugation can also damage the cells, but with too little, the cells are lost. The complete sample preparation protocols together with more results are available in the published article (Appendix B).

This work was done in close collaboration with Daria A. Popova at the Department of Clinical Medicine and the Tromsø *in vitro* fertilization (IVF) clinic.

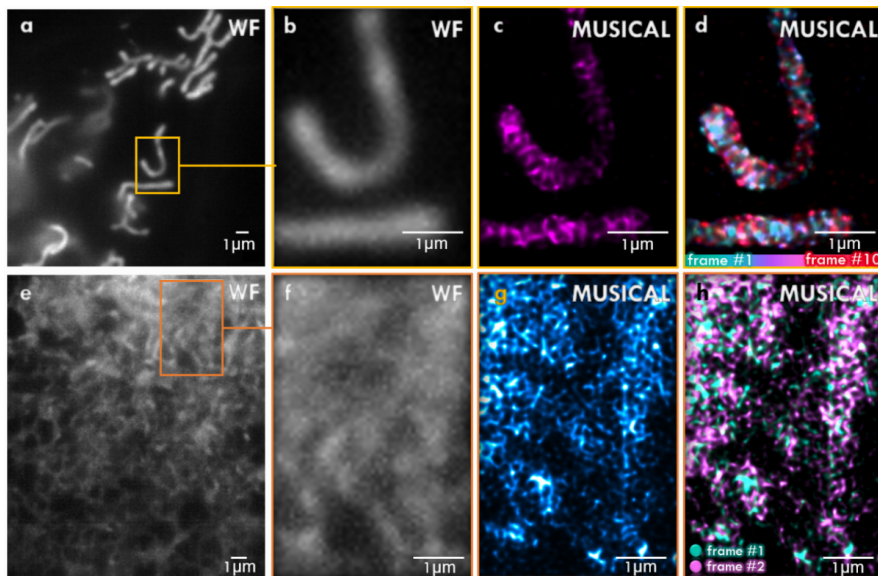


Figure 2.3: Pushing the limits of time resolution in live-cell nanoscopy. Obtainable MUSICAL frame rate is limited by achievable system imaging speed and the fluorescence intensity fluctuations of the raw time-lapse image data. Upper panels: mitochondrial inner membrane, lower panels: endoplasmic reticulum (ER). (a) and (e): Epi-fluorescence microscopy images (50 frames low-intensity images maximum intensity projected) with indicated regions magnified on the right. (c) and (g) corresponding MUSICAL images obtained from the 50 frames projected on the left. (d) and (h) MUSICAL time-lapse images color projected as indicated by the color bar. The different color projected time-points are 0.22 s apart (acquisition time for a sequence of 50 raw images). Considerable challenges encountered in this work are the presence of mesh artifacts and the lack of a ground truth reference for the underlying ever-changing biological structures. The figure was previously published in [74]

2.2 Fluorescence fluctuation-based super-resolution microscopy imaging

This section describes the published results related to FF-SRM.

2.2.1 Adaptive fluctuation imaging captures rapid subcellular dynamics

This initial work I was interested in testing MUSICAL for live-cell imaging of dynamic living systems. "Adaptive" in the title of this article refers to the flexibility of the algorithm in choosing the number of frames in the recon-

struction according to the desired or necessary time-resolution (likely at the expense of reconstruction quality). The title says fluctuation imaging rather than nanoscopy because I evaluated the reconstruction results as, at best, not trustworthy. Examples of MUSICAL (likely mesh artifact) results are provided in Figure 2.3. I recognized the lack of ground truth reference as a substantial challenge when evaluating SRM reconstructions and especially for the case of dynamic living cells.

The article (full version available in Appendix C) reports about rapid (up to 230 Hz) wide-field imaging, together with a straight-forward multi-channel extension of the nanoscopy algorithm, but also the hurdles of speed limitations and reconstruction artifacts, especially when the multi-channel imaging requires fluorescence filter-wheel switching between each (raw) image acquisition.

At this stage, in addition to the lack of a ground truth reference, I was struggling with the practical limitations of image reconstruction time, threshold selection, and the complete lack of an efficient user interface for applying the algorithm. In effect, I had created the need for a new piece of software which would allow for efficient multi-color time-lapse reconstruction of MUSICAL images, together with the extensive testing of different thresholds and acquisition conditions.

2.2.2 Musij: an ImageJ plugin for video nanoscopy

To overcome the practical limitations outlined in the previous section, and to advance the usability and availability of the computational SRM method MUSICAL, we created the ImageJ plugin MusiJ. The MUSICAL algorithm is briefly explained in Figure 2.4.

The plugin was designed according to my particular needs for a convenient and efficient user interface for testing of multi-color video nanoscopy. It is specialized for generating MUSICAL videos from large stacks of multi-color time-lapse images via an interleaved reconstruction, thus enabling easy-to-use imaging of dynamic systems. The number of frames used for each time-point, together with how the frames used for consecutive frames are reused for multiple time-points, are user-specified. This is particularly important for fast-moving samples. All user parameter are saved in a log file to keep track of the experimental parameters with the reconstruction results. The most important parameters like the threshold and number of frames used are also written in the filename of the MUSICAL image to more easily navigate through large amount of experimental data.

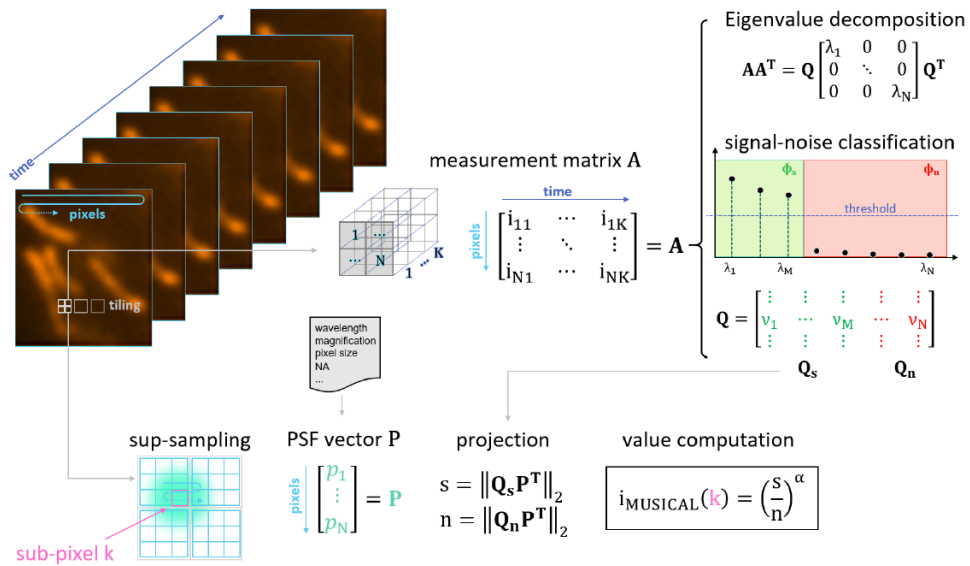


Figure 2.4: Depiction of the MUSICAL image generation. First, the movie is arranged into a two-dimensional measurement matrix A . On the square matrix AA^T , eigenvalue decomposition is performed. This arranges the image features contained in A according to their significance, encoded in the size of the eigenvalue (or singular value) associated with each eigenvector. Based on the plot of the singular values, a user-defined threshold, separating eigenvectors into the signal or noise space, is needed before the MUSICAL image computation. The sub-sampling determines the accuracy of the PSF center location and overlap with neighboring "test point" regions, together with the final image pixel number (or "resolution"). Estimation of a signal and noise value for each pixel in the sub-sampled image is done by the projection of the eigenvectors onto the PSF vector. The final MUSICAL image intensity values are the ratio of the signal-to-noise estimate, to the power of the user-defined parameter α . The figure was previously published in [75].

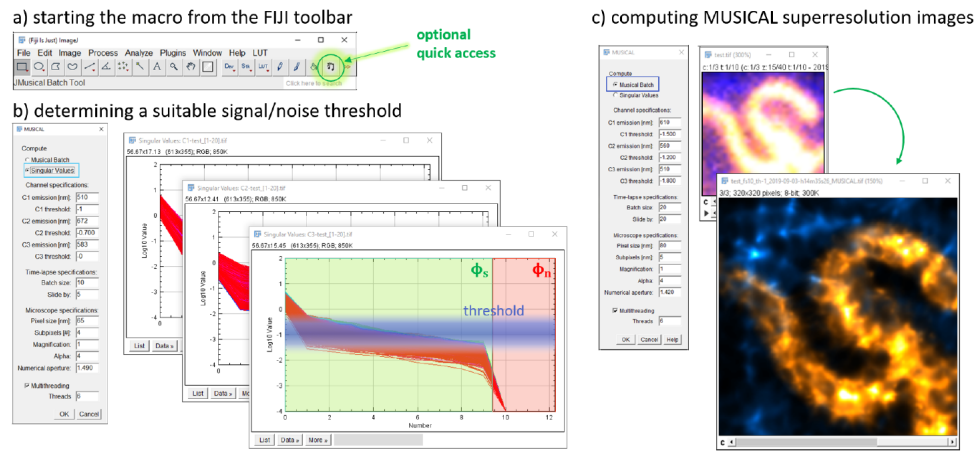


Figure 2.5: The graphical user interface of MusiJ with an exemplary threshold selection indicated on the plot of singular values. The figure was previously published in [75].

The computational speed-up is almost 30-fold compared to the original MATLAB implementation. This is done by 1) change of data type (from *binary64* to *binary32*), 2) modified computation of MUSICAL intensity values, and 3) multithreading. The third option is a user-specified parameter that should be adjusted according to the particular PC's number of cores and potentially other computer resources that might be needed by the user in parallel during the MUSICAL image reconstruction time.

In addition to recognizing the need for the MusiJ plugin, I contributed to this work in the user-interface design, with live-cell experimental data, and did extensive testing of different versions of the plugin.

The front end ImageJ graphical user interface (GUI) is showcased in Figure 2.5, and the complete publication is available in Appendix D.

2.2.3 Learning nanoscale motion patterns of vesicles in living cells

In the two previous sections, the acquisition and computation of nanoscopy videos of living cells were discussed. Another essential factor for the usability of nanoscopy in live-cell imaging applications, is the analysis and interpretability of the reconstructed images.

In this work, led by Dr. Arif A. Sekh, we adapted and employed ML for the detection and classification of nanoscale motion patterns in living cells (the

cardiomyoblast cell line H9c2). My contributions to this work consisted mainly in the experimental design, data acquisition, together with recognising suitable conditions for ML of fluorescently labeled and dynamic cells. Having the right training data for any application of ML is essential for the algorithms to create meaningful results and successful classifications.

The detection and classification of nanoscale motion patterns was done by combining ML with the motion-preserving nanoscopy algorithm MUSICAL. It is motion-preserving in the sense that the fluorescence signal from a moving object will by the algorithm be interpreted as an object spanning the entire motion path with a high-variance (or blinking-like) signal fluctuation that is likely to dominate other local image features. For example, if a small vesicle is moving in a straight line, the MUSICAL image of this movie will be a straight line (see the Flow motion state and other examples in Figure 2.6). Notably, also nanoscale motion patterns that are not observable from the videos directly can be extracted and analyzed via the nanoscopy algorithm.

The developed methodology can be divided into four modules:

1. Physics-based simulations for creating training datasets.
2. MUSICAL for nanoscale motion reconstruction.
3. Spatio-temporal region of interest (ROI) detection using localization-based tracking (QuickPALM [76]).
4. Classification of motion patterns.

The network was trained based on simulations with five different **motion states**:

- **Stationary**: The vesicle remains stationary and with diameter $\in [150, 400]$ nm.
- **Random walk**: The vesicle can move in any direction with equal probability, step size $\in (0, 1000]$ nm/frame.
- **Directed flow**: The vesicle moves along a path with a constant velocity in the range $[0, 1000]$ nm/frame.
- **Circular Motion**: The vesicle moves along the periphery of a virtual circle with a randomly selected center, radius $\in [200, 500]$ nm, and velocity $\in [0, 500]$ nm/frame.

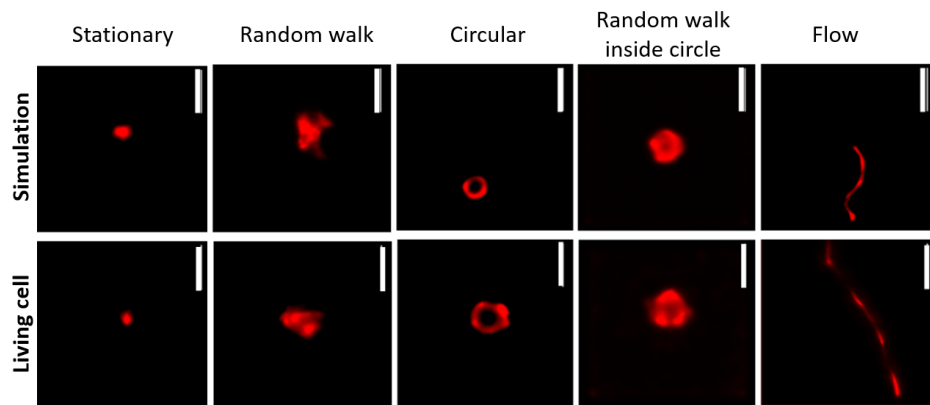


Figure 2.6: *Upper row:* The different simulated motion states used for network training (or machine learning). *Lower row:* Classified motion state examples from live-cell image data. The images were previously published in [77].

- **Random walk inside a circle:** The vesicle takes random positions within a circular area with a radius randomly selected $\in [200, 400]$ nm/frame.

This methodology was tested and the results compared for cells from three different pools:

- **Normal:** Cardiomyoblasts kept under normal cell culture conditions.
- **Hypoxia:** Cardiomyoblasts subjected to 1 hour hypoxic conditions (lack of oxygen) right before imaging.
- **Hypoxia+ADM:** Cardiomyoblasts subjected to 1-hour hypoxia with simultaneous treatment with the hormone adrenomedullin (ADM). ADM has been found to exhibit protective functions under the pathological condition of myocardial infarction (cardiac arrest).

All three pools were labeled in the same manner using the live-cell friendly membrane probe mCLING-ATTO647N. High frame rate fluorescence time-lapse movies of 2000 frames each were acquired.

The automated analysis of the motion states and changes in them was conducted for 9449 vesicles. While the random walk was the most prevalent motion state in all pools, also a clear demarcation was found between the motion states of the different pools (cell conditions), and also in their transitions between such states. For example, the vesicles in cells subjected to hypoxia without the ADM were the *least* stationary and demonstrated a higher number of transitions from the Circular and Flow to Random walk motion states compared to the

normal pool. The Hypoxia+ADM cellular vesicles had a reduced number of such transitions.

As the experiments were designed to provide an initial test dataset for the proposed ML framework for cell analysis, the results are not conclusive from the biological side. The rigorous biological study would need further biological and environmental controls with hypothesis-specific experimental design and large scale experimentation.

We envision this type of analysis to enable large scale studies of vesicle transport and interactions in living cells in the future.

The complete manuscript is included as Appendix E and also available online with supplementary information [77].

2.2.4 Fluorescence fluctuations-based super-resolution microscopy techniques: an experimental comparative study

We have seen that optical nanoscopy via MUSICAL involves considerable challenges like the generation of reconstruction artifacts, choice of parameters, and reconstruction time. Are there any better FF-SRM algorithms out there? How to they compare to one another?

In this study, I took leadership in an extensive comparative experimental study with the aim of recognizing the suitable (and unsuitable) experimental conditions for different FF-SRM methods. Although other PhD students contributed significantly towards their experimental sample expertise (e.g. liposomes, tissues, and simulations), my contributions were essential in paving a way through the experimental jungle and condensing the results into a comprehensive and usable study.

We applied five different FF-SRM methods (SOFI [79], SRRF [40], ESI [39], MUSICAL [41] and SACD [42]), also in combination with HAWK [80], to different types of both real and simulated microscopy data. HAWK is a data preprocessing technique used to increase the emitter temporal sparsity.

These techniques were chosen from code availability and practical limitations concerning time and resources. Techniques that were considered but left out were Bayesian analysis of blinking and bleaching (3B) [81], sparsity based super-resolution correlation microscopy (SPARCOM) [82] and unsupervised particle localization (UNLOC) [83]. 3B was left out for requiring extreme computational time and resources, SPARCOM is also processing intensive and in

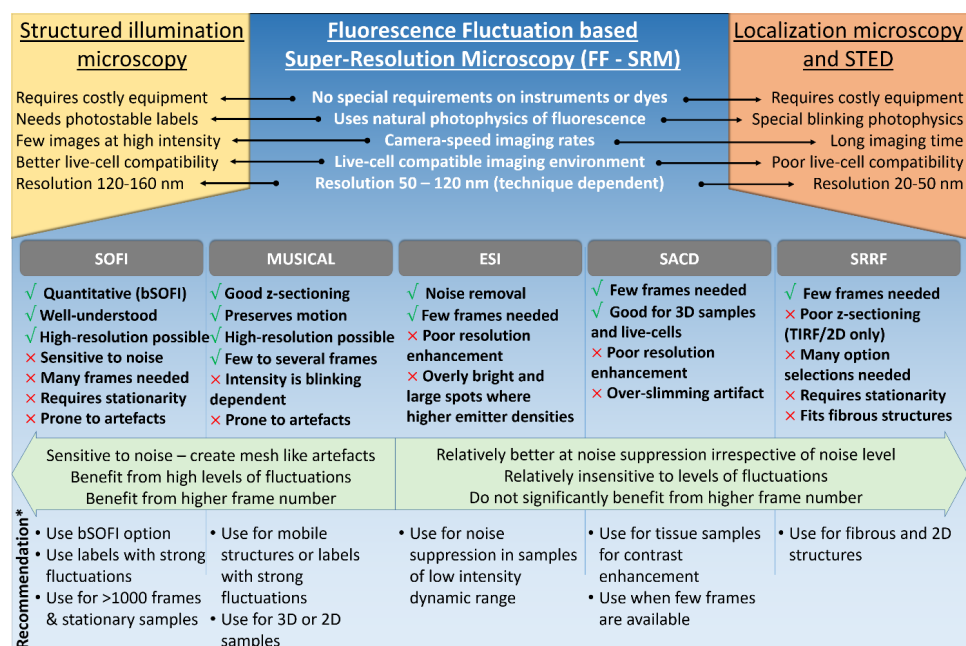


Figure 2.7: Summary of the FF-SRM comparative study and results. The figure was previously published in [78].

addition with a great variability in implementation/reconstruction options that hugely adds to the processing and analytical workload in method evaluation. UNLOC is parameter-free, but was left out for being mainly a technique for SMLM data.

Computational experiments on simulated data revealed the methods to belong to two different classes: sensitive to the level of intensity fluctuation level or not. While SOFI and MUSICAL required a high level of intensity fluctuations to perform well, ESI, SRRF and SACD displayed little difference for varying fluctuation level. MUSICAL and SOFI appeared to have the best super-resolution capability, but also the worst level of artifacts under sub-optimal conditions. SRRF and SACD were inclined to over-slimming artifacts: the collapse of wider (potentially complex) structures into slimmer lines. The main findings are summarized in Figure 2.7 and the complete published article is contained in Appendix F.

2.3 Chip-TIRF

2.3.1 A waveguide imaging platform for live-cell TIRF imaging of neurons over large fields of view

In this last results section, we consider a very different experimental setup, namely C-TIRFM. As the setup is no longer a commercial one, adapted for standard cell-culture dish geometry, also the challenges encountered were very different as compared to those described in the previous sections. The author list of this work is extensive and all with significant contributions. As before, my own was towards experimental design and execution, project leadership and writing of the manuscript.

This project was concerned with building and adapting a waveguide imaging platform for neuro-imaging applications. Neurons are delicate cell types that can span large areas and are very sensitive to changes in their environment. As commercial incubation systems are incompatible with C-TIRFM (and exceedingly costly), we found our own solution. In particular, we wanted the sensitive electronics of the piezo stage (used for laser coupling and mode-scanning) to be excluded from the humid environment inside the incubator, but at the same time keep the chip mount and objective inside and without obstructing the ability to navigate the sample.

Figure 2.8 (A) displays the imaging setup together with chip imaging (B) in open air (for species tolerating room environment like *Xenopus laevis*), or stage with heating and gas-controlled environment (C-D). In addition to the setup, we developed protocols for on-chip neuro-cultivation and showed neuro-imaging in a proof-of-concept microchannel-chip combi device. The full description of the components and on-chip cultivation protocols are available in the online supplementary of the published article (Appendix G) [84].

Although an asset, TIRFM becomes a limitation if it remains the only imaging mode possible, especially on a setup for live neuro-imaging, as the cells cannot readily be moved around on different imaging systems without risking detrimental effects on the cultures. To avoid being limited to solely substrate layer investigations, the C-TIRFM setup was also equipped with both brightfield and episcopic fluorescence options. Figure 2.9 shows imaging results from using the three imaging modes for the same neuronal culture.

The growth cones of retinal ganglion cells (cultures from excised eye primordia) were found a promising application of large-area TIRFM. These growth cones are of research interest in developmental biology. The tips of these axonal growth cones are important in guiding the neurons as they grow out of the eyes to connect to the brain. Figure 2.10 compares a *X. laevis* growth cone

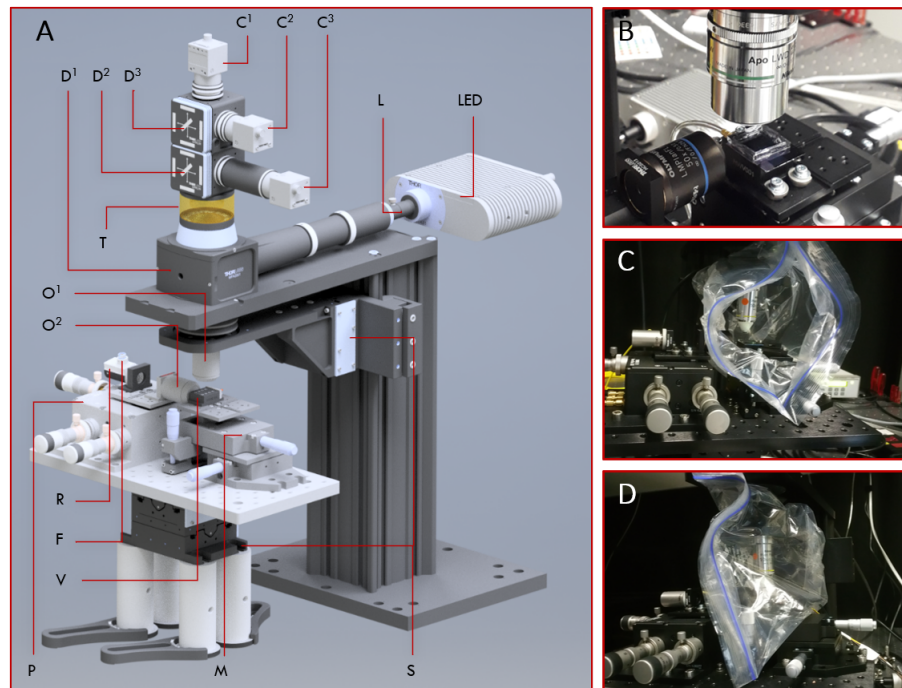


Figure 2.8: (A) ChipScope model. This upright microscope enables c-TIRFM, episcopic, and brightfield imaging with up to three colors simultaneously. (B) Microscope stage with waveguide chip and imaging chamber prepared for use with water dipping objective. The horizontal objective is for laser coupling into the waveguides. (C) ChipScope with an open incubation chamber for easy access to sample and objective. (D) Closed incubator supplied with high humidity and 5% CO_2 from a conventional stage top incubator. The figure has been adapted from work published in [84], where also detailed setup description is available.

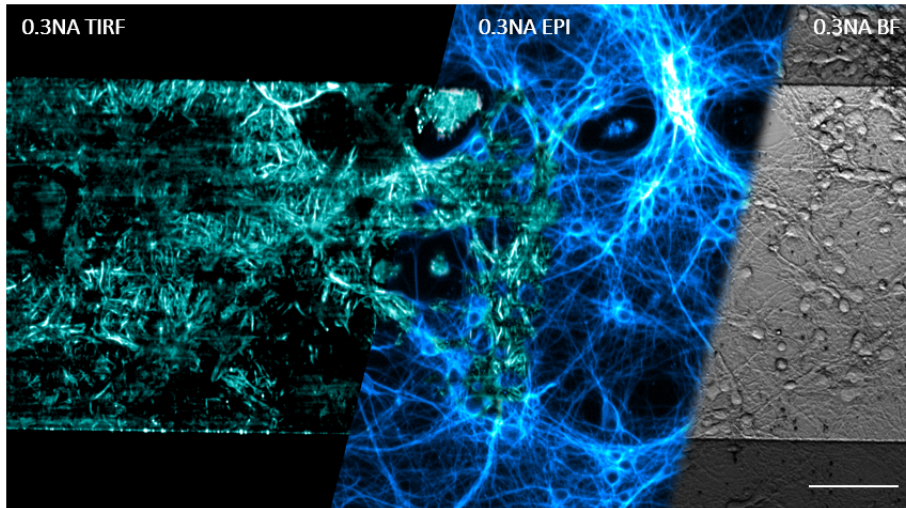


Figure 2.9: All panels show live-cell imaging of neurons labeled with SiR-Tubulin on adjacent regions of the same waveguide. Left: c-TIRFM image (obtained by mode-averaging). Middle: Single plane episcopic image overlaid with part of the corresponding TIRFM image. Right: brightfield image. Scale bar: 100 μm . The figure was previously published in [84].

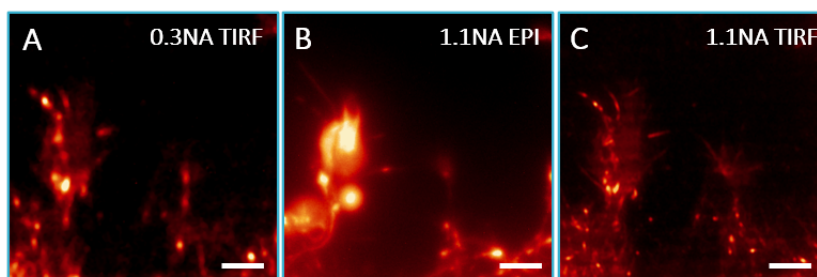


Figure 2.10: Actin in growth cones of *Xenopus laevis*. The tips of the cones exhibit greatly improved visibility using c-TIRFM imaging compared to episcopic illumination. The scale bars are 10 μm . The images were previously published in [84].

imaged using (A) episcopic and (B-C) c-TIRFM for both 0.3 NA and 1.1 NA. The tip of the axons exhibit a greatly improved visibility using TIRFM compared to episcopic illumination. The complete cell culture protocols, system details together with further discussion of on-chip neuro-imaging applications are available in the complete published article (Appendix G).

2.3.2 FF-SRM using waveguided multimode illumination

We saw in the previous section that c-TIRFM — with its compellingly large illumination areas — can be adapted for live-cell imaging applications of delicate samples like living neurons. Previously (first demonstrated by Diekmann and Helle et al. [70]), super-resolution on-chip was shown using the live-cell *in-compatible* method direct stochastic optical reconstruction microscopy (dSTORM), a particular type of SMLM. The large and fairly uniform illumination areas were for both dSTORM and conventional c-TIRFM (as presented in the previous section) accomplished via mode-scanning and averaging (as explained in section 1.4.2).

An interesting feature of the particular FF-SRM method MUSICAL (and different from e.g. SOFI), is that homogeneity of the illumination is nowhere assumed. This means that the intensity fluctuations can come from the fluorophores themselves or from fluctuations applied externally, e.g. by modulating the illumination. But, as we saw in section 2.2, the super-resolving abilities of MUSICAL relies heavily on the fluctuations being present in strong contrast.

In this work, we opted to exploit the intensity fluctuations resulting from waveguide mode-scanning for super-resolution imaging using MUSICAL. I recognized the experimental opportunity of obtaining a ground truth reference for the FF-SRM reconstructions by taking advantage of the detection objective being independent of the illumination path (i.e. the waveguides). In particular, the acquisition of 0.3 NA data for MUSICAL was accompanied with corresponding 1.0 NA data, featuring 3.33 times higher optical resolution (according to the Abbe diffraction limit). The results are summarised in Figure 2.11, where the 1.0 NA images serve as the ground truth reference for the 0.3 NA MUSICAL images. The images, together with the line profiles, indicate a clear resolution improvement in the MUSICAL images as compared to the conventional (mode-averaged) c-TIRFM images.

Compared to the MUSICAL results obtained initially (e.g. Figure 2.3), the improvements are astonishing. The images appear without severe artifacts, with reasonable intensity scaling, and in accordance with the ground truth reference.

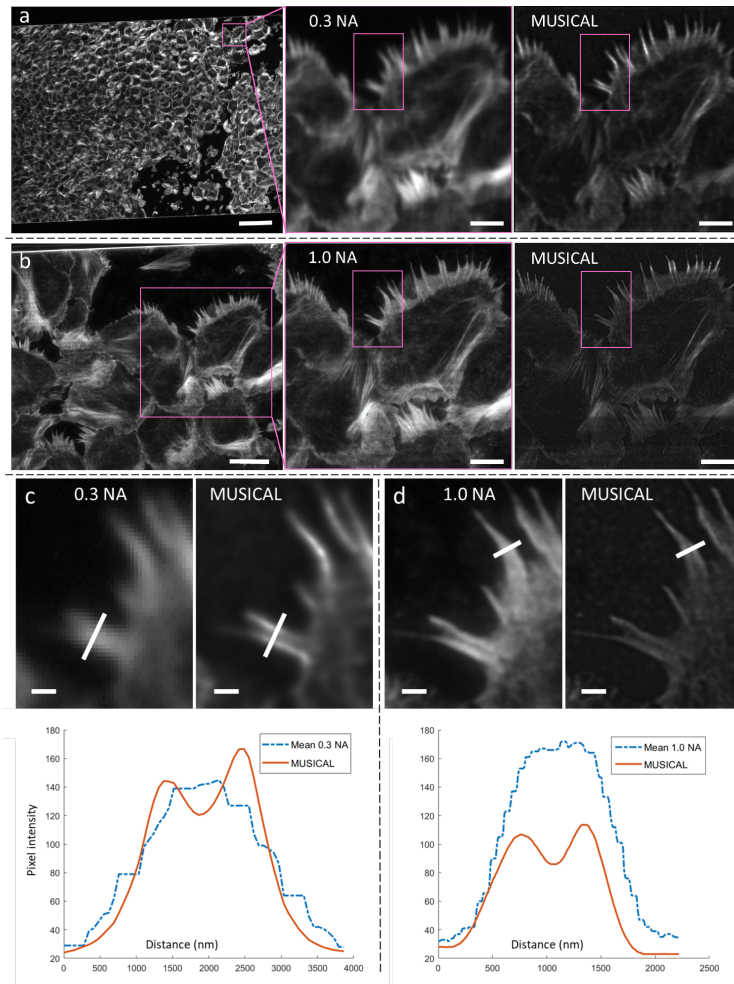


Figure 2.11: c-TIRFM of actin in salmon keratocytes. (a) *Left panel:* c-TIRFM of a 600 μm wide waveguide captured using a 0.3 NA objective (mode averaged intensities). Scale bar: 100 μm. *Mid panel:* magnified view, scale bar: 10 μm. *Right panel:* soft MUSICAL (MUSICAL-S) reconstruction using the same data. Scale bar: 10 μm. The indicated rectangles are displayed magnified in panel c. (b) Same as for left panel a, but using 1.0 NA. The magnified view (mid-panel) serves as a ground truth for the 0.3 NA MUSICAL-S image in panel a. The right panel shows the MUSICAL-S reconstruction for the mode-averaged data on the left. The indicated area is displayed magnified below in panel d. Scale bar left panel: 20 μm, mid and right panels: 10 μm. (c) 0.3 NA intensity line profiles for mode-averaged (left) and MUSICAL-S (right). (d) Same for 1.0 NA. The scale bars are 2 μm. The line profiles demonstrate a clear resolution improvement in the MUSICAL-S images as compared to the conventional (mode averaged) images.

Several aspects are here different compared to the MUSICAL results (strongly affected by artifacts) seen previously:

1. **The elimination of out-of-focus signal** by evanescent field illumination.
2. **Sharp intensity fluctuations** provided by waveguide mode-scanning.
3. **Verification** by the utilization of different objective NAs.
4. **A fixed sample** enables the verification process by changing collection objectives, improves the SNR, and eliminates motion-derived image artifacts.
5. **Automatic soft thresholding** is a newly developed version of MUSICAL and relieves subjectivity of the thresholding parameter choice and achieves a more balanced intensity scaling.

As noted in Acuña et al. [85], the MUSICAL threshold parameter is the least intuitive and most difficult user parameter when applying MUSICAL to bioimages. Also, often there will be no hard threshold correctly separating the eigenimages into signal or noise spaces due to the random and overlapping nature of both the signal and noise fluctuations. Therefore, Acuña et al. developed and tested different thresholding schemes, including soft thresholding methods, which use the different eigenimages in both the "signal" and "noise" sub-spaces, but scaled according to their singular values (which dictate the significance of the fluctuation signal contained in that particular eigenimages).

For the c-TIRFM data of Figure 2.11, the soft thresholding method MUSICAL-S from [85] was found the best. For a different type of data (like epi-fluorescence), the different methods would need to be tested experimentally to see which one might provide reliable results for that particular case. Overall, the automatic soft thresholding appears to be a huge step forwards for the applicability of MUSICAL in bioimaging and biomedical research.

Remaining aspects to be tested for waveguide multimodal illumination, together with the new MUSICAL thresholding schemes, include the challenging conditions of live-cell dynamics together with the detection of and elimination of reconstruction artifacts. A noteworthy recent contribution towards the latter challenge (employing deep learning) is provided by Jadhav et al. in [86].

The manuscript for the work presented in this section is upon thesis submission under preparation.

/ 3

Synthesis

This Ph.D. work has been an exploration of the emerging field of live-cell super-resolution microscopy, starting at the state of the art live-cell super-resolution microscopy using a commercial 3D SIM imaging system. Even with a ready microscope available, for SIM imaging to be successful it requires efforts to find suitable sample preparation protocols, and even more so for multi-channel imaging of living cells. Such work resulted in appended articles A and B.

In this initial work, in addition to finding suitable conditions for SIM imaging of living cells, also technical limitations were recognized and the necessity of further technological development and/or exploration of other techniques to truly follow subcellular nano-dynamics. 3D SIM was found too slow and photo-intense to be able to follow most of the rapid, and sensitive nano-environment of living mammalian cells.

I ventured into the field of FF-SRM, approaches to SRM based on analyzes of the intrinsic variations of fluorescence emission of fluorophores, intensity fluctuations that are present without introducing toxic buffers or intense laser illumination. Although in principle fantastic, and image data can be acquired rapidly on an ordinary wide-field microscope with relatively low photobleaching and phototoxicity, large analytical challenges still remain. Work related to the field of FF-SRM resulted in Article C, D, E, and F.

To analyze large bioimage data and enable conclusions to be drawn about cellular states and the changes in them, we developed and employed machine

learning in combination with the nanoscopy algorithm MUSICAL. This work resulted in a top-ranked journal publication in CVPR (Conference on computer vision and pattern recognition) 2020, here appended as Article E.

The new field of c-TIRFM with its great potential for high throughput, high-resolution substrate layer applications, was adapted and shown feasible for large FOV imaging of delicate samples like living primary neurons. This work resulted in article G.

Fluctuations induced by the scanning of multimode waveguide patterns were tested in combination with FF-SRM for MUSICAL with new and enhanced automatic and soft thresholding schemes. The results appeared promising and were verified by the correlated acquisition using objectives featuring different resolving powers. This manuscript is upon thesis submission under preparation.

Bringing FF-SRM onto photonic waveguide chips has the potential of alleviating and solving many of the challenges outlined in the introduction. However, the application of a chip imaging system also brings along additional challenges like the requirement of a specialized system, availability of photonic chips, and knowledge on basic chip-handling and on-chip sample preparation. Although silicon photonics can be inexpensively mass-produced, the surrounding scaffold of not so inexpensive lasers, camera(s), piezo stage and objectives, currently make the final prize tag significant. The combination of clever solutions making chip-imaging more convenient and user-friendly, together with overall reduced production costs of traditionally expensive components (like lasers and cameras) might eventually make chip microscopy an affordable and mainstream solution.

Out-of-focus signal, three-dimensional motion, morphing, and merging of initially separate subcellular entities, in combination with the effects of photobleaching and phototoxicity, is the microscopy data reality we are facing when trying to learn and understand even the simplest case of single cells in a glass-bottom dish. Although greatly simplified, developing analytical tools for the single-cell system is an important first step for later comprehending far more complex systems composed of heterogeneous, constantly interacting cells, like you and me. This is, in my opinion, one of the core components of biomedical research.

I have in this thesis discussed many of the challenges and limitations with current methods available for live-cell nanoscopy. Identifying these challenges and limitations, as well as opportunities, are the key contributions of my doctoral research to this forthcoming field in urgent need of fundamental knowledge on which future research can be built. There is yet no technique that can

master all the challenges posed by the desire of unraveling the nano-machinery of living samples. This includes imaging speed, light dose, and data analysis under challenging signal-to-noise conditions. For the developed setups to catch on as main-stream and usable tools in biomedical research, the nanoscopes must be user-friendly and engineered for the needs of particular samples and research questions. And this, of course, with an affordable price tag. In the end, there is a lot more work to be done in the sprouting field of live-cell nanoscopy. Likely, as the desire to learn more about the invisible, secret lives of cells is strong, a blooming future for live-cell nanoscopy is near.

/4

Future work

SIM is an already popular and mature technique for live-cell compatible SRM. Although recent developments have been made on lowering the necessary signal-to-background ratio for a reliable artifact-free super-resolved reconstruction [37][87][88], there is still much to be gained from volumetric reconstruction algorithms (especially adapted for a broad range of SIM imaging platforms) and volumetric image acquisition speeds.

For the young field of FF-SRM significant work remains to reduce the prevalence of reconstruction artifacts and achieve trustworthy reconstructions consistently for a broad range of samples. This might be achieved through a combination of analytical development of the techniques together with experimental tailoring for the particular techniques, e.g. by achieving a suitable signal fluctuation level via the choice of label fluorescent properties or engineered illumination. Understanding and reliably classifying the different sources of nano-scale signal fluctuations in living cells (with molecules moving in 3D, photobleaching, and noise signal) is undoubtedly a tough analytical task.

The spread and popularization of on-chip microscopy will depend on the successful development of an easy-to-use setup that can be conveniently fit into the workflow of target users (be it cell biologists or pathologists), preferably with a commercial solution and a reduced price tag.

Artificial intelligence and data simulation experiments are already impor-

tant analytical tools in the vast field of microscopy, and their importance appears unlikely to decline in either microscopy development or for the analysis of microscopy data (of any resolution claim) in the near future. It will be interesting to see how accurately trained machines can decipher different cellular organelles from unlabeled microscopy data (e.g. after being taught via labeled training data), as well as seeing where the practical limits of AI lie in deriving useful data about biological samples.

Appendices



Multi-color imaging of sub-mitochondrial structures in living cells using SIM

Ida S. Opstad, Deanna L. Wolfson, Cristina I. Øie and Balpreet S. Ahluwalia

Published in Nanophotonics March 2018.

Research article

Ida S. Opstad, Deanna L. Wolfson, Cristina I. Øie and Balpreet S. Ahluwalia*

Multi-color imaging of sub-mitochondrial structures in living cells using structured illumination microscopy

<https://doi.org/10.1515/nanoph-2017-0112>

Received November 14, 2017; revised February 27, 2018; accepted March 20, 2018

Abstract: The dimensions of mitochondria are close to the diffraction limit of conventional light microscopy techniques, making the complex internal structures of mitochondria unresolvable. In recent years, new fluorescence-based optical imaging techniques have emerged, which allow for optical imaging below the conventional limit, enabling super-resolution (SR). Possibly the most promising SR and diffraction-limited microscopy techniques for live-cell imaging are structured illumination microscopy (SIM) and deconvolution microscopy (DV), respectively. Both SIM and DV are widefield techniques and therefore provide fast-imaging speed as compared to scanning based microscopy techniques. We have exploited the capabilities of three-dimensional (3D) SIM and 3D DV to investigate different sub-mitochondrial structures in living cells: the outer membrane, the inter-membrane space, and the matrix. Using different mitochondrial probes, each of these sub-structures was first investigated individually and then in combination. We describe the challenges associated with simultaneous labeling and SR imaging and the optimized labeling protocol and imaging conditions to obtain simultaneous three-color SR imaging of multiple mitochondrial regions in living cells. To investigate both mitochondrial dynamics and structural details in the same cell, the combined usage of DV for long-term time-lapse imaging and 3D SIM for detailed, selected time point analysis was a useful strategy.

Keywords: super-resolution microscopy; structured illumination microscopy; mitochondria; bio-imaging; nanoscopy.

1 Introduction

Mitochondria are indispensable power plants of eukaryotic cells, performing diverse yet interconnected cellular functions. Mitochondrial dysfunction is associated with an increasingly large number of human inherited health disorders that can affect any organ and manifest at any age [1]. The importance of mitochondria and their involvement in many common diseases have made them the target of a vast number of imaging experiments [2–7]. However, despite decades of research, many aspects of their function remain elusive [8–11]. As their function is directly linked to membrane potential and dynamics [12, 13], visualizing these aspects can only be done using live-cell imaging techniques. However, the diameter of mitochondria is typically between 250 and 500 nm. This is quite close to the diffraction limit of conventional visible light microscopy techniques, which is about 200 nm and 500 nm in the lateral and axial directions, respectively. Imaging the complex internal structures of mitochondria using conventional light microscopy would thus be impossible. Their intricate membrane structure has traditionally only been visible through transmission electron microscopy, a method not suitable for live-cell imaging. In recent years, an array of fluorescence-based optical imaging methodologies has emerged, collectively termed super-resolution (SR) optical microscopy or optical nanoscopy [14, 15], which allows imaging beyond the conventional diffraction limit of optical microscopy. However, each technique possesses its own limitations, reducing its capability to rapidly image three-dimensional (3D) samples and similarly limiting its applicability to live-cell imaging [15, 16]. Such limitations include an inability to follow

*Corresponding author: Balpreet S. Ahluwalia, Department of Physics and Technology, UiT-The Arctic University of Norway, Tromsø 9037, Norway, e-mail: balpreet.singh.ahluwalia@uit.no
Ida S. Opstad, Deanna L. Wolfson and Cristina I. Øie: Department of Physics and Technology, UiT-The Arctic University of Norway, Tromsø 9037, Norway

dynamic processes at the speed dictated by nature, sample motion that can introduce artifacts in the final image reconstruction, or photodamage to delicate structures due to necessarily intense light exposure.

One of the most promising techniques for live-cell SR imaging is structured illumination microscopy (SIM). SIM [17, 18] is a widefield technique that achieves lateral and axial resolution of up to 100 nm and 250 nm, respectively, thus allowing for imaging over a large field of view at relatively high imaging speeds and at low illumination intensities compared to other SR techniques [14, 19, 20]. In addition, SIM is compatible with commonly used fluorescent probes, whereas other SR techniques like single molecule localization methods rely on suitable photoswitchable fluorophores [21], although newer fluctuation-based methods seem promising towards advancing the field in the directions of both live-cell imaging and the use of conventional fluorophores [22, 23]. The resolution doubling provided by SIM, compared to the diffraction limit, is suitable for a coarse determination of sub-mitochondrial structures. Combined with the relatively high imaging speed possible with SIM (0.5–1 Hz), super-resolved time-lapse visualization of live mitochondrial dynamics and even the interplay between different compartments are now possible.

Here, we used 3D SIM and deconvolution microscopy (DV) to simultaneously image three sub-mitochondrial compartments in the same living cell by using spectrally separated probes: mEmerald-TOMM20 (Gtom) for the mitochondrial outer membrane [24, 25], MitoTracker Deep Red (MT) for the mitochondrial intermembrane space, and CellLight Mitochondria-RFP BacMam 2.0 (BM) for the mitochondrial matrix [26, 27]. Each probe has a distinct localization relevant to mitochondrial structure and function. TOMM20 is a subunit of the translocase of the outer mitochondrial membrane complex, which mediates the import of the vast majority of proteins into mitochondria from the cytosol [24, 25]. Inhibition of TOMM20 import has recently been found to play an important role in the pathogenesis of Parkinson's disease [28]. MitoTracker probes accumulate electrophoretically into mitochondria because of their transmembrane potential [29]. Although the permeability of mitochondrial membranes can undergo drastic and rapid changes, MT will normally permeate the mitochondrial outer membrane and accumulate in the intermembrane space near the mitochondrial inner membrane due to its typically low permeability to ions [30]. Finally, BM labels a mitochondrial matrix enzyme (E1 alpha pyruvate dehydrogenase) [26] essential in converting chemical energy from imported nutrients into a usable form for the cell [31]. Deficiency of this enzyme correlates with a

buildup of lactic acid and is linked to severe neurological problems [32].

To the best of our knowledge, this is the first report on simultaneously imaging three distinct sub-mitochondrial structures in living cells using optical nanoscopy. Another contribution of this work is to investigate the challenges and opportunities associated with SR imaging and labeling multiple regions inside the same organelle, with an emphasis on mitochondria. Targeting three regions of mitochondria individually was relatively straightforward. However, labeling three sub-mitochondrial regions simultaneously for SR imaging with SIM was found challenging and required re-optimization of the labeling protocols.

2 Results and discussion

2.1 Live imaging of singly labeled mitochondria

To visualize mitochondrial structures, labeling protocols for each probe targeting a sub-mitochondrial structure were optimized on MCC13 cells (Merkel cell carcinoma). For this, we considered factors including label-induced toxicity during both labeling and imaging, the intensity of non-specific background signal, and the photostability of the probe. The optimized protocols are detailed in the methodology section and summarized in Table 1. Briefly, the essential parameters for effective labeling and imaging were as follows: for MT, a working concentration of 75–100 nM and 30-min incubation time and for Gtom and BM, extended post-transfection cell recovery and

Table 1: Overview of necessary re-optimizations for multicolor labeling experiments.

Probe	Optimized labeling
✓ Gtom	1 µg pDNA + 1 µl L3000, 2-day incubation
✓ BM	20 PPT, ~20-h incubation
✓ MT	75–100 nM, 30-min incubation, wash well
Probes combined	Re-optimization
✓ Gtom + BM	Increased time between each transfection (at least 2 days) and higher reagent density of BM (from 20 PPC to 40 PPC)
✓ BM + MT	Increased labeling concentration of MT (400–500 nM)
✓ Gtom + MT	No re-optimization required (individual protocols applicable)
✓ Gtom + BM + MT	Above combined

selection of cells with ideal expression levels for imaging. The sub-mitochondrial localization of each of the three probes evaluated by 3D SIM appeared to be largely in accordance with their expected target regions (Figure 1). For the BM mitochondrial matrix probe, however, larger or thicker aggregates of red fluorescent protein (RFP) were often seen along the mitochondrial network in contrast to their expected appearance as thin, continuous strands (Figure 1A and D). MT, accumulating on the mitochondrial inner membrane, highlighted a folded structure with dark regions or internal gaps, corresponding to the structure of cristae (Figure 1B and E). Gtom, corresponding to the mitochondrial outer membrane, manifested as a wider structure with internal gaps larger than those seen in the other two probes (Figure 1C and F). Supplementary Figure S1 shows a comparison between images obtained using the DV and 3D SIM techniques, where the DV image is mostly unable to reveal the outer membrane localization of the Gtom probe, as clearly shown by the 3D SIM image.

2.2 Time-lapse imaging of mitochondria

Static images cannot provide a complete view of the complex functioning of cellular systems, and an increased interest in mitochondrial dynamics in recent years has resulted in several significant new revelations. Capturing the dynamics of a living system provides a more complete view of its function, with mitochondria being of particular interest recently [33–39]. With this increased interest, however, comes the necessity to better understand how both the labeling and imaging processes themselves may alter the biological system under study and to choose the least invasive technique suited to each study. We attempted 3D SIM time-lapse (TL) imaging of mitochondria labeled as described above, but fast photobleaching hindered capturing dynamics for more than a few frames (typically 1–10).

Interestingly, similar 3D SIM TL experiments on HeLa cells labeled with MTG previously published by Shao et al. [40] did not show the same phototoxicity. They imaged

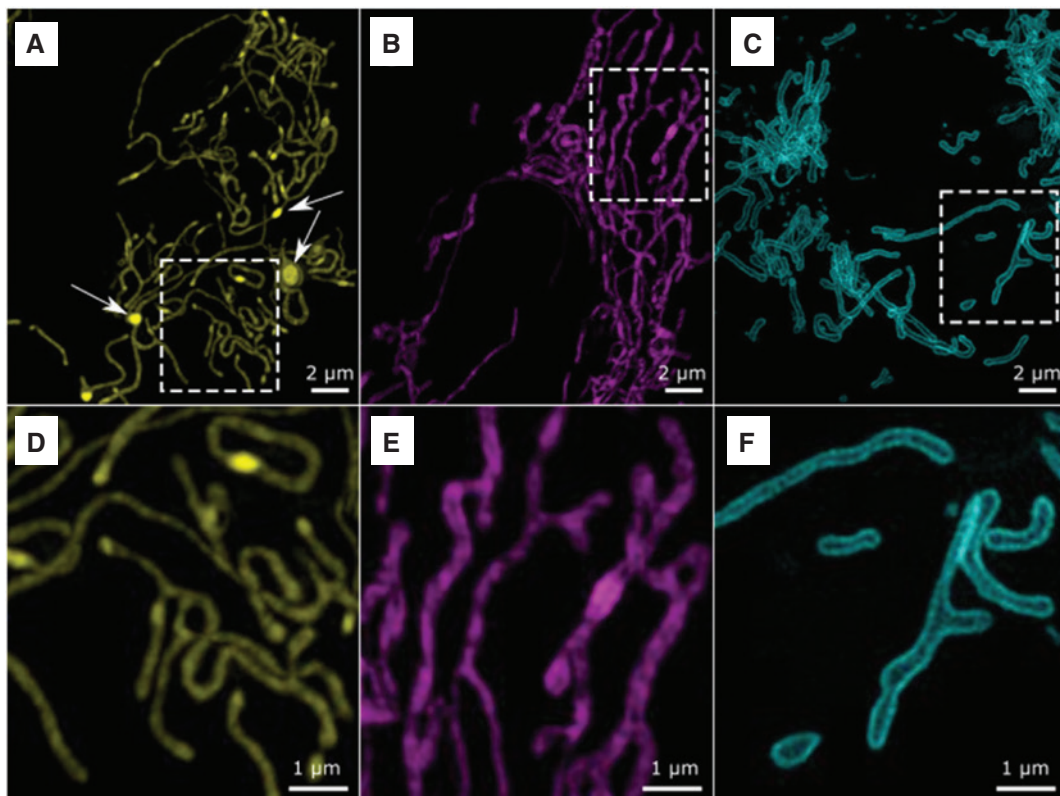


Figure 1: Live imaging of MCC13 cells individually labeled with three mitochondrial probes.

(A) CellLight Mitochondria-RFP BacMam 2.0 (BM) localizes in the mitochondrial matrix. Larger aggregates (indicated by arrows in A) are thought to be labeling artifacts. (B) MitoTracker Deep Red (MT) accumulates in the intermembrane space, and gaps correspond to the presence of cristae. (C) mEmerald-TOMM20 (Gtom) appears along the outer mitochondrial membrane. Panels (D–F) provide a closer look at the boxed regions in A–C. Images are maximum intensity projections of 3D SIM images.

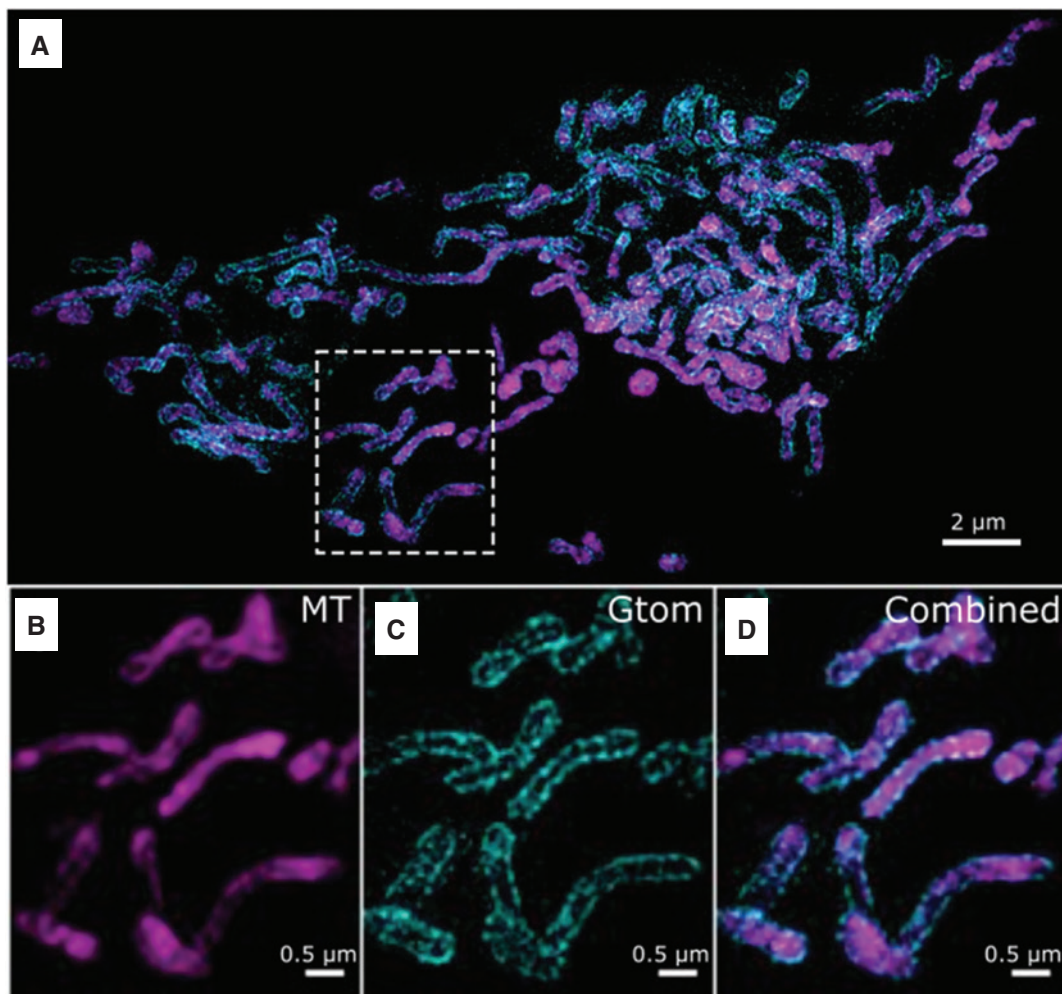


Figure 2: Live imaging of an MCC13 cell dually labeled with Gtom and MT. The region indicated in (A) is shown magnified below with separate (B, MT; and C, Gtom) and merged color channels (D). Images are maximum intensity projections of a 3- μm 3D SIM z-stack. A single z-slice image with orthogonal views are found in Supplemental Figure S2.

50 time-points seemingly without major morphological artifacts or detrimental photobleaching. Compared to our methods, they imaged approximately double the thickness (6.1 μm) and used half the labeling concentration of MTG (50 nM). The difference may be due to the different cell types used, as HeLa cells are known to be remarkably durable, due to lower label concentration or likely lower illumination intensities, as their exposure time (35 ms) is longer compared to our study (3–8 ms for 100-nM labeling concentration, depending on the brightness of the cell imaged). In our case, however, relatively longer exposure times and lower illumination intensities were not suitable because of the high motility of mitochondria in the chosen cell line (MCC13) and relative intensity of the MitoTracker.

DV, on the other hand, enabled long-term time-lapse imaging (60 time points over 30 min) of all probes. For extended discussion of TL imaging and details on the

SIM and DV imaging techniques, see Supplementary note 1: time-lapse imaging, and supplementary movie S1–S2.

As both 3D SIM and DV imaging modalities are available on our microscope, we were able to retain the ability to resolve sub-mitochondrial structures at selected time points by supplementing the DV TL images with 3D SIM images of the same cells. Supplementary Movies S3 and S4 (online material) show 3D renderings of data collected in this way, i.e. a single SIM image and a DV TL series of a Gtom-labeled MCC13 cell, respectively. The 3D SIM image (Supplementary Movie S3) was acquired as the first time point, with the DV TL sequence (Supplementary Movie S4) subsequently acquired after changing the imaging mode on the microscope. This multimodal approach enabled us to balance the need for speed and low light exposure with the desire for SR structural details.

2.3 Live imaging of dually labeled mitochondria

To confirm the sub-mitochondrial localization of the individual probes and their relative colocalization, we labeled the same cells with different live-cell mitochondrial probes. Combining mitochondrial labels in the same sample resulted in reduced labeling efficiency for both BM when following Gtom transfection and for MT following BM transduction (see Supplementary Figure S3). However, no such challenges were encountered for MT labeling following Gtom transfection. The reduced labeling efficiency of dually labeled mitochondria (Gtom + BM and BM + MT) limits the applicability for SIM imaging, as SIM requires a high number of frames with sufficient signal-to-background ratios in order to reconstruct a 3D SIM image. Low fluorophore density, as observed with some of the dually labeled samples, frequently results in rapid photobleaching, reduced image quality, and/or image reconstruction failure while imaging using 3D SIM. Re-optimization of the labeling protocol was therefore necessary for 3D SIM imaging of dually labeled mitochondria, the results of which are summarized in Table 1 and discussed below for different label combinations.

2.3.1 Imaging the mitochondrial outer membrane and intermembrane space (Gtom and MT)

MCC13 cells were first transfected with Gtom and thereafter labeled with MT. As MT resulted in reduced cell health after just a few hours of labeling, transfections, which require long incubation times (e.g. Gtom, see Methods), must be performed first. Figure 2 shows live 3D SIM images of mitochondria dually labeled with Gtom and MT probes. Figure 2B shows MT labeling of the intermembrane space, while Figure 2C shows Gtom labeling of the outer mitochondrial membrane. The resolution provided by 3D SIM is sufficient here to clearly distinguish between the two sub-mitochondrial structures. Supplementary Figure S2 shows a single z-slice image and orthogonal views of this same cell. No additional labeling protocol optimization was necessary beyond that which was used for the probes individually.

2.3.2 Imaging the mitochondrial outer membrane and matrix (Gtom and BM)

Both Gtom and BM labelings rely on the expression of genetically encoded fluorescent fusion constructs – a relatively

slow process. However, the transient nature of BM labeling combined with the necessary cell recovery and expression times thus required Gtom transfection to be performed before BM transduction.

Gtom transfection must be performed at least 48 h before imaging, while for the BM label, a shorter post-transfection incubation time is needed (16–20 h). This makes it tempting to add the BM reagent to the cells about 30 h post-Gtom transfection and thereby (in theory) enabling dual-imaging of both Gtom and BM after 2 days. Based on our experience, however, we do not recommend this approach, as it resulted in a very high cell death rate. Extending the time between the transduction to 2 days resulted in bright dual-labeling of few cells (about 5%), but for the highest possible dual-color labeling efficiency, it was preferable to first induce and maintain a stably transfected cell-line expressing the Gtom label by using antibiotic selection. Without this selection, the Gtom label was gradually lost within a few days post-transfection, thus making dual-labeling extremely unlikely. Under these conditions, many of the dually transfected cells displayed sufficient expression levels of both Gtom and BM for 3D SIM imaging. In Figure 3, 3D SIM images of a Gtom- and BM-labeled cell clearly show the Gtom signal enclosing the BM signal, as expected from their respective localizations on the mitochondrial outer membrane and matrix. Although Gtom labeling negatively impacted BM expression levels, it also appeared to reduce the incidence of morphological artifacts that were observed in cells labeled only with BM, i.e. large aggregates of RFP (shown and further discussed in Supplementary Figure S4).

2.3.3 Imaging the mitochondrial matrix and intermembrane space (BM and MT)

As BM tags an essential mitochondrial metabolic enzyme with a large fluorescent protein, the functioning of the enzyme itself, and thus the mitochondria, may be impacted. Indeed, we observed a reduced labeling efficiency for MT in cells expressing higher levels of BM, such that dual-color imaging was, for most cells, not possible using the same labeling concentration as optimized for MT alone (100 nM) (see Supplementary note 1: time-lapse imaging). However, within the same cultures, we found that some cells with lower expression levels of BM did retain sufficient (though reduced) levels of MT for dual-color SIM imaging, as shown in Figure 4. As higher signal-to-background ratios are needed for successful SIM reconstructions, the cells with higher BM expression

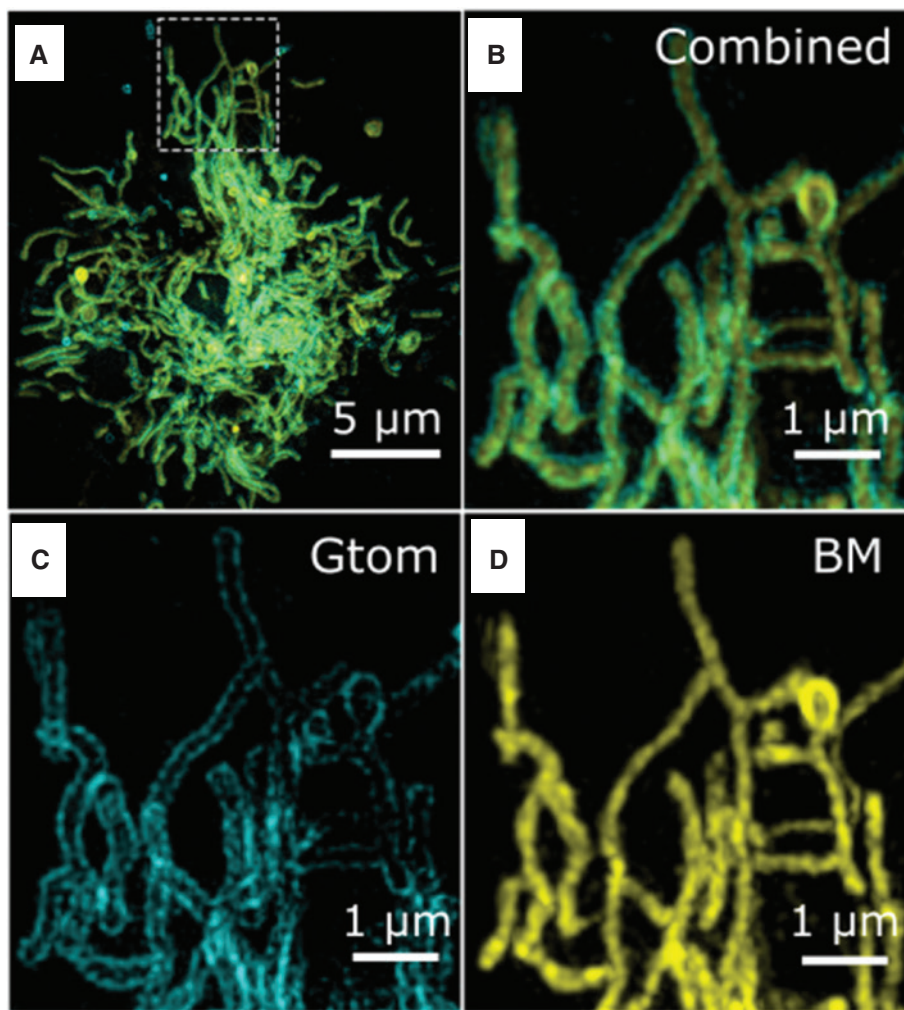


Figure 3: Live imaging of an MCC13 cell dually labeled with Gtom and BM.

The boxed region in (A) is shown magnified for the combined (B) and individual probes (C and D). Gtom (C) localizes at the mitochondrial outer membrane, and the BM label (D) localizes in the mitochondrial matrix. Gtom surrounding BM is shown in the merged image (B). Images are maximum intensity projections of a 1.25- μm 3D SIM z-stack.

levels (and thus higher signal) are better suited for imaging. To compensate for the reduced efficiency of MT labeling on cells showing higher BM expression, MT concentration was increased from 100 nM (the optimized concentration without BM) to 400–500 nM. Increasing the MT labeling concentration above 500 nM induced wider and irregular mitochondrial morphology, together with loss of label specificity, and hence, also poor image quality.

Although moderate increase in labeling concentration provided sufficient signal for dual-color 3D SIM imaging in a greater proportion of the BM-transduced cells, the cells with highest expression levels of BM still did not retain sufficient MT for SIM imaging. Supplementary Figure S5 online shows a SIM image of mitochondria brightly labeled with both BM and MT,

but many, with irregular or ring-shaped morphology. Furthermore, there appear to be very few differences between the BM and MT labels, as mitochondria appear as thin, fairly continuous strings with highly co-localized signals from both labels. It is not clear from these results if the labels are then localized in the mitochondrial intermembrane space or the mitochondrial matrix. This may be due either to the limitation of the resolution that is obtained by 3D SIM compared to the actual dimensions of the mitochondrial compartments or to a possible change in the fluorescent label localization, e.g. the MT label possibly localizing instead in the mitochondrial matrix. The duplication of information from this joint BM-MT approach therefore indicates that its use is limited outside extreme cases of sub-mitochondrial morphological disruption.

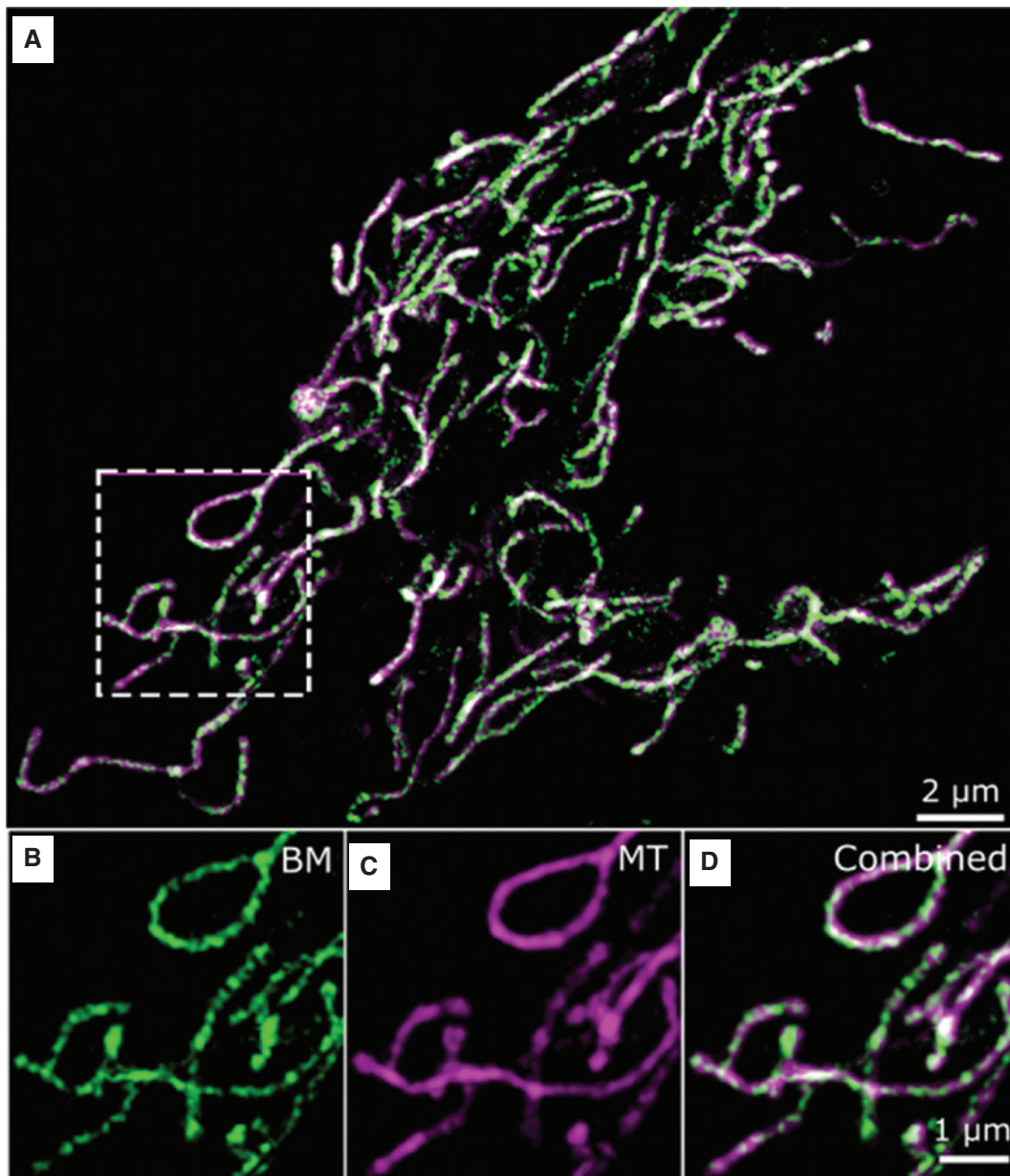


Figure 4: Live imaging of an MCC13 cell dually labeled with BM and MT.

The boxed region in (A) is shown magnified for the individual (B and C) and combined probes (D). For cells with low levels of BM expression, the same concentration of MT could be used as was optimized in MT-alone experiments (100 nM), but the low BM signal compromises image quality (B). Sub-mitochondrial localization cannot be determined in these samples, as the structure of cristae (which had been observable using MT alone) are no longer discernable in the MT channel (C). Images are maximum intensity projections of a 1- μm 3D SIM z-stack.

2.4 Live imaging of triply labeled mitochondria

Using 3D SIM, we imaged mitochondria in living MCC13 cells simultaneously labeled with three spectrally separated probes targeting different mitochondrial structures (outer membrane, intermembrane space, and matrix). Simultaneous labeling with the three probes required

overcoming the challenges of combining both Gtom with BM and BM with MT, as discussed in detail in the previous section and summarized in Table 1 and Figure 7. Briefly, this included extending the post-transfection recovery time and increasing the concentration of MT. Additional challenges and optimizations necessary concerning the technical side of multicolor live-cell 3D SIM imaging are discussed below under Imaging conditions.

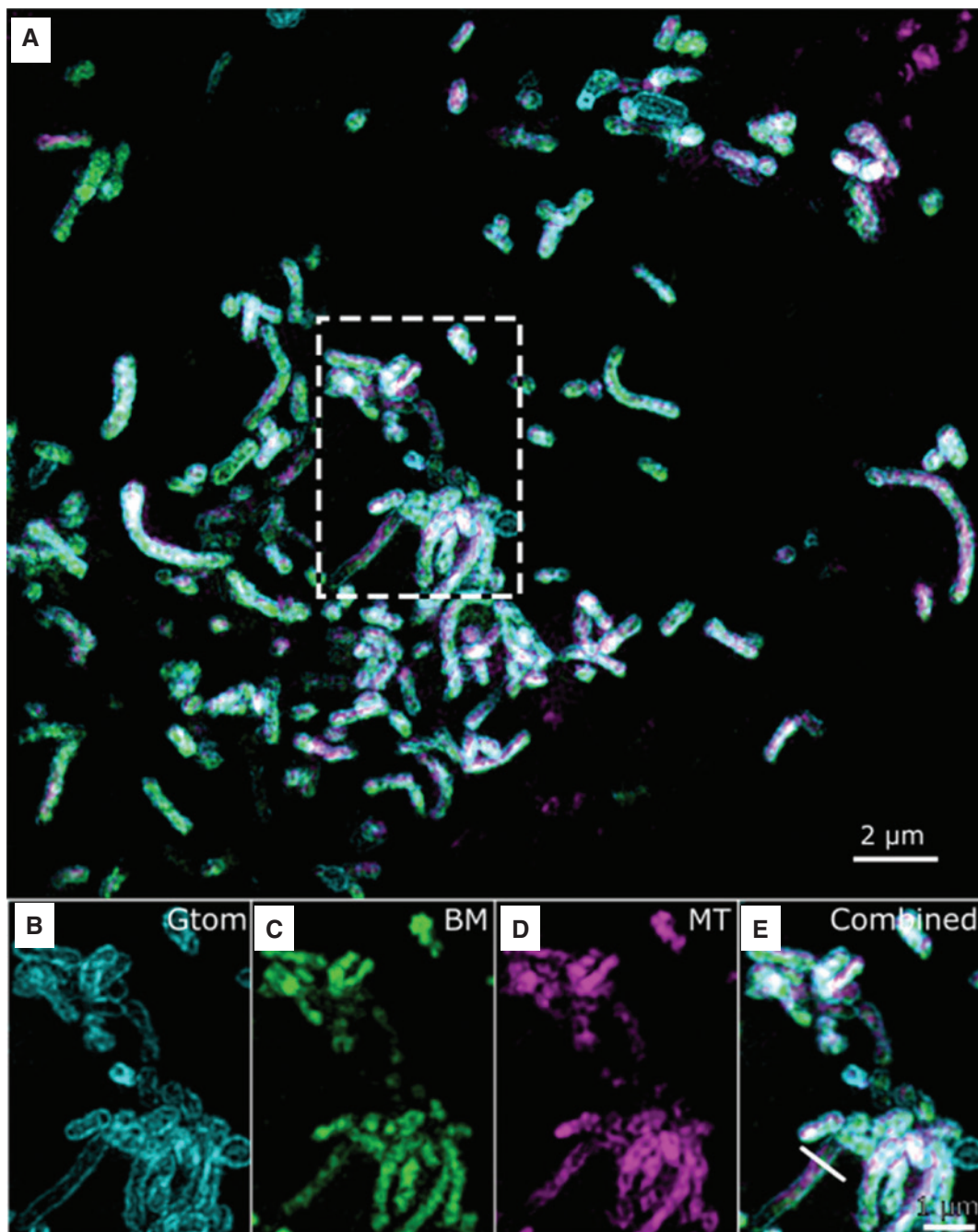


Figure 5: Live imaging of MCC13 cells triple labeled with Gtom, BM, and MT.

The indicated region in (A) is shown magnified below with separate (B) Gtom, (C) BM, (D) MT, and (E) merged color channels. Images are maximum intensity projections of a 1- μm 3D SIM z-stack. The line profile indicated in (E) is plotted in Figure 6, and Fourier plots with resolution estimates of these 3D SIM images are found in Supplemental Figure S8.

Figure 5 shows imaging of the three labeled sub-mitochondrial structures in a single living cell. The localization of the mitochondrial labels was in accordance with both the literature and our results from single-color labeling. BM labeling (mitochondrial matrix) had the slimmest appearance (Figure 5C), while MT (mitochondrial intermembrane space) had a slightly wider appearance

and showed discernable gaps or dark regions that corresponded to the inner membrane enveloping the mitochondrial matrix (Figure 5D). Gtom expression (outer mitochondrial membrane) resulted in wider structures (Figure 5B), which clearly enveloped the other two labels (Figure 5E). This enveloping relationship is further demonstrated in a line profile (Figure 6) of the mitochondrion

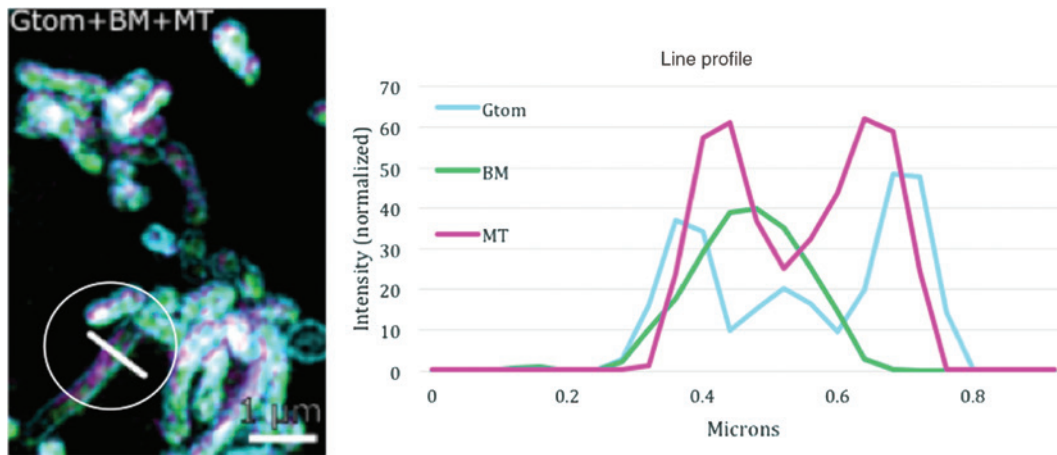


Figure 6: Cross-section of a triply labeled mitochondrion as indicated in Figure 5E and on the left panel. The plotted intensities have been normalized to the maximum intensity of each individual color channel. Here, BM shows a single peak contained amid the double peaks formed by both MT and Gtom. The width (FWHM) of the blue peaks is around 120 nm, reflecting the expected lateral resolution of the green channel (ex. 488 nm).

indicated in Figure 5E. A single z-slice image of a cell subjected to the same labeling conditions is found in Supplementary Figure S6. Fourier plots estimating the optical resolution are discussed in the Supplementary note and shown in Supplementary Figure S8.

Notably, we found that cells containing sufficient levels of all three probes were less prone to the BM over-expression artifact found in cells labeled only by BM (Supplementary Figure S3). An explanation for this might be that labeling the import protein TOMM20 (in the TOM complex on the outer mitochondrial membrane) may, to some extent, inhibit the import of the BM-fusion protein into the mitochondria. As the cells would thus express a lower and therefore more moderate level of BM, they may be less prone to reduction in mitochondrial transmembrane potential observed in cells with high expression levels of BM. In addition, the successful retention of the MT probe by these cells indicates that the cells were healthier and more viable, with more functional mitochondria.

2.5 Imaging conditions

In addition to optimization of the labeling protocol for live, multicolor 3D SIM of mitochondria, it is also necessary to carefully choose optimal imaging parameters in order to successfully obtain a super-resolved image. The additional light exposure of multicolor imaging increases photobleaching, and when combined with the reduced labeling density (compared to singly labeled samples), it results in an overall decrease in signal intensity. To reduce photodamage [41, 42], lower laser intensities are

often used and exposure times increased if higher signal is needed for reliable image reconstruction, although this may also increase motion blur.

Moreover, the SIM reconstruction algorithm for our system assumes a specific point spread function (PSF) for the instrument, yet this PSF is a variable dependent on imaging conditions such as wavelength, temperature, mounting medium, distance from the coverslip, and coverslip thickness. If the PSF used in the reconstruction algorithm does not match the PSF for the particular experimental conditions, image reconstruction may fail or lead to significant artifacts. As it is not practical to measure new system PSFs for each sample, a set of pre-measured PSFs is used, with one PSF optimized for each wavelength under standard conditions. One way to compensate for other experimental differences is to change the index of refraction (RI) of the immersion oil used on the objective. Choosing the correct immersion oil for assessment of dual or triple staining of mitochondria in live cells was almost as essential as choosing the correct excitation wavelength. For SIM imaging on fixed cells, it is possible to use mounting medium with a higher RI (i.e. RI close to that of the glass coverslips), which reduces the spherical aberrations, thus enabling larger z-stacks and a wider spectrum of colors to be imaged before artifacts from mismatched oil arise. However, for live-cell imaging, the cells are kept in a low RI buffer solution like RPMI or live-cell imaging buffer (RI ~ 1.33), which leads to additional spherical aberrations and loss of fluorescent signal at the sample-coverslip interface. Therefore, matching the RI of the immersion oil for live-cell imaging is even more critical than for fixed-cell imaging.

Because of these PSF variabilities, SIM imaging using more than one wavelength means using sub-optimal oil for at least one color. For example, in the three-color image in Figure 6, immersion oil with RI 1.516 was used, while the optimal oil RI for only Gtom (ex. $\lambda=488$ nm) in the same sample would be approximately 1.512, and 1.518 for MT only (ex. $\lambda=642$ nm). Although the different colors have different optimal oil RIs, well-prepared samples can often be successfully imaged using immersion oil with RI between the optimal for the longest and the shortest wavelengths. In this case, we found that using oil with RI 1.516 was most suitable to achieve the best image reconstructions for all three colors during live-cell imaging. In Supplementary Figure S6, the speckled honeycomb pattern in the green channel (Gtom shown in turquoise) is an imaging artifact likely caused by this compromise in oil RI but may also be caused in part by photobleaching.

3 Conclusions

Three distinct and spectrally separated probes were used to simultaneously label sub-mitochondrial compartments in living cells, then imaged using both DV and 3D SIM. DV enabled long-term time-lapse imaging of mitochondria (60 time points over 30 min), while 3D SIM provided details about the sub-mitochondrial morphologies at single time points.

We evaluated several mitochondrial probes and labeling protocols and observed their direct effects, both individually and combined, on mitochondrial morphology and function. While BM labeling (targeting the matrix) alone resulted in some morphological artifacts, cells first transfected with Gtom (targeting the outer membrane) and then transduced with BM showed lower incidence of these artifacts. Although lower concentrations of MT (targeting the intermembrane space) did not show morphological artifacts during single time point imaging, phototoxicity induced by extended imaging time resulted in a swollen appearance of the mitochondria. However, MT was the only probe with sufficient photostability for time-lapse 3D SIM imaging beyond five time points for our cells and labeling conditions, irrespective of the time interval between each point.

For dual-labeling experiments, the best results were obtained with Gtom and MT, such that no modification of the individual labeling protocols was required when the probes were used in combination, and no changes in morphology were noted as compared to cells labeled with the probes individually. For the other two combinations,

optimization of the labeling protocol was necessary, and morphological artifacts were observed. However, additional BM labeling of Gtom-transfected cells reduced the incidence of morphological artifacts compared to cells labeled only with BM.

In addition to reducing the suitability for 3D SIM imaging, the reduced labeling efficiency of the combined probes also serves as a reminder that altering cells with fluorescent probes necessarily changes the biological system under study. The effects of these changes, especially when combined with powerful investigative tools (e.g. imaging with high spatio-temporal resolution), may potentially lead to false interpretations and conclusions. For example, morphological artifacts from over-expression of a host protein may change from unnoticeable to especially noteworthy at SR. In addition, phototoxic effects present challenges to evaluating the dynamics of a system, as the simple act of observing a target can damage it or otherwise influence its behavior; these effects are compounded in SR microscopy, where the total light dose on the sample is significantly increased.

It is therefore important to evaluate and choose the best combination of techniques for each specific scientific inquiry. Although, on one hand, 3D SIM clearly provides higher resolution, it comes with a requirement for increased labeling, higher risks of phototoxic effects, lower imaging speed, and lower potential for time-lapse imaging. DV imaging, on the other hand, is a good choice for lower phototoxicity and higher speed compared to both SIM and confocal imaging, but it lacks the resolution of the former and is not as good for imaging thick samples as the latter. For imaging mitochondria in our study, the combination of DV for time-lapse and 3D SIM for detailed, single time-point analysis proved to be most useful. Similarly, the choice of probes is highly dependent on the goals and conditions of each experiment. MT labeling is fast, relatively bright, and photostable but prone to morphological artifacts depending on both labeling and imaging conditions. Gtom provides an excellent, distinct structure for imaging, but the requirements for transfection make it incompatible with some primary cells, and varying expression levels can make it difficult to find and image cells using 3D SIM. BM labeling is somewhat slower and more prone to artifacts, although it may still be a good choice for cells that do not tolerate MT labeling or imaging. As our study focused on MCC13 cells, the choice of labeling and imaging conditions may vary for different sample types and conditions and for the process or subject under evaluation. Our study also emphasizes the importance of and need for development of sub-cellular probes compatible with both SR microscopy and live-cell imaging.

Resolving and visualizing three different compartments of mitochondria at the same time in a living cell is an important step towards understanding the nanomachinery of the basic units of life. This work highlights the capability of current techniques to evaluate differences in nanoscale structures within a living system and the challenges involved in modifying and studying biological systems with high resolution. With current research trends emphasizing the dynamics of individual proteins or gene expression levels, the sub-organelle level of detail elucidated here will become increasingly relevant and, therefore, so will an understanding of the associated challenges and limitations of these advanced techniques.

4 Methods

4.1 Cell lines

The Merkel cell carcinoma (MCC13) cells were maintained in an incubator at 37°C with 20% O₂ and 5% CO₂, with a growth medium consisting of RPMI 1640 (Sigma-Aldrich Norway AS, Oslo, Norway) supplemented with 10% fetal bovine serum (FBS) (Sigma-Aldrich Norway AS, Oslo, Norway) and 1% penicillin/streptomycin (Sigma-Aldrich Norway AS, Oslo, Norway). Cultures used for experiments were thawed from stocks stored in liquid nitrogen a minimum of 1 week prior to transfection.

4.2 Transfection of cells using lipofectamine

Bacterial stabs for growing Gtom plasmids were obtained from Addgene (Cambridge, MA, USA) (plasmid # 54282) [43]. Selected bacterial colonies were inoculated overnight in liquid Luria-Bertani (LB) broth (Difco, Thermo Fisher Scientific, Waltham, MA, USA). Plasmid DNA (pDNA) was purified using the GeneJET Plasmid Miniprep Kit (Thermo Fisher, Waltham, MA, USA). Prior to transfection, the cells were seeded on glass-bottom culture dishes (MatTek Corporation, Ashland, MA, USA) and cultured in antibiotic-free medium until they reached 80% confluency. Transfection was performed using 1 µg purified pDNA and 1 µl Lipofectamine 3000 (Invitrogen, Thermo Fisher Scientific, Waltham, MA, USA) in Opti-MEM media for 5 h at 37°C before changing to normal growth medium without antibiotics and incubated for 2 days. The cells were then imaged or incubated further in medium containing 0.2 mg/ml Geneticin Selective Antibiotics (Thermo Fisher Scientific, Waltham, MA, USA) for selection of Gtom-expressing cells.

4.3 Labeling with CellLight Mitochondria-RFP BacMam 2.0 (BM)

Labeling with BM (Thermo Fisher Scientific, Waltham, MA, USA) was done according to manufacturer's protocol with 15–45 particles per cell (PPC) approximately 20 h prior to imaging. Transfected cells were grown under the same cell culture conditions as described above but in antibiotic-free medium.

4.4 Labeling with MitoTracker

MitoTracker labeling was optimized for MitoTracker Green (MTG) (Thermo Fisher Scientific, Waltham, MA, USA) with emphasis on TL imaging. The optimal concentration for MTG was also found suitable for MitoTracker Deep Red.

Labeling concentrations were tested in the range of 10–400 nM, with incubation times ranging from 15 to 45 min. The most suitable results (for non-BM transduced cells) were obtained with 75–100 nM MT with incubation for 30 min, followed by three washes for 10 s with 1-ml phosphate-buffered saline (PBS) or live-cell imaging medium (Thermo Fisher Scientific, Waltham, MA, USA). For MitoTracker Deep Red (Thermo Fisher Scientific, Waltham, MA, USA), an additional washing step was necessary to sufficiently reduce the background signal for optimal SIM image reconstruction. For combined experiments with BM and Gtom, MT incubation was applied as the final labeling step.

4.5 Three-color mitochondrial labeling

As described in more detail above, cells were first labeled with Gtom through lipofectamine transfection of plasmid DNA. Transfected cells were allowed to recover and then positively selected using Geneticin before further labeling. After 2 days, the Gtom-labeled cells were then transduced with BM and then incubated for an additional 16–20 h. Immediately before imaging, the cells were incubated with MT for 30 min then washed in PBS or live-cell imaging medium. The workflow is summarized below in Figure 7.

4.6 Imaging parameters

4.6.1 Microscope

Images were acquired using a DeltaVision OMX V4 Blaze imaging system (GE Healthcare Life Sciences,

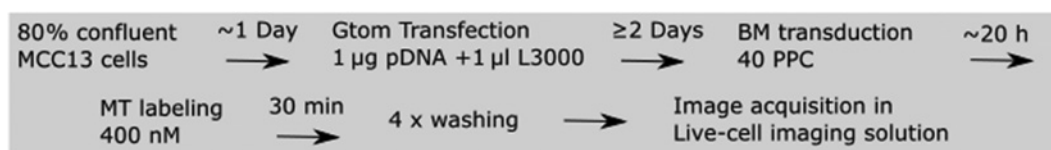


Figure 7: Flow chart summarizing the optimized protocol for three-color labeling of mitochondria.

Marlborough, MA, USA) equipped with a 60X 1.42NA oil-immersion objective (Olympus); three sCMOS cameras; and 488-, 568-, and 642-nm lasers for excitation. The vendor specified optical resolution of the system (3D SIM) is 110–160 nm laterally and 340–380 nm axially, depending on color channel. Multiple channels were imaged sequentially before stepping through z-planes. Illumination intensity, exposure time, and time-lapse period were optimized for each individual label. Supplementary Table S1 gives an overview of individual image parameters.

4.6.2 Image processing

Deconvolution and 3D SIM image reconstruction were completed using the manufacturer-supplied SoftWoRx program (GE Healthcare Life Sciences, Marlborough, MA, USA). Image registration (color alignment) was also performed in SoftWoRx using experimentally measured calibration values compensating for minor lateral and axial shifts, rotation, and magnification differences between cameras. Further image processing was done using Fiji [44], and 3D movies were generated using Volocity version 6.3 (Perkin Elmer, Waltham, MA, USA).

Acknowledgments: Addgene plasmid # 54282 was a gift to Addgene from Michael W. Davidson. Growth of bacteria and plasmid purification were performed by the Drug Transport and Delivery Research Group at the Pharmacy Department (UiT). The MCC13 cell line was a gift from Professor Ugo Moens, Molecular Inflammation Research Group, UiT, and originated from Professor Baki Akguel, University of Cologne, Institute of Virology, Germany. B.A. acknowledges the funding from the European Research Council (project number 336716). The publication charges for this article have been funded by a grant from the publication fund of UiT The Arctic University of Norway.

Author contributions statements: B.S.A. and D.L.W. conceived and supervised the project. I.S.O., B.S.A., and D.L.W. designed the research. I.S.O. performed all the experiments on microscopy and D.L.W. assisted during the experiments. I.S.O. and C.I.Ø. prepared and stained the cells. I.S.O. reconstructed the images, analyzed the

data, and prepared the figures. All authors contributed in writing the manuscript.

Competing financial interests: The authors declare no competing financial interests.

References

- [1] Nunnari J, Suomalainen A. Mitochondria: in sickness and in health. *Cell* 2012;148:1145–59.
- [2] Jakobs S, Wurm CA. Super-resolution microscopy of mitochondria. *Curr Opin Chem Biol* 2014;20:9–15.
- [3] Mitra K, Lippincott-Schwartz J. Analysis of mitochondrial dynamics and functions using imaging approaches. *Curr Protoc Cell Biol* 2010; Chapter 4: Unit 4.25.1–21. doi:10.1002/0471143030.cb0425s46.
- [4] York AG, Chandris P, Nogare DD, et al. Instant super-resolution imaging in live cells and embryos via analog image processing. *Nat Meth* 2013;10:1122–6.
- [5] Takihara Y, Inatani M, Eto K, et al. In vivo imaging of axonal transport of mitochondria in the diseased and aged mammalian CNS. *Proc Natl Acad Sci* 2015;112:10515–20.
- [6] Xu Y, Chen M, Hu B, Huang R, Hu B. In vivo imaging of mitochondrial transport in single-axon regeneration of zebrafish Mauthner cells. *Front Cell Neurosci* 2017;11:4.
- [7] Monteith A, Marszalec W, Chan P, et al. Imaging of mitochondrial and non-mitochondrial responses in cultured rat hippocampal neurons exposed to micromolar concentrations of TMRM. *PLoS One* 2013;8:e58059.
- [8] Goldenthal MJ. Mitochondrial involvement in myocyte death and heart failure. *Heart Fail Rev* 2016;21:137–55.
- [9] Murphy E, Ardehali H, Balaban RS, et al. Mitochondrial function, biology, and role in disease: a scientific statement from the American heart association. *Circ Res* 2016;118:1960–91.
- [10] O'Rourke B. Metabolism: beyond the power of mitochondria. *Nat Rev Cardiol* 2016;13:386–8.
- [11] Wai T, Langer T. Mitochondrial dynamics and metabolic regulation. *Trends Endocrinol Metab* 2016;27:105–17.
- [12] Scaduto RC Jr, Grotyohann LW. Measurement of mitochondrial membrane potential using fluorescent rhodamine derivatives. *Biophys J* 1999;76:469–77.
- [13] Detmer SA, Chan DC. Functions and dysfunctions of mitochondrial dynamics. *Nat Rev Mol Cell Biol* 2007;8:870–9.
- [14] Galbraith CG, Galbraith JA. Super-resolution microscopy at a glance. *J Cell Sci* 2011;124:1607–11.
- [15] Schermelleh L, Heintzmann R, Leonhardt H. A guide to super-resolution fluorescence microscopy. *J Cell Biol* 2010;190:165–75.
- [16] Waldchen S, Lehmann J, Klein T, van de Linde S, Sauer M. Light-induced cell damage in live-cell super-resolution microscopy. *Sci Rep* 2015;5:15348.

- [17] Gustafsson MG, Shao L, Carlton PM, et al. Three-dimensional resolution doubling in wide-field fluorescence microscopy by structured illumination. *Biophys J* 2008;94:4957–70.
- [18] Schermelleh L, Carlton PM, Haase S, et al. Subdiffraction multicolor imaging of the nuclear periphery with 3D structured illumination microscopy. *Science* 2008;320:1332–6.
- [19] Hirano Y, Matsuda A, Hiraoka Y. Recent advancements in structured-illumination microscopy toward live-cell imaging. *Microscopy (Oxf)* 2015;64:237–49.
- [20] Mönkemöller V, Øie C, Hübner W, Huser T, McCourt P. Multimodal super-resolution optical microscopy visualizes the close connection between membrane and the cytoskeleton in liver sinusoidal endothelial cell fenestrations. *Sci Rep* 2015;5:16279.
- [21] Dempsey GT, Vaughan JC, Chen KH, Bates M, Zhuang X. Evaluation of fluorophores for optimal performance in localization-based super-resolution imaging. *Nat Methods* 2011;8:1027–36.
- [22] Agarwal K, Macháň R. Multiple signal classification algorithm for super-resolution fluorescence microscopy. *Nat Commun* 2016;7:13752.
- [23] Szczurek A, Klewes L, Xing J, et al. Imaging chromatin nanostructure with binding-activated localization microscopy based on DNA structure fluctuations. *Nucleic Acids Res* 2017;45:e56.
- [24] Perry AJ, Rimmer KA, Mertens HD, et al. Structure, topology and function of the translocase of the outer membrane of mitochondria. *Plant Physiol Biochem* 2008;46:265–74.
- [25] Chacinska A, Koehler CM, Milenkovic D, Lithgow T, Pfanner N. Importing mitochondrial proteins: machineries and mechanisms. *Cell* 2009;138:628–44.
- [26] Thermo Fisher Scientific. Description of 'CellLight Mitochondria-RFP, BacMam 2.0'. Available at: <https://www.thermofisher.com/order/catalog/product/C10505>.
- [27] Melkko J, Hellevik T, Risteli L, Risteli J, Smedsrod B. Clearance of NH2-terminal propeptides of types I and III procollagen is a physiological function of the scavenger receptor in liver endothelial cells. *J Exp Med* 1994;179:405–12.
- [28] Di Maio R, Barrett PJ, Hoffman EK, et al. α -Synuclein binds to TOM20 and inhibits mitochondrial protein import in Parkinson's disease. *Sci Transl Med* 2016;8:342ra78.
- [29] Kholmukhamedov A, Schwartz JM, Lemasters JJ. MitoTracker probes and mitochondrial membrane potential. *Shock (Augusta, Ga.)* 2013;39:543.
- [30] Lemasters JJ. Modulation of mitochondrial membrane permeability in pathogenesis, autophagy and control of metabolism. *J Gastroenterol Hepatol* 2007;22:S31–7.
- [31] Genetics Home Reference. *PDHA1 gene*. Available at: <http://ghr.nlm.nih.gov/gene/PDHA1>.
- [32] Genetics Home Reference. Pyruvate dehydrogenase deficiency. <https://ghr.nlm.nih.gov/condition/pyruvate-dehydrogenase-deficiency>.
- [33] Burte F, Carelli V, Chinnery PF, Yu-Wai-Man P. Disturbed mitochondrial dynamics and neurodegenerative disorders. *Nat Rev Neurol* 2015;11:11–24.
- [34] Wang X, Gerdes HH. Transfer of mitochondria via tunneling nanotubes rescues apoptotic PC12 cells. *Cell Death Differ* 2015;22:1181–91.
- [35] Sanchez V, Villalba N, Fiore L, et al. Characterization of tunneling nanotubes in Wharton's jelly mesenchymal stem cells. An Intercellular exchange of components between neighboring cells. *Stem Cell Rev Rep* 2017;13:1–8.
- [36] Pasquier J, Guerrouahen BS, Al Thawadi H, et al. Preferential transfer of mitochondria from endothelial to cancer cells through tunneling nanotubes modulates chemoresistance. *J Transl Med* 2013;11:94.
- [37] Torralba D, Baixauli F, Sánchez-Madrid F. Mitochondria know no boundaries: mechanisms and functions of intercellular mitochondrial transfer. *Front Cell Dev Biol* 2016;4:107.
- [38] Berridge MV, McConnell MJ, Grasso C, Bajzikova M, Kovarova J, Neuzil J. Horizontal transfer of mitochondria between mammalian cells: beyond co-culture approaches. *Curr Opin Genet Dev* 2016;38:75–82.
- [39] Pouli D, Balu M, Alonzo CA, et al. Imaging mitochondrial dynamics in human skin reveals depth-dependent hypoxia and malignant potential for diagnosis. *Sci Transl Med* 2016;8:367ra169.
- [40] Shao L, Kner P, Rego EH, Gustafsson MG. Super-resolution 3D microscopy of live whole cells using structured illumination. *Nat Methods* 2011;8:1044–6.
- [41] Icha J, Weber M, Waters CJ, Norden C. Phototoxicity in live fluorescence microscopy, and how to avoid it. *Bioessays* 2017;39:1700003.
- [42] Magidson V, Khodjakov A. Circumventing photodamage in live-cell microscopy. *Methods Cell Biol* 2013;114:545–60.
- [43] Addgene. mEmerald-TOMM20-N-10. Available at: www.addgene.org/54282/.
- [44] Schindelin J, Arganda-Carreras I, Frise E, et al. Fiji: an open-source platform for biological-image analysis. *Nat Methods* 2012;9:676–82.

Supplemental Material: The online version of this article offers supplementary material (<https://doi.org/10.1515/nanoph-2017-0112>).



Live-cell imaging of human spermatozoa using SIM

Ida S. Opstad, Daria A. Popova, Ganesh Acharya, Purusotam Basnet And Balpreet S. Ahluwalia

Published in Biomedical Optics Express, December 2018.



Live-cell imaging of human spermatozoa using structured illumination microscopy

IDA S. OPSTAD,^{1,5} DARIA A. POPOVA,^{2,5} GANESH ACHARYA,^{2,3}
PURUSOTAM BASNET,^{2,4} AND BALPREET S. AHLUWALIA^{1,*}

¹Department of Physics and Technology, UiT The Arctic University of Norway, 9037 Tromsø, Norway

²Women's Health and Perinatology Research Group, Department of Clinical Medicine, UiT The Arctic University of Norway, Tromsø, Norway

³Department of Clinical Science, Intervention & Tech. Karolinska Institutet, Stockholm, Sweden

⁴IVF Unit, Department of Obstetrics & Gynecology, University Hospital North Norway, Tromsø, Norway

⁵Both authors contributed equally to this work

*balpreet.singh.ahluwalia@uit.no

Abstract: Structural details of spermatozoa are interesting from the perspectives of fundamental biology and growing reproductive health problems. Studies of nanostructural details of these extremely motile cells have been limited to fixed cells, largely using electron microscopy. Here we provide the protocols for and demonstrate live-cell multi-color super-resolution imaging of human spermatozoa using structured illumination microscopy (SIM). By using patches of agarose for immobilization, we achieved four-channel 3D SIM imaging of the plasma membrane, nucleus, mitochondria and microtubulin in the same living sperm cells. We expect that high-resolution imaging of living spermatozoa will be implemented for research on fundamental cellular mechanisms together with morphological aberrations involved in male infertility for a future improved cell selection process in in vitro fertilization treatments.

© 2018 Optical Society of America under the terms of the [OSA Open Access Publishing Agreement](#)

1. Introduction

Research on subcellular organization of human reproductive cells and preimplantation embryos is becoming increasingly popular as it is considered to be important to tackle growing reproductive health problems. Along with female infertility, male factor infertility is a significant issue which may result from different causes, such as anatomical anomalies, hormonal imbalances, infections or genetic abnormalities. However, the etiology of male infertility remains undiagnosed in about one third of the cases [1,2]. Nowadays, male reproductive health assessment is primarily based on sperm quality, and morphology is one of the main characteristics evaluated in clinical practice. Changes in the ultrastructure and general morphology of sperm cells serves as an indicator of the influence of different physical (e.g. freezing in reproductive technologies) [3,4], chemical (occupational exposure to toxic substances) or environmental factors on semen reflecting male reproductive health during life [5,6].

Until recently, numerous studies have been performed to study the ultrastructure of sperm cells using transmission electron microscopy (TEM) to obtain high resolution images [3,7–9]. Compared to TEM, optical microscopy often enables the analysis of living cells, resulting in the elimination of artifacts specific to cell fixation, such as changed protein conformation with associated loss of staining specificity [10,11]. Though a valuable tool, the diffraction limit renders conventional light microscopy unable to resolve details finer than about 250 nm laterally and 500 nm axially using a high-end microscope. Optical nanoscopy (or super-resolution optical microscopy) encompasses an array of techniques for overcoming the resolution limit of conventional microscopy, opening avenues for studying biological samples

in much greater detail than previously possible without the extensive sample preparation required for electron microscopy [12].

Structured illumination microscopy (SIM) is a live-cell compatible super-resolution technique that achieves greatly enhanced contrast along with a factor of two resolution enhancement in all three spatial dimensions as compared to the diffraction limit [13]. For biological structures just below the conventional resolution limit, SIM can thus be applied as a tool for valuable additional structural information in living cells. In the case of sperm cells, structural analysis using multi-color SIM offers opportunities for a more precise description of disease specific defects responsible for infertility, like morphological aberrations associated with teratozoospermia [14] or asthenozoospermia [15,16]. In addition to a better description of morphology, we expect that live-cell studies of sperm cells at super-resolution and enhanced contrast will contribute to a gain in knowledge about fundamental cellular mechanisms that might be implemented for an improved reproductive cell selection process in future in vitro fertilization (IVF) treatments.

The biggest hurdle for live-cell high-resolution imaging of sperm cells has been the extreme motility associated with their progressive swimming ($\sim 66 \mu\text{m/s}$ [17]), in addition to their free-floating nature as suspension cells. Until now, to the best of our knowledge, all super-resolution imaging of human spermatozoa has been limited to fixed cells. Other challenges associated with multi-color super-resolution microscopy of any cell type are labeling, label induced toxicity and phototoxicity. Here we provide a methodology for overcoming above-mentioned hurdles and demonstrate up to four-channel 3D SIM imaging of different sub-cellular structures in living human spermatozoa. We also provide labeling protocols and discuss associated challenges and opportunities.

2. Materials and methods

2.1 Sample preparation

Semen preparation

The Regional Committee for Medical and Health Research Ethics of Norway (REK-Nord) approved the project. Experiments were performed using semen of donors from the IVF clinic of the University Hospital of North Norway, Tromsø, Norway. All participants signed a written informed consent. Semen samples were collected according to the guidelines of the World Health Organization (WHO) with an abstinence period of 3–5 days.

After liquefaction, semen samples were examined using light microscopy and Neubauer-improved counting chambers. In the experiments, all samples contained no less than 60 million cells per milliliter and had progressive motility $>50\%$. The swim up method was used to wash the samples. The semen samples were diluted with 5 mL of sperm washing medium (Sage) and centrifuged for 10 min at $700 \times g$. Supernatant was removed and the pellet was washed again. After removing the supernatant, 0.5 mL of swim up medium was layered and the tube was put into an incubator ($5.0\% \text{CO}_2$, 37°C). During 60 min of incubation, highly motile spermatozoa migrated to the above layered medium. After incubation, the supernatant was aspirated with pipette, centrifuged and the sediment was used for the following procedures.

Labeling, immobilization and imaging conditions

Labeling and imaging were done at room temperature ($\sim 23^\circ\text{C}$) in PBS or Live Cell Imaging Solution (Molecular Probes) as summarized in Table 1. For multi-color experiments, the label requiring the longest incubation time was added to the cells first, and then sequentially the rest of the probes, so that at the end of the incubation time, the cells had been subjected to approximately the concentrations and labeling times as listed in Table 1. After incubation with the labels, the samples were diluted in PBS ($\sim 1:15$) and spun down using $800 \times g$ for 10 min. The supernatant was removed and the samples resuspended in PBS to a concentration

found suitable for the respective sample and experiment. Drops of about 8 μL were placed on coverslips (#1.5 washed in 100% ethanol and placed in sample holders for live-cell microscopy) and covered with refrigerated patches of ~2% agarose (High-resolution, Sigma-Aldrich) in PBS. When the cells after a couple of minutes had become fully immobilized, the samples were covered with a plastic lid to prevent further drying during imaging. SiR-tubulin was purchased from Spirochrome (Cytoskeleton kit), while all other probes were purchased from Thermo Fisher Scientific.

Table 1. Labeling conditions applied for SIM imaging

Label	Concentration	Incubation time
CellMask Orange	1:1000	10 min
MitoTracker Green	200 nM	20 min
Hoechst 34580	5 $\mu\text{g}/\text{mL}$	20 min
SiR-tubulin	1 μM	2 h

2.2 Microscope

Images were acquired using a DeltaVision OMX V4 Blaze imaging system (GE Healthcare) equipped with a 60X 1.42NA oil-immersion objective (Olympus), three sCMOS cameras, and 405, 488, 568, and 642 nm lasers for excitation. The vendor specified optical resolution of the system (3D SIM) is 110-160 nm laterally, and 340-380 nm axially, depending on color channel. To surpass the diffraction limit, this SIM set-up uses sinusoidal illumination patterns and acquires 120 images per 1 μm z-stack thickness (3 illumination angles times 5 phase shifts times 8 planes/ μm thickness) per color channel. Super-resolution 3D images are then obtained via image processing using the reconstruction software described below.

2.3 Image processing

Deconvolution and 3D SIM image reconstruction were completed using the manufacturer-supplied SoftWoRx program (GE Healthcare). Image registration (color alignment) was also performed in SoftWoRx using experimentally-measured calibration values compensating for minor lateral and axial shifts, rotation, and magnification differences between cameras. Further image processing was done using Fiji/ImageJ [18]

3. Results and discussion

3.1 Single-color imaging and immobilization

Immobilization using patches of agarose made high-resolution imaging of living spermatozoa possible. Figure 1 shows fluorescence microscopy images of living spermatozoa acquired using deconvolution microscopy (upper panel) and SIM (lower panel) for various live-cell compatible probes (CellMask Orange, panels (a) and (e); MitoTracker Green, panels (b) and (f); Hoechst 34580, panels (c) and (g); SiR-tubulin, panels (d) and (h)). The contrast and resolution enhancement for SIM compared to conventional deconvolution microscopy is apparent for all structures, but most prominent for the mitochondria-containing mid-piece, panels (a), (b), (e) and (f), where structures around 100 nm length-scale are prominent. For the nucleus, only minor contrast enhancement is visible, while for microtubulin (panels (d) and (h)) the resolution doubling provided by SIM makes it evident that the centriole (indicated by arrows) is completely separated from the rest of the axoneme.

Imaging from below through the coverslip (and not through the agarose) resulted in images not significantly affected by the agarose with absorbed leftover dye. Imaging a few planes below the agarose enabled us to acquire high quality SIM images of *most of* the living sperm cells, although not for the uppermost part (0.2 - 0.3 μm) of the cells, which was stuck in the agarose. To illustrate, the sample plane in Fig. 2(a) is unusable because of the signal from the agarose (with absorbed leftover dye), while for the neighboring sample planes shown in Fig. 2(b) and 2(c), the agarose is now above and not in the image plane, enabling us

to observe the cell at high resolution and contrast. In the particular cell depicted, an abnormally 'puffed up' membrane morphology is revealed, clearly different from the tightly wrapped membrane in e.g. Fig. 1(e).

Though immobilization for live-cell microscopy using patches of agarose (often combined with cell growth medium) is widely applied in microbiology (e.g. discussed in [19]), this technique is not extensively used in the 'eukaryotic cell community'. We expect this immobilization technique applied here successfully for SIM of spermatozoa to be also directly applicable to other types of suspension cells that are challenging to image live otherwise. The addition of an agarose patch on top of the sample is suitable for imaging set-ups where both illumination and detection are conducted through the coverslip (and not through the agarose), as is often the case in fluorescence microscopy.

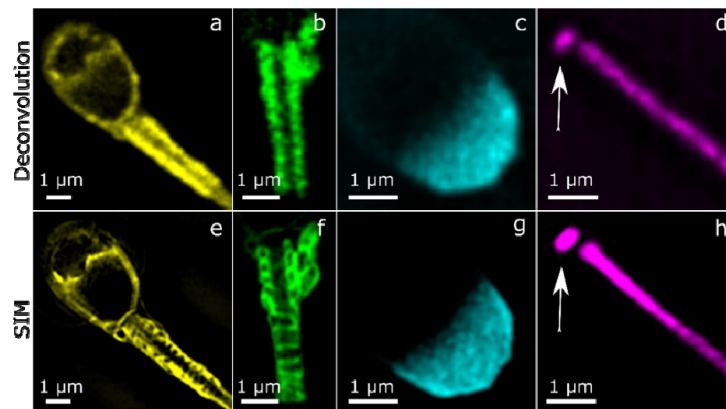


Fig. 1. Comparison of deconvolution microscopy (upper panels) and SIM (lower panels) images of living human spermatozoa for different probes. (a), (e) Plasma membrane labeled using CellMask Orange; (b), (f) Mitochondria labeled using MitoTracker Green; (c), (g) Nucleus labeled using Hoechst 34580; (d), (h) Microtubulin labeled using SiR-tubulin. The contrast and resolution enhancement are apparent for all probes, but most significant for the region containing mitochondria (panels (a), (b), (e) and (f)), but also for the centriole, indicated by arrows in panels (d) and (h). The images are single z-sections.

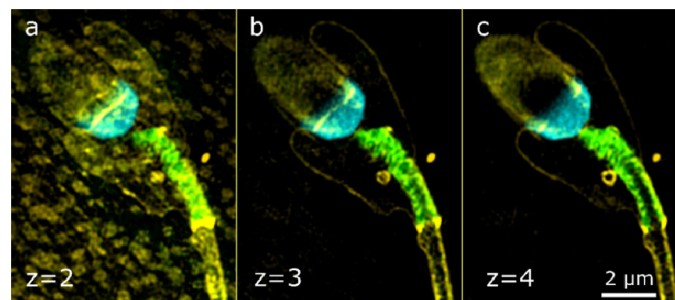


Fig. 2. Comparison of background signal in z-planes 2 (a), 3 (b) and 4 (c) counted from the agarose patch (top) used for immobilization. The distance between the z-slices is 125 nm. The agarose patch (with absorbed leftover dye) only causes significant background signal in the uppermost planes. The cells were labeled using CellMask Orange, MitoTracker Green and Hoechst 34580 and imaged live using SIM.

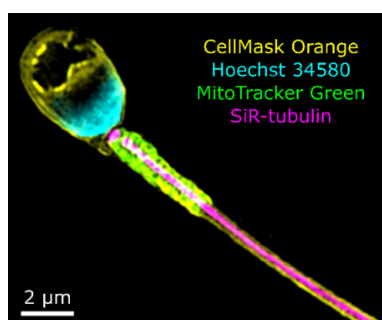


Fig. 3. Four-channel SIM image of living human spermatozoa labeled using CellMask Orange (yellow), MitoTracker Green (green), Hoechst 34580 (turquoise) and SiR-tubulin (magenta). The image is a 1 μm maximum intensity projected z-stack.

3.2 Multi-color SIM imaging

Figure 3 shows a four-channel SIM image of living human spermatozoa labeled using CellMask Orange, MitoTracker Green, Hoechst and SiR-tubulin. CellMask (yellow) labels the plasma membrane and outlines the entire cell, MitoTracker (green) labels mitochondria in the mid-piece clutched around the axoneme labeled using SiR-tubulin (magenta). Hoechst (cyan) labels DNA and is here visible only in the lower part of the head. For multi-color experiments, similar concentrations and labeling times were applicable as described for the single-probe experiments, though the labels were added sequentially to fit their individually optimized labeling time (with a single washing step in the end), resulting in slightly varying concentrations compared to the single-color experiments. Multi-color super-resolution imaging of living sperm cells unlocks exciting new possibilities regarding detailed analysis of subcellular structures for various cellular conditions, that can be employed to e.g. better understand diseases and the effect of different treatments in the field of reproductive medicine.

Four-channel SIM imaging of living cells is in general challenging for four reasons in particular: sample movement, photobleaching, phototoxicity, and depth-induced spherical aberrations. Sample movement was effectively eliminated using agarose patches. Photobleaching was countered using high labeling concentrations of bright photostable dyes with lowered illumination intensities and instead longer exposure times (20-30 ms) to ensure sufficient modulation contrast of the illumination pattern. Phototoxicity was not found problematic for these experiments as only single time-points were considered, although the four-channel imaging time for a 1.5 μm z-stack was around 20 s. Spherical aberrations were mitigated in these samples, through optimization of the immersion oil refractive index in use (1.516 was found appropriate for the four-channel imaging experiments), the tenuity of the samples ($\sim 0.5 - 3 \mu\text{m}$ thickness) and the sample placement directly on the coverslip. For thicker samples, spherical aberrations often cause SIM reconstruction artifacts, as the sample-induced aberrations can only be optimally corrected for one channel at a time.

4. Conclusions and summary

We provide a methodology for live-cell imaging of human spermatozoa using SIM, which is also applicable for a wide variety of other types of suspension cells and for imaging techniques where both illumination and detection are conducted through the coverslip. Labeling with fluorescent probes compatible with live-cell imaging, and subsequent immobilization using patches of agarose, enabled up to four-channel SIM imaging that revealed an unprecedented level of structural details of living sperm cells. This methodology shows great promise for shedding new light on sub-cellular structures and cellular mechanisms of the male reproductive cell in both healthy and diseased subjects, as live-cell imaging at super-resolution enables a much more precise description of e.g. morphological

aberrations responsible for infertility. As compared to electron microscopy, the proposed methodology not only enables live-cell experiments, but also eliminates fixation steps and fixation related artefacts. This enables reduced sample preparation time and allows for multi-channel colocalization experiments by means of standard labeling protocols. In addition to a better description of morphology, we expect that live-cell studies of sperm cells at high resolution and contrast will contribute to an increased knowledge of fundamental cellular mechanisms that might be implemented for an improved reproductive cell selection process in IVF treatments in the future.

Funding

UiT, The Arctic University of Norway, Tematiske Satsinger program.

Acknowledgments

We would like to thank the men who provided semen samples and bioengineers: Ms. Sissle A. Hansen, Ms. Inger K. Olausen and Ms. Sylvi Johansen at the IVF Clinic, University Hospital of North Norway, Tromsø for coordinating with the patients. The publication charges for this article have been funded by a grant from the publication fund of UiT The Arctic University of Norway.

Disclosures

The authors declare that there are no conflicts of interest related to this article.

References

1. G. Cavallini, "Male idiopathic oligoasthenozoospermia," *Asian J. Androl.* **8**(2), 143–157 (2006).
2. N. Kumar and A. K. Singh, "Trends of male factor infertility, an important cause of infertility: A review of literature," *J. Hum. Reprod. Sci.* **8**(4), 191–196 (2015).
3. S. Ozkavukcu, E. Erdemli, A. Isik, D. Oztuna, and S. Karahuseyinoglu, "Effects of cryopreservation on sperm parameters and ultrastructural morphology of human spermatozoa," *J. Assist. Reprod. Genet.* **25**(8), 403–411 (2008).
4. C. Barthelemy, D. Royere, S. Hammah, C. Lebos, M. J. Tharanne, and J. Lansac, "Ultrastructural changes in membranes and acrosome of human sperm during cryopreservation," *Arch. Androl.* **25**(1), 29–40 (1990).
5. N. Naha, R. B. Bhar, A. Mukherjee, and A. R. Chowdhury, "Structural alteration of spermatozoa in the persons employed in lead acid battery factory," *Indian J. Physiol. Pharmacol.* **49**(2), 153–162 (2005).
6. W. Asghar, H. Shafiee, V. Velasco, V. R. Sah, S. Guo, R. El Assal, F. Inci, A. Rajagopalan, M. Jahangir, R. M. Anchan, G. L. Mutter, M. Ozkan, C. S. Ozkan, and U. Demirci, "Toxicology Study of Single-walled Carbon Nanotubes and Reduced Graphene Oxide in Human Sperm," *Sci. Rep.* **6**(1), 30270 (2016).
7. D. Lacy, A. J. Pettitt, J. M. Pettitt, and B. S. Martin, "Application of scanning electron microscopy to semen analysis of the sub-fertile man utilising data obtained by transmission electron microscopy as an aid to interpretation," *Micron* (1969) **5**(2), 135–173 (1974).
8. B. Baccetti, S. Capitani, G. Collodel, G. Di Cairano, L. Gambera, E. Moretti, and P. Piomboni, "Genetic sperm defects and consanguinity," *Hum. Reprod.* **16**(7), 1365–1371 (2001).
9. E. H. Chemes and Y. V. Rawe, "Sperm pathology: a step beyond descriptive morphology. Origin, characterization and fertility potential of abnormal sperm phenotypes in infertile men," *Hum. Reprod. Update* **9**(5), 405–428 (2003).
10. A. J. Hobro and N. I. Smith, "An evaluation of fixation methods: Spatial and compositional cellular changes observed by Raman imaging," *Vib. Spectrosc.* **91**, 31–45 (2017).
11. J. Kiernan, *Formaldehyde, Formalin, Paraformaldehyde And Glutaraldehyde: What They Are And What They Do* (2000).
12. C. G. Galbraith and J. A. Galbraith, "Super-resolution microscopy at a glance," *J. Cell Sci.* **124**(10), 1607–1611 (2011).
13. R. Heintzmann and T. Huser, "Super-Resolution Structured Illumination Microscopy," *Chem. Rev.* **117**(23), 13890–13908 (2017).
14. E. Moretti, and G. Collodel, *Electron Microscopy in the Study of Human Sperm Pathologies* (2012).
15. V. Y. Rawe, G. D. Galaverna, A. A. Acosta, S. B. Olmedo, and H. E. Chemes, "Incidence of tail structure distortions associated with dysplasia of the fibrous sheath in human spermatozoa," *Hum. Reprod.* **16**(5), 879–886 (2001).
16. F. Pelliccione, A. Micillo, G. Cordeschi, A. D'Angeli, S. Necozone, L. Gandini, A. Lenzi, F. Francavilla, and S. Francavilla, "Altered ultrastructure of mitochondrial membranes is strongly associated with unexplained asthenozoospermia," *Fertil. Steril.* **95**(2), 641–646 (2011).

17. W. V. Holt, F. Shenfield, T. Leonard, T. D. Hartman, R. D. North, and H. D. Moore, "The value of sperm swimming speed measurements in assessing the fertility of human frozen semen," *Hum. Reprod.* **4**(3), 292–297 (1989).
18. J. Schindelin, I. Arganda-Carreras, E. Frise, V. Kaynig, M. Longair, T. Pietzsch, S. Preibisch, C. Rueden, S. Saalfeld, B. Schmid, J.-Y. Tinevez, D. J. White, V. Hartenstein, K. Eliceiri, P. Tomancak, and A. Cardona, "Fiji: an open-source platform for biological-image analysis," *Nat. Methods* **9**(7), 676–682 (2012).
19. G. Joyce, B. D. Robertson, and K. J. Williams, "A modified agar pad method for mycobacterial live-cell imaging," *BMC Res. Notes* **4**(1), 73 (2011).



Adaptive fluctuation imaging captures rapid subcellular dynamics

Ida S. Opstad, Florian Ströhl, Åsa B. Birgisdóttir, Sebastián Maldonado, Trine Kalstad, Truls Myrnes, Krishna Agarwal, and Balpreet S. Ahluwalia

Published in Proceedings of SPIE, the International Society for Optical Engineering, June 2019.

Adaptive fluctuation imaging captures rapid subcellular dynamics

Ida S. Opstad^{1,*}, Florian Ströhl¹, Åsa B. Birgisdottir², Sebastián Maldonado¹, Trine Kalstad², Truls Myrnes², Krishna Agarwal¹, and Balpreet S. Ahluwalia¹

¹Department of Physics and Technology, UiT The Arctic University of Norway, NO-9037 Tromsø, Norway

²Department of Clinical Medicine, UiT The Arctic University of Norway, NO-9037 Tromsø, Norway

ABSTRACT

In this work we have explored the live-cell friendly nanoscopy method Multiple Signal Classification Algorithm (MUSICAL) for multi-colour imaging of various organelles and sub-cellular structures in the cardiomyoblast cell line H2c9. We have tested MUSICAL for fast (up to 230Hz), multi-colour time-lapse sequences of various sub-cellular structures (mitochondria, endoplasmic reticulum, microtubules, endosomes and nuclei) in living cells using low excitation-light dose. Challenges and opportunities with applying MUSICAL for studying rapid sub-cellular dynamics are discussed.

Keywords: fluorescence nanoscopy, fluctuation imaging, live cells, cardiomyoblasts

1. INTRODUCTION

Structural components of living cells are challenging to study because of their size, sensitivity, and highly dynamic nature. Still, understanding the different cellular features and their interactions is crucial for comprehending basic cellular functions, and for finding potential treatments for cellular malfunction. Overcoming the challenges in monitoring the position and morphology of sub-cellular structures in living cells is hence of great interest. Fluorescence nanoscopy¹ offers excellent contrast and specificity, but time and photon budget are limiting factors when resolution beyond the Abbe limit is required in live-cell imaging. Temporal resolution is limited and determined by the imaging system, technique and implementation, while the photon budget depends on the selected fluorophores, illumination mode and cellular system with varying label densities and chemical environments. Fluctuation-based computational nanoscopy techniques like Multiple Signal Classification Algorithm (MUSICAL)² extract super-resolved information from image sequences and are highly feasible for multi-colour experiments, contrasting localization-based nanoscopy in these regards. A caveat of time-accumulated live-cell images created from image sequences is, however, that (intra-)cellular dynamics smear structural details, compromising achievable resolution and the reliability of reconstructed features. The resulting artifacts can be difficult to distinguish from stationary biological components and therefore, imaging speed is critical for reliable image reconstruction. In this work, we have acquired fluctuation data using a commercial widefield system and sCMOS cameras in fast acquisition mode and tested the abilities and challenges of MUSICAL in capturing cellular details and dynamics in the rapidly changing microenvironment of living cardiomyoblasts.

2. METHODS

The cardiomyoblast cell line H9c2 was cultivated in glass bottom dishes and transiently transfected with organelle targeted fluorescent fusion proteins and labelled with live-cell compatible fluorescent labels, taking care to reduce label-induced toxicity. The cells were imaged at room temperature, but in heated media and for less than 30-60 min. Widefield, time-lapse data was acquired as fast as the system (OMX V4 optical microscope with 3 cameras and up to four-channel imaging) allowed while maintaining a signal-to-background ratio (SBR) of about 4 to 1.

*Correspondence: ida.s.opstad@uit.no

For each colour channel various combinations of intensity and exposure time were acquired to find a good trade-off between SBR, photo-bleaching and temporal resolution. MUSICAL images were first generated for a single time-point for various numbers of frames (10-400) and threshold values (based on image stack singular values) to select suitable reconstruction parameters before generating MUSICAL time-lapses from raw, low intensity image sequences (up to 3000 frames per colour channel). The MUSICAL image reconstructions were generated using a new Python implementation of MUSICAL optimized for high-speed reconstruction, making it feasible to generate MUSICAL time-lapse images of large, multi-colour image stacks.³

3. RESULTS AND DISCUSSION

For the current state of MUSICAL, thresholds for reconstruction must be selected manually. We found that a suitable selection way to be such that image features appearing in-focus were emphasized and out-of-focus features were suppressed in the MUSICAL images. 50 frames were in most cases found to give a suitable compromise between motion-smearing and fluctuation data for the algorithm, though longer sequences often appeared to provide a more reliable reconstruction if the organelles remained reasonably stationary within the sequence. For time-lapse sequences where considerable dynamics occurred, the algorithm was found to give a very strong image intensity. On the one hand, structural motion creates strong image intensity fluctuations that out-compete the intrinsic intensity fluctuations of the fluorophores. On the other hand, the algorithm appears to provide a window into a new way of recognizing and analyzing sub-cellular dynamics, which is key to understanding living processes and systems. Figure 1 shows results applying the algorithm in fast-acquisition mode for one colour channel at a time for mitochondria (upper panels) and endoplasmic reticulum (ER; lower panels). Figure 2 displays results applying MUSICAL to four-colour time-lapse data of (b) endosomes, (c) mitochondria, (d) ER and (e) nucleus. Although no challenge for the algorithm in itself, four-colour acquisition was slow (0.49s per time-point) due to

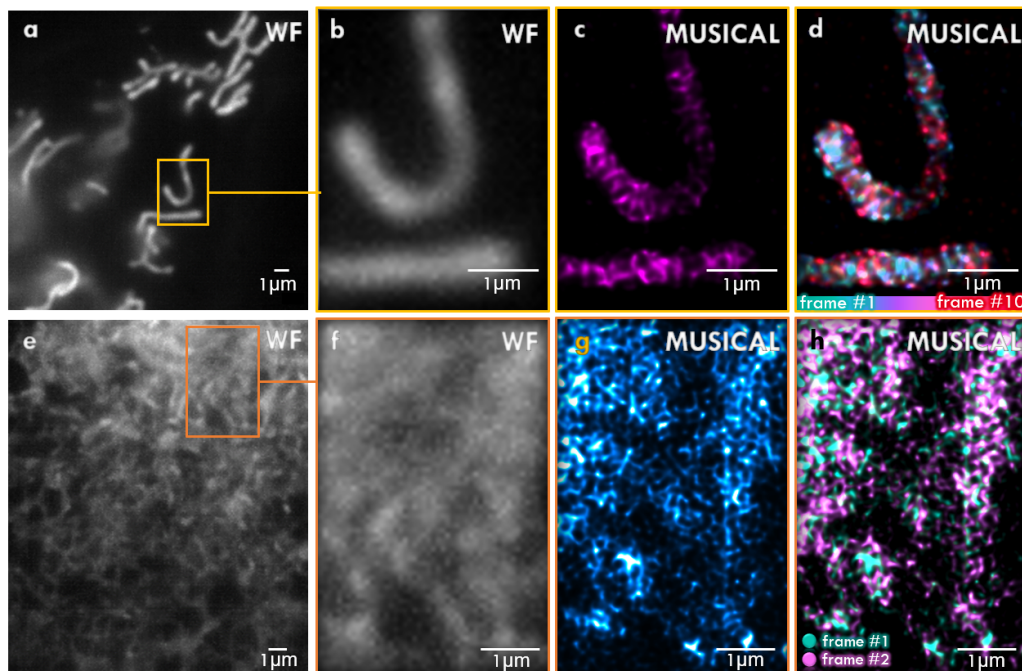


Figure 1. **Pushing the limits of time resolution in live-cell nanoscopy.** Obtainable MUSICAL frame rate is limited by achievable system imaging speed and the fluorescence intensity fluctuations of the raw time-lapse image data. *Upper panels:* mitochondrial inner membrane, *lower panels:* endoplasmic reticulum (ER). (a) and (e): widefield images (50 frames low intensity images maximum intensity projected) with indicated regions magnified on the right. (c) and (g) corresponding MUSICAL images obtained from the 50 frames projected on the left. (d) and (h) MUSICAL time-lapse images colour projected as indicated in the colour bars. The different colour projected time-points are 0.22s apart (acquisition time for a sequence of 50 widefield images).

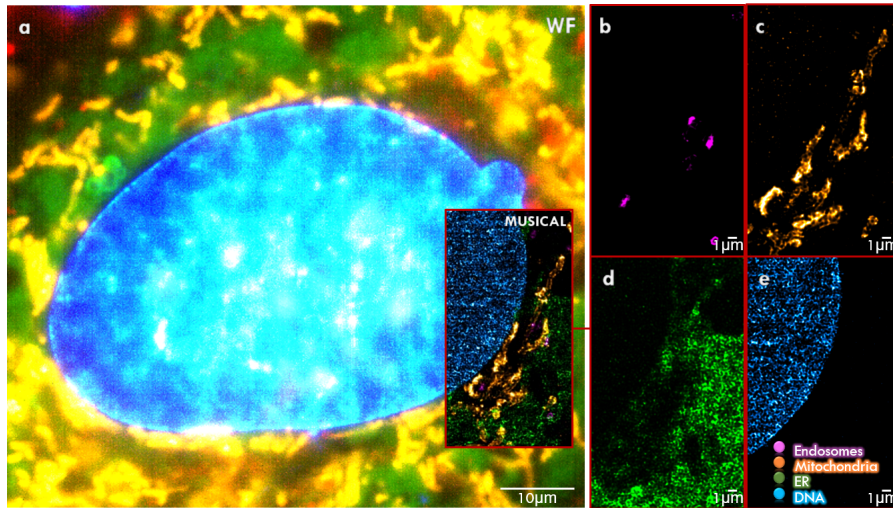


Figure 2. **Multi-colour imaging with MUSICAL.**(a) Single frame widefield image (raw MUSICAL data) of a living cardiomyoblast, labelled with four different fluorescent tags (acquisition time: 0.49s). The four-colour MUSICAL insert is shown to the right with separated channels. (b) Endosomes labelled using the membrane probe mCLING-ATTO647N, (c) mitochondrial inner membrane (dsRed-mito). (d) ER fusion protein eGFP-KDEL. (e) Nucleus labelled using Hoechs. The acquisition time for one four-colour MUSICAL image was 23s (obtained from 47 widefield images).

necessary switching of fluorescent filters between each time-point (number of channels > number of cameras), translating into algorithmic challenges in reconstructing moving objects even for short sequences.

4. CONCLUSION

In conclusion, we have explored the computational nanoscopy approach MUSICAL in fast, multi-colour nanoscopy of living cardiomyoblasts. The algorithm is promising with its multi-colour abilities and live-cell compatibility. Challenges include recognition and elimination of reconstruction artefacts, fast three-dimensional motion of living cellular features and modest intrinsic fluorescent intensity fluctuations compared to motion-induced signal fluctuations. Although an analytical challenge, this latter feature of the algorithm can be exploited in analyzing feature dynamics of e.g. cellular organelles.

ACKNOWLEDGMENTS

Funding information

FS acknowledges funding from the European Molecular Biology Organisation (#7411) and Marie Skłodowska-Curie actions (#836355). KA acknowledges funding from Marie Skłodowska-Curie actions (SEP-210382872). BSA acknowledges funding from UiT, The Arctic University of Norway, Tematiske Satsinger program. ÅBB and TM acknowledges funding from the Health Authorities of North Norway.

Competing interests statement

The authors declare no competing interests.

REFERENCES

- [1] Sahl, S. J., Hell, S. W., and Jakobs, S., “Fluorescence nanoscopy in cell biology,” *Nature reviews Molecular cell biology* **18**(11), 685 (2017).
- [2] Agarwal, K. and Macháň, R., “Multiple signal classification algorithm for super-resolution fluorescence microscopy,” *Nature communications* **7**, 13752 (2016).
- [3] Acuña-Maldonado, S. A., *Multiple Signal Classification Algorithm: computational time reduction and pattern recognition applications*, Master’s thesis, UiT The Arctic University of Norway, Tromsø, Norway (2019).



Musij: an ImageJ plugin for video nanoscopy

*Sebastian Acuña, Florian Ströhl, Ida S. Opstad, Balpreet S. Ahluwalia, Krishna
Agarwal*

Published in Biomedical Optics Express, April 2020.

MusiJ: an ImageJ plugin for video nanoscopy

SEBASTIAN ACUÑA,^{1,†} FLORIAN STRÖHL,^{1,†} IDA S. OPSTAD,¹
BALPREET S. AHLUWALIA,^{1,2} KRISHNA AGARWAL^{1,*}

¹Department of Physics and Technology, UiT The Arctic University of Norway, NO-9037 Tromsø, Norway

²Department of Clinical Science, Intervention and Technology, Karolinska Institute, 17177 Stockholm, Sweden

[†] These authors contributed equally.

*krishna.agarwal@uit.no

Abstract: We present an open-source implementation of the fluctuation-based nanoscopy method MUSICAL for ImageJ. This implementation improves the algorithm's computational efficiency and takes advantage of multi-threading to provide orders of magnitude faster reconstructions than the original MATLAB implementation. In addition, the plugin is capable of generating super-resolution videos from large stacks of time-lapse images via an interleaved reconstruction, thus enabling easy-to-use multi-color super-resolution imaging of dynamic systems.

© 2020 Optical Society of America under the terms of the [OSA Open Access Publishing Agreement](#)

1. Introduction

The past two decades have witnessed a huge development in nanoscopy techniques that allow to surpass the resolution limit of optical microscopy and thus provide *super-resolution* [1]. One way of classifying the broad range of those techniques is to distinguish all-optical, hybrid, and purely computational approaches. All-optical nanoscopy techniques manage to shrink the effective point spread function before detection and include stimulated emission depletion (STED) microscopy [2] or instant structured illumination microscopy (iSIM) [3]. Hybrid and purely computational techniques, in contrast, make use of temporal changes in the sample's fluorescent emission profile and extract additional information from time-series of raw frames of the same underlying sample structure. Such changes can be induced extrinsically via spatially varying illumination patterns [4, 5] or intrinsically by exploiting fluorophore photokinetics that result in fluctuations in the measured fluorescence intensity [6, 7].

Despite the often simplified optical setup of computational and hybrid nanoscopy techniques in comparison to all-optical ones, a lack of user-friendly and open-source implementations has often hindered fast integration of nanoscopy into biological research routines. A prime example for such a delay is the case of structured illumination microscopy (SIM). Its complex reconstruction algorithm was published in 2000, just to be implemented anew countless times in microscopy laboratories all over the world until the release of the easy-to-use FairSIM plugin [8], more than 15 years after the original publication. Further, as all nanoscopy techniques vary in their strengths and weaknesses, it is desirable to make as many different techniques available as possible, ideally in a single standard analysis environment. For microscopy, this environment is the image processing toolbox ImageJ [9] or its advanced version Fiji (*Fiji is just ImageJ*) [10].

Akin to the SIM reconstruction plugin FairSIM, single molecule localisation microscopy (SMLM) software has been made freely available by a vibrant community (for a comprehensive list see [11–13]). Similar to SIM, SMLM techniques can be regarded as hybrid nanoscopy methods due to the requirements of multiple high-power lasers and additional optical elements for field flattening [14] or when 3D information is desired [15]. A notable exception are 3D SMLM techniques with purely computational 3D information extraction based on aberrations in the microscope's point spread function (PSF) - these are also available in Fiji [16]. Despite their impressive resolution, SMLM reconstruction algorithms require data sets comprising thousands

of raw frames with sparse single molecule blinking events, which renders live-cell, let alone time-lapse imaging challenging.

Approaches to extract sub-diffraction features from data sets with densely packed emitters and with well below thousand raw frames taken on conventional, non-specialized microscopes, can be grouped as fluctuation-based nanoscopy techniques. Fluctuation-based algorithms exploit small intensity variations in time-series via statistical analyses to generate better resolved images. The actual algorithm depends on the statistical approach, thus giving rise to various flavors of this idea. Examples include SOFI (super-resolution optical fluctuation imaging) [17], 3B (Bayesian analysis of blinking and bleaching) [18], ESI (entropy-based super-resolution imaging) [19], and SRRF (super-resolution radial fluctuations) [20]. All of the above mentioned algorithms (except SOFI) have been translated to ImageJ. The recently developed fluctuation-based method MUSICAL (multiple signal classification algorithm) [21], however, has not been translated to ImageJ until now.

MUSICAL's origin can be traced to MUSIC (multiple signal classification) first developed for direction of arrival measurements [22]. In MUSIC, the number of independent sources, often equal to the number of targets (aeroplanes or ships for example), is determined by the number of non-zero eigenvalues if the number of sources is less than the number of independent measurements taken at multiple time instances over an array of radar/sonar sensors. The multiple time instances provide multiple independent measurements from the sources and the problem of determining the direction of arrival is an inverse source problem. An indicator function is computed for each candidate point (also called test point) r_{test} in the target region by taking the reciprocal of a distance function d_n .

$$f(r_{\text{test}}) = \frac{1}{d_n(r_{\text{test}})} \quad (1)$$

The distance function d_n is the projection of the expected output vector for a test point onto the eigenvectors with zero eigenvalues. The presence and direction of arrival of the target is then indicated if the indicator function has a large value at a candidate target point. MUSIC has survived the test of times and is constantly being reinvented for modern applications such as cognitive radars [23] and inverse imaging in the microwave domain [24, 25]. In the case of inverse imaging in the microwave domain, the full electromagnetic wave model of scattering applies and a multiple input multiple output system is used for taking measurements. Compared to the case of radars, the problem here is an inverse scattering problem and not an inverse source problem. This means the number of non-zero eigenvalues indicates the number of independent dipoles induced on the scatterers, as long as the number of transmitters and receivers is more than the number of induced dipoles. This number is equal to or more than the number of scatterers, depending upon the degrees of freedom for the induced dipole, which in turn depends upon isotropicity of the scatterers as well as the polarization constraints on the incident waves [24].

In the case of optical microscopy or nanoscopy, the measurements are comprised of fluorescent intensity detections on an optical detector array (i.e. the microscope's camera) at multiple time instances. At each time instance, the number of photons emitted by any fluorescent molecule is independent of the other molecules and follows a statistical distribution [26]. Therefore, the underlying problem is an inverse source problem like as in MUSIC. Nonetheless, adapting MUSIC to MUSICAL for optical nanoscopy is a non-trivial task and only a short intuitive understanding shall be given here without resorting to the detailed mathematical formulation.

Consider a small window around a given pixel of the size of the point spread function (PSF) of the microscope as the region of influence for the fluorescent emitters within the region of that pixel. Despite the main region of interest being within the pixel, the structure on which fluorophores are attached may extend beyond it. Therefore, it is important that the MUSIC indicator function is computed over the entire window. This is applicable to a first approximation. Nevertheless, as PSFs has not hard boundary, the PSF of fluorophores never lie completely

within the window but will stretch outside. Similarly, the window may contain data from the trailing part of the PSFs of fluorophores completely outside the window. This non-reliability is suppressed in MUSICAL by using a soft window function on the measurement in the window as well as the PSF of candidate locations of emitters (i.e. the test points). This is equivalent to weighing the indicator function at a test point on the basis of distance from the center pixel of the window. Moreover, for stitching the reconstructions of all the windows, instead of using conventional image-processing techniques, MUSICAL takes a physics-based route in which an additional distance metric d_s in the numerator is the indicator function.

$$f(r_{\text{test}}) = \frac{d_s(r_{\text{test}})}{d_n(r_{\text{test}})} \quad (2)$$

The distance function d_s is the projection of the expected output vector for a candidate target point on the eigenvectors with non-zero eigenvalues. Introducing this distance is equivalent to stitching the reconstructed images based on the energy contributed by the test point in the numerical space of measurements.

In essence, MUSICAL identifies spatio-temporal patterns present in the image sequence through patch-wise singular value decomposition. A manually selected threshold then partitions the spatio-temporal patterns (i.e. eigenvectors) into two sets, 'signal' set Q_s that contains those eigenvectors whose corresponding singular value is larger than the threshold and 'noise' set Q_n containing the remaining eigenvectors. This is illustrated in Fig. 1). The final MUSICAL values are then computed as the ratio between sub-sampled image patches projected onto signal and noise vectors. A detailed derivation can be found in Appendix A and in the original MUSICAL publication [21].

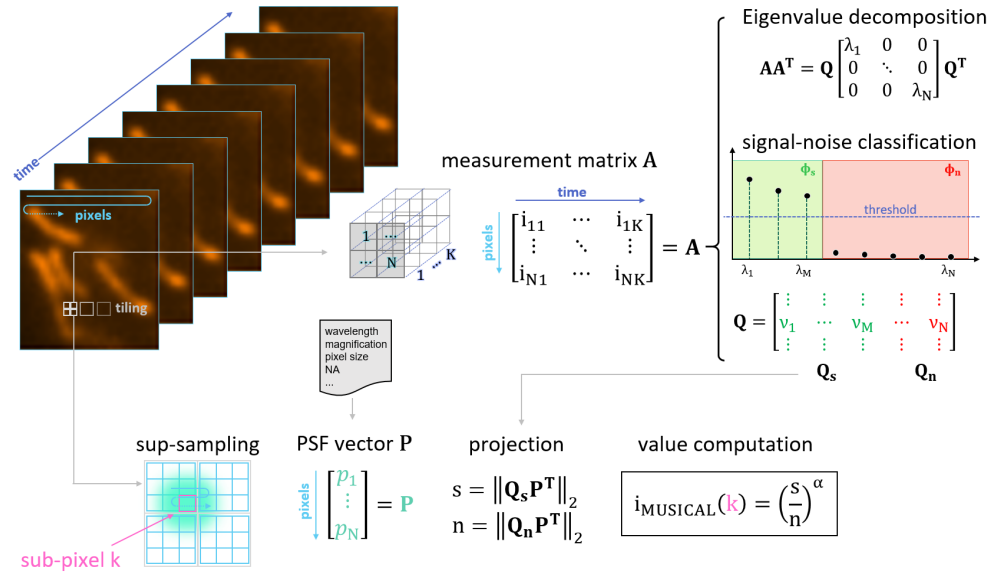


Fig. 1. Summary of the multiple signal classification algorithm (MUSICAL) [21].

MUSICAL was initially implemented in MATLAB with a focus on code-readability with respect to the mathematical background of the technique, rather than computational efficiency. Also, the MATLAB version provided only a rudimentary user interface with no extended capabilities for video generation or multi-color imaging. Hence, for a successful translation into

a handy tool, we have developed MusiJ, a plugin for Fiji that improves both on the front end and back end of the original MATLAB implementation in several ways.

2. MusiJ: MUSICAL for ImageJ

2.1. Back end

MusiJ has three main differences compared to the previously released MATLAB version in terms of back end implementation of the algorithm. The most basic change is the data type. MATLAB uses by default double-precision floating-point format, defined by the IEEE Standard 754 [27] (named as *binary64* from 2008) which means that every value requires 64 bits of memory. In contrast, our implementation works with the single-precision floating-point or *binary32* format which halves the memory usage and speeds up individual computation steps. Although, in principle, this comes at the cost of numerical precision, we found no noticeable difference in image quality between the outputs generated by the two data types in practice. The second change is in the computation of MUSICAL image values i_{MUSICAL} (also called the indicator function) during image synthesis (see Fig. 1). In order to compute the values \mathbf{s} and \mathbf{n} for the indicator function i_{MUSICAL} , we perform eigenvalue decomposition to obtain \mathbf{Q} . The columns of \mathbf{Q} correspond to a basis with orthonormal columns. Thanks to the Pythagorean theorem, it is therefore sufficient to compute only one of them since the vector \mathbf{P} is projected into the subspace spanned by \mathbf{Q}_s and its orthogonal complement \mathbf{Q}_n . Hence, the following holds:

$$\|\mathbf{P}\|^2 = \|\mathbf{Q}_s \mathbf{P}^T\|^2 + \|\mathbf{Q}_n \mathbf{P}^T\|^2. \quad (3)$$

In practice, the cardinality of \mathbf{Q}_s is significantly smaller than that of \mathbf{Q}_n . Moreover, the PSF vector \mathbf{P} is purely defined by optical system parameters. Therefore, we redefine the indicator function in its equivalent form given in Eq. (4). This permits a reduction in the number of operations by computing the norm of \mathbf{P} in advance.

$$i_{\text{MUSICAL}} = \left(\frac{\mathbf{s}^2}{\|\mathbf{P}\|^2 - \mathbf{s}^2} \right)^{\frac{\alpha}{2}}. \quad (4)$$

The final improvement is via multi-threading. As the image contains many non-overlapping regions, it is possible to process them in different threads of execution simultaneously, before merging the results into a single final image. This improvement is available as an option to the user, and the user may specify the number of used threads based on their system configuration and the load that the system may be experiencing due to other applications executing concurrently.

2.2. Front end

Along with changes in the computational efficiency in MusiJ, the developed plugin offers a range of features to simplify the usage and adds to MUSICAL's capabilities. The most prominent feature is the graphical user interface, GUI, which is shown in Fig. 2.

It provides easy access to the plugin's two main functions: (1) singular value computation and (2) MUSICAL image computation. Note that eigenvalues are the squares of singular values and thus equivalent for the purpose of signal/noise thresholding. In accordance with the original MUSICAL publication the plugin hence displays singular values. Additionally, a quick-access button can be added to the Fiji toolbar, which is especially convenient for heavy use. In the main GUI window, all necessary parameters can be filled in for MUSICAL image computation. It is possible and recommended to change the values stored as default in the accompanying MusiJ macro when the same parameters are in regular use, for example for repeat-experiments on the same microscope. This is to save time and to avoid typographical errors. The required thresholds to separate 'signal' from 'noise' (one per color channel) is estimated through visual inspection of

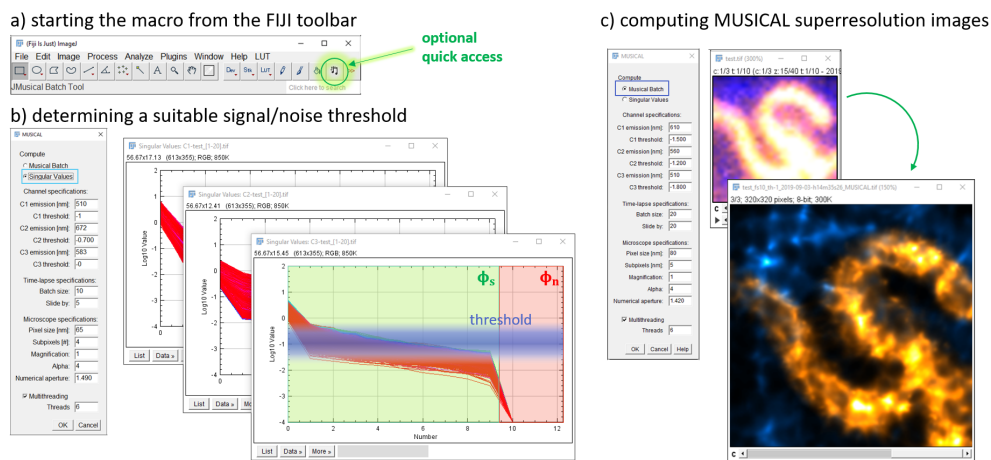


Fig. 2. The graphical user interface of MusiJ. (a) The plugin can be found in the regular 'Plugins' tab or directly launched via the optional quick-access button. (b) Using the raw data and microscope parameters as input, singular values can be computed that allow the user to find suitable thresholds for signal/noise classification. The blue region in the image above shows a region in which a suitable threshold is likely to lie. Note that each color channel has its own threshold. (c) With the determined thresholds, a nanoscopy image or a time-series can be computed from the raw data temporal stack. Here, mitochondria (orange) and microtubules (blue) are shown.

the singular value plots and normally computed before the MUSICAL image generation. At the top of the GUI, the user may select among two options ('Singular Values' or 'Musical Batch'). The first option allows visual inspection and selection of the threshold value to separate signal and noise. The other option allows batch processing of the entire data set for the pre-selected and specified threshold value. Under 'Time-lapse specifications', parameters for video generation can be set. For instance, if only a single image is to be reconstructed from the first 100 images of a much longer time sequence (e.g. to optimize thresholds quickly), use 'Batch size' 100, and 'Slide by' a number larger than the remaining number of frames in the image stack subjected to analysis. To reconstruct super-resolved details and visualize the changes over time, use 'Slide by' equal to or smaller than the batch size. We call this feature *interleaved reconstruction*, and it allows for a time-resolution smaller than dictated by the total acquisition time of all frames used for image reconstruction. The maximum interleave of an image stack (at a significant increase in computation time) is achieved by using 'Slide by' 1. We do not recommend this as a starting point for MUSICAL video analysis. The 'Multithreading' option allows to choose how much of the computers resources to be made accessible for MUSICAL image computation. For fastest multi-thread reconstructions use 'Threads' equal to the number of CPU cores. In practice, if running MusiJ on an office computer, we recommend to not use all cores but spare some processing power for other applications to continue executing in the background. When all parameters are set, clicking on the 'OK' button generates a super-resolved MUSICAL image or time-lapse batch and saves it along with a log file of all parameters.

3. Results and Discussion

A summary of the improvements upon the MATLAB version and new capabilities only available in MusiJ is provided in Table 1.

We tested both MATLAB and ImageJ implementations on a desktop computer running

Table 1. Comparison of MUSICAL implementations for MATLAB and MusiJ.

	MATLAB	MusiJ
processing time	417.25 s	14.75 s
graphical user interface	(✓)	✓
multi-color capability	✗	✓
video capability	✗	✓
interleaved reconstruction	✗	✓

Windows 10, with an Intel Xeon Gold 5118 processor (12 physical cores) and 128 GB DDR4 RAM. The MATLAB version was obtained from the official MUSICAL website (<https://sites.google.com/site/uthkrishth/musical>) and executed using MATLAB version R2018b. MusiJ was tested using FIJI 2.0.0-rc-69 with ImageJ 1.52b. For algebraic operations, MusiJ relies on Nd4j version 1.0.0-beta2 using CPU as back end, with MKL 2019.1 installed. In addition, we set the number of threads used by this library to 1 by setting the *Environment Variable OMP_NUM_THREADS* in our system. To test the speed of both implementations, we used a 256×256 pixel image stack with 50 frames and set the subpixel parameter to 10. For MusiJ we used an increasing number of threads from 1 to 8. The results are shown in the plot of Fig. 3 and a visual comparison of the generated MusiJ reconstruction to the MATLAB reconstruction is provided in Supplementary Figure S3.

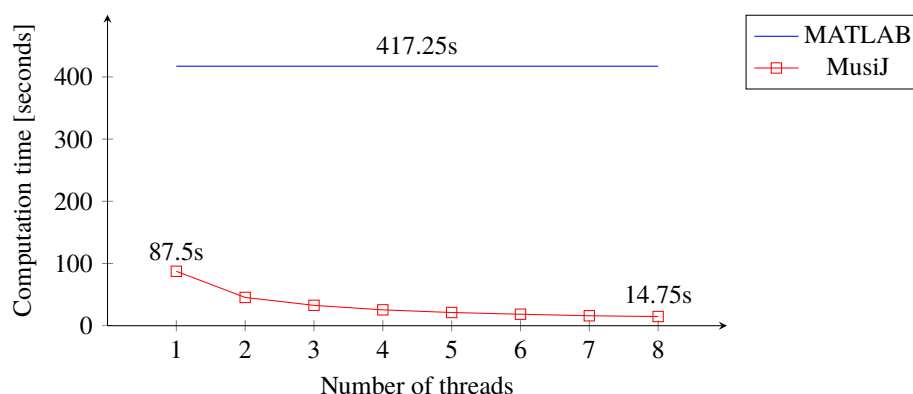


Fig. 3. Time used for a single reconstruction of an image of size 256×256 pixels, 50 frames, and subpixelation of 10. The results for MATLAB were replicated to make this comparison.

Due to the increased speed of the reconstruction process, a multitude of MUSICAL frames can be computed from a long time-series with overlapping raw-frames, termed as interleaved reconstruction. This is beneficial to enhance time-resolution when the imaged objects are changing their morphology or moving fast compared to the capture time of the entire raw frame series to determine the onset of events. The exact number of raw frames used for each MUSICAL time-point has to be adapted individually to the system dynamics. As can be seen in Fig. 4, interleaved reconstruction presents a trade-off between time and spatial resolution. Fig. 4 illustrates the principle of interleaved reconstruction on exemplary time-lapse image data of mitochondria.

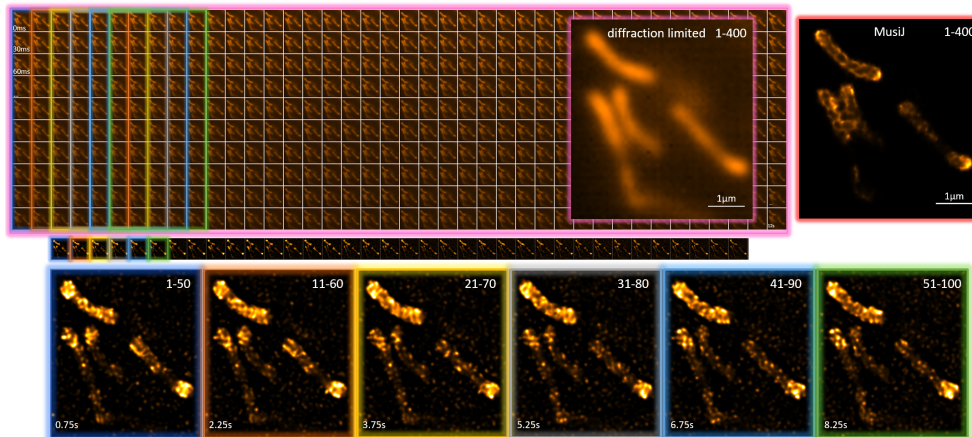


Fig. 4. Using MusiJ's interleaved reconstruction feature, dynamics of sub-cellular organelles like mitochondria can be visualised with super-resolution. In this example, a total of 400 time frames (30ms raw frame exposure time) were reconstructed into the MUSICAL image in the rightmost panel, while batches of 50 images with a 10 frame 'Slide-by' were converted into the time series displayed underneath. In the bottom six panels, zooms of the first few frames are shown. Labelled is the inner membrane of mitochondria in a cardiomyoblast cell line using dsRed. The imaging set-up was a commercial OMX microscope in widefield mode with LED illumination. A 60× 1.42NA oil immersion objective was equipped.

Many sources of signal fluctuations arise in living cells in addition to the intrinsic photokinetic fluctuations of fluorescent molecules that MUSICAL relies on. This is a challenge for threshold selection and when interpreting the results. Objects moving in and out of the imaged focal plane, or any other motion of the fluorescent emitters at nanometer scales, create signal fluctuations that are picked up by the algorithm. These different sources of signal fluctuations can be a potential source of misinterpretation. Trying different thresholds and cross-checking the reconstruction results with the system dynamics visible in the raw data is thus helpful and necessary to reach interpretations consistent with both raw data and MUSICAL reconstruction. On our data, a suitable threshold for most samples was found to be in the mid-range of the 2nd singular values (around the first *elbow* visible in the singular value plot of Fig. 2). For data with strong signal and low background fluctuations, the threshold can be set even lower to include more information in the computation for enhanced resolution. Figures S1 and S2 contain a visual comparison of images generated with different thresholds.

4. Conclusion

We have presented a user-friendly implementation of the fluctuation-based super-resolution algorithm MUSICAL for ImageJ/Fiji with a significant speed-up by a factor of almost 30 compared to the previous MATLAB version. The plugin can be kept up-to-date automatically via Fiji's update site. A step-by-step tutorial for installation and usage can be found at github.com/sebsacuna/MusiJ. Fluctuation-based video nanoscopy is an advancing field, but requires further experimentation and computational speed-up for increased understanding and usability of these techniques. Hence, this plugin was created with the objective of advancing the availability and usability of computational live-cell friendly super-resolution methods.

5. Acknowledgements

FS acknowledges funding from a Horizon 2020 Marie Skłodowska-Curie Action (836355). KA acknowledges funding from a Horizon 2020 Marie Skłodowska-Curie Action (SEP-210382872) and a Horizon 2020 ERC Starting Grant (804233). SA also acknowledges funding from the Horizon 2020 Marie Skłodowska-Curie Action (SEP-210382872). BSA acknowledges funding from a FP7 ERC Starting Grant (336716) and RCN BioTek2021 (285571). The authors thank Åsa Birgisdóttir for kind provision of cultured cells.

6. Author contributions

KA conceived the project. SA developed the eigenvalue-based version of MUSICAL images and implemented the back end of the ImageJ plugin. ISO prepared samples for microscopy, acquired data for MUSICAL and tested the plugin on a broad range of multi-color live-cell data for different reconstruction parameters. ISO provided feedback on necessary functionalities of the plugin and ease of use. FS and ISO designed the front end of the plugin. FS wrote the front end wrapper macro. FS, SA, ISO, and KA wrote the manuscript. BSA provided guidance and research tools. All authors commented on the manuscript.

7. Disclosures

The computational enhancements in the back end are a part of the invention disclosure 2019/3595 claimed by UiT The Arctic University of Norway. This part of the invention disclosure is not intended for commercialization and does not conflict with the commercialization of the remaining part. The authors declare that there are no conflicts of interest related to this article.

References

1. L. Schermelleh, A. Ferrand, T. Huser, C. Eggeling, M. Sauer, O. Biehlmaier, and G. P. Drummen, "Super-resolution microscopy demystified," *Nat. cell biology* **21**, 72–84 (2019).
2. S. W. Hell and J. Wichmann, "Breaking the diffraction resolution limit by stimulated emission: stimulated-emission-depletion fluorescence microscopy," *Opt. letters* **19**, 780–782 (1994).
3. A. G. York, P. Chandris, D. Dalle Nogare, J. Head, P. Wawrzusin, R. S. Fischer, A. Chitnis, and H. Shroff, "Instant super-resolution imaging in live cells and embryos via analog image processing," *Nat. methods* **10**, 1122 (2013).
4. M. G. Gustafsson, "Surpassing the lateral resolution limit by a factor of two using structured illumination microscopy," *J. microscopy* **198**, 82–87 (2000).
5. E. Mudry, K. Belkebir, J. Girard, J. Savatier, E. Le Moal, C. Nicoletti, M. Allain, and A. Sentenac, "Structured illumination microscopy using unknown speckle patterns," *Nat. Photonics* **6**, 312 (2012).
6. M. J. Rust, M. Bates, and X. Zhuang, "Sub-diffraction-limit imaging by stochastic optical reconstruction microscopy (storm)," *Nat. methods* **3**, 793 (2006).
7. T. Dertinger, R. Colyer, G. Iyer, S. Weiss, and J. Enderlein, "Fast, background-free, 3d super-resolution optical fluctuation imaging (sofi)," *Proc. Natl. Acad. Sci.* **106**, 22287–22292 (2009).
8. M. Müller, V. Mönkemöller, S. Hennig, W. Hübner, and T. Huser, "Open-source image reconstruction of super-resolution structured illumination microscopy data in imagej," *Nat. communications* **7**, 10980 (2016).
9. C. A. Schneider, W. S. Rasband, and K. W. Eliceiri, "Nih image to imagej: 25 years of image analysis," *Nat. methods* **9**, 671 (2012).
10. J. Schindelin, I. Arganda-Carreras, E. Frise, V. Kaynig, M. Longair, T. Pietzsch, S. Preibisch, C. Rueden, S. Saalfeld, B. Schmid *et al.*, "Fiji: an open-source platform for biological-image analysis," *Nat. methods* **9**, 676 (2012).
11. D. Sage, H. Kirshner, T. Pengo, N. Stuurman, J. Min, S. Manley, and M. Unser, "Quantitative evaluation of software packages for single-molecule localization microscopy," *Nat. methods* **12**, 717 (2015).
12. D. Sage, T.-A. Pham, H. Babcock, T. Lukes, T. Pengo, J. Chao, R. Velmurugan, A. Herbert, A. Agrawal, S. Colabrese *et al.*, "Super-resolution fight club: assessment of 2d and 3d single-molecule localization microscopy software," *Nat. methods* **16**, 387–395 (2019).
13. S. van de Linde, "Single-molecule localization microscopy analysis with imagej," *J. Phys. D: Appl. Phys.* **52**, 203002 (2019).
14. C. J. Rowlands, F. Ströhl, P. P. V. Ramirez, K. M. Scherer, and C. F. Kaminski, "Flat-field super-resolution localization microscopy with a low-cost refractive beam-shaping element," *Sci. reports* **8**, 5630 (2018).
15. H. Deschout, F. C. Zanacchi, M. Młodzianowski, A. Diaspro, J. Bewersdorf, S. T. Hess, and K. Braeckmans, "Precisely and accurately localizing single emitters in fluorescence microscopy," *Nat. methods* **11**, 253 (2014).

16. C. Franke, M. Sauer, and S. van de Linde, "Photometry unlocks 3d information from 2d localization microscopy data," *Nat. methods* **14**, 41 (2017).
17. T. Dertinger, R. Colyer, R. Vogel, M. Heilemann, M. Sauer, J. Enderlein, and S. Weiss, "Superresolution optical fluctuation imaging (sofi)," in *Nano-Biotechnology for Biomedical and Diagnostic Research*, (Springer, 2012), pp. 17–21.
18. S. Cox, E. Rosten, J. Monypenny, T. Jovanovic-Talisman, D. T. Burnette, J. Lippincott-Schwartz, G. E. Jones, and R. Heintzmann, "Bayesian localization microscopy reveals nanoscale podosome dynamics," *Nat. methods* **9**, 195 (2012).
19. I. Yahiatene, S. Hennig, M. Müller, and T. Huser, "Entropy-based super-resolution imaging (esi): From disorder to fine detail," *Acs Photonics* **2**, 1049–1056 (2015).
20. N. Gustafsson, S. Culley, G. Ashdown, D. M. Owen, P. M. Pereira, and R. Henriques, "Fast live-cell conventional fluorophore nanoscopy with imagej through super-resolution radial fluctuations," *Nat. communications* **7**, 12471 (2016).
21. K. Agarwal and R. Macháň, "Multiple signal classification algorithm for super-resolution fluorescence microscopy," *Nat. communications* **7**, 13752 (2016).
22. R. Schmidt, "Multiple emitter location and signal parameter estimation," *IEEE transactions on antennas propagation* **34**, 276–280 (1986).
23. A. M. Elbir, "Deepmusic: Multiple signal classification via deep learning," arXiv pp. arXiv–1912 (2019).
24. K. Agarwal and X. Chen, "Applicability of music-type imaging in two-dimensional electromagnetic inverse problems," *IEEE Transactions on Antennas Propag.* **56**, 3217–3223 (2008).
25. K. Agarwal, L. Pan, Y. K. Leong, M. Han, O. Y. Chan, X. Chen, and S. P. Yeo, "Practical applications of multiple signal classification," *Int. J. RF Microw. Comput. Eng.* **22**, 359–369 (2012).
26. G. T. Dempsey, J. C. Vaughan, K. H. Chen, M. Bates, and X. Zhuang, "Evaluation of fluorophores for optimal performance in localization-based super-resolution imaging," *Nat. methods* **8**, 1027 (2011).
27. D. Zuras, M. Cowlishaw, A. Aiken, M. Applegate, D. Bailey, S. Bass, D. Bhandarkar, M. Bhat, D. Bindel, S. Boldo *et al.*, "IEEE standard for floating-point arithmetic," *IEEE Std* **754**, 1–70 (2008).
28. S. Acuña and I. Opstad, "MusIJ: example of results," <https://www.doi.org/10.6084/m9.figshare.12006615.v3> (2020). Accessed: 2020-03-20.

Appendix A: Mathematical background of MUSICAL

MUSICAL is an algorithm that allows to obtain super-resolution from a short (<100) sequence of frames. Here, a brief mathematical background is presented.

For a sensor with M pixels and a sample composed of N emitters, and under the assumption that emitters' locations do not change with time, the imaging model can be approximated as the matrix-vector multiplication shown in Eq. (5). This model is generalizable to moving emitters by making a hypothetical list of emitters, which take unique positions along the motion trajectory of the emitter. One hypothetical emitter is then modeled as having zero emissions at all other times except at the time when the real emitter is at the location of the hypothetical emitter.

$$\bar{I}(t) = \begin{bmatrix} G(\vec{r}_{em}^{(1)}, \vec{r}_{im}^{(1)}) & \dots & G(\vec{r}_{em}^{(N)}, \vec{r}_{im}^{(1)}) \\ \vdots & \ddots & \vdots \\ G(\vec{r}_{em}^{(1)}, \vec{r}_{im}^{(M)}) & \dots & G(\vec{r}_{em}^{(N)}, \vec{r}_{im}^{(M)}) \end{bmatrix} \begin{bmatrix} e_1(t) \\ \vdots \\ e_N(t) \end{bmatrix} \quad (5)$$

This model defines the acquired image in time $\bar{I}(t)$ as a column vector where each element correspond to the intensity value for every pixel. The matrix that contains the values obtained from the mapping function $G(\vec{r}_{em}, \vec{r}_{im})$ will be referred to as (G) . The function $G(\vec{r}_{em}, \vec{r}_{im})$ maps the intensity produced by an emitter located at \vec{r}_{em} to the pixel located in \vec{r}_{im} using the known point spread function (PSF) of the system. Finally, $e_i(t)$ corresponds to the brightness of emitter i during time t . Note that each image is obtained then as a linear combination of the columns of \mathbf{G} which is not time dependent.

Let's consider now a sequence of K image vectors to form the matrix \mathbf{I} and corresponding Singular Value Decomposition (SVD) shown in Eq. (6). This allow us to generate an orthonormal basis for M - dimensional space of real numbers \mathfrak{R}^M given by the columns of \mathbf{U} .

$$\mathbf{I} = \mathbf{U}\mathbf{S}\mathbf{V}^T \quad (6)$$

Eq (5) and Eq (6) are two fundamental relations used by MUSICAL. The simplest case is when the number of emitters is less than the number of pixels ($N < M$), and assuming $M < K$. In this case, \mathbf{G} has N columns, meaning that its rank can be at most N . These columns span a subspace of \mathfrak{R}^M , and this is what we will call the signal space, corresponding to all the images that a set of N emitters can produce. Another implication is that the rank of \mathbf{I} is equal to the rank of \mathbf{G} , which means that there must be N non-zero singular values. The vectors associated to these singular values then, must span the same subspace as \mathbf{G} . Alternatively, the subspace associated to the vectors with singular value zero, referred to as the null space, is orthogonal to the signal space. In this scenario, we can test if a point \vec{r}_s belongs to the set of emitters by evaluating the expression shown in Eq. (7).

$$\bar{G}(\vec{r}_s) \cdot \bar{u}_{\sigma=0} = \begin{cases} 0 & \text{if an emitter is present at } \vec{r}_s \\ \text{non-zero} & \text{if no emitter is present at } \vec{r}_s \end{cases} \quad (7)$$

In reality, noise coming from undesired emission in the sample, shot-noise, and electronics is present in the images. Due to these factors, the singular values are unlikely to be zero. In order to split the space into signal and null space, a threshold σ_0 is given by the user. The final function used by MUSICAL is given by Eq. (8).

$$f(\vec{r}_{test}) = \left(\frac{\sqrt{\sum_{\sigma < \sigma_0} \|G(\vec{r}_{test}) \cdot \bar{u}_i\|^2}}{\sqrt{\sum_{\sigma \geq \sigma_0} \|G(\vec{r}_{test}) \cdot \bar{u}_i\|^2}} \right)^\alpha \quad (8)$$

Appendix B: Effect of hyper-parameters

MusiJ works over a stack of images, following a workflow similar to SRRF. Fig 5 presents a series of reconstructed images from the same source file comparing MUSICAL and SRRF. The sample used as example was cardiomyoblast cells with labelled mitochondria and is available in [28]. Since the sample presented significant motion only 50 frames were used for reconstructions. The parameters relevant for a MUSICAL reconstruction were as follows:

- Emission wavelength of the fluorophore: 525 nm
- Numerical aperture: 1.42
- Magnification: 1× (as pixel size was scaled directly)
- Pixel size: 80 nm
- Exposure time per frame: 30 ms
- Number of raw image frames: 50

The parameter for alpha was set to 4, and the subpixelation to 10. In the case of SRRF the method picked was TRAC with all parameters set to default. Fig. 5 address the importance of the threshold in the quality of the reconstruction. Note that as the threshold increases the relation between background and foreground get diffused. The corresponding SRRF image shows as characteristic property that all features are presented as uniform lines. This discrepancy between fluctuation techniques is known and a current topic of research. Fig 6 shows the parameters used for MUSICAL reconstructions in Fig 5. This figure uses the plotting tool included in MusiJ.

Fig 7 presents a comparison between the previous MATLAB implementation and MusiJ. Note that, by default, MATLAB uses 64 bits as data type, but the final printed result is presented as a PNG image of 8bits. It is hence less than the resolution used internally. Another minor difference in the implementation is the size of the sliding window. In MATLAB, the window size (in pixels) is always matched to exactly an airy disk, while in MusiJ the minimum size is 7 pixels. Hence, whenever the computed size is less than 7, the sliding window adds additional content. Nevertheless, no significant difference can be seen between the implementations.

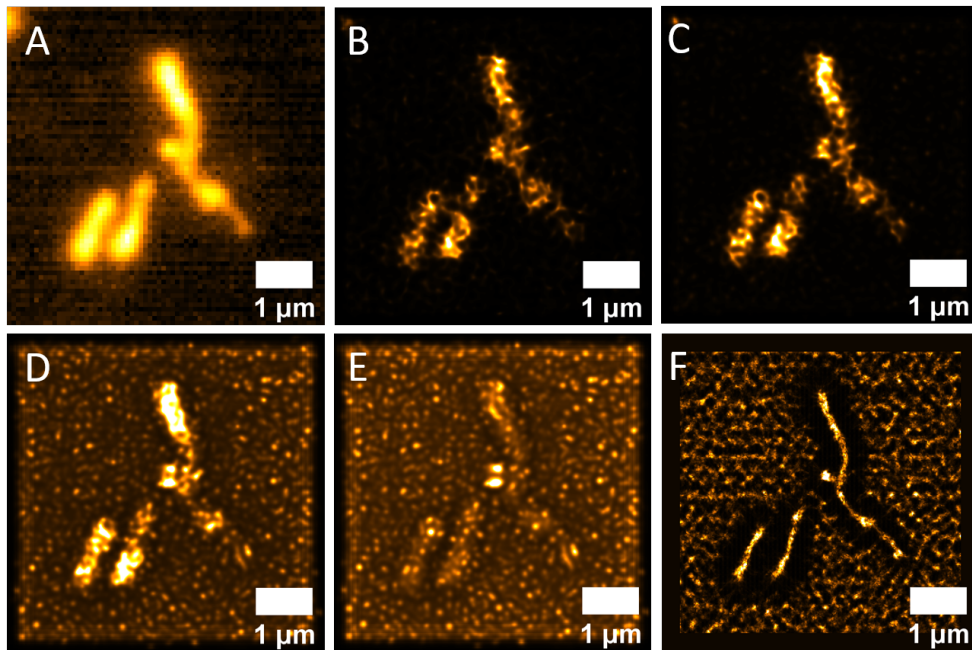


Fig. 5. A comparison between fluctuation images of the same raw data generated by MusiJ and SRRF. (A) average of 50 frames. (B-E) are MUSICAL reconstructions using MusiJ with thresholds -1.0, -0.75, -0.5 and -0.25. (F) correspond to a reconstruction made with SRRF.

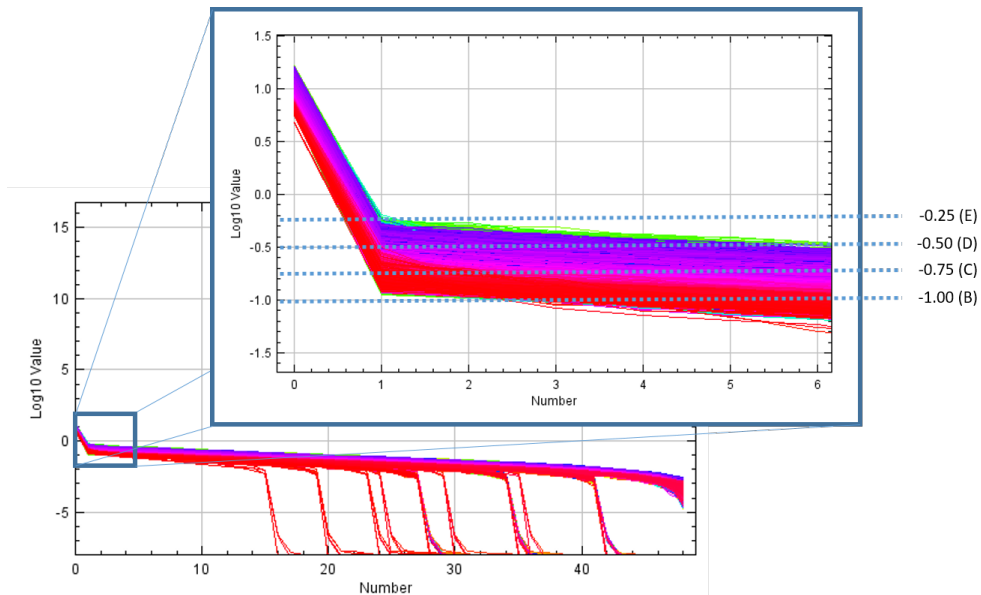


Fig. 6. The singular values for each sliding window in the cardiomyoblast sample shown in Fig 5. This was obtained using the tool included in MusiJ. The horizontal axis corresponds to the index of the singular value. The dashed lines correspond to the threshold used for every reconstruction.

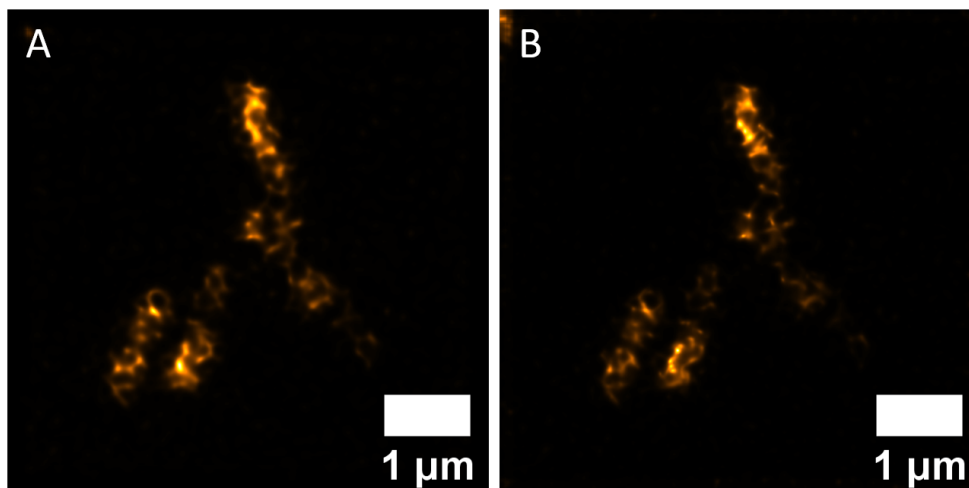


Fig. 7. A reconstructed nanoscopy image as produced by the previous (A) Matlab implementation and (B) MusiJ. A threshold of -1.0 was used in both versions of MUSICAL. The other parameters were the same as used in Fig. 5.



Learning nanoscale motion patterns of vesicles in living cells

Arif Ahmed Sekh, Ida Sundvor Opstad, Ása Birna Birgisdottir, Truls Myrnel, Balpreet Singh Ahluwalia, Krishna Agarwal, Dilip Prasad

Published in Conference on Computer Vision and Pattern Recognition (CVPR), April 2020.

Learning nanoscale motion patterns of vesicles in living cells

Arif Ahmed Sekh¹ Ida Sundvor Opstad¹ Åsa Birna Birgisdottir^{1,2} Truls Myrmmel^{1,2}
 Balpreet Singh Ahluwalia¹ Krishna Agarwal¹ Dilip K. Prasad^{1*}
¹UiT The Arctic University of Norway, Tromsø, Norway
² University Hospital of North Norway, Tromsø, Norway
 *dilip.prasad@uit.no

Abstract

Detecting and analyzing nanoscale motion patterns of vesicles, smaller than the microscope resolution (~ 250 nm), inside living biological cells is a challenging problem. State-of-the-art CV approaches based on detection, tracking, optical flow or deep learning perform poorly on this problem. We propose an integrative approach built upon physics-based simulations, nanoscopy algorithms and shallow residual attention network to permit for the first time analysis of sub-resolution motion patterns in vesicles, also of sub-resolution diameter. Our results show state-of-the-art performance, 89% validation accuracy on simulated dataset and 82% testing accuracy on an experimental dataset of images of living heart muscle cells grown under three different pathophysiologically relevant conditions. We demonstrate automated analysis of the motion states and changes in them for over 9000 vesicles. Such analysis will enable large scale biological studies of vesicle transport and interactions in living cells in the future.

1. Introduction

Microscopy images and videos are the only visual windows to the life in biological cells. The life events in a cell are orchestrated by a variety of organelles, such as nanoscale vesicles (30 nm to ~ 1 μ m). The vesicles perform their tasks by undergoing diverse motions in the scale of tens of nanometers to a few micrometers and interacting with other sub-cellular structures. The analysis of dynamic behaviour of vesicles may hold key to understanding and treating diverse neurological and immunological disorders [21, 27, 35]. However, learning about their motion patterns from microscopy videos of vesicles inside living cells is an imposing task, both visually and through computer vision (CV), for multiple reasons presented next:

- **Optical and digital resolutions** – The digital resolution (effective pixel size) of the most advanced live-cell compatible fluorescence microscopes are limited to ~ 100 nm and their optical resolution (smallest resolvable feature

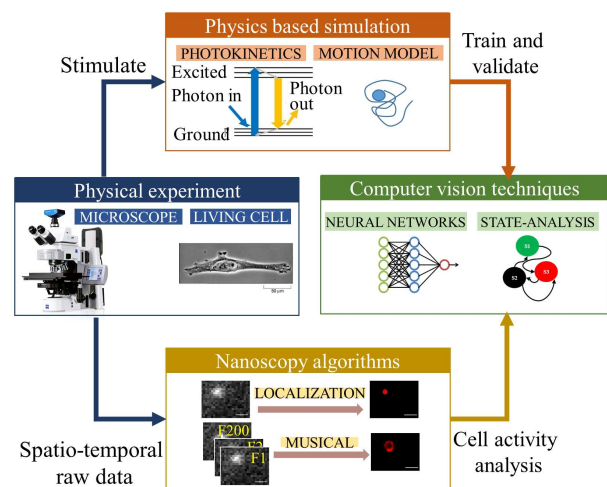


Figure 1. Our integrative approach of experiments, physics, nanoscopy, and computer vision allows analysis of nanoscale motion patterns of vesicles inside living cells.

size) is ~ 250 nm. As a consequence, the structures as well as the motion patterns of nanometer scale (< 250 nm) are not discernible by the microscopes, unless super-resolution microscopy (i.e. nanoscopy) approaches are employed.

- **Noise** – As compared to conventional imaging and videography, fluorescence microscopy deals with light of the order of a few photons per pixel. The shot noise and the dark noise of the camera often make the measurements significantly noisy. This has further negative effect on identification of motion patterns from microscopy videos.

- **Lack of data** – Live-cell experiments are not quite repeatable. Small variations in cell culture and imaging processes introduce differences in cell behaviour. Further, the age of the cells and the number of times of cell culture result in variations in the frequencies of normative life-events. Moreover, generating ground truth for such data is practically impossible. Therefore, generating large, controlled, statistically consistent, and suitably annotated

dataset for machine learning is quite challenging.

• **Number of vesicles and variety of motions** – A single living cell can easily contain a few hundred vesicles within the focal region of the microscope. Their diameters have a large range (30 nm to $\sim 1 \mu\text{m}$) and motion patterns have a large variety and complexity. Designing a method that caters to such diversity is challenging.

We present an integrative approach of physics-based nanoscopy-integrated artificial intelligence for learning motion patterns of vesicles in the biological system under consideration (see Fig. 1). Our approach addresses the aforementioned problems using four key propositions.

- The complex motion patterns of individual vesicles are broken down into piece-wise simple patterns. Small spatio-temporal regions of interest (ROIs), each potentially containing a simple motion pattern of a single vesicle are identified using a combination of localization nanoscopy and particle tracking.
- Vesicles' nanoscale motion patterns smaller than the microscope resolution are reconstructed using a motion-preserving live-cell compatible nanoscopy algorithm.
- Sufficiently large annotated dataset for CV is created synthetically for diverse simple motion patterns of vesicles with a wide range of diameters using a physics-based simulation approach which emulates physical motion, fluorescence photo-kinetics, optical properties of the microscope, as well as noise. This is significantly more advanced than the previous state-of-the-art simulated vesicles' dataset [8], as discussed in the supplementary.
- A shallow residual attention network is used for learning the relatively small information content (the type of motion pattern) from a large motion-encoded nanoscopy image (hundreds of thousands of pixels for every vesicle).

We show that our approach provides significantly better results than the state-of-the-art spatio-temporal CV approaches on true microscopy videos of vesicles in heart muscle cells (cardiomyoblasts). We demonstrate that the motion patterns can be analyzed and that meaningful analytics can be derived using our approach. This analysis and the corresponding datasets is the first such contribution to the family of CV for microscopy-related research problems.

2. Related work

We note two separate bodies of related work. The first one pertains to the microscopy community, which is increasingly adopting CV for a variety of tasks. The second one pertains to analogous problems in CV where motion patterns of individual entities are learnt. We discuss also how our approach bridges the gaps between them.

CV in microscopy: Advances in microscopes and computational hardware are expanding the possibilities for live-cell image analysis, which is of importance to research in biology. Deep neural networks [50, 55] are used for

tracking of cells or simulated particles. Detection based tracking [49] and feature tracking [36, 40] were successfully applied in cell migration analysis [26]. For vesicles larger than the microscope resolution, tracking and activity analysis of vesicles have been performed using single-particle tracking [8, 38, 45, 51]. Zhao et al. [58] proposed an analysis of large scale and collective motion of lysosomes (a type of vesicles) by tracking. Feature tracking works fine when particles move continuously and the signal-to-noise ratio (SNR) is high. Detection based tracking performs well when the object being tracked is a few times larger than the microscope resolution. Neither condition is satisfied in our problem. Recurrent neural networks have been used to classify spatio-temporal events [34]. Optical flow guided event detection has been applied in live-cell analysis [10]. These methods reflect promising results regarding temporal activity analysis from microscopy videos of live-cells. However, *they inherently assume that the structures and motion patterns are larger than the microscope resolution.*

Motion pattern analysis in computer vision: Video analysis for understanding crowd patterns [39], monitoring traffic [46], and event detection [18] are gaining popularity. They are equivalent to collective motion pattern analysis [58], single-particle tracking [38, 45], and interaction detection [51], respectively. Alexander et al. [3] introduced a computational sensor for 3D velocity measurement using a per-pixel linear constraint composed of spatial and temporal image derivatives. The challenges are however different when the sub-resolution nanoscale motion patterns in the presence of significant noise have to be investigated. Recently, micro-motion analysis [6, 13] has been proposed to extract small motion from videos that can not be observed with the naked eye. The method has been applied for extraction of micro expressions [24]. We found that these methods are sensitive to noise and therefore have limited applicability in our problem. Kim et al. [22] proposed a method for classifying human-car activity using simulated data for training. This is analogous to our approach of physics-based simulations for training. Baradel et al. [4] proposed a framework for causal learning of dynamics in mechanical systems from visual input. This is roughly analogous to our investigation of transition of vesicles from one simple motion state to another.

Gaps bridged by our work: The main challenge of identifying nanoscale motion patterns is solved by selecting a motion-preserving nanoscopy algorithm, namely multiple signal classification algorithm (MUSICAL) [1], for performing optical and digital super-resolution for live-cell imaging. Through this, we introduce live-cell compatible nanoscopy algorithms [1, 9, 12, 42] as valuable tools for CV at the nanometer scale. Although analysing nanoscopy images using neural networks may help in various biological experiments, the application of state-of-the-art deep learn-

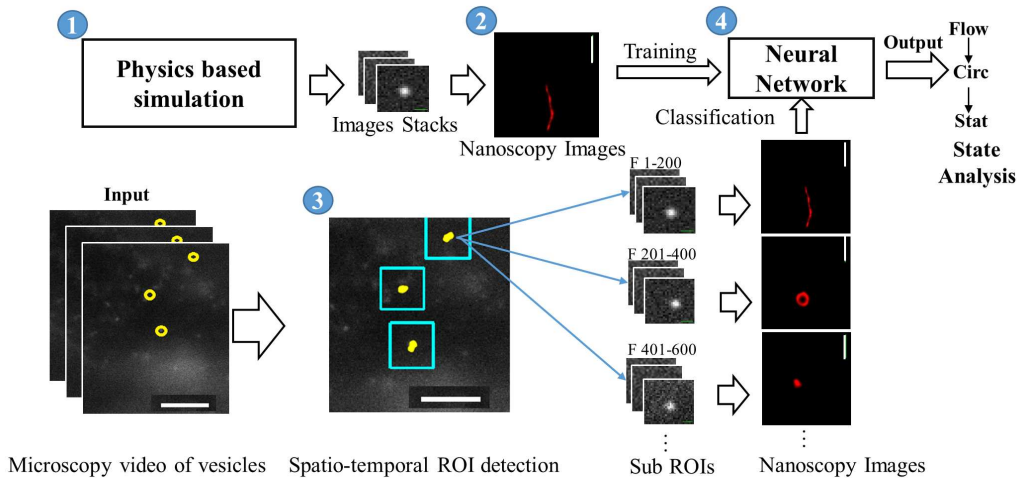


Figure 2. Overview of the proposed framework. Scale bars: 5 μm horizontal, 500 nm vertical. F indicates frame number hereon.

ing methods for nanoscopy image analysis is limited. This, we opine, is due to 1) limited availability of annotated large datasets, and 2) presence of fewer features in nanoscopy images compared to the real-world camera images. The first problem is solved in our case by employing a rigorous physics-based simulation framework which emulates both the dynamic organelles and the presence of noise in the experiments. All details of the physics-based simulations are included in the supplementary. For problems in biology where ground truth on experimental data is nearly impossible, such approaches will be indispensable for developing CV solutions. Such approach will also find value in other ground-truth deficient applications such as astronomy, geology and climate if suitable physics-based simulation frameworks of sufficient detail can be developed. The second problem is solved by using a shallow residual attention network. The features exploited in state-of-the-art deep models based CV, namely textures, edges, and colors, are missing in the microscopy data. Moreover, the dynamic range of intensity is quite small in microscopy images and the noise is comparable to the signal. The microscopy images contain only few features encoded mainly in intensity variations. Due to these reasons, we expect shallow networks to perform better than deep models. This introduces a valuable CV tool to the microscopy community, which currently depends heavily on visual inspection.

3. Method

The proposed methodology is shown in Fig. 2. It consists of four modules: (1) physics-based simulations for creating training dataset, (2) MUSICAL for nanoscale motion reconstruction, (3) spatio-temporal ROI detection using localization based tracking, and (4) classification of motion patterns. We discuss each module next.

3.1. Physics-based simulations

Our simulation flowchart is shown in Fig. 3(a). We first simulate a vesicle labeled with several fluorescent molecules. The diameters of the simulated vesicles is in the range [150, 400] nm. The fluorescent molecules are randomly placed inside the volume of the vesicle. The number of photons emitted by each molecule are simulated using the photokinetic model of [1]. Code provided by its authors used for this. It includes blinking, bleaching, and non-radiative energy dissipation of fluorescent molecules [9]. It has been reported that the vesicles may demonstrate random movement in a confined space [2], directed flow-like motion [7], circular motion [32], and sometimes they become stationary during interaction with other organelles [14]. Inspired by the biological evidence, we have simulated five types of vesicular motion patterns (also called motion states) in 2D, described below:

- **Circular Motion (Circ):** The vesicle moves along the periphery of a virtual circle with randomly selected center, radius, and velocity. The radius of the circle and the velocity of the vesicle are in the ranges [200, 500] nm and [0, 500] nm/frame, respectively.
- **Random walk inside a circle (RCir):** The vesicle takes random positions within a circular area. The radius of the circle is chosen randomly from the range [200, 400] nm.
- **Flow (Flow):** The vesicle moves along a path with a constant velocity. First, a random curve is generated. Next, the vesicle is transported along the curve with velocity selected randomly from the range [0, 1000] nm/frame.
- **Random walk (RanW):** During a random walk, the vesicle may move in any direction with equal probability. For each movement, the velocity is randomly selected from the range (0, 1000] nm/frame.
- **Stationary (Stat):** The vesicle remains stationary.

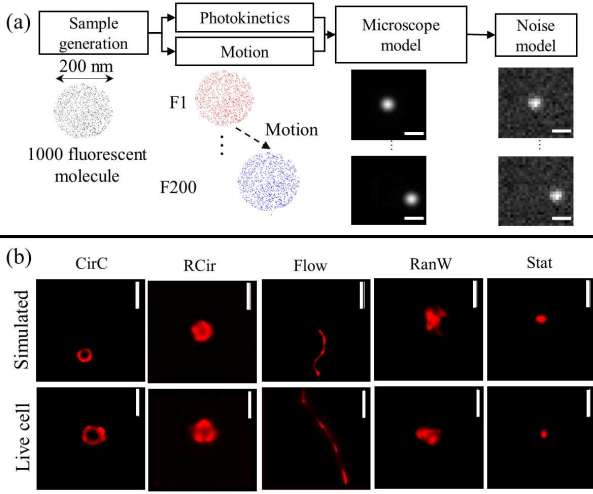


Figure 3. Physics-based simulation framework. (a) The flow chart and its illustration using an example of a vesicle of diameter 200 nm. (b) A visual comparison of a few randomly selected examples of the chosen motion patterns. Scale bar: 500 nm.

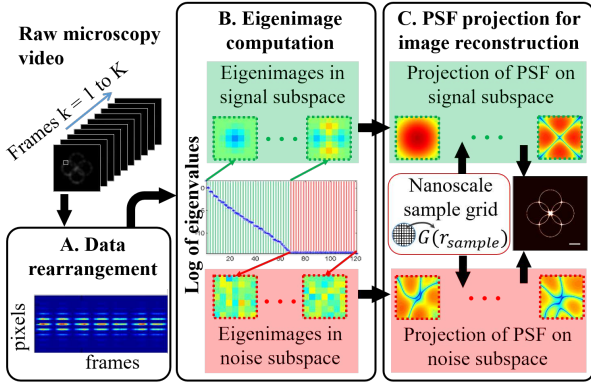


Figure 4. MUSICAL preserves spatio-temporal features in images using eigenimages (block B) and reconstructs the nanoscale patterns by projecting microscope’s PSF from a nanoscale sample grid onto the signal and noise subspaces (block C).

We note that our library of motion patterns is not exhaustive. It is expandable to include other patterns in the future. After forming the coordinate list of all the fluorescent molecules at all the time points, we compute the raw noise-free microscopy video by emulating the point spread function (PSF) [31] using the optical parameters relevant to the molecules, the microscope, and the imaging conditions. Then, the noise characteristics of the camera are incorporated [44]. All the details are included in the supplementary. We show an example of simulation below the block diagram presented in Fig. 3(a). We also illustrate examples of simulated motion patterns reconstructed using MUSICAL as compared to similar reconstructions from the experimental live-cell data in Fig. 3(b).

3.2. MUSICAL

The function of MUSICAL [1] is explained in two parts, namely eigenimages and identifying nanoscale patterns.

Spatio-temporal features in eigenimages: For small optical windows (size given by the span of the microscope PSF), MUSICAL computes eigenimages from the microscopy video. The eigenimages order the spatio-temporal information from the most consistent ones to most random ones. The first few eigenimages with largest eigenvalues correspond to vesicle motion patterns (spanning the signal subspace) and the remaining correspond to noise patterns (spanning the noise subspace), see Fig. 4.

Nanoscale pattern identification: Even if two points are separated by a distance below both the optical and the digital resolution, the PSFs at such points are slightly different from each other. Their projection onto the signal and noise subspaces are therefore different. Precisely, at a point in the sample space, the projection of the PSF onto every single eigenimage in the noise subspace is zero if two conditions are satisfied. First, the separation of signal and noise subspaces is robust. Second, a fluorescent molecule ever emitted fluorescence photons from that location during the video. The condition of zero projection on the noise subspace is violated at a point even slightly away from such a location. This property is mathematically enhanced in MUSICAL to reconstruct nanoscopy image with pronounced nanoscale features.

3.3. Spatio-temporal ROI detection

This step comprises of two tasks - detecting vesicles and linking the detections across frames (Fig. 5).

Detection of vesicles: Localization nanoscopy [41] can localize individual fluorescent molecules by fitting Gaussian functions in microscopy images. This is possible only if extreme spatio-temporal sparsity in fluorescence emissions is enforced, which is not possible while imaging living cells. Nonetheless, the nearly spherical geometry of vesicles implies that their image can also be roughly approximated as a Gaussian functions. Thus, we use localization nanoscopy in an unconventional setting for detecting vesicles in the microscopy videos. We have used quick-PALM [17] implementation for this purpose.

Linking the detections and creating sub ROIs: The detected vesicles are linked using Hungarian method and Kalman filter [5] to construct their trajectories. Let a given live-cell sequence contain n number of tracks as: $\{T_1, T_2, \dots, T_n\}$. Each track is defined by series of positions of the vesicle over time, i.e. $\{p_1, p_2, \dots, p_m\}$, where $p_i = (x_i, y_i)$. For each track, a set of sequential non-overlapping sub ROIs is created such that each sub ROI contains \bar{K} continuous positions of the particle. The key idea behind using sub ROIs is that each sub ROI is likely to contain one simple motion pattern, potentially among *Circ*, *RCir*, *Flow*,

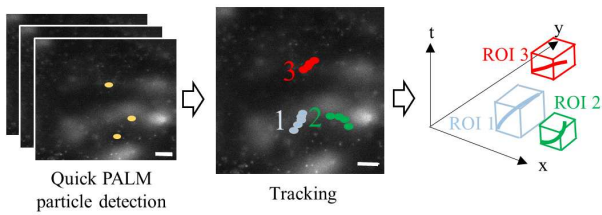


Figure 5. ROI detection using localization based tracking.

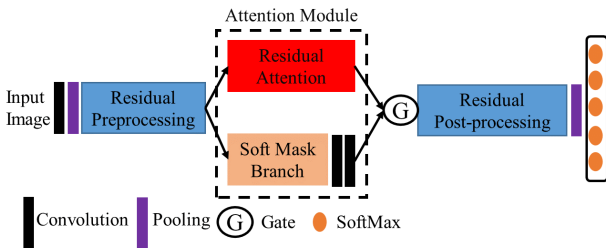


Figure 6. Architecture of the shallow residual attention network.

RanW, and *Stat*. The number \hat{K} can either be selected for the chosen biological cell type and image acquisition rate heuristically or more sophisticated automatic sub ROI selection may be designed, which is out of the scope of the current work. We have heuristically selected $\hat{K} = 200$.

3.4. Motion Classification

The choice of the depth of the network depends on the task, image features, and class variation. Several biological classification tasks have been solved using shallow networks [11, 15, 33] due to the unavailability of large microscopy and nanoscopy datasets as well as fewer features in live-cell images compared to the real-world RGB images. We have observed that the state-of-the-art deep neural networks such as deep CNN [23], VGG16 [56], Inception [52], and ResNet50 [16] performed poorly in our dataset (results in section 4). Furthermore, the use of pretrained models did not improve the classification accuracy significantly. We found that comparatively shallow networks such as a 3-layered MLP, shallow CNN [28], and ResNet20 perform better on our data. The observations inspired us to design a shallow network for motion pattern classification.

In the last few years, the use of residual connection among layers has proven its ability to improve accuracy in several computer vision tasks [16]. On the other hand, attention-based neural networks inspired by the human perception have become popular in various computer vision tasks. They employ attention mechanism [53] to identify and highlight useful features during learning. Recently, residual-attention mechanism [47] demonstrated state-of-the-art or comparable accuracy in certain computer vision tasks [20, 30, 57], and also serve as an inspiration for us.

Shallow Residual Attention Network: We combine the concept of residual and attention mechanisms with a shal-

low neural network to propose a Shallow Residual Attention Network (SRAN). The network architecture is presented in Fig. 6. It consists of a set of initial pre-processing layers including a residual pre-processing block, an attention module, and a gated residual post-processing block connected to the classification layer. The attention module further consists of a residual attention block (also called trunk branch) and a soft mask branch. The trunk branch has a down-sample and an up-sample unit, for top-down and bottom-up attention mechanisms [47] respectively. The soft mask branch is a form of residual block. The outputs of the trunk and soft mask branches are combined using a controlled gate similar to long short-term memory. The attention module suppresses the noise and highlights important information by applying dot product between the residual attention features and soft masks learnt in the trunk branch and the soft mask branch respectively. The details of SRAN are given in the supplementary.

4. Experimental results

4.1. Dataset

In order to evaluate the effectiveness of the proposed method, we use two datasets described below. We make both the datasets and supplementary public for research purposes at our project page¹.

Simulation dataset: This dataset is used for training and evaluation of the classifier. It contains 3000 data samples for each type of motion pattern. Each data sample is a small video of 200 frames corresponding to simulated microscopy images of 25×25 pixels of a single vesicle exhibiting a single motion pattern. The optical and camera parameters used for the simulation were based on the experimental setup used for creating live-cell dataset. The simulated noise was chosen such that the signal to noise ratio was similar to the videos in the live-cell dataset.

Live-cell dataset: Cardiomyoblasts (heart muscle cells) were divided into 3 different pools and labelled using live-cell friendly fluorescent dye. The pools are: • **Normal:** These cells were kept under normal cell-culture conditions. • **Hypoxia:** These cells were subjected to hypoxia (deficiency of oxygen) for 1 hour. • **HypoxiaADM:** These cells were subjected to hypoxia like the cells above, but were simultaneously treated with the hormone adrenomedullin (ADM). This hormone is found to exhibit protective functions under pathological conditions like myocardial infarction (cardiac arrest).

For each pool, 10 videos of 2000 frames each and 1024×1024 pixels were imaged using GE DeltaVision Elite fluorescent microscope. Other experimental details are provided in the supplementary. We counted the number of vesicles in the cells that were imaged in each pool. These

¹<https://nonoscalemotion.github.io/>

Table 1. Multiple Object Tracking Accuracy [19] of different methods on live-cell dataset.

Condition	Feature Tracking [40]	Deep Tracking [49]	Proposed
Normal	0.48	0.69	0.91
Hypoxia	0.39	0.62	0.93
HypoxiaADM	0.41	0.68	0.87

Table 2. Classification accuracy of different neural networks using various input features. Format: Validation/Testing

Method	Raw Images	Micro Motion	Optical Flow
RNN [29]	0.29 / 0.26	0.26 / 0.24	0.32 / 0.21
BLSTM [25]	0.32 / 0.21	0.27 / 0.18	0.36 / 0.24
Con3D [54]	0.28 / 0.26	0.22 / 0.22	0.46 / 0.39

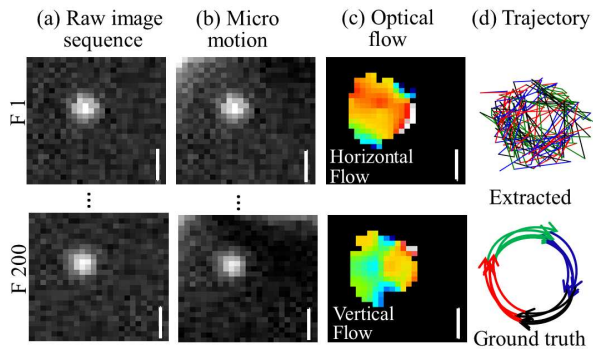


Figure 7. Feature representations of a vesicle in *Circ* state using different approaches for motion classification. In (d), each colour represents different direction quadrant. Scale bar: 500 nm.

numbers are 3283 vesicles for normal, 3186 vesicles for hypoxia, and 2980 vesicles for hypoxiaADM. Thus, we performed activity analysis of experimental data of a total of 9449 vesicles. The motion patterns of sub ROIs of each vesicle were manually annotated for generating ground truth by visual inspection of raw image sequences and nanoscopy images reconstructed using MUSICAL. Live-cell dataset refers to all the data, except in section 4.5 4.4 where pool-specific results are presented.

4.2. Vesicle Localization and Tracking

We experimented with feature tracking [40], deep learning based tracking [43], and the proposed localization based tracking. In deep learning based tracking, the neural network was trained with the simulated dataset and tested on live-cell dataset. We evaluated the tracking performance using multiple object tracking accuracy (MOTA) [19] metric with manually generated ground truth, see results in Table 1. Feature based tracking method failed to distinguish between features and noise, therefore failing to track. Deep learning based tracking methods also perform poor due to noise and tiny size of the vesicles.

4.3. Results of Motion Classification

We conducted different experiments using a variety of spatio-temporal features and learning methods. We tried using raw image sequences, micro-motion magnified sequences [13], optical flow, and the trajectories constructed in the proposed ROI detection approach as the input for classification. Fig. 7 depicts a visual comparison of the different features extracted for a vesicle in *Circ* state. It can be observed from Fig. 7 that the naked eye can not detect the *Circ* pattern from either the raw image sequence or the micro-motion magnified sequence (example in the supplementary videos). The micro-motion magnified sequence contains larger noise compared to the raw image sequence. Due to high noise levels in the raw data, optical flow spans a larger area, therefore failing to detect the nanoscale motion. Localization nanoscopy can detect the vesicle but can not extract the trajectory of nanoscale movement accurately. We experimented using LSTM (baseline) and a deep CNN [48] using the detected trajectories as input and found the accuracy of (validation/testing) as (0.38/0.29) and (0.40/0.35) for LSTM and deep CNN, respectively. For the other features, namely raw image sequence, micro-motion magnified sequence, and optical flow, we experimented using different baseline learning algorithms. For all the experiments, the simulation dataset is used for training and validation. Five-fold cross-validation is used. The live-cell dataset is used for testing. Parameters of all the baseline methods are set similar to the original implementations. We have included early stopping and data augmentation, and verified that no over-fitting exists (see the supplementary for training details, hyperparameters, and hyperparameter study). The classification accuracy is presented in Table 2. The results indicate that these features are not suitable for the classification of nanoscale movement.

Next, we performed experiments to classify the motion patterns using the nanoscopy images obtained using MUSICAL as inputs. SRAN is trained and tested with a similar weight initialization method and residual blocks reported in [47]. We used 2-stage attention block (compared to a 3 stage attention block reported in [47]); training details are in the supplementary. It took 35 epochs to stabilize the learning (see Fig. 8). In the case of the baseline methods, we keep most of the settings same as the original implementations. The results are summarized in Table 3. It is observed that most shallow networks perform better compared to deep networks and SRAN performs the best. Fig. 8 presents the comparative epoch vs accuracy and loss of a deep residual attention network [47] (DRAN) and SRAN. It is seen that SRAN stabilizes and converges quicker and to a lower loss than the deep counterpart.

Failure cases: Fig. 9 depicts the confusion matrix of SRAN for the live-cell dataset. Although the accuracy for each individual class is better than 70%, we make some in-

Table 3. Classification accuracy of different methods using nanoscopy images. Format: Validation/Testing

Method	Pre-training	Accuracy
Deep CNN [23]	Imagenet	0.32 / 0.29
Deep CNN [23]	-	0.36 / 0.31
VGG16 [56]	Imagenet	0.42 / 0.33
VGG16 [56]	-	0.33 / 0.33
Attention Model [53]	-	0.71 / 0.56
Shallow Network [28]	-	0.82/ 0.63
ResNet50 [16]	-	0.71/ 0.69
ResNet20 [16]	-	0.82/ 0.74
MLP (Bayesian Optimization) [37]	-	0.72/ 0.68
Inception V3 [52]	Imagenet	0.46 / 0.36
Inception V3 [52]	-	0.43 / 0.29
Deep residual attention [47]	-	0.85/ 0.78
Proposed SRAN	-	0.89/ 0.82

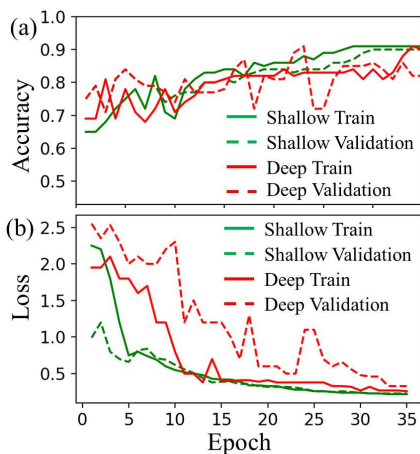


Figure 8. Accuracy & loss curves of DRAN and SRAN.

interesting observations. The miss-classifications are generally among the classes where randomness at nanoscale is involved and therefore random patterns of two kinds may have significant overlap. In other cases, artefacts due to noise in the nanoscale reconstruction may be easily confused with an equivalent nanoscale random motion pattern. In yet other cases, more than one vesicles present may be present in close vicinity, resulting in multiple motion reconstructions in a single ROI. Fig. 10 presents some failure cases related to the points mentioned above.

4.4. Analysis of Events

We analyzed the frequency of motion patterns and changes in motion patterns (i.e. events) in the live-cell dataset. Fig. 11(a) shows the statistics of motion states in normal, hypoxia, and hypoxiaADM pools. A clear demarcation is observed between them, except for the *Stat* motion state. Here, we see that vesicles in the case of hypoxia are least stationary. Potentially, adding ADM restores the occurrence of vesicles in this state towards normal pool.

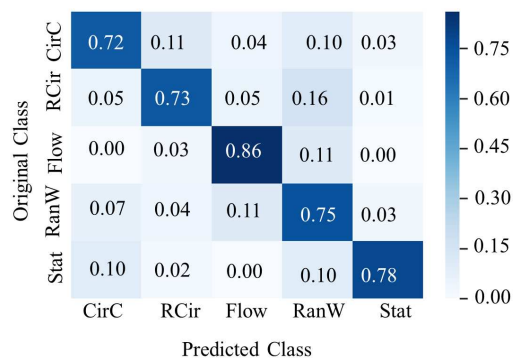


Figure 9. Confusion matrix on the live-cell dataset using SRAN.

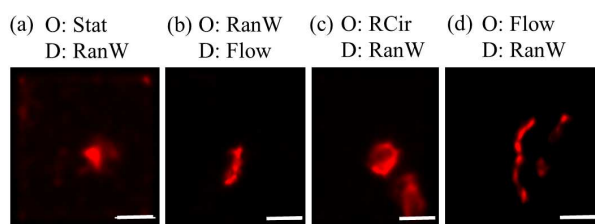


Figure 10. Example failure cases. D: detected, O: ground truth.

We also note that most vesicles in any pool are in the *RanW* state. Fig. 11(b) shows the statistics of changes in motion states in normal, hypoxia, and hypoxiaADM pools. It is of particular interest to note the squares with green background. They indicate that ADM may have resulted into change in the trend introduced by hypoxia. For example, as compared to normal pool, hypoxia pool demonstrated more number of transitions from *Circ* and *Flow* to *RanW* states. But, hypoxiaADM demonstrated reduced number of such transitions. Other similar behaviours may indicate some potential mechanisms of action of ADM. It is important to note that these results are not conclusive from biological perspective since these experiments were designed to provide an initial test dataset for the proposed framework. A rigorous biological study needs further biological and environmental controls, hypothesis-specific experiment design, and large scale experimentation.

We further show that our analysis may indicate nanoscale nature of interaction of two sub-cellular structures. For example, in Fig. 12, green colored low resolution structures are mitochondria. A vesicle flows towards it and interacts with it. This is visible in the microscopy video, included in the supplementary. However, the nanoscale detail of interaction is not known. The result of our framework, with 200 frames for each sub ROI, is presented in Fig. 12(a). The interaction is contained in sub ROI 2, which is classified as *RCir*. Then, we used the proposed framework with only 50 frames per sub ROI. This result, presented in Fig. 12(b), indicates that sub ROIs 5-8 contain the inter-

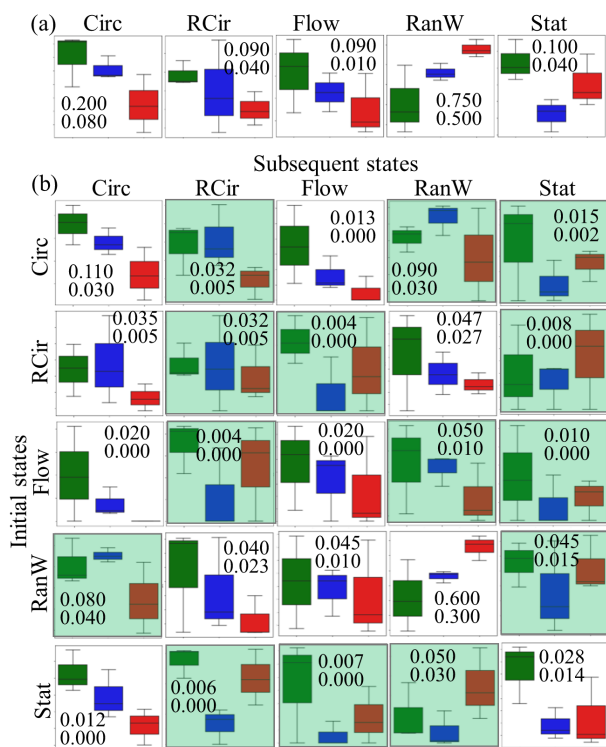


Figure 11. Analytics of motion patterns and changes in them. Legend for box plots: normal (green), hypoxia (blue), and hypoxiaADM (red). Numbers in each square indicate the maximum and minimum values for that square. (a) frequency of occurrence of motion patterns (ratio of sub ROIs in a particular motion state to the total number of sub ROIs in a pool). (b) ratio of number of consecutive-motion-state-pairs exhibiting a certain combination of initial and subsequent motion states to the total number of consecutive-motion-state-pairs. In (b), squares with green background indicate a trend reversal in hypoxiaADM as compared to trend of change between normal and hypoxia pools.

action. Among them, sub ROIs 5-7 are classified as *Stat* and generate nanoscopy spots at three different locations (see magenta, cyan, and blue spots below the white pattern) while the sub ROI 8 is classified as *Circ*. This indicates that the vesicle may have spent some time being stationary at different locations (hopping action) in close vicinity of mitochondrion, before performing a circular motion (spinning action) close to it. Such analysis will open possibilities of understanding detailed mechanisms of interactions.

5. Discussion and conclusion

We report a first framework and an important step towards studying motion and interaction of vesicles in living biological cells and cell systems with sub-resolution nanoscale details. Our approach indicates the utility of hybrid learning approaches which combine non-CV ap-

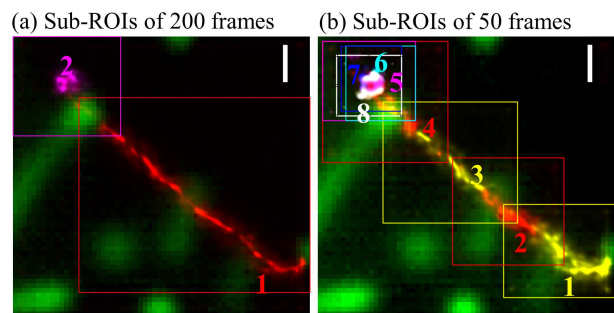


Figure 12. Example of interaction of a vesicle (nanoscopy images obtained using MUSICAL in colors other than green) with another sub-cellular structure namely mitochondrion (green microscopy image) and effect of choosing sub ROIs of different temporal sizes. In (a), sub ROIs 1 and 2 are classified as *Flow* and *RCir*, respectively. In (b), sub ROIs 1-4 are classified as *Flow*, sub ROIs 5-7 as *Stat*, and sub ROI 8 as *Circ*. Scale bars: 500 nm.

proaches with conventional CV approaches to perform challenging tasks with specific limitations due to the nature and physics of microscopy data. Our work also highlights that shallow learning networks may outperform deep learning networks for certain tasks where feature sparsity is an important characteristic of the data. We envision at least three future directions for the developed framework of analysis. First, the simulation framework can be extended to 3D to incorporate out of focus light and limited depth of focus of microscopes. Second, more variety of motion patterns can be incorporated in this framework or custom motion states may be learnt for different sub-cellular and inter-cellular structures. Third, the complete sequence of motion states can be formed to identify specific events of interest. The correlation of such events with activities of other sub-cellular structures can be used to identify and better understand biological interactions.

Our framework can accommodate different time scales (as demonstrated in Fig. 12) for extracting motion details of different levels. In this sense, the framework is easily adaptable to different imaging conditions. In the future, the applicability of this framework for sub-resolution analysis of microscopy images and videos from a wide variety of microscopes and biological problems will be explored.

Acknowledgement

The following funding is acknowledged: ERC starting grant 804233 (Agarwal), Research Council of Norway's Nano2021 grant 288565 (Ahluwalia), Northern Norway Regional Health Authority grant HNF1449-19 (Myrmel and Birgisdottiir), UiT's strategic funding program (Sekh), and UiT's Tematiske Satsinger grants (all authors). All data and codes are available at <https://nonoscalemotion.github.io/>.

References

- [1] K. Agarwal and R. Macháň. Multiple signal classification algorithm for super-resolution fluorescence microscopy. *Nature Communications*, 7:13752, 2016. 2, 3, 4
- [2] H. Al-Obaidi, B. Nasser, and A. T. Florence. Dynamics of microparticles inside lipid vesicles: movement in confined spaces. *Journal of Drug Targeting*, 18(10):821–830, 2010. 3
- [3] E. Alexander, Q. Guo, S. Koppal, S. Gortler, and T. Zickler. Focal flow: Measuring distance and velocity with defocus and differential motion. In *European Conference on Computer Vision*, pages 667–682, 2016. 2
- [4] F. Baradel, N. Neverova, J. Mille, G. Mori, and C. Wolf. Cophy: Counterfactual learning of physical dynamics. *arXiv preprint arXiv:1909.12000*, 2019. 2
- [5] A. Bewley, Z. Ge, L. Ott, F. Ramos, and B. Upcroft. Simple online and realtime tracking. In *IEEE International Conference on Image Processing*, pages 3464–3468, 2016. 4
- [6] S. Bharadwaj, T. I. Dhamecha, M. Vatsa, and R. Singh. Computationally efficient face spoofing detection with motion magnification. In *IEEE Conference on Computer Vision and Pattern Recognition Workshops*, pages 105–110, 2013. 2
- [7] B. Cabukusta and J. Neefjes. Mechanisms of lysosomal positioning and movement. *Traffic*, 19(10):761–769, 2018. 3
- [8] N. Chenouard, I. Smal, F. De Chaumont, M. Maška, I. F. Sbalzarini, Y. Gong, J. Cardinale, C. Carthel, S. Coraluppi, M. Winter, et al. Objective comparison of particle tracking methods. *Nature methods*, 11(3):281, 2014. 2
- [9] S. Cox, E. Rosten, J. Monypenny, T. Jovanovic-Talisan, D. T. Burnette, J. Lippincott-Schwartz, G. E. Jones, and R. Heintzmann. Bayesian localization microscopy reveals nanoscale podosome dynamics. *Nature Methods*, 9(2):195, 2012. 2, 3
- [10] A. Czirok, D. G. Isai, E. Kosa, S. Rajasingh, W. Kinsey, Z. Neufeld, and J. Rajasingh. Optical-flow based non-invasive analysis of cardiomyocyte contractility. *Scientific Reports*, 7(1):10404, 2017. 2
- [11] M. R. de Souza, R. Ruschel, A. Susin, J. M. Boeira, L. V. Guimares, and A. Parraga. A framework for automatic recognition of cell damage on microscopic images using artificial neural networks. In *International Conference of Engineering in Medicine and Biology Society*, pages 636–639, 2018. 5
- [12] T. Dertinger, R. Colyer, G. Iyer, S. Weiss, and J. Enderlein. Fast, background-free, 3D super-resolution optical fluctuation imaging (sofi). *Proceedings of the National Academy of Sciences*, 106(52):22287–22292, 2009. 2
- [13] M. Elgharib, M. Hefeeda, F. Durand, and W. T. Freeman. Video magnification in presence of large motions. In *IEEE Conference on Computer Vision and Pattern Recognition*, pages 4119–4127, 2015. 2, 6
- [14] Y. Han, M. Li, F. Qiu, M. Zhang, and Y.-H. Zhang. Cell-permeable organic fluorescent probes for live-cell long-term super-resolution imaging reveal lysosome-mitochondrion interactions. *Nature Communications*, 8(1):1307, 2017. 3
- [15] E. A. Hay and R. Parthasarathy. Performance of convolutional neural networks for identification of bacteria in 3D microscopy datasets. *PLoS Computational Biology*, 14(12):e1006628, 2018. 5
- [16] K. He, X. Zhang, S. Ren, and J. Sun. Deep residual learning for image recognition. In *IEEE Conference on Computer Vision and Pattern Recognition*, pages 770–778, 2016. 5, 7
- [17] R. Henriques, M. Lelek, E. F. Fornasiero, F. Valtorta, C. Zimmer, and M. M. Mhlanga. Quickpalm: 3D real-time photoactivation nanoscopy image processing in ImageJ. *Nature Methods*, 7(5):339, 2010. 4
- [18] R. T. Ionescu, F. S. Khan, M.-I. Georgescu, and L. Shao. Object-centric auto-encoders and dummy anomalies for abnormal event detection in video. In *Proceedings of the IEEE Conference on Computer Vision and Pattern Recognition*, pages 7842–7851, 2019. 2
- [19] R. Kasturi, D. Goldgof, P. Soundararajan, V. Manohar, J. Garofolo, R. Bowers, M. Boonstra, V. Korzhova, and J. Zhang. Framework for performance evaluation of face, text, and vehicle detection and tracking in video: Data, metrics, and protocol. *IEEE Transactions on Pattern Analysis and Machine Intelligence*, 31(2):319–336, 2008. 6
- [20] J.-H. Kim, S.-W. Lee, D. Kwak, M.-O. Heo, J. Kim, J.-W. Ha, and B.-T. Zhang. Multimodal residual learning for visual QA. In *Advances in Neural Information Processing Systems*, pages 361–369, 2016. 5
- [21] S. Kim, Y. Sato, P. S. Mohan, C. Peterhoff, A. Pensalfini, A. Rigoglioso, Y. Jiang, and R. A. Nixon. Evidence that the rab5 effector appl1 mediates app- β ctf-induced dysfunction of endosomes in down syndrome and alzheimer’s disease. *Molecular Psychiatry*, 21(5):707, 2016. 1
- [22] T. S. Kim, M. Peven, W. Qiu, A. Yuille, and G. D. Hager. Synthesizing attributes with unreal engine for fine-grained activity analysis. In *IEEE Winter Applications of Computer Vision Workshops*, pages 35–37, 2019. 2
- [23] A. Krizhevsky, I. Sutskever, and G. E. Hinton. Imagenet classification with deep convolutional neural networks. In *Advances in Neural Information Processing Systems*, pages 1097–1105, 2012. 5, 7
- [24] X. Li, X. Hong, A. Moilanen, X. Huang, T. Pfister, G. Zhao, and M. Pietikäinen. Towards reading hidden emotions: A comparative study of spontaneous micro-expression spotting and recognition methods. *IEEE Transactions on Affective Computing*, 9(4):563–577, 2017. 2
- [25] Y. Mao and Z. Yin. Two-stream bidirectional long short-term memory for mitosis event detection and stage localization in phase-contrast microscopy images. In *International Conference on Medical Image Computing and Computer-Assisted Intervention*, pages 56–64, 2017. 6
- [26] P. Masuzzo, M. Van Troys, C. Ampe, and L. Martens. Taking aim at moving targets in computational cell migration. *Trends in Cell Biology*, 26(2):88–110, 2016. 2
- [27] J. M. Mc Donald and D. Krainc. Lysosomal proteins as a therapeutic target in neurodegeneration. *Annual Review of Medicine*, 68:445–458, 2017. 1
- [28] M. D. McDonnell and T. Vladusich. Enhanced image classification with a fast-learning shallow convolutional neural network. In *IEEE International Joint Conference on Neural Networks*, pages 1–7, 2015. 5, 7

- [29] A. Montes, A. Salvador, S. Pascual, and X. Giro-i Nieto. Temporal activity detection in untrimmed videos with recurrent neural networks. *arXiv preprint arXiv:1608.08128*, 2016. 6
- [30] H. Noh, S. Hong, and B. Han. Learning deconvolution network for semantic segmentation. In *IEEE International Conference on Computer Vision*, pages 1520–1528, 2015. 5
- [31] L. Novotny and B. Hecht. *Principles of Nano-optics*. Cambridge university press, 2012. 4
- [32] N. Okabe, B. Xu, and R. D. Burdine. Fluid dynamics in zebrafish kupffer’s vesicle. *Developmental Dynamics: an official publication of the American Association of Anatomists*, 237(12):3602–3612, 2008. 3
- [33] T. Pärnamaa and L. Parts. Accurate classification of protein subcellular localization from high-throughput microscopy images using deep learning. *G3: Genes, Genomes, Genetics*, 7(5):1385–1392, 2017. 5
- [34] H. T. H. Phan, A. Kumar, D. Feng, M. Fulham, and J. Kim. Unsupervised two-path neural network for cell event detection and classification using spatiotemporal patterns. *IEEE Transactions on Medical Imaging*, 38(6):1477–1487, 2018. 2
- [35] N. Plotegher and M. R. Duchon. Mitochondrial dysfunction and neurodegeneration in lysosomal storage disorders. *Trends in Molecular Medicine*, 23(2):116–134, 2017. 1
- [36] I. F. Sbalzarini and P. Koumoutsakos. Feature point tracking and trajectory analysis for video imaging in cell biology. *Journal of Structural Biology*, 151(2):182–195, 2005. 2
- [37] B. Shahriari, A. Bouchard-Côté, and N. Freitas. Unbounded bayesian optimization via regularization. In *Artificial Intelligence and Statistics*, pages 1168–1176, 2016. 7
- [38] H. Shen, L. J. Tauzin, R. Baiyasi, W. Wang, N. Moringo, B. Shuang, and C. F. Landes. Single particle tracking: from theory to biophysical applications. *Chemical Reviews*, 117(11):7331–7376, 2017. 2
- [39] Z. Shen, Y. Xu, B. Ni, M. Wang, J. Hu, and X. Yang. Crowd counting via adversarial cross-scale consistency pursuit. In *IEEE Conference on Computer Vision and Pattern Recognition*, pages 5245–5254, 2018. 2
- [40] S. N. Sinha, J.-M. Frahm, M. Pollefeys, and Y. Genc. Feature tracking and matching in video using programmable graphics hardware. *Machine Vision and Applications*, 22(1):207–217, 2011. 2, 6
- [41] A. R. Small and R. Parthasarathy. Superresolution localization methods. *Annual Review of Physical Chemistry*, 65:107–125, 2014. 4
- [42] O. Solomon, Y. C. Eldar, M. Mutzafi, and M. Segev. Sparcom: sparsity based super-resolution correlation microscopy. *SIAM Journal on Imaging Sciences*, 12(1):392–419, 2019. 2
- [43] R. Spilger, T. Wollmann, Y. Qiang, A. Imle, J. Y. Lee, B. Müller, O. T. Fackler, R. Bartenschlager, and K. Rohr. Deep particle tracker: Automatic tracking of particles in fluorescence microscopy images using deep learning. In *Deep Learning in Medical Image Analysis and Multimodal Learning for Clinical Decision Support*, pages 128–136. 2018. 6
- [44] E. T. T. T. Stephanie Fullerton, Keith Bennett. ORCA-flash4.0 - changing the game. Technical report, Hamamatsu, 2010. 4
- [45] J.-Y. Tinevez, N. Perry, J. Schindelin, G. M. Hoopes, G. D. Reynolds, E. Laplantine, S. Y. Bednarek, S. L. Shorte, and K. W. Eliceiri. Trackmate: An open and extensible platform for single-particle tracking. *Methods*, 115:80–90, 2017. 2
- [46] M.-T. Tran, T. Dinh-Duy, T.-D. Truong, V. Ton-That, T.-N. Do, Q.-A. Luong, T.-A. Nguyen, V.-T. Nguyen, and M. N. Do. Traffic flow analysis with multiple adaptive vehicle detectors and velocity estimation with landmark-based scanlines. In *IEEE Conference on Computer Vision and Pattern Recognition Workshops*, pages 100–107, 2018. 2
- [47] F. Wang, M. Jiang, C. Qian, S. Yang, C. Li, H. Zhang, X. Wang, and X. Tang. Residual attention network for image classification. In *IEEE Conference on Computer Vision and Pattern Recognition*, pages 3156–3164, 2017. 5, 6, 7
- [48] L. Wang, Y. Qiao, and X. Tang. Action recognition with trajectory-pooled deep-convolutional descriptors. In *IEEE Conference on Computer Vision and Pattern Recognition*, pages 4305–4314, 2015. 6
- [49] Y. Wang, M. Ali, Y. Wang, S. Kucenas, and G. Yu. Detection and tracking of migrating oligodendrocyte progenitor cells from in vivo fluorescence time-lapse imaging data. In *IEEE International Symposium on Biomedical Imaging*, pages 961–964, 2018. 2, 6
- [50] Y. Wang, H. Mao, and Z. Yi. Stem cell motion-tracking by using deep neural networks with multi-output. *Neural Computing and Applications*, pages 1–13, 2017. 2
- [51] Y. C. Wong, D. Ysselstein, and D. Krainc. Mitochondria-lysosome contacts regulate mitochondrial fission via rab7 gtp hydrolysis. *Nature*, 554(7692):382, 2018. 2
- [52] X. Xia, C. Xu, and B. Nan. Inception-v3 for flower classification. In *International Conference on Image, Vision and Computing*, pages 783–787, 2017. 5, 7
- [53] T. Xiao, Y. Xu, K. Yang, J. Zhang, Y. Peng, and Z. Zhang. The application of two-level attention models in deep convolutional neural network for fine-grained image classification. In *IEEE Conference on Computer Vision and Pattern Recognition*, pages 842–850, 2015. 5, 7
- [54] H. Xu, A. Das, and K. Saenko. R-c3d: Region convolutional 3D network for temporal activity detection. In *Proceedings of the IEEE international conference on computer vision*, pages 5783–5792, 2017. 6
- [55] Y. Yao, I. Smal, and E. Meijering. Deep neural networks for data association in particle tracking. In *IEEE International Symposium on Biomedical Imaging*, pages 458–461, 2018. 2
- [56] X. Zhang, J. Zou, K. He, and J. Sun. Accelerating very deep convolutional networks for classification and detection. *IEEE Transactions on Pattern Analysis and Machine Intelligence*, 38(10):1943–1955, 2015. 5, 7
- [57] Y. Zhang, K. Li, K. Li, L. Wang, B. Zhong, and Y. Fu. Image super-resolution using very deep residual channel attention networks. In *European Conference on Computer Vision*, pages 286–301, 2018. 5
- [58] H. Zhao, Q. Zhou, M. Xia, J. Feng, Y. Chen, S. Zhang, and X. Zhang. Characterize collective lysosome heterogeneous dynamics in live cell with a space-and time-resolved method. *Analytical Chemistry*, 90(15):9138–9147, 2018. 2



Fluorescence fluctuations-based super-resolution microscopy techniques: an experimental comparative study

Ida S. Opstad, Sebastián Maldonado, Luís Villegas, Jennifer Cauzzo, Nataša Škalko-Basnet, Balpreet S. Ahluwalia and Krishna Agarwal

The manuscript is under peer review, November 2020.

Fluorescence fluctuations-based super-resolution microscopy techniques: an experimental comparative study

Ida S. Opstad,^{1,} Sebastian Acuña,¹ Luís Enrique Villegas Hernandez,¹ Jennifer Cauzzo,² Nataša Škalko-Basnet², Balpreet S. Ahluwalia¹, Krishna Agarwal^{1,#}*

¹Department of Physics and Technology, and ²Department of Pharmacy, UiT The Arctic University of Norway, NO-9037 Tromsø, Norway.

**ida.s.opstad@uit.no ; #uthkrishth@gmail.com*

Abstract

Fluorescence fluctuations-based super-resolution microscopy (FF-SRM) is an emerging field promising low-cost and live-cell compatible imaging beyond the resolution of conventional optical microscopy. A comprehensive overview on how the nature of fluctuations, label density, out-of-focus light, sub-cellular dynamics, and the sample itself influence the reconstruction in FF-SRM is crucial to design appropriate biological experiments. We have experimentally compared several of the recently developed FF-SRM techniques (namely ESI, bSOFI, SRRF, SACD, MUSICAL and HAWK) on widefield fluorescence image sequences of a diverse set of samples (namely liposomes, tissues, fixed and living cells), and on three-dimensional simulated data where the ground truth is available. The simulated microscopy data showed that the different techniques have different requirements for signal fluctuation to achieve their optimal performance. While different levels of signal fluctuations had little effect on the SRRF, ESI and SACD images, image reconstructions from both bSOFI and MUSICAL displayed a substantial improvement in their noise rejection, z-sectioning, and overall super-resolution capabilities.

Abbreviations

(b)SOFI: (balanced) super-resolution optical fluorescence imaging

ESI: entropy-based super-resolution imaging

FF-SRM: fluorescence fluctuations-based super-resolution microscopy

HAWK: Haar wavelet kernel

MUSICAL: multiple signal classification algorithm

TIRFM: total internal reflection fluorescence microscopy

SACD: super-resolution imaging with autocorrelation two-step deconvolution

SBR: signal-to-background ratio

SIM: structured illumination microscopy

SNR: signal-to-noise ratio

SMLM: single molecule localization microscopy

SRM: super-resolution microscopy

SRRF: super-resolution radial fluctuations SRM: Super-resolution microscopy

STED: stimulated emission depletion microscopy

2D/3D: two/three-dimensional

Introduction

Super-resolution microscopy (SRM) has revolutionized the field of microscopy, allowing visualization of nanoscale sub-cellular details smaller than the diffraction limit of optical microscopy. The spectrum of techniques in SRM is spanned by single molecule localization microscopy (SMLM), stimulated emission depletion microscopy (STED) and structured illumination microscopy (SIM). All SRM techniques require an expensive high-end acquisition system, expert sample preparation and system operation. Live-cell imaging is demonstrated for all of these SRM techniques ¹, but remains extremely challenging because of especially two reasons. Firstly, the fast dynamics of many cellular processes in combination with relatively weak fluorescent signal, render acquisition of sufficient signal-to-noise ratio (SNR) for most analytical tasks challenging. Secondly, the cellular functions and morphology are sensitive to small changes in the cellular biochemical environment that can be significantly altered by introducing fluorescent probes, imaging buffers and excitation light exposure. As a consequence, SIM is arguably the best SRM technique for living samples currently available due to its comparatively fast widefield and volumetric acquisition together with lesser requirements on fluorophore photophysical properties and illumination intensities. However, under sub-optimal acquisition conditions such as fast-moving samples, low signal-to-background ratio (SBR) and/or significant photobleaching, SIM reconstruction often fails and is prone to reconstruction artifacts. Furthermore, the SIM imaging systems are not commonly available, likely due to their cost and complexity, and the requirement for trained personnel for system maintenance and operation.

Structured illumination microscopy	Fluorescence Fluctuation based Super-Resolution Microscopy (FF - SRM)					Localization microscopy and STED
Requires costly equipment	No special requirements on instruments or dyes					May need specialized equipment
Needs photostable labels	Uses natural photophysics of fluorescence					Special blinking photophysics
Few images at high intensity	Camera-speed imaging rates					Long imaging time
Better live-cell compatibility	Live-cell compatible imaging environment					Poor live-cell compatibility
Resolution 120-160 nm	Resolution 50 – 120 nm (technique dependent)					Resolution 20-50 nm
SOFI	MUSICAL	ESI	SACD	SRRF		
<ul style="list-style-type: none"> ✓ Quantitative (bSOFI) ✓ Well-understood ✓ High-resolution possible ✗ Sensitive to noise ✗ Many frames needed ✗ Requires stationarity ✗ Prone to artefacts 	<ul style="list-style-type: none"> ✓ Good z-sectioning ✓ Preserves motion ✓ High-resolution possible ✓ Few to several frames ✗ Intensity is blinking dependent ✗ Prone to artefacts 	<ul style="list-style-type: none"> ✓ Noise removal ✓ Few frames needed ✗ Poor resolution enhancement ✗ Overly bright and large spots where higher emitter densities 	<ul style="list-style-type: none"> ✓ Few frames needed ✓ Good for 3D samples and live-cells ✗ Poor resolution enhancement ✗ Over-slimming artifact 	<ul style="list-style-type: none"> ✓ Few frames needed ✗ Poor z-sectioning (TIRF/2D only) ✗ Many option selections needed ✗ Requires stationarity ✗ Fits fibrous structures 		
Sensitive to noise – create mesh like artefacts Benefit from high levels of fluctuations Benefit from higher frame number		Relatively better at noise suppression irrespective of noise level Relatively insensitive to levels of fluctuations Do not significantly benefit from higher frame number				
Recommendation* <ul style="list-style-type: none"> • Use bSOFI option • Use labels with strong fluctuations • Use for >1000 frames & stationary samples 		<ul style="list-style-type: none"> • Use for mobile structures or labels with strong fluctuations • Use for 3D or 2D samples 	<ul style="list-style-type: none"> • Use for noise suppression in samples of low intensity dynamic range 	<ul style="list-style-type: none"> • Use for tissue samples for contrast enhancement • Use when few frames are available 	<ul style="list-style-type: none"> • Use for fibrous and 2D structures 	

Figure 1: Summary of our observations and recommendations for FF-SRM and comparison to other super-resolution microscopy techniques.

There is a new set of techniques, namely fluorescence fluctuations-based super-resolution microscopy (FF-SRM) techniques that, like SMLM, use the photokinetics of fluorescence emission, but do not rely on the external introduction of spatio-temporal sparsity via the chemical environment and high-power

laser modulation. This is an interesting avenue for bio-image analysis, possibly with the potential of democratizing SRM by greatly reduced system cost, and overall live-cell capabilities of high-resolution microscopy. The core phenomenon utilized in FF-SRM is the stochasticity of the number of photons emitted by fluorescent labels over time. These techniques use statistical analysis as the core mechanism to super-resolve the fluorescent molecule distribution, where each molecule independently contributes to fluctuations in the measured fluorescence intensity. FF-SRM in the context of super-resolution fluorescence microscopy techniques is presented in Figure 1.

Although the development of FF-SRM techniques is fairly recent, several techniques have been proposed in the short duration of a few years. Each of these techniques differs in the treatment of the raw data and statistical approach used. Some of them are super-resolution optical fluorescence imaging (SOFI) ² and balanced SOFI (bSOFI) ³, entropy-based super-resolution imaging (ESI) ⁴, super-resolution radial fluctuations (SRRF) ⁵, multiple signal classification algorithm (MUSICAL) ⁶, super-resolution imaging with autocorrelation two-step deconvolution (SACD) ⁷, Bayesian analysis of blinking and bleaching (3B) ⁸, and sparsity based super-resolution correlation optical microscopy (SPARCOM) ⁹. Additionally, the data pre-processing technique Haar wavelet kernel (HAWK) analysis has been developed as a tool to enable SRM of higher-density emitter data for both SMLM and FF-SRM, thus 'enabling high-speed, artifact-free super-resolution imaging of live cells' ¹⁰.

As evaluated and benchmarked in the original papers (by using reference examples from single molecule localization microscopy dataset and simulation examples), they provide a resolution in the range of 50-120 nm. Notably, all of the above-mentioned FF-SRM techniques use two-dimensional (2D) PSF considerations only (not 3D), and the simulated emitters lie perfectly in the focal plane, except for the noteworthy exception shown by Solomon et al. ⁹, where also emitters at 1 μm distance from the focal plane were considered. More details on the individual methods and their reconstruction parameters are provided in the Supplementary Methods.

When imaging real three-dimensional samples for biological or biomedical applications, the reliability of the reconstruction is of more significance than any of the quantitative merits such as the image resolution or contrast. We are not aware of any comprehensive study of how these methods perform on real biological samples in comparison to each other and under various conditions of intensity fluctuation.

Each of the methods has been demonstrated on experimental data of samples that have been arguably designed to illustrate the best characteristics of their own method or on SMLM benchmark data in which case all the methods benefit from the spatio-temporal sparsity in the fluorescence. A comparative study of these techniques on a wide variety of data is important to understand the opportunities and potential pitfalls of the different methods. Therefore, an in-depth analysis is needed on the sample and imaging conditions and how they affect the performances of FF-SRM methods. For example, how the sample and label density, out-of-focus signal, nature of fluctuations, and sub-cellular dynamics affect the reconstruction would be insightful for the experimental design and choice of technique. Moreover, such a comparative study will contribute in setting the right expectations and assigning suitable confidence in the biological interpretations derived from these methods. To this end, we have undertaken a first large-scale experimental study of FF-SRM techniques covering the following aspects:

1. We present an extensive study encompassing nanoparticles (liposomes), actin and membrane in fixed cells and tissues, and mitochondria and the endoplasmic reticulum (ER) in living cells.
2. We tested all the methods on exactly the same data, thereby performing the first unbiased comparative analysis of the performances of the techniques. In most situations, factors such

as fluctuation density, number of frames, and a variety of relevant conditions for imaging or processing the data are considered. The control parameters of each method are tuned within reasonable limits to identify the best performance of the method and the related algorithmic settings.

3. We elucidate the performances of the techniques through three-dimensional (3D) simulation examples that closely emulate the sample conditions. We explain how and why the actual samples challenge the fluctuations-based techniques beyond the scope of design. We consider effects such as out-of-focus light, density of labeling, temporal density of photon emission, practical noise models and the number of frames used for reconstruction.
4. We elucidate the favorable conditions for methods and highlight the challenges that must be addressed in the algorithmic development of these FF-SRM techniques towards making them reliable tools in biomedical research.

Results and Discussion

Simulated data

To obtain fair and definitive answers about the different methods' performance, simulated samples with known ground truth were generated. Two different 3D test samples with varying levels of intensity fluctuations were generated and processed using ESI, SRRF, SACD, SOFI and MUSCIAL. The ground truth emitter locations with axial color coding as a distance from the focal plane are displayed in the upper panels of Figure 2, while their corresponding microscopy images are displayed in the panels below (simulating 510 nm emission wavelength and 1.42NA microscope objective). The biological relevance and structural details of the two samples are as follows:

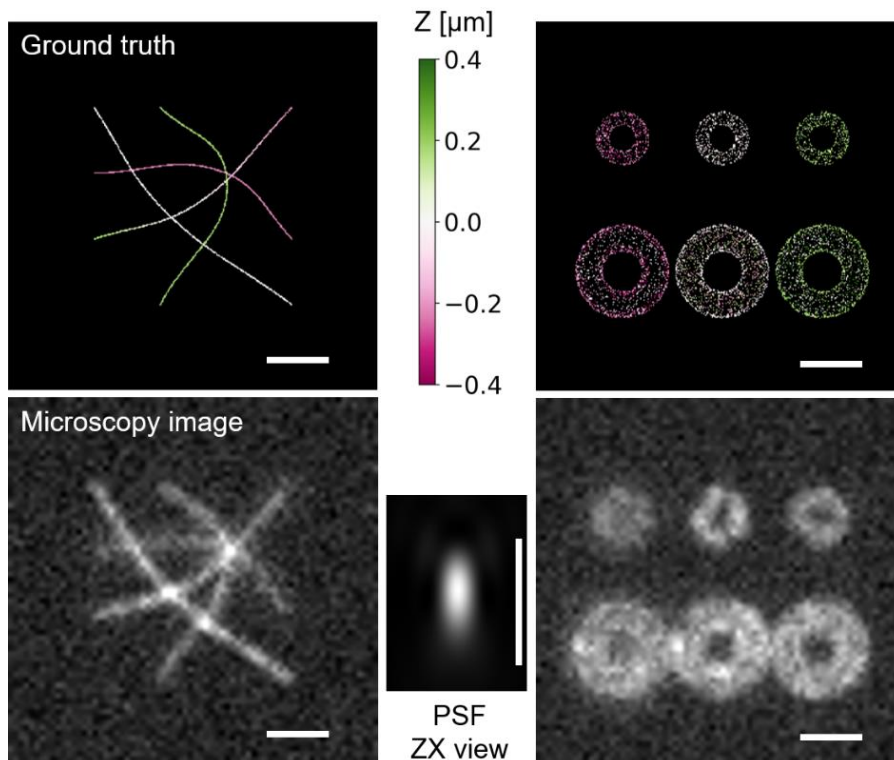


Figure 2: The top row displays the simulated data's ground truth with color coded z-position compared to the focal plane ($Z=0$). The bottom row shows the corresponding microscopy images (single frames) after noise addition and the simulated PSF (orthogonal view) using 1.42NA and emission wavelength 510 nm. The Abbe resolution limits under these conditions are laterally 180 nm and axially 506 nm. The scale bars are 1 μm .

- 1) **Actin strands.** There are four non-intersecting actin strands. Three strands are parallel with the coverglass in different z-planes, one in the focal plane and two of them above and below the focal plane by 0.4 μm respectively. The fourth actin strand is inclined and positioned across several z-planes, having one end 0.2 μm below and the other 0.2 μm above the focal plane. None of the strands are physically touching, but their (projected) microscopy image has overlapping signal in the regions where their lateral positioning is the same. These overlapping regions are where the algorithms' performance is of particular interest.
- 2) **Tori (hollow doughnuts).** The upper row of tori corresponds to tubes of 200 nm diameter, while the lower row has tubes of 400 nm diameter. Both rows have tori centered at three different z-positions. The tori in the lower row are resolvable using conventional microscopy, while the tori in the upper row are not. These structures were chosen to emulate significant cellular organelles like mitochondria and the endoplasmic reticulum (ER) which are outlined by 3D tubular membranes. To resolve both the inner and outer peripheries, the FF-SRM methods must exhibit a good z-sectioning, recognition of small intensity differences but only minor lateral resolution improvement compared to the diffraction limit of optical microscopy.

A higher number of frames for the reconstructions (5000 frames) were used for ESI and SOFI compared to the other techniques (16 to 100 frames). This was due to negative results of initial testing, their capability of fast computations for larger stack sizes, together with the much higher frame number indicated by the methods' original publications.

We will especially consider three aspects of the reconstructions: i) background signal and effect of noise, ii) reconstruction quality and artifacts, iii) the effect of out-of-focus objects and z-sectioning abilities.

Actin strand simulations

The best results achieved from a variation of tested parameters by the five FF-SRM methods are displayed in Figure 3 in the case of simulated 3D actin strands for different levels of intensity fluctuations. A higher level of intensity fluctuations was achieved via sparser fluorescence emission from individual molecules on a densely labelled sample. The different levels are defined quantitatively in the supplementary information.

The *noise* present in the simulated microscopy images (Figure 2) appears not to pose a challenge to ESI, SRRF or SACD. The *structural representations* are accurate except at the intersections of the actin strands (or their projected images). Specifically, in the case of ESI the joints are excessively large and bright (the images are non-linearly intensity adjusted to also allow for visualization of the dimmer structures), and in the case of SRRF and SACD, the strands are completely missing close to the intersections. The performance of ESI, SRRF and SACD appears also largely unaffected by the varying level of fluorescence fluctuations, except for an additional out-of-focus strand appearing in the ESI images at higher levels of fluorescence fluctuations. SRRF does not exclude out-of-focus signal, while SACD does, both independently of the level of intensity fluctuations.

This is very different from the results of SOFI and MUSICAL; whose performance was highly dependent on signal fluctuation level. As opposed to ESI, MUSICAL rejects more out-of-focus structures the higher the level of intensity fluctuations, and the reconstruction of the in-focus sample area are notably better. SOFI and MUSICAL do not appear to have the same issues close to the intersection points as ESI, SRRF and SACD, but SOFI is badly affected by the noise, which results in a dominating background signal that could be difficult to distinguish from the image objects. HAWK preprocessing alleviated the background issue of SOFI, especially for the highest level of fluorescence fluctuations. No improvement was found using HAWK for the other techniques. Further results using additional reconstruction

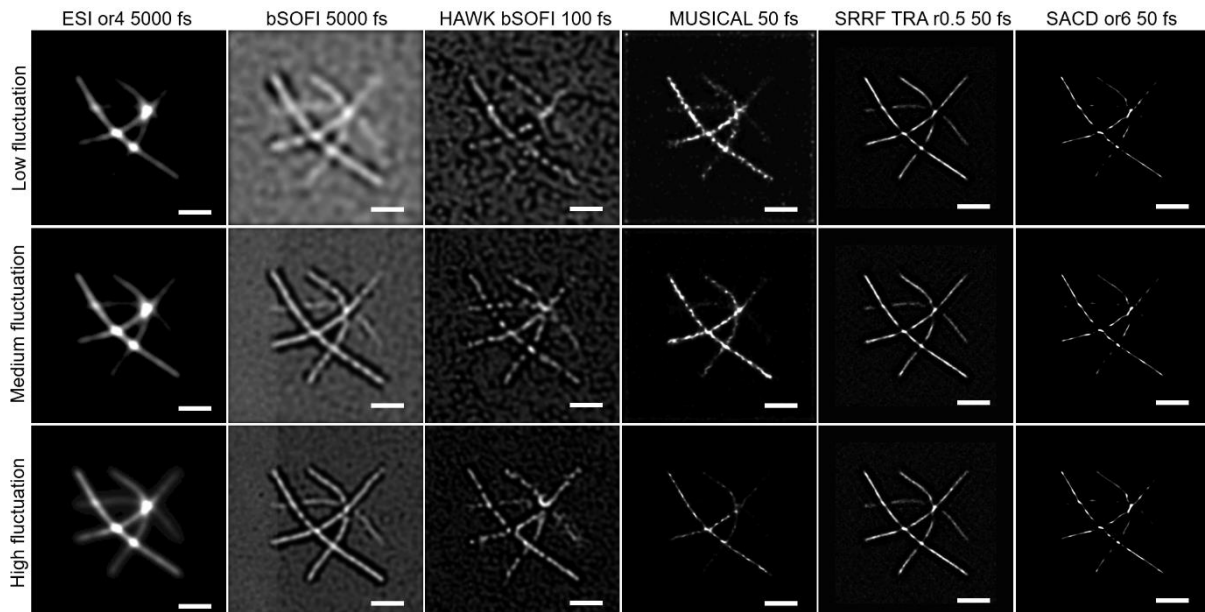


Figure 3: FF-SRM reconstructions of simulated actin strands for three different levels of fluctuations for all five tested methods. Note that only one of the strands lies completely in the focal plane. The bSOFI and MUSICAL images are clearly improved for higher fluctuation levels, while the ESI, SRRF and SACD images display no improvement for higher levels of fluctuations. The headers indicate method and some details about the reconstruction parameters: fs: number of frames; or: order; TRA r0.5: temporal radially average with SRRF ring radius 0.5. The ESI images are intensity adjusted using $\gamma = 0.5$ intensity adjusted, while all other panels have linearly adjusted intensities. The scale bars are $1 \mu\text{m}$.

parameters and other image stack sizes are found in Suppl. Figure S1 together with a more elaborate discussion on the performance of the different techniques and their artifacts under varying conditions.

Mitochondria/tori simulations

Although useful insights can be derived from simple examples like crossing actin strands, they are too simplistic to reveal how the techniques might perform on more complex biological structures such as 3D tubes.

The results for the simulated tori are summarized in Figure 4 for two different fluctuation levels and for each case one torus centered at perfect focus and one 200 nm above the focal plane. These tori correspond to the upper right and middle torus of Figure 2. Results for the complete sample are available in the SI together with results using additional reconstruction parameters (Suppl. Figures S2-S4).

As also noted for the actin strand example, ESI, SRRF and SACD eliminate noise and appear insensitive to fluctuation level as well as the 200 nm shift from the focal plane. Compared to the ground truth structures, which no longer are single lines, none of these techniques can make out the double rings (or 3D tubes). SRRF and SACD reconstruct rings way too slim compared to the actual structures. This reconstruction artifact would not be noticeable using the actin strand example alone.

SOFI, as for the simulated actin strands, is sensitive to noise which gives some artifacts in the background but is able to reconstruct the tubes for the case of 5000 frames and a high fluctuation level (but fails for 100 frames or low level of fluctuations). For a high level of signal fluctuations, MUSICAL is able to discern the double ring of the in-focus torus for only 100 frames, but better for 1000 frames and then also for the low fluctuation level. MUSICAL does not show any background artifacts from the noise for these cases.

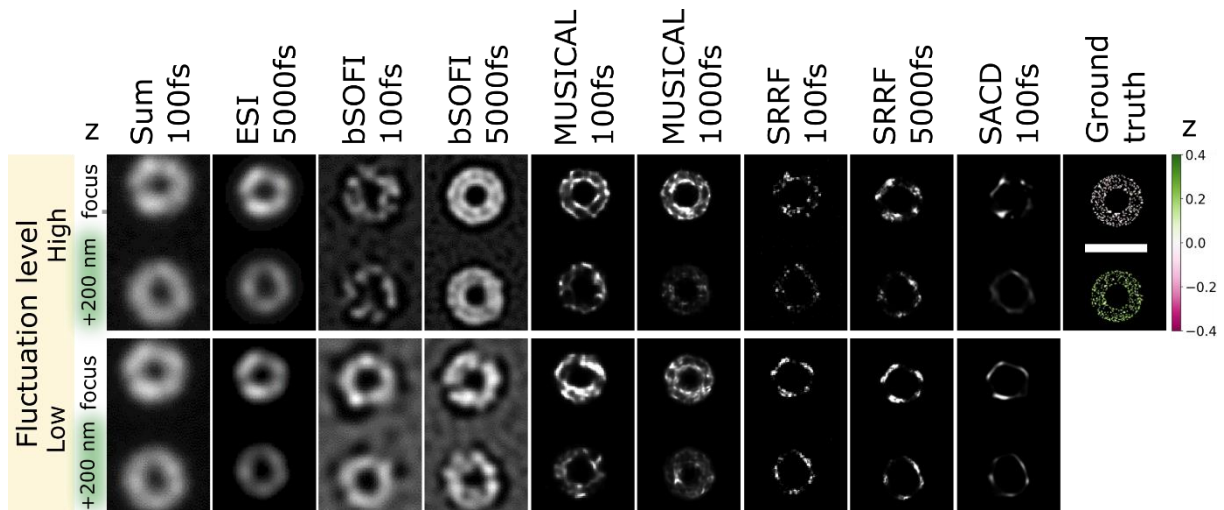


Figure 4: : Reconstructions of tori (tubes of diameter 200 nm) for high (top row) and low signal fluctuation (bottom row), for a torus centered at the focal plane and 200 nm above focus. The tube shape emulates cellular structures like mitochondria and the ER. The scale bar in the ground truth image is 1 μm , and the color bar describes the emitters' axial positions in μm . Only MUSICAL manages to resolve the outer rings for 100 frames (in-focus torus at high fluctuation level), while SOFI provided good reconstruction using 5000 frames, but only for the high fluctuation level and still with significant background artifacts, likely cause by the simulated noise addition. Using 1000 frames, MUSICAL could resolve parts of the inner and outer circles also for the low fluctuation level. The ESI ($\gamma = 0.5$ intensity adjusted), SRRF and SACD results show only a single circle for each torus (for any number of frames or parameters tested), but also with complete noise removal. The circles are in the case of SRRF and SACD significantly slimmer than the ground truth 'double circle', which illustrates a typical reconstruction artifact with these techniques that can be difficult to spot when the ground truth is not available.

These simulation examples have revealed some strengths and weaknesses with all five FF-SRM techniques under scrutiny. We will in the following consider their performance on actual experimental data and see how the results compare to the ones from the simulated data.

Liposomes

The small size, agile and delicate nature of liposomes make their characterization by microscopy challenging and a non-standard procedure. We tested three different sample preparations for liposomes with integrated fluorescence (NBD with excitation and emission maxima 476 nm and 537) directly on microscopy cover glasses: Free floating in suspension, dried-on, and small droplets immobilized under a patch of solid agarose gel.

The samples were imaged in fast time-lapse mode using standard epi-fluorescence microscopy. The free-floating liposomes were, as expected, moving too fast in especially axial direction for acquisition of multiple time point videos of the particles. The dried liposome suspensions appeared to be destroyed, while the suspensions of liposomes covered by solid agarose appeared intact and stationary over the course of 200-300 time points. Hence, only the samples with liposomes immobilized via agarose were considered for further analysis.

We tested the five FF-SRM methods' ability to accurately reveal liposome size from two different known size distributions: 100 nm and 250 nm, respectively. To this end, we first assessed the optimal number of frames to be used for the analysis (Suppl. Figure S5-S6). When not clear which number of frames were best, 100 frames were used, which in most cases was found to provide the optimal tradeoff between fluctuation data (i.e. number of frames) and (rapid) photobleaching together with potential instability of the supporting agarose. The autofluorescence of the agarose patch was also found to photobleach faster than the fluorophores for the first 100-200 frames, possibly beneficial to some of the FF-SRM methods.

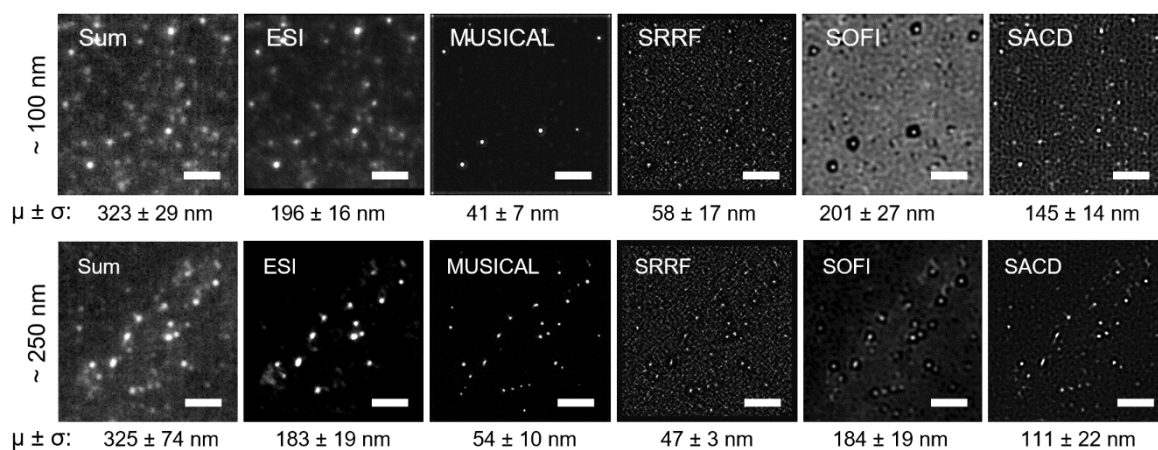


Figure 5: Reconstruction results for liposomes of about 100 nm (upper row) and 250 nm (bottom row) size distributions for the five different methods: ESI order 4 (100 fs), MUSICAL (100 fs) threshold -0.21 (100 nm) and -0.57 (250 nm), SRRF TRAC ring radius 0.5 (100 fs), bSOFI (100 fs for 100 nm and 200 fs for 250 nm), and SACD order 2 (100 fs for 100 nm and 25 fs for 250 nm). The mean value and standard deviation from measuring liposome FWHMs (Gaussian fit) are stated below the panels. Notably, the measured sizes depend on FF-SRM method (and their parameters) and seemingly not on the liposome size distribution. When 100 fs were used for both size distributions for SACD and SOFI, the mean values were 145 nm and 146 nm for SACD, and 201 nm and 203 nm for bSOFI.

Figure 5 shows the results evaluated as best for both the 100 and 250 nm liposomes for the five FF-SRM methods (additional results are available in Suppl. Figures S5-S7). From these images, five FWHM measurements for each case were measured, with the resulting mean and standard deviation displayed under the panels of the respective reconstructions. Notably, the estimated size depends on the FF-SRM method used, and seemingly not on the underlying liposome size distribution. Each technique gives a different result, but the same technique gives a similar result (< 35 nm difference on the mean value) for the two significantly different size distributions (about 100 nm and 250 nm). When the same number of frames were used for the two size distributions for SOFI and SACD (different #fs were found best for the two different size distribution for these cases), the difference was even smaller (1 nm for SACD and 2 nm for bSOFI), see captions of Figure 5 and Suppl. Figure S5. The individual measurements and chosen liposomes are shown in Suppl. Figure S8.

This small ensemble study illustrates some of the challenges with these FF-SRM methods. Although we cannot completely exclude the possibility that one of these techniques provides the right answer for all measured lipid particles (as the ground truth is not available), the size measurements seem completely off and unlikely to be correct for either technique. Changing any reconstruction parameters of the individual techniques also changed the measurements. For example, on the ~250 nm sample, using 25 frames for SACD gave 111 nm mean value for the FWHM, while using 100 fs resulted in mean of 146 nm. Similarly, SOFI with 100 fs gave 203 nm, while using 200 fs gave 184 nm mean value for the FWHM measurements. Better signal of the larger liposomes also appears to 'make the localization better' resulting in smaller size estimates (for all methods except MUSICAL, although also these size estimates are also clearly too small).

The agarose patch appears to have caused notably background artifacts in the reconstruction for SRRF, SOFI and SACD, but not as significantly for ESI or MUSICAL for these particular samples. This problem would likely be alleviated if a more stable fluorophore were available. This was however not the case

for this sample, as fluorescent molecules in general are challenging to stably incorporate into liposomes.

The achieved image resolutions were estimated via line profiles over a sample area with an elongated spot, indicating the presence of at least two closely separated liposomes (Suppl. Figure S9). The MUSICAL, SRRF and SACD images show clear dips between two (or more) peaks, but the high prevalence of reconstruction artifacts in especially the SRRF and SACD images (likely caused by the agarose autofluorescence) render these measurements unreliable.

For future experiments, it might be of interest to ensure that the liposomes are arranged as a flat, monolayer sample that remains stably in perfect focus during image acquisition. Even small deviations from focus could alter the liposome size measurements. The use of total internal reflection fluorescence microscopy (TIRFM) would also likely help reducing the effects of agarose unevenness, autofluorescence and out-of-focus signal. These points could also be used as a general consideration for size profiling applications that use FF-SRM for particles of dimensions close to or smaller than the resolution limit.

Although quantitative analysis does not seem promising from this initial approach, it might be possible via calibration of the individual techniques' parameters on known size distributions to obtain more reliable size estimates. Especially the integration of more photostable fluorophores into the liposomes would be a game changer. As we saw from the simulation examples for the SOFI images, reliable reconstruction was not achieved for ~ 100 frames, but for 5000 frames with a high level of intensity fluctuations.

We will now proceed to samples where often the *qualitative* information is of considerable interest, namely biological tissues and cells.

Fixed cells and tissues

The five different FF-SRM methods were tested on fixed cell cultures (macrophages) and tissues (placenta and heart cryo-sections) using the commonly applied fluorescent probes CellMask Orange (membrane marker) and Phalloidin-ATTO647N (labeling filamentous actin), as before, illuminated using incoherent wide-field illumination for standard epi-fluorescence microscopy.

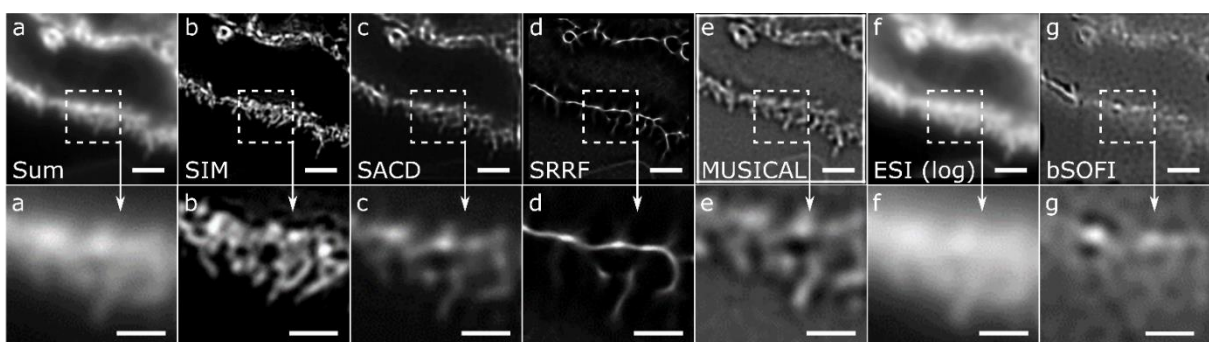


Figure 6: FF-SRM reconstructions of $1\ \mu\text{m}$ -thick cryo-preserved placental tissue section fluorescently labelled with Phalloidin-ATTO647N for identification of F-actin. The regions indicated in the upper panels are shown magnified below revealing the microvilli brush-border of a chorionic villus. (a) The summed image of 500 frames; (b) a single z-plane 3D SIM image; (c) SACD using 50 frames and order 2; (d) SRRF using 500 frames along with TRA option and radius 0.5; (e) MUSICAL using 200 frames and threshold -0.33267; (f) ESI order 4 using 500 frames (log intensity adjusted); bSOFI using 500 frames. The scale bars are $2\ \mu\text{m}$ on the upper-row panels and $1\ \mu\text{m}$ in the lower-row panels.

The results were evaluated from a broad range of different reconstruction parameters for the different methods and the results considered best for each method are displayed in Figure 6 and Suppl. Figure S10 for the case of placenta tissue, and Suppl. Fig S12 for fixed cells. Results using additional reconstruction parameters/options and a data overview are available in Suppl. Figures S11-S15.

The results for the different FF-SRM methods applied to the same sample are strikingly different. Comparing with the sum and the 'reference' SIM image (providing resolution doubling compared to the diffraction limit) of Figure 6, only SACD and MUSICAL give a minor improvement in detail visibility over conventional microscopy. The ESI image appears similar to the sum image, the SRRF image generates thin lines partly corresponding to the SIM image, while the SOFI image is a complete mesh of artifacts.

Results on ultrathin tissue sections (100 nm thickness) and TIRFM data gave similar discouraging results (Suppl. Figures S16-S18). This strongly indicates that out-of-focus signal is not the main reason for the methods' failure.

Comparing with the simulation results presented earlier, the results indicate that the high background intensities and in general poor performance of both MUSICAL and SOFI could be explained by the photo-physical properties of the fluorescent labels used, and that these problems could be countered by experimentally introducing a higher level of fluorescence intensity fluctuation (e.g. using different fluorophores or imaging conditions). Also using longer sequences (>400 frames) might have improved the results, this data is however not available.

Living cells and dynamics

One major motivation for performing FF-SRM instead of other nanoscopy techniques is the opportunity for data acquisition under live-cell friendly environment. In this section, we consider epi-fluorescence time-lapse data of living cells. Because of the dynamic and delicate nature of living cells, fewer frames and lower illumination intensities were used for these data sequences.

The different FF-SRM methods were applied to three different test samples: mitochondrial outer membrane and ER where little to no dynamics were visible in the conventional image stack (64 frames), and a 100 frames image sequence of mitochondria undergoing fast dynamics. The results on mitochondria for stationary and fast dynamics are displayed in Figure 7, while the results for ER and additional HAWK results for mitochondria are displayed in Suppl. Figure S19.

As seen for the fixed samples, all the different methods gave vastly different pictures when applied to the same image sequence. For the stationary sample, the reconstructions show similar patterns as seen for the fixed cells and tissues: ESI provides noise removal and structure slimming, but no real resolution improvement. MUSICAL provides a dominating artefact network over the entire object area. SRRF fits thin single lines to the wider tubular structure. SACD impresses with sturdily recognizing and reconstructing the outer mitochondrial membrane. The great improvement over the simulation results on the tori seen in Figure 3, can be explained by the real mitochondria (in this particular sample) are wider (~250-500nm) than the 200 nm tubes of the tori, and not beyond the resolution limit of SACD. This can be also seen from Suppl. Figure S3, where SACD results on the entire tori simulation sample is shown. Here, the SACD images of the larger tori (400 nm tubes) show two concentric circles, while the smaller tubes (200 nm) are represented as thin mono-circles. Notably, the mitochondrial outer membrane is discernible in some places in the raw data, and especially for the summed image.

HAWK preprocessing resulted in an overall noisy and degraded image, but also a more discernible outer membrane in the case of ESI, MUSICAL and SRRF. The ER sample displayed similar patterns of

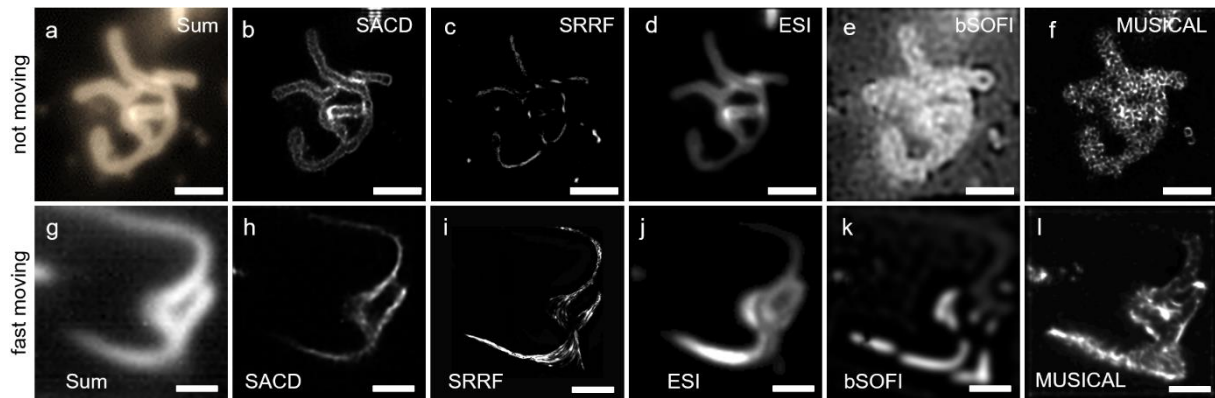


Figure 7: Reconstructions on live-cell data of mitochondrial outer membrane (OMP25- mCherry). Top row: stationary organelles (scale bars: 2 μm); bottom row: fast moving mitochondria (scale bars: 1 μm). The mitochondrial dynamics introduce a new type of signal fluctuation that is not accounted for by any of the FF-SRM algorithms and introduces different artifacts compared to those of stationary objects. The object dynamics has a clearly different effect on all the five different methods. Interestingly, the mitochondrial outer membrane appears much better reconstructed by MUSICAL in the case of dynamic mitochondria compared to the stationary mitochondria.

reconstruction artifacts as for the mitochondria but is also an extremely difficult sample to evaluate as this tubular membrane network could take on almost any shape (shown in Suppl. Figure S19).

For the extremely dynamic sample, ESI appears similar to the sum image, SACD similar to a strongly deconvolved sum image, while SOFI has deleted parts of the moving structure, presumably because dynamics give less pixel-wise signal correlation. SRRF appears to fit a different thin line for every time-point, resulting in a fine grid of multiple lines. The MUSICAL image of mitochondria looks strikingly different from the one in the previous figure, with sharp contours of the outer membrane instead of the dominating artefact network seen in the previous figure and for the results on fixed cells. The signal fluctuations introduced by the mitochondrial dynamics appear to be exploited by the MUSICAL algorithm.

Results and discussion summary

We have processed datasets from a broad range of samples and applied to them the fluctuation nanoscopy techniques (b)SOFI, ESI, MUSICAL SRRF and SACD, trying out many different reconstruction parameters along the way. Figure 1 presented a summary of our observations, which are discussed in detail below.

Observations regarding SOFI and MUSICAL: The simulations revealed that only two of the techniques, namely SOFI and MUSICAL, required a high level of intensity fluctuations to achieve their optimal results. Also only these techniques were able to resolve the more challenging 3D tube-like structures of 200 nm diameter, simulating membrane-bound cellular organelles like mitochondria and the ER. The SOFI images displayed dominating artifacts in presence of noise, but for data of high level of fluorescence signal fluctuations and thousands of time-point image sequences displayed reliable reconstruction even for the 3D samples. HAWK lowered SOFI's sensitivity to noise and greatly improved the SOFI reconstructions for few raw image (~ 100), but only for a high level of fluorescence intensity fluctuations. In the case of short image sequences with a high level of intensity fluctuations, MUSICAL performed the best. MUSICAL also showed an additional ability to exploit signal fluctuations arising from sample dynamics. For fixed cells and tissues, the disappointing performance of SOFI and MUSICAL was shown to be due to a too low level of signal fluctuations in our experimental data. This was especially inferred from the results on simulated data, where SOFI and MUSICAL displayed poor performance for low fluctuation levels, but good performance for higher fluctuation levels.

Additionally, SOFI and MUSICAL performed poorly in the case of slow-moving (or stationary) structures in living cells, both producing a dominating circular mesh. This can be explained by a low level of intensity fluctuations, but importantly, also the use of short image sequences (to assure sample stationarity). However, in the case of the fast-moving sample, MUSICAL was able to exploit the fluctuations induced by the sample dynamics, producing a significantly better results than seen for the slow-moving structures.

Observations regarding ESI, SRRF and SACD: Although ESI displayed faithful noise removal and was possibly the technique the least prone to artifacts, it failed to show super-resolution capabilities for our data. SRRF had also strong noise-reduction capabilities for all fluctuation levels but failed to reveal the true underlying structures where the ground truth (beyond the diffraction limit) was available. Both SRRF and SACD were shown to produce ‘over-slimming’ of structures, rather than revealing the true nanoscopic details in the case of the 3D simulations of doughnuts. In the case of low signal fluctuations and ‘ultra-short’ image sequences (16 frames), SACD had the decidedly best performance of 3D structures close to the resolution limit (like the mitochondrial outer membrane), although its tendency towards producing over-slimming artifacts must be kept in mind while analyzing SACD imaging results. We noted that for fixed cells and tissues, the performance of ESI, SRRF and SACD are generally better than for SOFI and MUSICAL in the sense that the images overall look closer to the actual samples with less obvious artifacts, even though they did not display super-resolving abilities. This is in agreement with our simulated 3D examples in the case of low fluctuations, where we did notice better robustness of these techniques irrespective of the super-resolution ability. Nonetheless, these techniques might generate subtle artefacts that are difficult to spot. The possible influence of these subtle artifacts in the analysis of bio-images needs further investigation. SACD showed a strong ability in producing reliable reconstructions for structural details close to the diffraction limit, as evident from the live-cell data of slow-moving mitochondria. None of them however could withstand the challenge of fast-moving mitochondria.

General observations that apply to all the FF-SRM techniques under scrutiny: The simulated 3D examples do provide some important insights into the performance of these methods. A significant one is that FF-SRM methods can perform well for actin or other fiber-like structures and these might be good examples for studying resolution. However, these results may not be suitable for setting the expectations regarding the performance of these methods for more complex 3D samples such as mitochondria and the ER. Two more important insights from simulations are regarding (a) the effect of out-of-focus structures and level of fluctuations on the reconstructions and (b) the artefacts arising from noise and overlapping structures.

Our results showed an overall poor performance of all FF-SRM methods for the tested conditions for liposomes, fixed cells and tissues. We noted that even if the samples are ultrathin or optical sectioning is not a challenge, FF-SRM can often fail in the case of low fluctuation levels, high background signal and/or insufficient data (number of frames). The measured sizes of liposomes from different known size distributions, revealed that the measured FWHM depend more on chosen FF-SRM technique than on nanoparticle size. Further experimental optimization and calibration of the individual methods reconstruction parameters would be needed before trustworthy nanoparticle size measurements can be carried out using FF-SRM.

The use of dense labelling and photo-stable fluorophores that are optimal for other nanoscopy techniques led to failed reconstructions and image artifacts in the case of fixed cells and tissues. Nonetheless, acquiring a large number of frames, using better-suited dyes, and introducing a higher level of fluctuations through use of imaging buffers, might assist these techniques in performing better. Depending on the resolution requirements and system availability, it might be preferable to use SRM

techniques like SIM, STED or localization microscopy for fixed cells and tissues, as the considerations related to live-cell imaging do not apply for these samples.

The many different parameters offered by some of the techniques could be a potential strength allowing for super-resolution imaging for a broader range of samples and imaging conditions. It is however problematic that, to our knowledge, there are no clear guidelines for when the different parameters should be used, leaving the user with difficult and subjective choices about what might be 'the best' reconstruction. Usually the ground truth is not available for bio-image data, which only complicates the path to derive good guidelines for parameter selection.

Live-cell compatibility is advertised by all evaluated FF-SRM methods. Still, and somewhat unfortunately, stationarity of the imaged objects (during the course of the analyzed image sequence) is also assumed by the FF-SRM algorithms (all apart from MUSICAL). Our computational experiments on extremely dynamic samples displayed very different effects of the sample dynamics on the reconstructed images depending on the FF-SRM method used. Notably, the MUSICAL algorithm appeared to exploit the signal fluctuations introduced via the sample dynamics, offering a greatly improved reconstruction of the mitochondrial outer membrane as compared to the stationary samples.

A considerable challenge for real samples, and especially for living samples, is the complete lack of ground truth. We can use what is known about the samples (e.g. the mitochondrial outer membrane is labelled) and our knowledge and experience with the different methods to aid our evaluation (e.g. circular mesh is a sign of failed MUSICAL reconstruction), the results will still be somewhat subjective and only useful until a certain point. If, for example, all the different methods showed different patterns of membrane domain proteins (only) in a plausible outer mitochondrial membrane area, we would have great difficulty in determining which one, if any of them, provided the correct picture of the membrane protein distribution. Therefore, simulations will be extremely important in the future development and evaluation of FF-SRM methods. They must, however, encompass sufficient complexity to be representative of real image data of dynamic and 3D biological systems¹¹. This is not an easy task, but neither an impossible task in the current era of open science, global collaboration, and ever-expanding computational resources.

Conclusion and outlook

We have seen that reliable reconstruction can be achieved for certain imaging conditions revealed via simulations of microscopy experiments. There are however still some challenges ahead for the young field of FF-SRM on the way towards reliable super-resolution image reconstructions from image sequences of densely fluctuating fluorophores for deriving useful biological inferences.

SOFI and MUSICAL were shown to have a different and superior ability to work with intensity fluctuations compared to other techniques. Both exhibited greatly improved reconstructions with longer image sequences and with higher rate of signal fluctuations. Lamentably, they also displayed the highest level of image degradation compared to the raw image data when the necessary requirements of the image data (like signal fluctuations) were not present. ESI, SRRF and SACD on the other hand, showed little to no improvement with the length of the image sequences and level of intensity fluctuation, but for all conditions gave less obvious artifacts and image structures that were usually more robustly in accordance with the conventional image data. As shown by simulations, the artifacts are still present and severe when considering details beyond the diffraction limit.

Choosing the right reconstruction parameters poses an additional challenge and introduces unwanted user subjectivity to the super-resolution images. The future development of these techniques should

therefore encompass ‘parameter-free reconstruction’, intelligent pre-analysis of the data allowing for automatic selection of the optimal reconstruction parameters and feedback to the users about reconstruction quality and potential deficiencies of the image data. Examples of feedback include poor signal fluctuations, low SBR, sample is moving, sample appears out-of-focus, more frames needed, etc. The general lack of ground truth for living, dynamic samples is a substantial analytical challenge. Therefore, realistic 3D simulations of living cells (with known ground truth) will be important in the future development of these techniques.

We hope that this first comparative study of FF-SRM techniques highlighting the strengths and weaknesses of the different techniques will accelerate the arrival of a reliable and democratic nanoscopy technique suitable for a broad range of samples, likely combining strengths from the already suggested approaches. The potential rewards of true and reliable optical nanoscopy via conventional image sequences of ‘any sample’ together with the promising glints of reconstruction successes suggest that the many challenges along the way will be worth the effort.

Data availability

The microscopy image data and reconstructions are available from <https://www.3dnanoscopy.com/ff-srm-review/> or upon reasonable request. The password of the webpage is reviewpaper. This password protection will be removed when the manuscript is accepted and the data can be made public.

Funding

IO and SA acknowledge strategic funding from UiT The Arctic University of Norway. KA acknowledges funding from a Horizon 2020 Marie Skłodowska-Curie Action (749666) and a Horizon 2020 ERC Starting Grant (804233). SA acknowledges funding from the Horizon 2020 Marie Skłodowska-Curie Action (749666). BSA acknowledges funding from RCN BioTek2021 (285571) and Marie Skłodowska-Curie grant agreement No. 766181. JC and NSB received funding from the European Union’s Horizon 2020 research and innovation program under the Marie Skłodowska-Curie grant agreement No. 766181.

Acknowledgements

The authors kindly thank Åsa B. Birgisdottir for providing cultures of fluorescently labelled H9c2 cells and pig heart tissue samples. Also, our gratitude to Mona Nystad for providing the placental sections and Randi Olsen for cutting all the ultrathin cryo-sections used in this study.

Author contributions

KA conceived the idea. SA generated the simulation microscopy datasets and reconstructions for liposomes. JC produced and prepared the liposomes together with their size analysis. LV did the tissue sample preparation, acquisition and analysis. JC provided cultured macrophages for the fixed-cell experiments. ISO prepared, imaged and analyzed the live and fixed cell-culture samples. ISO wrote the draft manuscript and prepared the figures. KA, BSA and NSB supervised the project. Writing – review & editing, all authors. All authors have read and agreed to the submitted version of the manuscript.

Ethics declarations

Competing interests

The authors declare no competing interests.

Ethical approval of tissue sections

Human placenta sections were collected at the University Hospital of North Norway according to the ethical protocol approved by the Regional Committee for Medical and Health Research Ethics of North

Norway (REK Nord reference no. 2010/2058-4). Written informed consent was obtained from the participant and the sample was treated anonymously. All methods were carried out in accordance with relevant guidelines and regulations.

Pig heart sections were obtained following the ethical protocols approved by the Animal Welfare Board at *UiT The Arctic University of Norway*, NO-9037 Tromsø, Norway, and the Norwegian Food Safety Authority *Mattilsynet*, NO-9008 Tromsø. All methods were carried out in accordance with relevant guidelines and regulations.

Supplementary information

Supplementary results (pdf containing files) and the supplementary figure captions

Supplementary methods

References

- 1 Lothar Schermelleh, Alexia Ferrand, Thomas Huser, Christian Eggeling, Markus Sauer, Oliver Biehlmaier, and Gregor P. C. Drummen, "Super-resolution microscopy demystified," *Nature Cell Biology* **21** (1), 72-84 (2019).
- 2 Thomas Dertinger, Ryan Colyer, Gopal Iyer, Shimon Weiss, and Jörg Enderlein, "Fast, background-free, 3D super-resolution optical fluctuation imaging (SOFI)," *Proceedings of the National Academy of Sciences* **106** (52), 22287-22292 (2009).
- 3 Stefan Geissbuehler, Noelia L Bocchio, Claudio Dellagiacoma, Corinne Berclaz, Marcel Leutenegger, and Theo Lasser, "Mapping molecular statistics with balanced super-resolution optical fluctuation imaging (bSOFI)," *Optical Nanoscopy* **1** (1), 4 (2012).
- 4 Idir Yahiatene, Simon Hennig, Marcel Müller, and Thomas Huser, "Entropy-based super-resolution imaging (ESI): From disorder to fine detail," *Acs Photonics* **2** (8), 1049-1056 (2015).
- 5 Nils Gustafsson, Siân Culley, George Ashdown, Dylan M Owen, Pedro Matos Pereira, and Ricardo Henriques, "Fast live-cell conventional fluorophore nanoscopy with ImageJ through super-resolution radial fluctuations," *Nature communications* **7** (1), 1-9 (2016).
- 6 Krishna Agarwal and Radek Macháň, "Multiple signal classification algorithm for super-resolution fluorescence microscopy," *Nature communications* **7** (1), 1-9 (2016).
- 7 Weisong Zhao, Jian Liu, Chenqi Kong, Yixuan Zhao, Changliang Guo, Chenguang Liu, Xiangyan Ding, Xumin Ding, Jiubin Tan, and Haoyu Li, "Faster super-resolution imaging with auto-correlation two-step deconvolution," *arXiv preprint arXiv:1809.07410* (2018).
- 8 Fan Xu, Mingshu Zhang, Wenting He, Renmin Han, Fudong Xue, Zhiyong Liu, Fa Zhang, Jennifer Lippincott-Schwartz, and Pingyong Xu, "Live cell single molecule-guided Bayesian localization super resolution microscopy," *Cell research* **27** (5), 713-716 (2017).

- 9 Yonina Eldar, Mordechai Segev, Oren Solomon, and Maor Mutzafi, "Sparsity-based super-resolution correlation microscopy", (Google Patents, 2020).
- 10 Richard J Marsh, Karin Pfisterer, Pauline Bennett, Liisa M Hirvonen, Mathias Gautel, Gareth E Jones, and Susan Cox, "Artifact-free high-density localization microscopy analysis," *Nature methods* **15** (9), 689-692 (2018).
- 11 Arif Ahmed Sekh, Ida Sundvor Opstad, Asa Birna Birgisdottir, Truls Myrmel, Balpreet Singh Ahluwalia, Krishna Agarwal, and Dilip K Prasad, presented at the Proceedings of the IEEE/CVF Conference on Computer Vision and Pattern Recognition, 2020 (unpublished).














A waveguide imaging platform for live-cell TIRF imaging of neurons over large fields of view

Ida S. Opstad, Florian Ströhl, Marcus Fantham, Colin Hockings, Oliver Vanderpoorten, Francesca W. van Tartwijk, Julie Qiaojin Lin, Jean-Claude Tinguely, Firehun T. Dullo, Gabriele S. Kaminski-Schierle, Balpreet S. Ahluwalia, Clemens F. Kaminski

Published in Journal of Biophotonics, February 2020.

LETTER

A waveguide imaging platform for live-cell TIRF imaging of neurons over large fields of view

Ida S. Opstad^{1*}  | Florian Ströhl^{1,2}  | Marcus Fantham²  |
Colin Hockings²  | Oliver Vanderpoorten²  | Francesca W. van Tartwijk²  |
Julie Qiaojin Lin^{2,3}  | Jean-Claude Tinguely¹  | Firehun T. Dullo¹ |
Gabriele S. Kaminski-Schierle²  | Balpreet S. Ahluwalia¹  | Clemens F. Kaminski² 

¹Department of Physics and Technology, UiT The Arctic University of Norway, Tromsø, Norway

²Department of Chemical Engineering and Biotechnology, University of Cambridge, Cambridge, UK

³UK Dementia Research Institute at University of Cambridge, Department of Clinical Neurosciences, Island Research Building, Cambridge Biomedical Campus, Cambridge, UK

*Correspondence

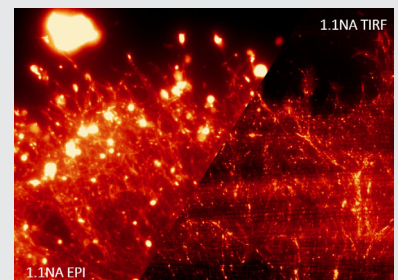
Ida S. Opstad, Department of Physics and Technology, UiT The Arctic University of Norway, NO-9037 Tromsø, Norway.
Email: ida.s.opstad@uit.no

Funding information

Engineering and Physical Sciences Research Council, Grant/Award Number: EP/H018301/1; FP7 Ideas: European Research Council, Grant/Award Number: 336716; H2020 Marie Skłodowska-Curie Actions, Grant/Award Number: 836355; Medical Research Council, Grant/Award Number: MR/K015850/1 and MR/K02292X/1; MedImmune | AstraZeneca and Infinitus China Ltd.; Universitetet i Tromsø, Grant/Award Number: Tematiske Satsinger; Wellcome Trust, Grant/Award Number: 089703/Z/09/Z

Abstract

Large fields of view (FOVs) in total internal reflection fluorescence microscopy (TIRFM) via waveguides have been shown to be highly beneficial for single molecule localisation microscopy on fixed cells [1,2] and have also been demonstrated for short-term live-imaging of robust cell types [3-5], but not yet for delicate primary neurons nor over extended periods of time. Here, we present a waveguide-based TIRFM set-up for live-cell imaging of demanding samples. Using the developed microscope, referred to as *the ChipScope*, we demonstrate successful culturing and imaging of fibroblasts, primary rat hippocampal neurons and axons of *Xenopus* retinal ganglion cells (RGCs). The high contrast and gentle illumination mode provided by TIRFM coupled with the exceptionally large excitation areas and superior illumination homogeneity offered by photonic waveguides have potential for a wide application span in neuroscience applications.



TIRFM provides an effective means for the spatially confined illumination of a sample close to the coverslip/substrate via evanescent fields [6-8]. It provides particular advantages for fluorescence imaging as out of focus

signal is intrinsically avoided leading to high signal to noise ratios and image contrast. In addition to the molecular specificity afforded by fluorescence imaging and image contrast, TIRFM reduces the overall illumination dose on the sample. This minimises phototoxicity, making TIRF the method of choice for many live-

Ida S. Opstad and Florian Ströhl contributed equally to this work.

This is an open access article under the terms of the Creative Commons Attribution License, which permits use, distribution and reproduction in any medium, provided the original work is properly cited.

© 2020 The Authors. *Journal of Biophotonics* published by WILEY-VCH Verlag GmbH & Co. KGaA, Weinheim

cell imaging applications with delicate samples such as live neurons [9].

TIRFM is usually accomplished by using a large numerical aperture (NA) objective lens for both the excitation and the detection paths. Unfortunately, the high magnification of lenses required for TIRFM limits the accomplishable FOVs and imaging throughput, but also which studies, both qualitative and quantitative, are possible to perform. For instance, in conventional TIRF, it would not be possible to measure the cellular response to a drug treatment or other stimulus over a large population of cells or even across a single polarised cell that spans wider than the conventional TIRF FOV. This inhibits the acquisition of statistically significant biological data from studies that rely on correlation in both space and time, as these are not simultaneously accessible. Our chip-TIRF imaging platform allows for the generation of large data sets which capture the correlation in both space and time, which facilitates the obtaining of statistically significant results also for studies where the time dimension is of essence. Moreover, if samples are fast-moving, cellular events become close to impossible to follow using a small FOV. For example, in Reference [10], elongated tubules in hippocampal neurons are reported to move extremely fast: on average 4.5 $\mu\text{m/s}$.

The restriction on the TIRF FOV is removed if waveguides are used for TIRF illumination and in principle, arbitrarily large areas could be achieved through appropriately designed waveguide geometries (width and length). Because the excitation and the detection paths are completely decoupled from one another, full flexibility in choice of the imaging objective lens is retained, allowing for control over the FOV size, as illustrated on fibroblasts in Figure S1. In the so-called *ChipScope* microscopy system [1], multiple colours can be admitted simultaneously into the photonic chip, enabling the simultaneous TIRF excitation of multiple fluorophores (see Figure S2).

Waveguides have previously been shown to be a viable growth substrate for cell culture [3, 4], but to fully exploit the gentle TIRF illumination for live-cell image applications, especially in the neurosciences, additional considerations and adaptations must be made to maintain the cells alive under suitable conditions. The scope of this work was to adapt a waveguide TIRF microscopy set-up for the imaging of sensitive cell types like primary neurons, and to develop means of performing measurements on primary cell-cultures on photonic chips. These are demanding and challenging cells to grow in general and especially on waveguide materials (illustrated in Figure S3), as the surface properties are different compared to cover glasses, which are currently standard for neuronal culturing.

Cultured neurons from *Xenopus laevis* (African clawed frog) are viable at room temperature under atmospheric levels of oxygen and CO_2 , making them an attractive and practical choice for studies requiring prolonged live imaging and a suitable initial test specimen for the *ChipScope*. Retinal neurons cultured from eye primordia are an interesting model system where both TIRFM and large FOV are highly beneficial [11]. The growth cones at the tip of extending axons are flat, hand-shaped structures that are responsive to extracellular chemical and mechanical stimuli and support axon pathfinding during embryonic development [12]. To image the growth of live RGC axons in culture, we explored the capabilities of our waveguide imaging platform in simultaneously capturing tens of growth cones of far-reaching axons from explanted *Xenopus* eye primordia. Different from previous waveguide imaging implementations, we employed water dipping objective lenses, which greatly facilitate high-resolution live-cell imaging and permit access to the sample during imaging, e.g. to optimise labelling conditions or study the response of different treatments in actu [13]. The results of imaging of filamentous actin in live developing axons and growth cones of RGC are shown in Figure 1. The benefit of TIRFM over episcopic (EPI) illumination is apparent when comparing identifiable single cortical filaments of growth cones, as shown in Figure 1, panels D-F. Additionally, the vastly increased FOV simplifies and improves both qualitative and quantitative analyses.

While *Xenopus* neurons can be imaged under ambient conditions, mammalian cells require 37°C and 5% CO_2 . To allow for long-term imaging of mammalian neurons under physiologically relevant conditions, we equipped the *ChipScope* with a heater system and a custom-made environmental chamber. As laser coupling together with its delicate piezo stage electronics precludes the use of common commercially available microscope stage incubators on the *Chipscope*, we custom designed a chamber connected to a commercial (Okolab) stage top incubator system, supplying 5% CO_2 and high humidity. Our chamber is made of transparent, flexible and low heat conductivity low-density polyethylene (LDPE) thermoplastic, which can be easily cut and stretched to tightly fit around all necessary microscope components, while maintaining easy access for changing sample or objective through a zip open/close mechanism (Figure 2E, F). A heating strip and temperature sensor are fitted to the sample holder to maintain the chip at 37°C during imaging experiments. Further details are provided in Suppl. Note 1.

Standard protocols for culturing rat hippocampal neurons [14] require tall, slim chambers (as in Figure 2B, second row). These culture chambers are incompatible with upright microscopes featuring short working distance,

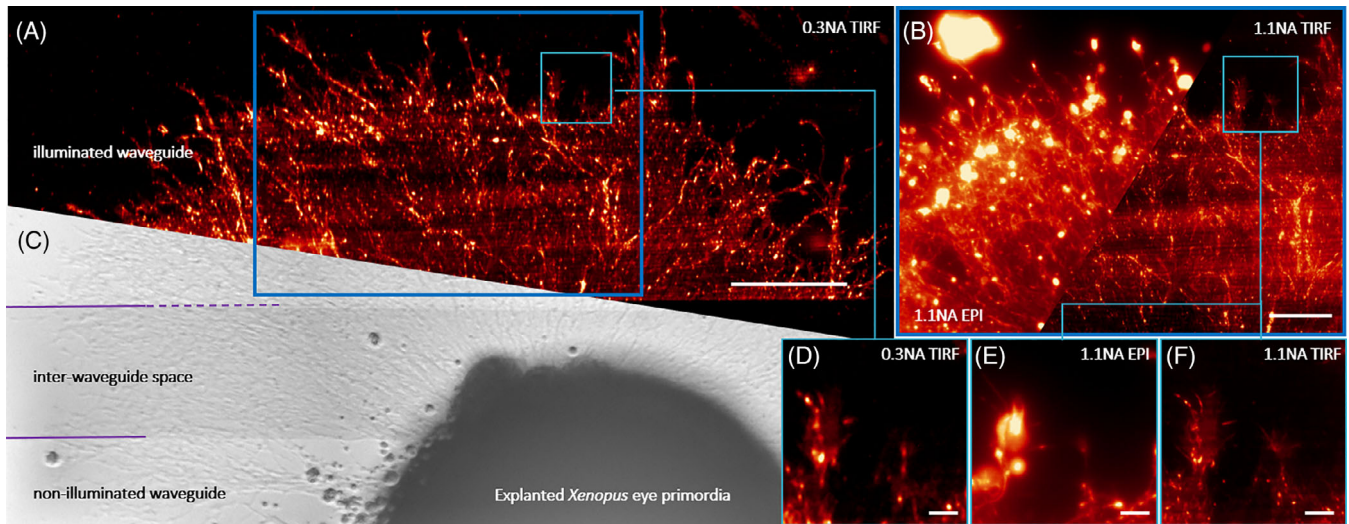


FIGURE 1 Chip microscopy is a method for imaging of large areas of live *Xenopus* RGC axons in TIRF. All panels show images of the same living *Xenopus* eye explant cultured on chip and labelled with SiR-Actin. A, Overview image captured using 0.3NA water dipping objective in both TIRF (upper panel) and BF (lower panel) mode. B, Overview image captured using 1.1NA water dipping objective using EPI (left panel) and TIRF (right panel) illumination modes. D-F, Excerpts from region indicated in B, comparing available growth cone details for different NAs in TIRF and EPI illumination modes. TIRF illumination together with 1.1NA in panel f reveals the most identifiable single cortical filaments. TIRF images were obtained via summation of 100 frames illuminated by different waveguide illumination modes. Scale bars: A, 100 μm ; B, 50 μm and D-F, 10 μm

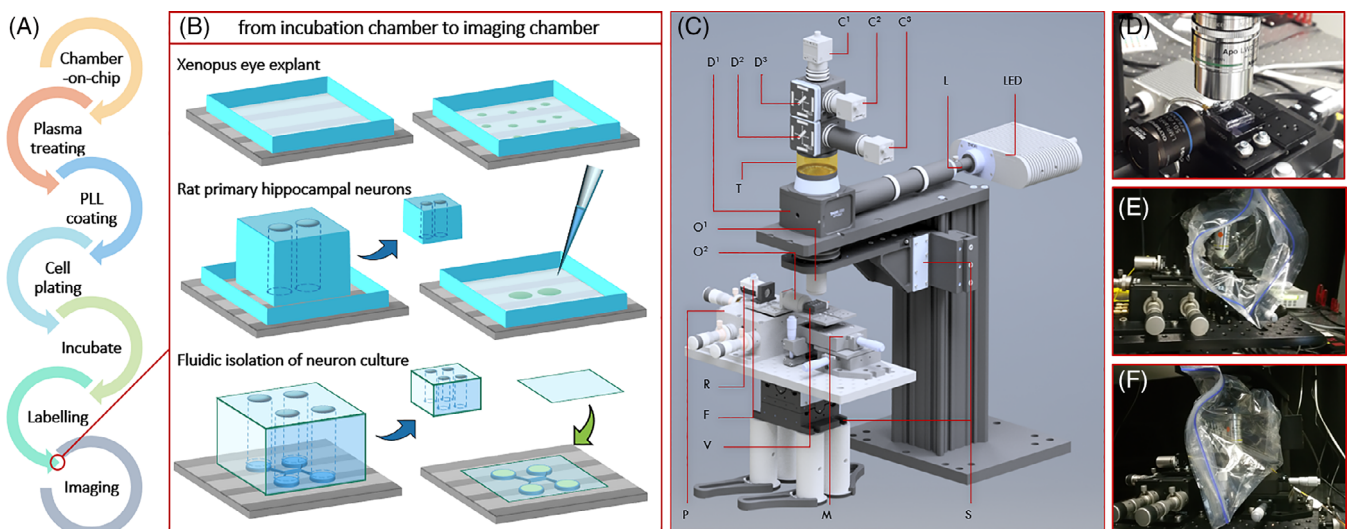


FIGURE 2 Chip microscopy can be adapted for live-cell imaging and various cell culture approaches. A, Experimental flowchart. B, Photonic chip preparation for cell culture and imaging. *Top*: chambers for *Xenopus* retinal ganglion cells. The chambers are about 20 mm by 20 mm wide and 3 mm tall; *Middle*: chambers for rat hippocampal neurons. The outer chamber is as above, while the inner block is about 10 mm by 15 mm wide and 10 mm tall. The inner circular wells containing neurons and cell culture medium are of diameter 6 mm; *Bottom*: two layers of PDMS for cultivating neurons in microgrooves. The dimensions are as above, but with a rectangular PDMS block of about 15 mm by 15 mm sustaining the circular wells. The thin bottom layer containing the microchannels remains for imaging with a coverslip on top to reduce evaporation. C, *ChipScope* model. This upright microscope enables TIRF, EPI, and BF imaging with up to three colours simultaneously. C1-3: cameras, D1-3: dichroic mirrors, T: tube lens, L: liquid lightguide, LED: 4-colour LED combiner, O1-2: objectives, R: reflective collimator, F: fibre, V: vacuum-stage, P: piezo-stage, M: micrometre long-travel stage, S: sample xyz -stage. A detailed description of the optical set-up is provided in Suppl. Note 1. D, Microscope stage with waveguide chip and imaging chamber prepared for use with water dipping objective. The horizontal objective is for laser coupling into the waveguides. E, *ChipScope* with open incubation chamber for easy access to sample and objective. F, Closed incubator supplied with high humidity and 5% CO_2 from a conventional stage top incubator

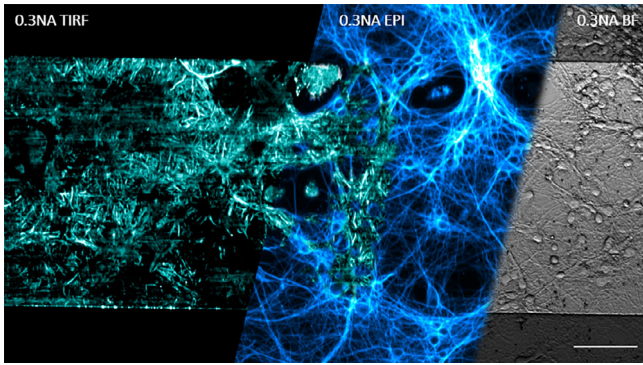


FIGURE 3 Rat hippocampal neurons can be cultured on chip for weeks and imaged live for hours in ChipScope incubator. All panels show live-cell imaging of neurons labelled with SiR-Tubulin on adjacent regions of the same waveguide providing a $400\ \mu\text{m}$ wide TIRF excitation area. The length of the *imaged* TIRF region is limited by the system magnification and camera chip size, in this case giving a total TIRF field of view of $400\ \mu\text{m} \times 847\ \mu\text{m}$. *Left*: TIRF image obtained by mode-averaging as in Figure 1. *Middle*: Single plane EPI image overlaid with part of the corresponding TIRF image. *Right*: BF image. Scale bar: $100\ \mu\text{m}$

high-NA objectives, while inverted microscopy is rendered impractical by the opaque base layer of silicon that forms a supporting platform for the waveguides. We

solved this difficulty via separate custom-made wells for culturing and imaging, as displayed in Figure 2B. After growing the neurons on-chip in their preferred polydimethylsiloxane (PDMS) cell culture wells, we exchanged the tall PDMS blocks right before imaging for wider and lower “fences” adapted for the particular waveguide chip and imaging objective of choice. To monitor the on-chip hippocampal cultures in the time between excision and laser lab TIRF imaging, we built a simple upright microscope that could conveniently be fitted on a standard biological lab bench, see Figure S4. A flowchart of our on-chip sample preparation is shown in Figure 2A,B and the imaging set-up in Figure 2C,F.

The satisfactory performance of this incubator was validated through longer-term live-cell imaging of delicate primary hippocampal neurons (excised from rat embryos). The results, displayed in Figure 3, show the microtubule network imaged in TIRF, EPI and brightfield (BF) mode (from left to right). After 1.5 hours of imaging, the primary neurons were observed to be in a healthy condition (Figure S5). To the best of our knowledge, this is the first chip-based imaging system with incubation chamber that has been successfully adapted for live-cell imaging of mammalian neurons.

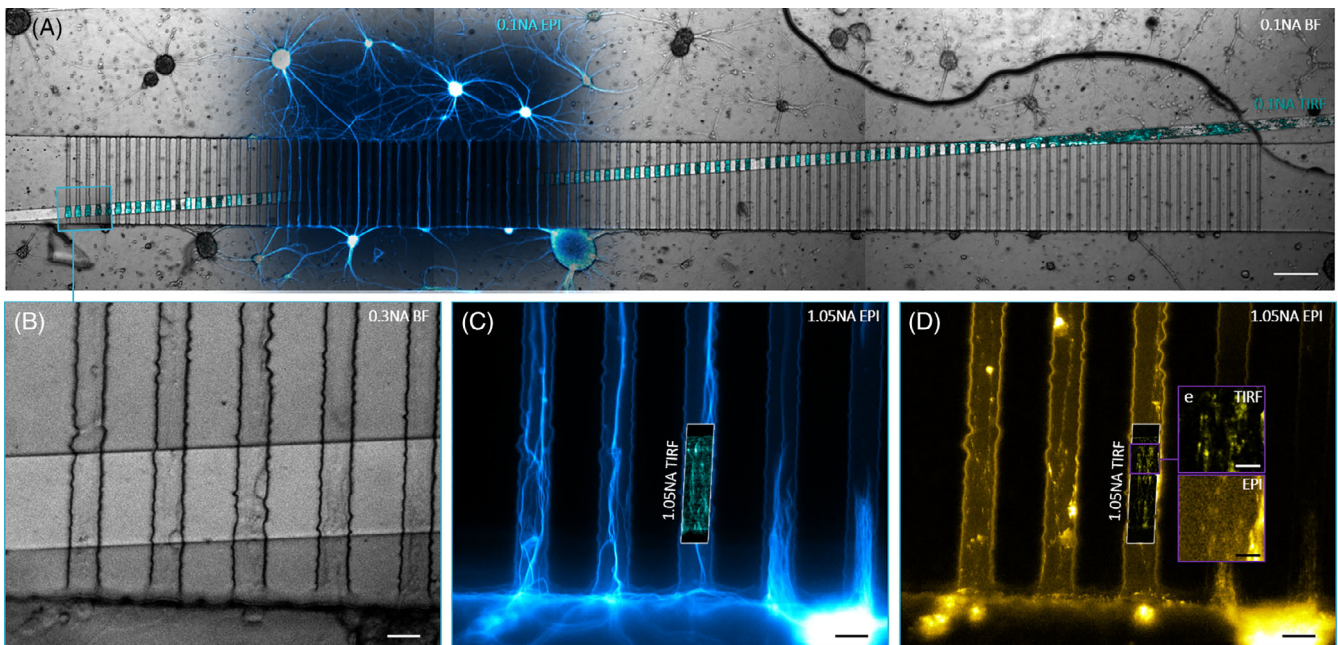


FIGURE 4 Advanced cell culture approaches like microchannel devices can be combined with large FOV chip TIRFM. All panels show rat hippocampal neurons cultured in a chip-microchannel combi device and labelled using SiR-Tubulin and MitoTracker Orange. A, Stitched overview image acquired using a $4\times 0.3\text{NA}$ air objective. BF mode overlaid with EPI (blue) and TIRF (cyan) illumination. Scale bar: $200\ \mu\text{m}$. B-D, Images acquired using a $30\times 1.05\text{NA}$ silicon oil immersion objective, scale bars are $20\ \mu\text{m}$. B, BF image of microchannels on waveguide. C, Corresponding EPI image of microtubules with TIRF image inlay. D, EPI image of MitoTracker Orange with TIRF inlay. E, Zoomed view of TIRF and EPI image of mitochondria in microchannels, scale bar $5\ \mu\text{m}$. The particular Ta_2O_5 waveguide used for this experiment was $50\ \mu\text{m}$ wide, although any waveguide dimension could be applied in general

Advanced cell culture approaches are becoming more and more important in neuroscience research, such as the microgroove cell culture chambers used in studies of axonal injury or protein transport [15–17]. We therefore sought to use PDMS microgroove chambers in combination with the photonic chip imaging system. One complication is that the cell culture chambers are usually permanently bonded to the substrate, but the chips are—at present—too expensive to be disposed of after a single experiment. We found that clean PDMS was sufficiently tacky to adhere to the photonic chip and to contain media while the neurons grew. Furthermore, as the chips are opaque, signal must be collected from above. This requires the PDMS to be thin enough to match the working distance of the desired imaging objective, and to be uniform and optically clear, so that high quality imaging can be performed through the PDMS layer. However, such a thin PDMS layer would not contain sufficient medium to support the neurons and overcome evaporation. We addressed these challenges by using a second PDMS layer on top of the microfluidic devices to contain the medium, which was removed before imaging, as depicted in Figure 2B, bottom row. As displayed in Figure 4, we successfully performed TIRF, EPI and BF microscopy on photonic chips through PDMS microgrooves of living primary hippocampal neurons using a high NA silicon oil immersion objective. The results show that this multimodal imaging scheme is feasible, although the TIRF imaging success in this case was modest as the axons appeared to have detached from the waveguide TIRF excitation area. This might be addressed in future experiments e.g. by selective coating of the waveguide surface with poly-L-lysine, without coating the microchannel walls, thus removing possible attachment points for the growing axons above the waveguide surface. Another challenge with fluorescence imaging in microgrooves concerns the labelling and consecutive washing steps required in many protocols, which are difficult to achieve in the narrow channels. In our data, this resulted in high background signal from the used MitoTracker label, causing the mitochondria to be barely visible in the EPI image of Figure 4E. Supplementary Note 4 provides details on the procedures and microgroove production steps.

In summary, we have adapted photonic chip large area TIRFM for live-cell neuroimaging applications by developing on-chip cell culture protocols and integrating chip microscopy with a heater system and incubation chamber. We have shown successful cell culture of primary rat hippocampal neurons and explanted *Xenopus* eye primordia and performed large FOV live-cell TIRFM of these sensitive cell types. We have demonstrated imaging on combined microgroove-waveguide devices and the capabilities of our system. We expect the integration of

environmental control with the unique advantages of TIRF illumination provided by waveguides to inspire and enable many new imaging applications for photonic chips.

ACKNOWLEDGMENTS

The authors thank Omid Siddiqui for performing simulations on heat transfer of the sample stage and Christine E. Holt for providing means of *Xenopus* culturing and loan of silicon oil objectives. This work was supported by grants from the European Research Council, project number 336716 to BA and the Tematiske Satsinger funding program to BA by UiT The Arctic University of Norway. FS acknowledges funding via Horizon 2020 Marie Skłodowska-Curie actions (#836355). CFK acknowledges funding from the Physical Sciences Research Council (EP/H018301/1), Medical Research Council (MR/K015850/1 and MR/K02292X/1), Wellcome Trust (089703/Z/09/Z), MedImmune | AstraZeneca and Infinitus China Ltd.

CONFLICT OF INTEREST

CFK received funding from MedImmune | AstraZeneca and Infinitus China Ltd. The other authors declare no competing interests.

AUTHOR CONTRIBUTIONS

I.S.O. led the project and performed the imaging. F.S. designed the ChipScope. I.S.O. and F.S. built and calibrated the system. B.S.A., F.T.D., and J.C.T. provided waveguides and advised on chip microscopy. I.S.O., F.S., and O.V. designed and installed the custom imaging incubator. M.F. wrote the ChipScope control software. C.H. excised, cultured and prepared labelled samples of primary rat hippocampal neurons on chip. C.H. advised on the incubator and helped plan and conduct the imaging experiments. O.V. designed and fabricated the microchannel moulds. I.S.O., C.H., and O.V. made microchannels and PDMS chambers. J.Q.L. and F.W.v.T. provided expertise on *Xenopus* biology and handling. F.W.v.T. performed *Xenopus* dissections and on-chip culturing and advised on the labelling and imaging of RGCs. C.F.K. and B.S.A. provided supervision and funding for the project. G.S.K.S. provided facilities for primary neurons excision and cell culture, and CFK microscopy lab area and equipment. I.S.O. and F.S. wrote the manuscript. All authors contributed to or commented on the manuscript.

ORCID

Ida S. Opstad  <https://orcid.org/0000-0003-4462-4600>
Florian Ströhl  <https://orcid.org/0000-0002-2603-0780>
Marcus Fantham  <https://orcid.org/0000-0002-9921-3334>

Colin Hockings  <https://orcid.org/0000-0002-0248-0517>
 Oliver Vanderpoorten  <https://orcid.org/0000-0001-5611-470X>
 Francesca W. van Tartwijk  <https://orcid.org/0000-0002-9795-2571>
 Julie Qiaojin Lin  <https://orcid.org/0000-0002-2669-6478>
 Jean-Claude Tinguely  <https://orcid.org/0000-0003-4281-0370>
 Gabriele S. Kaminski-Schierle  <https://orcid.org/0000-0002-1843-2202>
 Balpreet S. Ahluwalia  <https://orcid.org/0000-0001-7841-6952>
 Clemens F. Kaminski  <https://orcid.org/0000-0002-5194-0962>

REFERENCES

- [1] R. Diekmann, Ø. I. Helle, C. I. Øie, P. McCourt, T. R. Huser, M. Schüttpelz, B. S. Ahluwalia, *Nat. Photon.* **2017**, *11*(5), 322.
- [2] Ø. I. Helle, D. A. Coucheron, J. C. Tinguely, C. I. Øie, B. S. Ahluwalia, *Opt. Express* **2019**, *27*(5), 6700.
- [3] J.-C. Tinguely, Ø. I. Helle, B. S. Ahluwalia, *Opt. Express* **2017**, *25*(22), 27678.
- [4] B. Agnarsson, A. B. Jonsdottir, N. B. Arnfinnsdottir, K. Leosson, *Opt. Express* **2011**, *19*(23), 22929.
- [5] S. Mittler, Waveguide evanescent field fluorescence and scattering microscopy: The status quo. in *Optics, Photonics and Laser Technology* (Eds: P. A. Ribeiro, M. Raposo), Springer International Publishing, Cham **2018**, p. 1.
- [6] H. Grandin et al., *Biosens. Bioelectron.* **2006**, *21*(8), 1476.
- [7] A. Hassanzadeh, M. Nitsche, S. Mittler, S. Armstrong, J. Dixon, U. Langbein, *Appl. Phys. Lett.* **2008**, *92*(23), 233503.
- [8] D. Axelrod, TIRF microscopy and variants. in *Encyclopedia of Modern Optics (Second Edition)* (Eds: B. D. Guenther, D. G. Steel), Elsevier, Oxford **2018**, p. 168.
- [9] J. Icha, M. Weber, J. C. Waters, C. Norden, *Bioessays* **2017**, *39*(8), 1700003.
- [10] C. Kaether, P. Skehel, C. G. Dotti, *Mol. Biol. Cell* **2000**, *11*(4), 1213.
- [11] F. Ströhl, H. H. W. Wong, C. E. Holt, C. F. Kaminski, *Methods Appl. Fluoresc.* **2017**, *6*(1), 014004.
- [12] L. Leung, C. E. Holt, *Cold Spring Harb. Protoc.* **2012**, *2012*(9), pdb prot070003.
- [13] F. Ströhl, J. Q. Lin, R. F. Laine, H. H. W. Wong, V. Urbančič, R. Cagnetta, C. E. Holt, C. F. Kaminski, *Sci. Rep.* **2017**, *7*(1), 709.
- [14] A. M. Taylor, S. W. Rhee, C. H. Tu, D. H. Cribbs, C. W. Cotman, N. L. Jeon, *Langmuir* **2003**, *19*(5), 1551.
- [15] J. W. Wu, S. A. Hussaini, I. M. Bastille, G. A. Rodriguez, A. Mrejeru, K. Rilett, D. W. Sanders, C. Cook, H. Fu, R. A. C. M. Boonen, M. Herman, E. Nahmani, S. Emrani, Y. H. Figueroa, M. I. Diamond, C. L. Clelland, S. Wray, K. E. Duff, *Nat. Neurosci.* **2016**, *19*(8), 1085.
- [16] M. K. Lewandowska, D. J. Bakkum, S. B. Rompani, A. Hierlemann, *PLoS one* **2015**, *10*(3), e0118514.
- [17] A. M. Taylor, M. Blurton-Jones, S. W. Rhee, D. H. Cribbs, C. W. Cotman, N. L. Jeon, *Nat. Methods* **2005**, *2*(8), 599.

SUPPORTING INFORMATION

Additional supporting information may be found online in the Supporting Information section at the end of this article.

How to cite this article: Opstad IS, Ströhl F, Fantham M, et al. A waveguide imaging platform for live-cell TIRF imaging of neurons over large fields of view. *J. Biophotonics*. 2020;e201960222. <https://doi.org/10.1002/jbio.201960222>



Complete list of published articles

- **Multi-color imaging of sub-mitochondrial structures in living cells using SIM.** *Ida S. Opstad, Deanna L. Wolfson, Cristina I. Øie and Balpreet S. Ahluwalia.* Published in Nanophotonics March 2018.
- **Live-cell imaging of human spermatozoa using SIM.** *Ida S. Opstad, Daria A. Popova, Ganesh Acharya, Purusotam Basnet And Balpreet S. Ahluwalia.* Published in Biomedical Optics Express, December 2018.
- **Adaptive fluctuation imaging captures rapid subcellular dynamics.** *Ida S. Opstad, Florian Ströhl, Åsa B. Birgisdottir, Sebastián Maldonado, Trine Kalstad, Truls Myrnel, Krishna Agarwal, and Balpreet S. Ahluwalia.* Published in Proceedings of SPIE, the International Society for Optical Engineering, June 2019.
- **MusiJ: an ImageJ plugin for video nanoscopy.** *Sebastian Acuña, Florian Ströhl, Ida S. Opstad, Balpreet S. Ahluwalia, Krishna Agarwal.* Published in Biomedical Optics Express, April 2020.
- **Learning nanoscale motion patterns of vesicles in living cells.** *Arif Ahmed Sekh, Ida Sundvor Opstad, Åsa Birna Birgisdottir, Truls Myrnel, Balpreet Singh Ahluwalia, Krishna Agarwal, Dilip Prasad.* Published in

Conference on Computer Vision and Pattern Recognition (CVPR), April 2020.

- **Fluorescence fluctuations-based super-resolution microscopy techniques: an experimental comparative study.** *Ida S. Opstad, Sebastián Maldonado, Luís Villegas, Jennifer Cauzzo, Nataša Škalko-Basnet, Balpreet S. Ahluwalia and Krishna Agarwal.* The manuscript is under peer review, November 2020.
- **Label-free nanoscopy enabled by coherent imaging with photonic waveguides.** *Florian Ströhl, Ida S. Opstad, Jean-Claude Tinguely, Firehun T. Dullo, Clemens F. Kaminski, and Balpreet S. Ahluwalia.* Published in SPIE Proceedings, 2019
- **Super-condenser enables labelfree nanoscopy.** *Florian Ströhl, Ida S. Opstad, Jean-Claude Tinguely, Firehun T. Dullo, Ioanna Mela, Johannes W. M. Osterrieth, Balpreet S. Ahluwalia, and Clemens F. Kaminski.* Published in Optics Express, 2019
- **Simulation-supervised deep learning for analysing organelles states and behaviour in living cells.** *Arif Ahmed Sekh, Ida S. Opstad, Rohit Agarwal, Asa Birna Birgisdottir, Truls Myrnel, Balpreet Singh Ahluwalia, Krishna Agarwal, Dilip K. Prasad.* On ArXiv from Aug 2020.
- **Soft thresholding schemes for multiple signal classification algorithm.** *Sebastian Acuña, Ida S. Opstad, Fred Godtlielsen, Balpreet Singh Ahluwalia, Krishna Agarwal.* Published in Optics Express, 2020.
- **Artefact removal in ground truth deficient fluctuations-based nanoscopy images using deep learning.** *Suyog Jadhav, Sebastian Acuña, Ida S. Opstad, Balpreet Singh Ahluwalia, Krishna Agarwal, Dilip K. Prasad.* Accepted in Optics Express, November 2020.



Scientific dissemination and exchange

Presented scientific talks

- Three-Color Live Cell Super-Resolution Imaging of Sub-Mitochondrial Regions. Focus on Microscopy, Bordeaux, France, April 2017.
- Live-cell multi-colour 3D SIM of human spermatozoa. Focus on microscopy, Singapore, March 2018.
- Live-cell imaging beyond conventional limits. Tekna X - Teknologi for fremtiden, Tromsø, Nov 2019
- Advanced microscopy at the Arctic University – from pathology to live-cell imaging. Universitätsklinikum Regensburg, Germany, June 2019.
- Microscopy with photonic waveguide chips. School of advanced optical technologies, Erlangen, Germany, June 2019.
- Fast, live-cell compatible nanoscopy on photonic waveguides. EMBL-UiT Joint Workshop, Tromsø, Sept 2019.
- A chip-based imaging system for fast-crawling skin cells of atlantic salmon

–A cool surface layer investigation. Next generation live-cell microscopy workshop, Tromsø, Feb 2020.

Presented scientific posters

- Live-cell optical nanoscopy of human spermatozoa. Norwegian Electro-Optics Meeting, Lofoten, April 2018.
- Adaptive fluctuation imaging captures rapid subcellular dynamics. European Conferences on Biomedical Optics, Munich, Germany, June 2019.
- A chip-based imaging system for fast-crawling skin cells of Atlantic salmon –a cool surface layer investigation. Next generation live-cell microscopy workshop, Tromsø, Feb 2020.

Research stay

- Laser Analytics Group, University of Cambridge, UK. Aug 2018 - Mar 2019.

Bibliography

- [1] Katarina Logg, Kristofer Bodvard, and Mikael Käll. Optical microscopy. *Chalmers Dept, Appl. Phys.*, pages 1–20, 2006.
- [2] Aashish Ranjan, Brad T Townsley, Yasunori Ichihashi, Neelima R Sinha, and Daniel H Chitwood. An intracellular transcriptomic atlas of the giant coenocyte caulerpa taxifolia. *PLoS genetics*, 11(1), 2015.
- [3] James T Staley. Bacteria, their smallest representatives and subcellular structures, and the purported precambrian fossil “metallogenium”. In *Size Limits of Very Small Microorganisms: Proceedings of a Workshop*, pages 62–67. National Academies Press, 1999.
- [4] Sheila A Stewart, Derek M Dykxhoorn, Deborah Palliser, Hana Mizuno, Evan Y Yu, Dong Sung An, David M Sabatini, Irvin SY Chen, William C Hahn, Phillip A Sharp, et al. Lentivirus-delivered stable gene silencing by rnaï in primary cells. *Rna*, 9(4):493–501, 2003.
- [5] Kelvinsong. Animal cell.svg. https://commons.wikimedia.org/wiki/File:Animal_Cell.svg, Accessed: 06.03.2020.
- [6] Louisa Howard. Lung mitochondria. https://commons.wikimedia.org/wiki/File:Mitochondria_mammalian_lung_-_TEM.jpg, Accessed: 06.03.2020.
- [7] Ron Milo and Rob Phillips. Cell biology by the numbers. <http://book.bionumbers.org/how-big-is-a-human-cell>, Accessed: 06.03.2020.
- [8] Laura L Lackner. The expanding and unexpected functions of mitochondria contact sites. *Trends in cell biology*, 2019.
- [9] Jatta Huotari and Ari Helenius. Endosome maturation. *The EMBO journal*, 30(17):3481–3500, 2011.
- [10] Ulrike Schnell, Freark Dijk, Klaas A Sjollema, and Ben NG Giepmans.

- Immunolabeling artifacts and the need for live-cell imaging. *Nature methods*, 9(2):152, 2012.
- [11] Niels de Jonge and Diana B Peckys. Live cell electron microscopy is probably impossible. *ACS nano*, 10(10):9061–9063, 2016.
- [12] ThermoFisher Scientific. Fluorescence spectraviewer. <https://www.thermofisher.com/no/en/home/life-science/cell-analysis/labeling-chemistry/fluorescence-spectraviewer.html>, Accessed: 18.11.2020.
- [13] Jacobkhed. Jablonski diagram of absorbance, non-radiative decay, and fluorescence. <https://commons.wikimedia.org/w/index.php?curid=19180813>, Accessed: 13.10.2020.
- [14] Ulrich Kubitscheck. *Fluorescence Microscopy From Principles to Biological Applications*. Second edition. Wiley-VCH Verlag GmbH Co., 2017.
- [15] Scott A Hilderbrand. Labels and probes for live cell imaging: overview and selection guide. In *Live Cell Imaging*, pages 17–45. Springer, 2010.
- [16] Sascha Conic, Dominique Desplancq, László Tora, and Etienne Weiss. Electroporation of labeled antibodies to visualize endogenous proteins and posttranslational modifications in living metazoan cell types. *Bio-protocol*, 8(21), 2018.
- [17] National institute on alcohol abuse and alcoholism (NIAAA). Structural changes of cells undergoing necrosis or apoptosis. https://commons.wikimedia.org/wiki/File:Structural_changes_of_cells_undergoing_necrosis_or_apoptosis.png, Accessed: 18.11.2020.
- [18] Sina Wäldchen, Julian Lehmann, Teresa Klein, Sebastian Van De Linde, and Markus Sauer. Light-induced cell damage in live-cell super-resolution microscopy. *Scientific reports*, 5:15348, 2015.
- [19] Singlet oxygen–mediated protein oxidation: Evidence for the formation of reactive side chain peroxides on tyrosine residues¶.
- [20] RA Hoebe, CH Van Oven, Th WJ Gadella, PB Dhonukshe, CJF Van Noorden, and EMM Manders. Controlled light-exposure microscopy reduces photobleaching and phototoxicity in fluorescence live-cell imaging. *Nature biotechnology*, 25(2):249–253, 2007.
- [21] John H Stockley, Kimberley Evans, Moritz Matthey, Katrin Volbracht, Sylvia Agathou, Jana Mukanowa, Juan Burrone, and Ragnhildur T Káradóttir.

- Surpassing light-induced cell damage in vitro with novel cell culture media. *Scientific reports*, 7(1):1–11, 2017.
- [22] Jaroslav Icha, Michael Weber, Jennifer C Waters, and Caren Norden. Phototoxicity in live fluorescence microscopy, and how to avoid it. *BioEssays*, 39(8):1700003, 2017.
- [23] P Philippe Laissue, Rana A Alghamdi, Pavel Tomancak, Emmanuel G Reynaud, and Hari Shroff. Assessing phototoxicity in live fluorescence imaging. *Nature methods*, 14(7):657–661, 2017.
- [24] Kalina L Tosheva, Yue Yuan, Pedro Matos Pereira, Siân Culley, and Ricardo Henriques. Between life and death: strategies to reduce phototoxicity in super-resolution microscopy. *Journal of Physics D: Applied Physics*, 53(16):163001, feb 2020.
- [25] Ida S Opstad, Deanna L Wolfson, Cristina I Øie, and Balpreet S Ahluwalia. Multi-color imaging of sub-mitochondrial structures in living cells using structured illumination microscopy. *Nanophotonics*, 7(5):935–947, 2018.
- [26] Sakurambo. Airy-3d. <https://commons.wikimedia.org/w/index.php?curid=51666894>, Accessed: 24.03.2020.
- [27] Spencer Bliven. Airy disk spacing near rayleigh criterion. https://commons.wikimedia.org/wiki/File:Airy_disk_spacing_near_Rayleigh_criterion.png, Accessed: 24.03.2020.
- [28] Silvio O. Rizzoli Eugenio F. Fornasiero. *Super-Resolution Microscopy Techniques in the Neurosciences*. Humana press, Springer protocols, 2014.
- [29] Default007. Convolution illustrated eng.png. <https://commons.wikimedia.org/w/index.php?curid=877065>, Accessed: 15.10.2020.
- [30] Justin Demmerle, Cassandravictoria Innocent, Alison J North, Graeme Ball, Marcel Müller, Ezequiel Miron, Atsushi Matsuda, Ian M Dobbie, Yolanda Markaki, and Lothar Schermelleh. Strategic and practical guidelines for successful structured illumination microscopy. *Nature protocols*, 12(5):988–1010, 2017.
- [31] Jean-Baptiste Sibarita. Deconvolution microscopy. In *Microscopy Techniques*, pages 201–243. Springer, 2005.
- [32] Christian Eggeling, Katrin I. Willig, Steffen J. Sahl, and Stefan W. Hell. Lens-based fluorescence nanoscopy. *Quarterly Reviews of Biophysics*,

48(2):178–243, 2015.

- [33] Markus Sauer and Mike Heilemann. Single-molecule localization microscopy in eukaryotes. *Chemical Reviews*, 117(11):7478–7509, 2017. PMID: 28287710.
- [34] Sven Truckenbrodt, Christoph Sommer, Silvio O Rizzoli, and Johann G Danzl. A practical guide to optimization in x10 expansion microscopy. *Nature protocols*, 14(3):832–863, 2019.
- [35] Ponor. Moiré pattern arising from the superposition of two graphene lattices twisted by 4° . <https://commons.wikimedia.org/w/index.php?curid=91250759>, Accessed: 17.10.2020.
- [36] Randy J Giedt, Douglas R Pfeiffer, Anastasios Matzavinos, Chiu-Yen Kao, and B Rita Alevriadou. Mitochondrial dynamics and motility inside living vascular endothelial cells: role of bioenergetics. *Annals of biomedical engineering*, 40(9):1903–1916, 2012.
- [37] Xiaoshuai Huang, Junchao Fan, Liuju Li, Haosen Liu, Runlong Wu, Yi Wu, Lisi Wei, Heng Mao, Amit Lal, Peng Xi, et al. Fast, long-term, super-resolution imaging with hessian structured illumination microscopy. *Nature biotechnology*, 36(5):451, 2018.
- [38] Thomas Dertinger, Ryan Colyer, Gopal Iyer, Shimon Weiss, and Jörg Enderlein. Fast, background-free, 3d super-resolution optical fluctuation imaging (sofi). *Proceedings of the National Academy of Sciences*, 106(52):22287–22292, 2009.
- [39] Idir Yahiatene, Simon Hennig, Marcel Muller, and Thomas Huser. Entropy-based super-resolution imaging (esi): From disorder to fine detail. *Acs Photonics*, 2(8):1049–1056, 2015.
- [40] Nils Gustafsson, Siân Culley, George Ashdown, Dylan M Owen, Pedro Matos Pereira, and Ricardo Henriques. Fast live-cell conventional fluorophore nanoscopy with imagej through super-resolution radial fluctuations. *Nature communications*, 7(1):1–9, 2016.
- [41] Krishna Agarwal and Radek Macháň. Multiple signal classification algorithm for super-resolution fluorescence microscopy. *Nature communications*, 7(1):1–9, 2016.
- [42] Weisong Zhao, Jian Liu, Chenqi Kong, Yixuan Zhao, Changliang Guo, Chenguang Liu, Xiangyan Ding, Xumin Ding, Jiubin Tan, and Haoyu Li.

- Faster super-resolution imaging with auto-correlation two-step deconvolution. *arXiv preprint arXiv:1809.07410*, 2018.
- [43] Justin Demmerle, Eva Wegel, Lothar Schermelleh, and Ian M. Dobbie. Assessing resolution in super-resolution imaging. *Methods*, 88:3 – 10, 2015. Super-resolution Light Microscopy.
- [44] M. Erdélyi, J. Sinkó, R. Kákonyi, A. Kelemen, E. Rees, D. Varga, and G. Szabó. Origin and compensation of imaging artefacts in localization-based super-resolution microscopy. *Methods*, 88:122 – 132, 2015. Super-resolution Light Microscopy.
- [45] Sami Koho, Elnaz Fazeli, John E Eriksson, and Pekka E Hänninen. Image quality ranking method for microscopy. *Scientific reports*, 6:28962, 2016.
- [46] Graeme Ball, Justin Demmerle, Rainer Kaufmann, Ilan Davis, Ian M Dobbie, and Lothar Schermelleh. Erratum: Simcheck: a toolbox for successful super-resolution structured illumination microscopy. *Scientific reports*, 6(1):1–1, 2016.
- [47] Jürgen J Schmied, Andreas Gietl, Phil Holzmeister, Carsten Forthmann, Christian Steinhauer, Thorben Dammeyer, and Philip Tinnefeld. Fluorescence and super-resolution standards based on dna origami. *Nature methods*, 9(12):1133–1134, 2012.
- [48] Niccolò Banterle, Khanh Huy Bui, Edward A. Lemke, and Martin Beck. Fourier ring correlation as a resolution criterion for super-resolution microscopy. *Journal of Structural Biology*, 183(3):363 – 367, 2013.
- [49] Adrien Charles Descloux, Kristin Stefanie Grussmayer, and Aleksandra Radenovic. Parameter-free image resolution estimation based on decorrelation analysis. *Nature methods*, 16(ARTICLE):918–924, 2019.
- [50] Siân Culley, David Albrecht, Caron Jacobs, Pedro Matos Pereira, Christophe Leterrier, Jason Mercer, and Ricardo Henriques. Nanoj-squirrel: quantitative mapping and minimisation of super-resolution optical imaging artefacts. *BioRxiv*, page 158279, 2017.
- [51] Romain F Laine, Kalina L Tosheva, Nils Gustafsson, Robert DM Gray, Pedro Almada, David Albrecht, Gabriel T Risa, Fredrik Hurtig, Ann-Christin Lindås, Buzz Baum, et al. Nanoj: a high-performance open-source super-resolution microscopy toolbox. *Journal of Physics D: Applied Physics*, 52(16):163001, 2019.

- [52] Lucas von Chamier, Johanna Jukkala, Christoph Spahn, Martina Lerche, Sara Hernández-pérez, Pieta Mattila, Eleni Karinou, Seamus Holden, Ahmet Can Solak, Alexander Krull, Tim-Oliver Buchholz, Florian Jug, Loic Alain Royer, Mike Heilemann, Romain F. Laine, Guillaume Jacquemet, and Ricardo Henriques. Zerocostdl4mic: an open platform to simplify access and use of deep-learning in microscopy. *bioRxiv*, 2020.
- [53] Martin Weigert, Uwe Schmidt, Tobias Boothe, Andreas Müller, Alexandr Dibrov, Akanksha Jain, Benjamin Wilhelm, Deborah Schmidt, Coleman Broaddus, Siân Culley, et al. Content-aware image restoration: pushing the limits of fluorescence microscopy. *Nature methods*, 15(12):1090–1097, 2018.
- [54] Eric M. Christiansen, Samuel J. Yang, D. Michael Ando, Ashkan Javaherian, Gaia Skibinski, Scott Lipnick, Elliot Mount, Alison O’Neil, Kevan Shah, Alicia K. Lee, Piyush Goyal, William Fedus, Ryan Poplin, Andre Esteva, Marc Berndl, Lee L. Rubin, Philip Nelson, and Steven Finkbeiner. In silico labeling: Predicting fluorescent labels in unlabeled images. *Cell*, 173(3):792 – 803.e19, 2018.
- [55] Yair Rivenson, Zoltán Göröcs, Harun Günaydin, Yibo Zhang, Hongda Wang, and Aydogan Ozcan. Deep learning microscopy. *Optica*, 4(11):1437–1443, 2017.
- [56] Wenming Yang, Xuechen Zhang, Yapeng Tian, Wei Wang, Jing-Hao Xue, and Qingmin Liao. Deep learning for single image super-resolution: A brief review. *IEEE Transactions on Multimedia*, 21(12):3106–3121, 2019.
- [57] Elias Nehme, Lucien E. Weiss, Tomer Michaeli, and Yoav Shechtman. Deep-storm: super-resolution single-molecule microscopy by deep learning. *Optica*, 5(4):458–464, Apr 2018.
- [58] Wei Ouyang, Andrey Aristov, Mickaël Lelek, Xian Hao, and Christophe Zimmer. Deep learning massively accelerates super-resolution localization microscopy. *Nature biotechnology*, 36(5):460–468, 2018.
- [59] Luhong Jin, Bei Liu, Fenqiang Zhao, Stephen Hahn, Bowei Dong, Ruiyan Song, Timothy C Elston, Yingke Xu, and Klaus M Hahn. Deep learning enables structured illumination microscopy with low light levels and enhanced speed. *bioRxiv*, page 866822, 2019.
- [60] Hongda Wang, Yair Rivenson, Yiyin Jin, Zhensong Wei, Ronald Gao, Harun Günaydin, Laurent A Bentolila, Comert Kural, and Aydogan Ozcan. Deep learning enables cross-modality super-resolution in fluorescence

- microscopy. *Nature Methods*, 16(1):103–110, 2019.
- [61] ML Martin-Fernandez, CJ Tynan, and SED Webb. A ‘pocket guide’ to total internal reflection fluorescence. *Journal of microscopy*, 252(1):16–22, 2013.
- [62] Jfmelero (adapted by Gavin R Putland). File:reflexiontotal.svg. <https://commons.wikimedia.org/w/index.php?curid=77502540>, Accessed: 05.04.2020.
- [63] D.Derigs (adapted from Kondelphy’s work). File:fitr penetration depth.svg. <https://commons.wikimedia.org/w/index.php?curid=26758687>, Accessed: 05.04.2020.
- [64] Jérôme Boulanger, Charles Gueudry, Daniel Münch, Bertrand Cinquin, Perrine Paul-Gilloteaux, Sabine Bardin, Christophe Guérin, Fabrice Senger, Laurent Blanchoin, and Jean Salamero. Fast high-resolution 3d total internal reflection fluorescence microscopy by incidence angle scanning and azimuthal averaging. *Proceedings of the National Academy of Sciences*, 111(48):17164–17169, 2014.
- [65] Cheng Zheng, Guangyuan Zhao, Wenjie Liu, Youhua Chen, Zhimin Zhang, Luhong Jin, Yingke Xu, Cuifang Kuang, and Xu Liu. 3d super-resolved multi-angle tfrf via polarization modulation. *arXiv preprint arXiv:1801.00882*, 2018.
- [66] Alan M. Szalai, Bruno Siarry, Jerónimo Lukin, David J. Williamson, Nicolás Unsain, Raquel Becerra, Damián Refojo, Alfredo Cáceres, Mauricio Pilo-Pais, Guillermo Acuna, Dylan M. Owen, Sabrina Simoncelli, and Fernando D. Stefani. Three-dimensional total internal reflection fluorescence nanoscopy with sub-10 nm resolution. *bioRxiv*, 2019.
- [67] Gringer talk. Optical-fibre.png. Public Domain, <https://commons.wikimedia.org/w/index.php?curid=91250759>, Accessed: 17.10.2020.
- [68] Shankar Kumar Selvaraja and Purnima Sethi. Review on optical waveguides. *Emerging Waveguide Technol*, 95, 2018.
- [69] Jean-Claude Tinguely, Øystein Ivar Helle, and Balpreet Singh Ahluwalia. Silicon nitride waveguide platform for fluorescence microscopy of living cells. *Optics express*, 25(22):27678–27690, 2017.
- [70] Robin Diekmann, Øystein I Helle, Cristina I Øie, Peter McCourt, Thomas R Huser, Mark Schützel, and Balpreet S Ahluwalia. Chip-based wide field-of-view nanoscopy. *Nature Photonics*, 11(5):322, 2017.

- [71] Dawid Kulik. Total internal reflection fluorescence microscope. https://commons.wikimedia.org/wiki/File:Total_Internal_Reflection_Fluorescence_Microscopy.svg, Accessed: 24.03.2020.
- [72] WV Holt, F Shenfield, T Leonard, TD Hartman, RD North, and HDM Moore. The value of sperm swimming speed measurements in assessing the fertility of human frozen semen. *Human Reproduction*, 4(3):292–297, 1989.
- [73] Ida S Opstad, Daria A Popova, Ganesh Acharya, Purusotam Basnet, and Balpreet S Ahluwalia. Live-cell imaging of human spermatozoa using structured illumination microscopy. *Biomedical optics express*, 9(12):5939–5945, 2018.
- [74] Ida S Opstad, Florian Ströhl, Ása B Birgisdottir, Sebastián Maldonado, Trine Kalstad, Truls Myrmel, Krishna Agarwal, and Balpreet S Ahluwalia. Adaptive fluctuation imaging captures rapid subcellular dynamics. In *European Conference on Biomedical Optics*, page 11076_72. Optical Society of America, 2019.
- [75] Sebastian Acuña, Florian Ströhl, Ida S Opstad, Balpreet S Ahluwalia, and Krishna Agarwal. Musij: an imagej plugin for video nanoscopy. *Biomedical Optics Express*, 11(5):2548–2559, 2020.
- [76] Ricardo Henriques, Mickael Lelek, Eugenio F Fornasiero, Flavia Valtorta, Christophe Zimmer, and Musa M Mhlanga. Quickpalm: 3d real-time photoactivation nanoscopy image processing in imagej. *Nature methods*, 7(5):339–340, 2010.
- [77] Arif Ahmed Sekh, Ida Sundvor Opstad, Asa Birna Birgisdottir, Truls Myrmel, Balpreet Singh Ahluwalia, Krishna Agarwal, and Dilip K Prasad. Learning nanoscale motion patterns of vesicles in living cells. In *Proceedings of the IEEE/CVF Conference on Computer Vision and Pattern Recognition*, pages 14014–14023, 2020.
- [78] Ida S Opstad, Sebastian Acuña, Luís Enrique Villegas Hernandez, Jennifer Cauzzo, Nataša Škalko-Basnet, Balpreet S Ahluwalia, and Krishna Agarwal. Fluorescence fluctuations-based super-resolution microscopy techniques: an experimental comparative study. *arXiv preprint arXiv:2008.09195*, 2020.
- [79] Stefan Geissbuehler, Noelia L Bocchio, Claudio Dellagiacoma, Corinne Berclaz, Marcel Leutenegger, and Theo Lasser. Mapping molecular statistics with balanced super-resolution optical fluctuation imaging (bsofi). *Optical Nanoscopy*, 1(1):4, 2012.

- [80] Richard J Marsh, Karin Pfisterer, Pauline Bennett, Liisa M Hirvonen, Mathias Gautel, Gareth E Jones, and Susan Cox. Artifact-free high-density localization microscopy analysis. *Nature methods*, 15(9):689–692, 2018.
- [81] Susan Cox, Edward Rosten, James Monypenny, Tijana Jovanovic-Talisman, Dylan T Burnette, Jennifer Lippincott-Schwartz, Gareth E Jones, and Rainer Heintzmann. Bayesian localization microscopy reveals nanoscale podosome dynamics. *Nature methods*, 9(2):195–200, 2012.
- [82] Oren Solomon, Yonina C Eldar, Maor Mutzafi, and Mordechai Segev. Sparcom: Sparsity based super-resolution correlation microscopy. *SIAM Journal on Imaging Sciences*, 12(1):392–419, 2019.
- [83] Sébastien Mailfert, Jérôme Touvier, Lamia Benyoussef, Roxane Fabre, Asma Rabaoui, Marie-Claire Blache, Yannick Hamon, Sophie Brustlein, Serge Monneret, Didier Marguet, et al. A theoretical high-density nanoscopy study leads to the design of unloc, a parameter-free algorithm. *Biophysical journal*, 115(3):565–576, 2018.
- [84] Ida S Opstad, Florian Strohl, Marcus Fantham, Colin Hockings, Oliver Vanderpoorten, Francesca van Tartwijk, Julie Qiaojin Lin, Jean-Claude Tinguely, Firehun T Dullo, Gabriele S Kaminski-Schierle, et al. A waveguide imaging platform for live-cell tirf imaging of neurons over large fields of view. *bioRxiv*, 2019.
- [85] Sebastian Acuña, Ida S Opstad, Fred Godtlielsen, Balpreet Singh Ahluwalia, and Krishna Agarwal. Soft thresholding schemes for multiple signal classification algorithm. *Optics Express*, 28(23):34434–34449, 2020.
- [86] Suyog Jadhav, Sebastian Acuña, Krishna Agarwal, et al. Artefact removal in ground truth and noise model deficient sub-cellular nanoscopy images using auto-encoder deep learning. *arXiv preprint arXiv:2009.02617*, 2020.
- [87] Chang Ling, Chonglei Zhang, Mingqun Wang, Fanfei Meng, Luping Du, and Xiaocong Yuan. Fast structured illumination microscopy via deep learning. *Photonics Research*, 8(8):1350–1359, 2020.
- [88] Luhong Jin, Bei Liu, Fenqiang Zhao, Stephen Hahn, Bowei Dong, Ruiyan Song, Timothy C Elston, Yingke Xu, and Klaus M Hahn. Deep learning enables structured illumination microscopy with low light levels and enhanced speed. *Nature Communications*, 11(1):1–7, 2020.

